

**NON-INVASIVE VISUALIZATION AND QUANTIFICATION OF  
(DISTURBED) HEPATOBILIARY TRANSPORT**

**Sara Neyt**

Thesis submitted to obtain the degree of  
Doctor in Pharmaceutical Sciences

**2016**

Promotor: Prof. dr. Apr. Filip De Vos

Copromotor: Prof. dr. ir. Christian Vanhove

*Members of the Examination Committee*

Prof. dr. Christophe Stove

Faculty of Pharmaceutical Sciences, Ghent University

Prof. dr. Katrien Remaut

Faculty of Pharmaceutical Sciences, Ghent University

Prof. Dr. Bieke Lambert

Faculty of Medicine, Ghent University

Prof. dr. Pieter Annaert

Faculty of Pharmaceutical Sciences, KULeuven

dr. Geert Mannens

Janssen Pharmaceutical Companies of Johnson & Johnson, Beerse

The author and promoters give the authorization to consult and to copy parts of this thesis for personal use only. Any other use is limited by the Laws of Copyright, especially concerning the obligation to refer to the source whenever results are cited from this thesis.

De auteur en promotoren geven de toestemming dit proefschrift voor raadpleging ter beschikking te stellen en delen ervan te kopiëren voor persoonlijk gebruik. Elk ander gebruik valt onder de beperking van het auteursrecht, in het bijzonder tot de verplichting de bron te vermelden bij het aanhalen van resultaten uit deze thesis.

Gent, Mei 2016

Sara Neyt



# Table of contents

TABLE OF CONTENTS

LIST OF ABBREVIATIONS

<b>Chapter 1. General introduction</b>	<b>1</b>
OVERVIEW	3
PART I: THE LIVER	4
Anatomy and physiology of the liver	4
The enterohepatic cycle	7
Bile acid biosynthesis	10
Initiation	11
Ring structure modification	13
Side chain oxidation	14
Conjugation	16
Secondary bile acids	18
Bile acid transporters of the enterohepatic cycle	18
Sinusoidal (basolateral) uptake	19
Alternative basolateral bile acid efflux	22
Canalicular excretion	22
Intestinal bile acid uptake	24
Intestinal bile acid efflux	24
Bile acid transporters in cholangiocytes and renal epithelial cells	25
Drug-induced liver injury	27
PART II: MOLECULAR IMAGING	31
Medical Imaging	31
Multi-modality	32
Molecular imaging	32
Molecular imaging and nuclear medicine	36

PET	36
SPECT	38
Small animal imaging	40
Dynamic imaging and kinetic modeling	45
REFERENCES	48
<b>Chapter 2. Functional hepatobiliary imaging</b>	<b>55</b>
INTRODUCTION	57
HEPATOBIILIARY CONTRAST AGENTS IN MAGNETIC RESONANCE IMAGING	58
Extracellular contrast agents	58
Reticuloendothelial contrast agents	59
Blood pool contrast agents	59
Hepatobiliary contrast agents	60
Hepatobiliary contrast agents used in the clinic – transporter substrates	60
Bile acid analogues	62
FLUORESCENT HEPATOBIILIARY CONTRAST AGENTS	65
PET TRACERS	68
Transporter substrates	68
Bile acid analogues	69
SPECT TRACERS	72
[ <sup>99m</sup> Tc]mebrofenin	72
[ <sup>99m</sup> Tc]Galactosyl serum albumin	73
Bile acid analogues	74
REFERENCES	75
<b>Chapter 3. Scope and aims</b>	<b>79</b>
<b>Chapter 4. Calibration curves</b>	<b>85</b>
NAI(TL) SCINTILLATION DETECTOR	87
μSPECT	87

**Chapter 5. *In vivo* visualization and quantification of normal and disturbed hepatobiliary transport by means of [<sup>99m</sup>Tc]mebrofenin 89**

INTRODUCTION	91
MATERIALS AND METHODS	94
<i>In vitro</i> assays	94
Murine models	95
Radionuclides, radiopharmaceuticals and chemicals	95
Molecular imaging	95
Determination of the [ <sup>99m</sup> Tc]mebrofenin blood curve	98
Statistical and kinetic analysis	99
RESULTS	100
<i>In vitro</i> assessment of the potential role of OCT1	100
Interanimal and intra-animal variation of the dynamic $\mu$ SPECT acquisitions	101
Interanimal variation	101
Intra-animal variation of the dynamic $\mu$ SPECT acquisitions	102
Wild-type FVB mice	103
Bile duct ligation: proof-of-principle	105
Role of Oatp1a/1b transporters in the hepatic transport of [ <sup>99m</sup> Tc]mebrofenin	107
Role of the Mrp2 transporter in the hepatic transport of [ <sup>99m</sup> Tc]-mebrofenin	109
The effect of different rifampicin doses on the hepatic transport of [ <sup>99m</sup> Tc]mebrofenin	110
DISCUSSION	114
REFERENCES	117

**Chapter 6. Kinetic modeling of [<sup>99m</sup>Tc]mebrofenin as a tool to quantify altered hepatobiliary transport 119**

INTRODUCTION	121
MATERIALS AND METHODS	123
Animal Model	123

Molecular Imaging	123
Correlation of image derived blood function with manual blood samples	125
Kinetic modeling	125
Statistical Analysis	126
RESULTS	127
Correlation of image derived blood function with manual blood samples	127
Kinetic Modeling	128
DISCUSSION	130
REFERENCES	132
<b>Chapter 7. [<sup>99m</sup>Tc]mebrofenin transport in a humanized mouse model</b>	<b>133</b>
INTRODUCTION	135
MATERIALS AND METHODS	138
Animal Model	138
Molecular Imaging	138
Statistical analysis	139
RESULTS	140
[ <sup>99m</sup> Tc]MEB disposition in mice with liver disease (heterozygous mice)	140
[ <sup>99m</sup> Tc]MEB disposition in chimeric (humanized) mice	141
DISCUSSION	144
REFERENCES	147
<b>Chapter 8. Synthesis, <i>in vitro</i> and <i>in vivo</i> evaluation of technetium labeled bile acid analogues</b>	<b>149</b>
INTRODUCTION	151
MATERIALS AND METHODS	153
General procedures and materials	153
Animal models	153
Chemistry	153



<i>In vitro</i> uptake assays	156
<i>In vitro</i> vesicular efflux assay	157
Molecular imaging	157
Statistical analysis	158
RESULTS	160
Radiosynthesis	160
<i>In vitro</i> uptake assays	160
<i>In vitro</i> vesicular efflux assay	163
Molecular imaging	163
DISCUSSION	167
REFERENCES	171
<b>Chapter 9. General discussion</b>	<b>173</b>
<b>Chapter 10. Broader international context, relevance, and future perspectives</b>	<b>181</b>
REFERENCES	189
<b>Chapter 11. Summary – Samenvatting Curriculum Vitae</b>	<b>191</b>
SUMMARY	193
SAMENVATTING	195
CURRICULUM VITAE	198

# List of abbreviations

%CV	Coefficient of variation
%ID/g	Percentage injected dose per gram
[ <sup>11</sup> C]TIC-Me	[ <sup>11</sup> C]tetranisocarbacyclin methyl ester
[ <sup>99m</sup> Tc]DTPA-CA	[ <sup>99m</sup> Tc]diethylene triamine pentaacetic acid cholic acid
[ <sup>99m</sup> Tc]DTPA-CDCA	[ <sup>99m</sup> Tc]diethylene triamine pentaacetic acid chenodeoxycholic acid
[ <sup>99m</sup> Tc]GSA	[ <sup>99m</sup> Tc]diethylenetriamine-pentaacetic acid-galactosyl human serum albumin
[ <sup>99m</sup> Tc]MEB	[ <sup>99m</sup> Tc]mebrofenin
[ <sup>99m</sup> Tc]TcO <sub>4</sub> <sup>-</sup>	Pertechnetate
μPET	Preclinical positron emission tomography
μSPECT	Preclinical single photon emission computed tomography
2D	Two dimensional
3D	Three dimensional
ABC	ATP-binding cassette superfamily
AKR1C4	3α-hydroxysteroid dehydrogenase
AKR1D1	Δ <sup>4</sup> -3-oxosteroid 5β reductase
ASBT/Asbt	Apical sodium dependent bile acid transporter
ATP	Adenosine triphosphate
AUC	Area under the curve
BA	Bile acids
BDL	Bile duct ligation

BP	Biliary pigments
BSA	Bovine serum albumin
BSEP/Bsep	Bile salt export pump
C <sub>27</sub> -3 $\beta$ -HSD=HSD3B7	3 $\beta$ -hydroxy- $\Delta^5$ -C <sub>27</sub> -steroid oxidoreductase
CA	Cholic acid
CA-lys-TFA	Cholic acid-trifluoroacetyl lysine
CDCA	Cheodeoxycholic acid
CDC-NBD-L	Chenodeoxycholy1-NBD-lysine
CGamF	Cholylglycylamido fluorescein
CH25H	Cholesterol 25-hydroxylase
CHO	Chinese hamster ovary
Chol	Cholesterol
CLF	Cholyl-lysyl-fluorescein
CO <sub>2</sub>	carbon dioxide
CT	Computed Tomography
CYP27A1	Sterol 27-hydroxylase
CYP39A1	Oxysterol 7 $\alpha$ -hydroxylase
CYP46A1	Cholesterol 24-hydroxylase
CYP7A1	Cholesterol 7 $\alpha$ -hydroxylase
CYP8B1	Sterol 12 $\alpha$ -hydroxylase
Da	Dalton
DCM	Dichloromethane
DIC	Drug induced cholestasis

DILI	Drug-induced liver injury
DMEM	Dulbecco's modified Eagle's medium
DMF	Dimethylformamide
DMSO	Dimethyl sulfoxide
DTPA	Diethylenetriaminepentaacetic acid
E17 $\beta$ G	Estradiol-17 $\beta$ -glucuronide
EC	Electron capture
FDG	Fluoro-2-deoxy-D-glucose
FNH	Focal nodular hyperplasia
GBCA	Gadolinium based contrast agent
Gd-BOPTA	Gadobenate dimeglumine
Gd-EOB-DTPA	Gadoxetate disodium
HBSS	Hank's balanced salt solution
HCA	Hepatocellular adenoma
HCC	Hepatocellular carcinoma
HCl	hydrochloric acid
HCO <sub>3</sub> <sup>-</sup>	Bicarbonate
HEK	Human embryonic kidney
HEPES	4-(2-hydroxyethyl)-1-piperazineethanesulfonic acid
HIDA	Hepatic imino diacetic acid
HuAlb	Human Albumin
IBABP/Ibabp	Ileal bile acid binding protein
ICG	Indocyanine green

IDIF	Image-derived input function
IP	Intraperitoneal
IT	Isomeric transition
IV	Intravenous
k	Kinetic rate constant
K	Potassium
kDa	kilodalton
$k_m$	Michaelis menten constant
KO	Knock-out
MeCN	Acetonitrile
MeOH	Methanol
MgSO <sub>4</sub>	Magnesiumsulphate
MI	Molecular imaging
MRI	Magnetic Resonance Imaging
MRP/Mrp	Multidrug resistance-associated protein
N <sub>2</sub>	Nitrogen gas
Na	Sodium
NaHCO <sub>3</sub>	Sodium bicarbonate
NaOH	Sodium hydroxide
NBD	Nitrobenzoaxdiazolyl
NTCP/Ntcp	Na <sup>+</sup> dependent taurocholate cotransporting protein
O <sub>2</sub>	Oxygen
OATP/Oatp	Organic anion transporting polypeptide

OCT1	Organic cation transporter 1
OI	Optical imaging
OST $\alpha/\beta$ / Ost $\alpha/\beta$	Organic solute transporter $\alpha$ and $\beta$
PE	Polyethylene
PEG	Polyethyleneglycol
PET	Positron emission tomography
PL	Phospholipids
R <sub>i</sub>	Intrinsic resolution
ROI	Region of interest
RP-HPLC	Reversed phase high performance liquid chromatography
R <sub>s</sub>	Spatial resolution
S	Sensitivity
SD	Standard deviation
SLC	Solute carrier family
SLCO	Solute carrier organic anion transporter superfamily
SnCl <sub>2</sub> .2H <sub>2</sub> O	Tin(II) chloride dehydrate
SPECT	Single photon emission computed tomography
SPIO	Superparamagnetic iron oxide
TAC	Time activity curve
t-ASBT	Truncated apical sodium dependent bile acid transporter
TCA	Taurocholic acid
TEA	Tetra-ethyl-ammonium
ToF	Time of flight

uPA	Urokinase-plasminogen activator
US	Ultrasound imaging
$V_{\max}$	Maximum transport rate
WT	Wild type

# Chapter 1.

# General introduction





## Overview

The liver is an important organ for homeostasis. Drugs can interfere with the functions of the liver, which can lead to drug induced liver injury. Drug induced liver injury is a form of acquired liver disease and is a major cause of safety-related withdrawal of drugs from the market. Additionally, it is a major cause of attrition during the drug development process. Therefore, new strategies are needed to identify and characterize interactions of new candidate drugs with hepatic transporters early in the developmental process. It is important to improve the currently available prediction methods to identify and mitigate potential compound-related safety issues. This will result in safer drugs and a more efficient drug development process.

In the first part of this chapter, an overview of main liver functions is provided, with a focus on the enterohepatic cycling of bile acids, their biosynthesis and the most common bile acid transporters. Additionally, an introduction on drug induced liver injury is given. In the second part, molecular imaging and more specifically Single Photon Emission Tomography will be discussed, since these techniques will be used in this work to investigate drug-induced liver injury in a non-invasive manner.

## Part I: The Liver

### Anatomy and physiology of the liver

The liver is the biggest organ in the body and is functionally very complex. It is an important organ for homeostasis and its most important functions include glycogen storage, production of plasma proteins and bile acids, elimination of endogenous substances (e.g. cholesterol, bilirubin and their metabolites) and secretion of toxic compounds (e.g. drugs, carcinogens) (Kullak-Ublick *et al.*, 2000; Wolkoff *et al.*, 2003; Erlinger *et al.*, 1996)

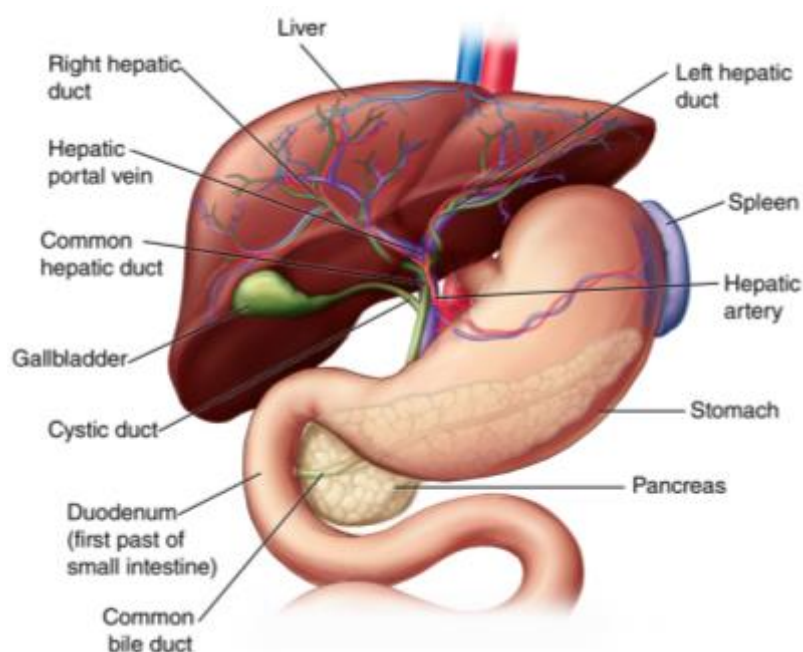


**Figure 1.1:** Anatomy of the liver and surroundings (adapted from [www.urmc.rochester.edu](http://www.urmc.rochester.edu))

The liver is located in the right upper quadrant of the abdominal cavity and it overlies the gallbladder (Figure 1.1). It consists of a left and right lobe, which each have an independent vascular supply and duct drainage. The lobes, in turn, consists of lobules, that form the functional units of the liver (Roberts *et al.*, 2002) (Figure 1.2).

The blood circuit of the liver is a unique system with a double blood supply: venous blood from the gut, pancreas and the spleen and arterial blood from the hepatic artery are delivered to the liver via a highly branched network of fenestrated blood vessels known as the liver sinusoids. In the liver sinusoids, the blood mixture has a near-direct contact with the hepatocytes. Processed blood is delivered from the sinusoids to the central veins which empty into the vena cava inferior (Treyer *et al.*, 2013)

Histologically, the liver comprises thousands of nearly identical lobules that are divided by sheets of connective tissue. The lobule is the structural and functional subunit of the liver and has a hexagonal structure, 2 mm in height and 1–1.3 mm in diameter (Figure 1.2). The lobule consists mainly of hepatocytes that are arranged radially in plates from the central vein to the portal triads. Hepatocytes account for approximately 65% of the nuclear population in the liver. They are polarized cells since they absorb substrates from the blood and secrete molecules in the bile (*Treyer et al., 2013*). They have basolateral (sinusoidal) and apical (canalicular) plasma membrane domains (*Trauner et al., 2003*). The sinusoids can be found between the hepatocyte plates, also arranged radially, and connect the vessels in the portal triad to the central vein, thus allowing nutrient and oxygen-rich blood to enter the lobule from the portal vessels and empty into the central vein. The hepatocyte sinusoidal membrane faces the small perisinusoidal space of Disse, which is located between the hepatocytes and the endothelium of the sinusoid and gives rise to a two-way exchange between the blood and hepatocytes (Figure 1.3). The sinusoid lumen houses the mononuclear phagocytic system, which comprises generally stationary Kupffer cells as well as some migrating macrophages. These cells play an essential role in host defense mechanisms and the removal of foreign small particles and substances that enter the liver (*Esteller, 2008*).

Immediately under the liver, the gallbladder can be found. The gallbladder contains bile that is produced by hepatocytes and is collected in bile canaliculi, which merge to form bile ductules (Figure 1.2). These intrahepatic ducts (within the liver) drain into the left and right hepatic ducts, which merge to form the common hepatic duct. The cystic duct from the gallbladder joins with the common hepatic duct to form the common bile duct (Figure 1.1). Bile is a major excretion route for endogenous substances and secretion of toxic compounds (*Hofmann et al., 2008*).

The biliary apparatus is a convergent system of canals that begins in the canaliculi, followed by the bile ducts, and ending with the common bile duct (choledochus) (Figure 1.2). Bile secretion depends on the function of membrane transport systems in hepatocytes and cholangiocytes and on the structural integrity of the biliary tree. The hepatocytes generate the primary bile in their canaliculi (*Esteller, 2008*). Biliary canaliculi are blind tubular structures that favor the formation of bile flow by means of osmotic gradients. Osmosis is considered to be the major mechanism of water movement during bile formation. The osmotic gradient is provided by organic and inorganic solutes secreted into bile. Therefore, bile formation is intimately related to hepatobiliary transport of biliary constituents (*Strazzabosco et al., 2008*).

The cholangiocytes, which are epithelial cells that line intrahepatic bile ducts, account for 3 to 5% of the liver cell population. They modify the canalicular bile by secretory and reabsorptive processes as bile passes through the bile ducts.

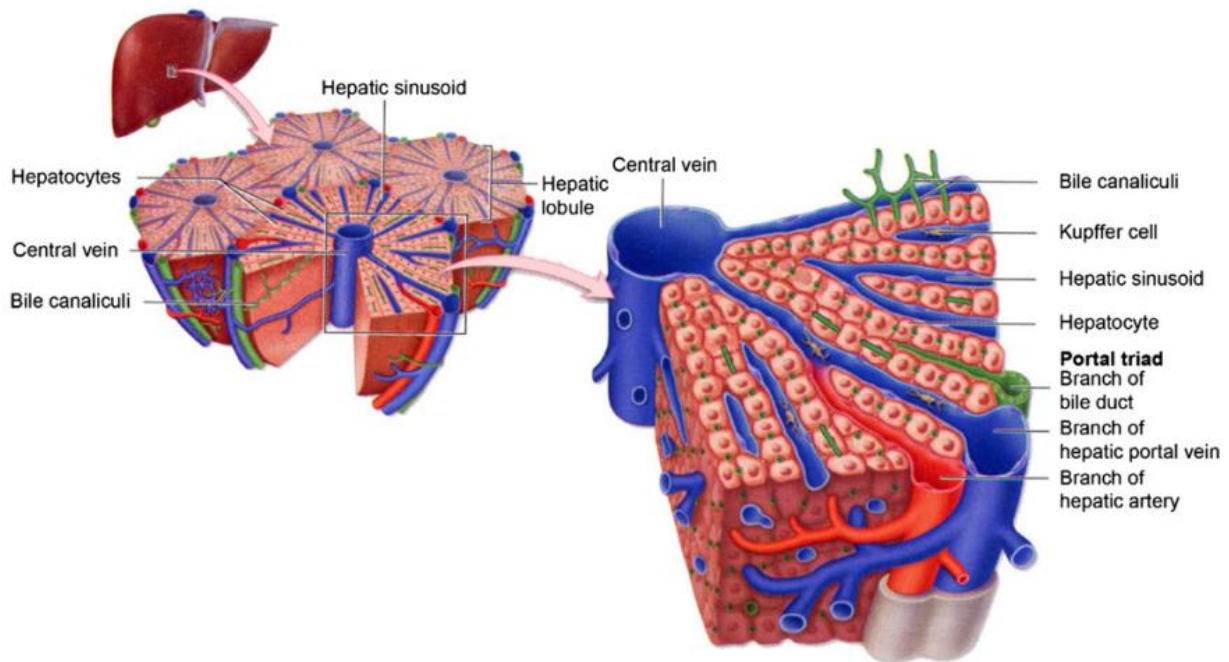


**Figure 1.2:** Microanatomy of the liver. Overview of the hepatic functional subunits or lobules. (Stenvall et al., 2014)

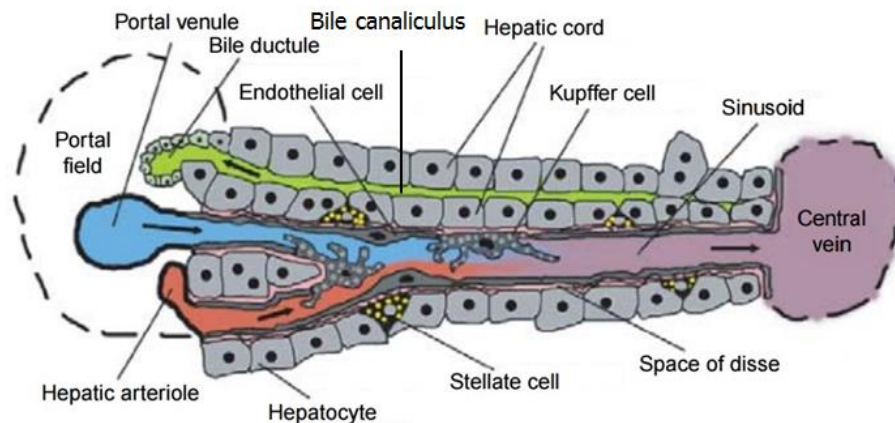


**Figure 1.3:** Liver sinusoids and surrounding tissue. Liver sinusoids are lined with fenestrated endothelia and Kupffer cells. They are separated from hepatocytes by the space of Disse. Stellate cells embrace the sinusoids inside the space of Disse. The arrows display the flow in the vessel. Hepatocytes form hepatic cords (adapted from Frevert et al., 2004).

## The enterohepatic cycle

Bile formation is a unique feature of the liver and is vital for survival of the organism (*Boyer, 2013*). Bile is a complex fluid that consists of approximately 95% water in which a number of endogenous molecules, including bile acids, bilirubin, phospholipid, cholesterol, proteins, peptides, amino acids, steroids, enzymes, vitamins and heavy metals, as well as exogenous drugs, xenobiotics and environmental toxins are dissolved (Figure 1.4). These compounds flow through the biliary tract into the small intestine (*Pellicoro et al., 2007*).

The important functions of bile according to Boyer et al. (*Boyer et al., 2013*) are:

- 1) Bile is the major excretory route for potentially harmful exogenous lipophilic substances and for other endogenous substrates such as bilirubin and bile acids whose molecular weights are >300 to 500 dalton (Da) and not readily filtered or excreted by the kidneys.
- 2) Bile acids are the major organic components in bile and normally function to emulsify dietary fat, cholesterol and fat-soluble vitamins, and facilitate their intestinal absorption.
- 3) Bile is the major elimination route of cholesterol.
- 4) Bile protects the organism from enteric infections by excreting immunoglobulin A (IgA), inflammatory cytokines, and by stimulating the innate immune system in the intestine.
- 5) Bile is an essential component of the cholehepatic and enterohepatic circulation.
- 6) Many hormones and pheromones are excreted in bile.

The main driving force of bile flow is the secretion of bile acids. The average bile flow in humans is 1.5 to 2.0 mL/min/kg body weight (*Roberts et al., 2002*). In healthy individuals, the basal concentrations of bile acids in peripheral blood are lower than 10  $\mu$ M, whereas they are in the mM range in bile (*Marin et al., 2016*). These bile acids are synthesized in the liver from cholesterol or are taken up from the sinusoidal blood as part of the enterohepatic circulation, and are actively secreted into bile and stored in the gallbladder between meals. Upon food ingestion, the duodenum secretes cholecystokinin into the blood, which consequently leads to contraction of the gallbladder and release of bile into the intestines. In the small intestine, bile has a detergent function to keep fat-soluble compounds in solution for uptake (vitamins) or excretion (cholesterol, lipophilic toxins/drugs). In the bile, bile acids form mixed micelles

with phospholipids and these are the vehicles that carry cholesterol and other lipophilic compounds through the intestine.

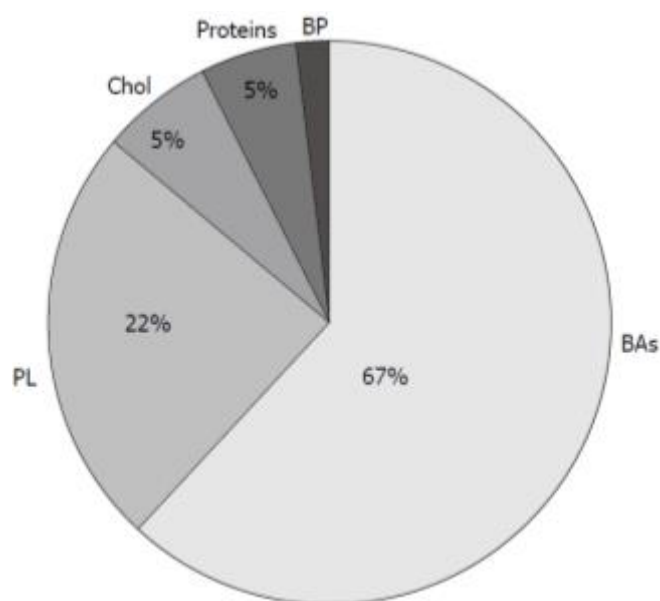


**Figure 1.4:** Composition of bile. BA=bile acids; PL=phospholipids; Chol=cholesterol; BP=biliary pigments; proteins (Esteller et al., 2008).

Figure 1.5 displays the enterohepatic cycle of bile acids. The enterohepatic circulation maintains a bile acid pool size of approximately 2-4 g in humans, and 4 mg in mice. This pool cycles 3-4 times per day and as such, the intestinal bile acids absorbed may be as much as 30 g per day in humans, and 20 mg/day in mice. This enterohepatic circulation of bile acids is an extremely efficient process, since less than 5% of the intestinal bile acids escapes reabsorption and is eliminated in the feces (Hulzebos et al., 2001; Hofmann et al., 1983; Dietschy et al., 1993; Dietschy et al., 2002). Bile acids are highly albumin bound. However, bile acids in the sinusoidal blood are efficiently taken up by the hepatocytes from Disse's space due to the existence of transporters in the basolateral membrane (Alrefai et al., 2007; Esteller et al., 2008; Kullak-Ublick et al., 2000; Kosters et al., 2008). After their dissociation from albumin, bile acids are transported across the hepatocytes to the canaliculus. Bile acid uptake across the basolateral membrane of the hepatocytes is mainly mediated by the Na<sup>+</sup>-dependent Taurocholate Cotransporting Polypeptide (NTCP). Additionally, Organic Anion Transporting Polypeptides (OATPs) are also responsible for bile acid uptake in a Na<sup>+</sup>-independent manner. Efflux to the bile across the canalicular membrane occurs via the Bile Salt Export Pump

(BSEP) and Multidrug Resistance-associated Protein 2 (MRP2). The bile acids arrive in the intestinal lumen via the bile duct. Some of the excreted bile acids are deconjugated there by the action of the bacterial flora. 95% of bile acids are efficiently reabsorbed from the intestinal lumen via passive diffusion and actively via Na<sup>+</sup>-dependent Apical Sodium Dependent Bile Acid Transporter (ASBT). Whereas passive absorption occurs down the length of the intestine, active transport of bile acids is restricted to the ileum (Dawson *et al.*, 2009). The intracellular transport of bile acids across the enterocytes is facilitated by the Ileal Bile Acid Binding Protein (IBABP), followed by efflux through Organic Solute Transporter  $\alpha$  and  $\beta$  (OST $\alpha$ /OST $\beta$ ). Bile acids then re-enter the portal blood and complete the enterohepatic cycle. Hepatic conversion of cholesterol to bile acid balances fecal excretion and this process represents a major route of cholesterol elimination from the body.

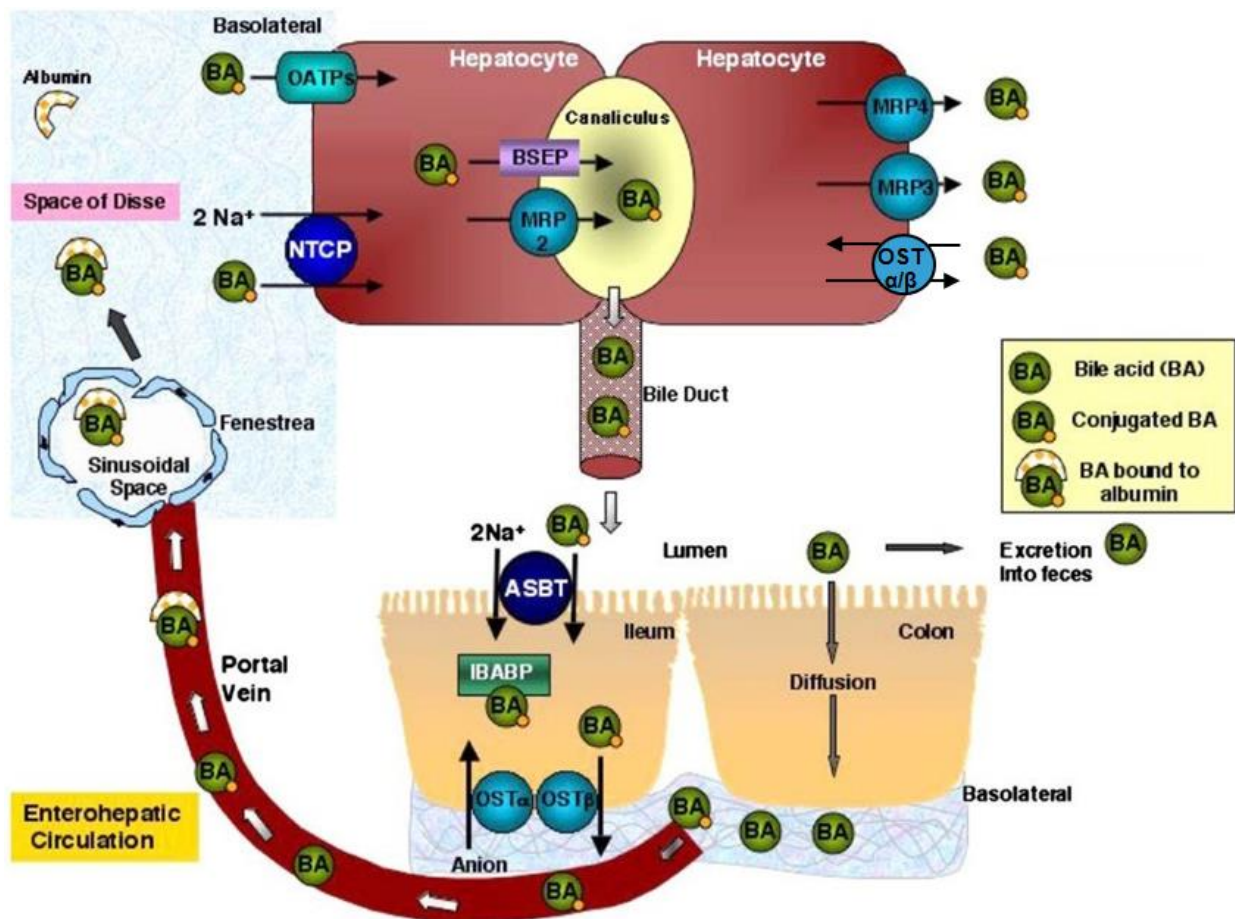
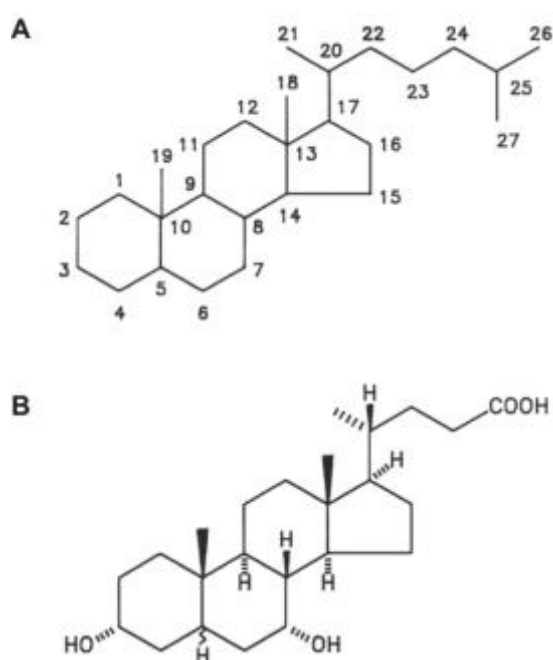


Figure 1.5: Enterohepatic circulation of bile acids (adapted from Alrefai *et al.*, 2008).



## Bile acid biosynthesis

In the 1930s, the steroid structure of bile acids was finally established (*Hofmann et al., 2014*). The first ideas came from Nobel Prize winners Heinrich Wieland and Adolf Windaus (*Wieland, 1928; Windaus, 1928*). These two chemists had slowly developed the idea that both cholesterol and bile acids share a four-ring structure with a side chain of five carbon atoms for bile acids and eight carbons for cholesterol. However, the structures of the steroid nucleus shown in their Nobel lectures were not correct. The path to the correct structure came from Desmond Bernal, a physicist, who undertook X-ray diffraction studies of organic molecules. He studied cholesterol, among other things, and published his findings in *Nature* in 1932 (*Bernal, 1932*). Finally, Rosenheim and King in London, and Wieland and Dane in Munich, published the application of Bernal's pioneering studies to the extensive literature on bile acid structure (*Rosenheim et al., 1934*). Each group proposed the cyclopentanoperhydrophenanthrene structure for the steroid nucleus. Figure 1.6 shows the structure of chenodeoxycholic acid (CDCA) and the numbering system for the steroid nucleus and side chain that was proposed in the 1930s and has been used ever since.



**Figure 1.6:** Numbering system of bile acids and bile alcohols (A). Frontal view of CDCA (B). The numbering system was developed in the 1930s when the steroid structure was finally established. (*adapted from Hofmann et al., 2014*)

Bile acid biosynthesis is an exclusively liver-specific process and starts from cholesterol and involves 17 different enzymes, many of which are preferentially expressed in the liver (*Pellicoro et al., 2007*).

The biosynthesis can be subdivided into a classic or neutral and an alternative or acidic pathway. The products that derive from these pathways are the primary bile acids. The classic pathway results in the formation of the primary bile acid cholic acid (CA) and accounts for 90% of bile acid synthesis. In contrast, the alternative pathway, which is initiated in the plasma, leads to formation of the primary bile acid CDCA. The most important difference between these two pathways is the order of reactions that transforms cholesterol to CA or CDCA and the cellular site where the first reactions take place. The chemical diversity of the bile acid pool is further expanded by the action of anaerobic bacteria in the gut, which convert primary bile acids into dozens of secondary bile acids (*Hofmann et al., 2008*).

For the conversion of cholesterol into primary bile acids, different steps can be distinguished:

- a) Initiation
- b) ring structure modification
- c) side chain oxidation and
- d) amino acid conjugation.

### Initiation

The initiation of the classic pathway includes conversion of cholesterol into 7 $\alpha$ -hydroxycholesterol by the enzyme cholesterol 7 $\alpha$ -hydroxylase (CYP7A1), expressed exclusively in the liver (Figure 1.7, reaction 1). This reaction is considered as the rate-limiting step in this route.

Cholesterol can be hydroxylated at three different positions on the side chain and this leads to formation of 24-hydroxycholesterol, 25-hydroxycholesterol and 27-hydroxycholesterol. These oxysterols serve as substrates for bile acid synthesis. Cholesterol 24-hydroxylase is the enzyme that synthesizes 24(S)-hydroxycholesterol (Figure 1.7, reaction 2) and is detectable in neurons of the brain. The enzyme contributes little to overall bile acid synthesis but is important in the turnover of cholesterol in the brain. Cholesterol 25-hydroxylase (Figure 1.7, reaction 3) that synthesizes 25-hydroxycholesterol does not contribute significantly to bile

acid synthesis, but may play a role in cholesterol catabolism in a tissue-specific fashion, as does the cholesterol 24-hydroxylase.

Sterol 27-hydroxylase (CYP27A1) synthesizes 27-hydroxycholesterol from cholesterol, which is the most abundant oxysterol in the plasma of mice and human (Figure 1.7, reaction 4). This reaction is the start of the alternative biosynthesis pathway.

To be converted into bile acids, oxysterols must undergo  $7\alpha$ -hydroxylation. Two enzymes can catalyze this step, namely CYP39A1 oxysterol  $7\alpha$ -hydroxylase and CYP7B1 oxysterol  $7\alpha$ -hydroxylase. CYP39A1 acts on 24(S)-hydroxycholesterol (Figure 1.7, reaction 5) and CYP7B1 acts on 25- and 27-hydroxycholesterol (Figure 1.7, reaction 6). CYP7B1 oxysterol  $7\alpha$ -hydroxylase is expressed at high levels in the adult liver. 5-10% of the bile acid pool in humans derives from oxysterols. (Russell, 2003)

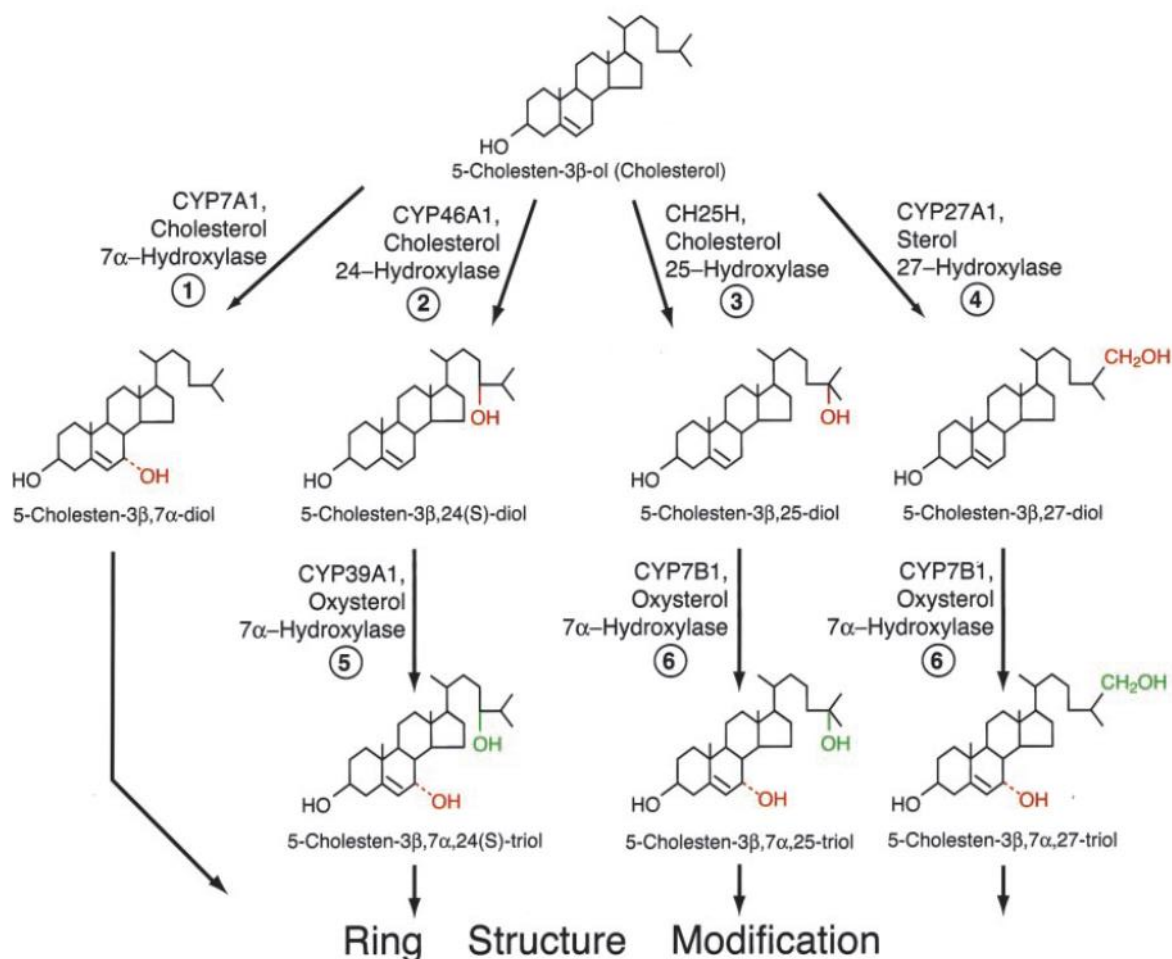


**Figure 1.7:** Hydroxylation. Cholesterol can be hydroxylated at 4 different positions. (adapted from Russell, 2003)

### Ring structure modification

Next, the  $7\alpha$ -hydroxylated intermediates derived from cholesterol and the oxysterols are converted into their 3-oxo,  $\Delta^4$  forms (Figure 1.8, reaction 7) by  $3\beta$ -hydroxy- $\Delta^5$ - $C_{27}$ -steroid oxidoreductase ( $C_{27}$ - $3\beta$ -HSD). This enzyme will act only on sterols with a  $7\alpha$ -hydroxyl group, and thus this step lies downstream of the cholesterol and oxysterol  $7\alpha$ -hydroxylases. The reaction catalyzed by these enzymes is complex and involves isomerization of the double bond from 5 to 4 position and the oxidation of the  $3\beta$ -hydroxyl to a 3-oxo group (Figure 1.8, reaction 7). Since the  $C_{27}$ - $3\beta$ -HSD enzyme is unique, loss of this enzyme blocks the synthesis of bile acids.

In a subsequent step, the products of this reaction can take one of the two routes of bile acid synthesis. In the presence of sterol  $12\alpha$ -hydroxylase, the resulting product will be converted ultimately into cholic acid (Figure 1.8, reaction 8). In the absence of sterol  $12\alpha$ -hydroxylase, the intermediates are converted into chenodeoxycholic acid or another bile acid. The concentration of sterol  $12\alpha$ -hydroxylase in the liver determines the relative amounts of the two primary bile acids, cholic acid and chenodeoxycholic acid.

Both, the  $12\alpha$ -hydroxylated intermediates and the  $C_{27}$ - $3\beta$ -HSD intermediates that escape the  $12\alpha$ -hydroxylation, are subject to reduction of the double bond in the A-ring by the enzyme  $\Delta^4$ -3-oxosteroid  $5\beta$  reductase (Figure 1.8, reaction 9).

The final step of ring modification is the reduction of the 3-oxo-group to an alcohol in the alpha stereochemical configuration and is catalyzed by  $3\alpha$ -hydroxysteroid dehydrogenase (Figure 1.8, reaction 10) (Russell, 2003)

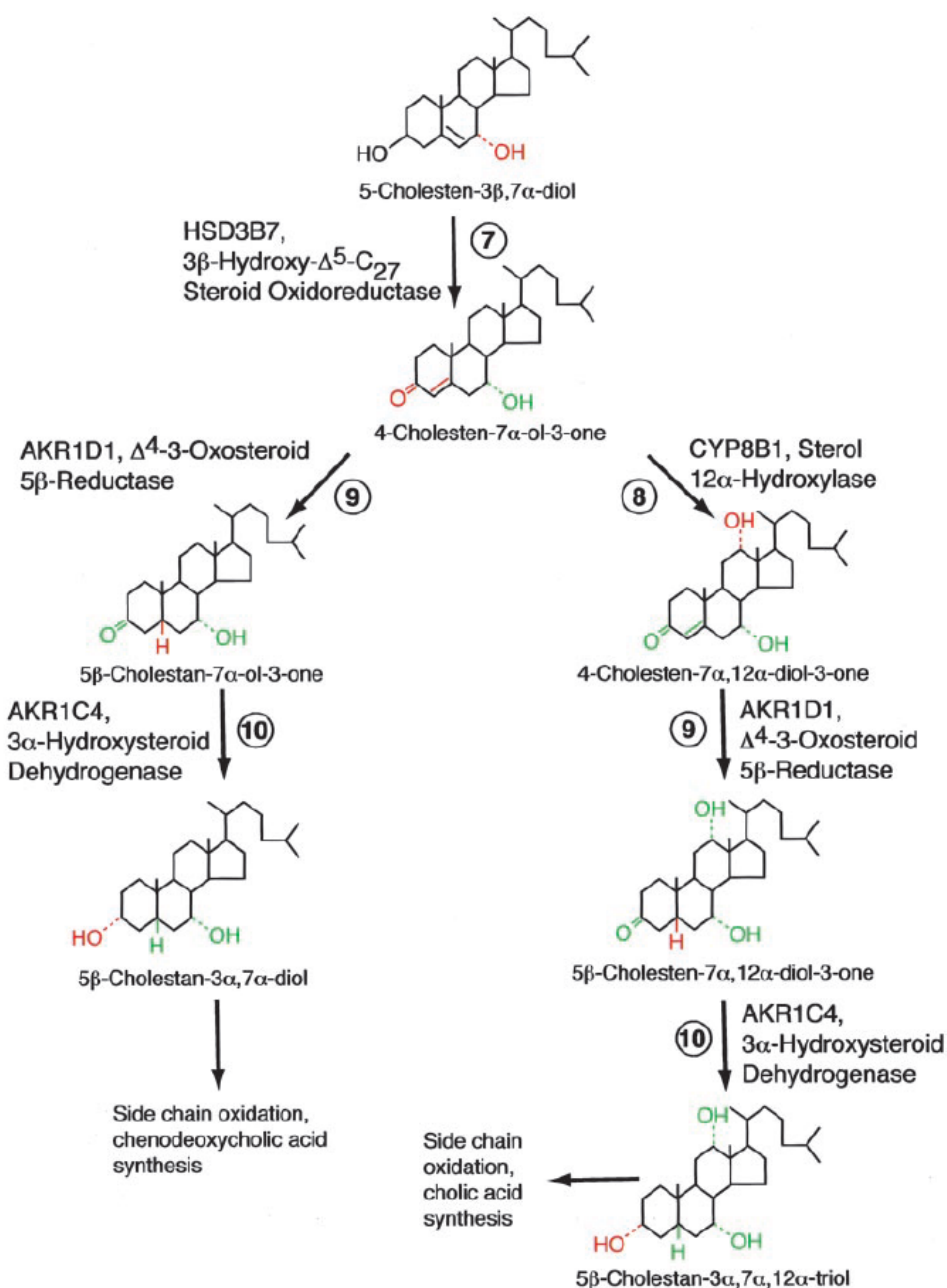


**Figure 1.8:** Ring structure modifications. 7 $\alpha$ -hydroxylated intermediates and oxysterols are converted into their 3-oxo,  $\Delta^4$  forms. In presence of sterol 12 $\alpha$ -hydroxylase, the synthesis will result in cholic acid; in the absence, it will result in chenodeoxycholic acid or another bile acid. Then, the double bonds of the A-ring are reduced. In the final step, the 3-oxo-group is reduced to an alcohol. (adapted from Russell, 2003).

### Side chain oxidation

After ring modifications, the bile acid precursors undergo progressive oxidation and shortening of the sterol side chain. The first few steps are performed by sterol 27-hydroxylase (Figure 1.9, reaction 11), the same mitochondrial cytochrome P450 (CYP27A1) that initiates

bile acid synthesis through the formation of 27-hydroxycholesterol (Figure 1.7, reaction 4). This enzyme introduces a hydroxyl group at carbon 27, oxidizes this group to an aldehyde and then to a carboxylic acid.

The oxidized bile acid intermediates are then subject to shortening of the side chain. The terminal three carbon atoms are removed by a series of reactions. The first reaction is catalyzed by bile acid coenzyme A ligase (Figure 1.9, reaction 12), which activates the sterol intermediate by conjugation with coenzyme A. After activation, the 25(R) isomers must be converted into 25(S) isomers before subsequent steps in side chain shortening can take place. This reaction is catalyzed by 2-methylacyl-coenzyme A racemase (Figure 1.9, reaction 13).

The sterol products are then subject to dehydrogenation catalyzed by the branched chain acyl coenzyme A oxidase enzyme (Figure 1.9, reaction 14). The next step involves hydration and oxidation at the  $\Delta^{24}$  bond and is catalyzed by the D-bifunctional protein (Figure 1.9, reaction 15).

The last step in the side chain shortening process is cleaving of the C<sub>24</sub>-C<sub>25</sub> bond to form propionyl-coenzyme A and a C<sub>24</sub>-coenzyme A bile acid intermediate (Figure 1.9, reaction 16). This reaction is catalyzed by peroxisomal thiolase 2 (*Russell et al., 2003*).

Coenzyme A esterase in the peroxisomes can catalyze the hydrolysis of bile acid thioesters in free bile acids and CoA, hereby generating cholic acid and chenodeoxycholic acid.

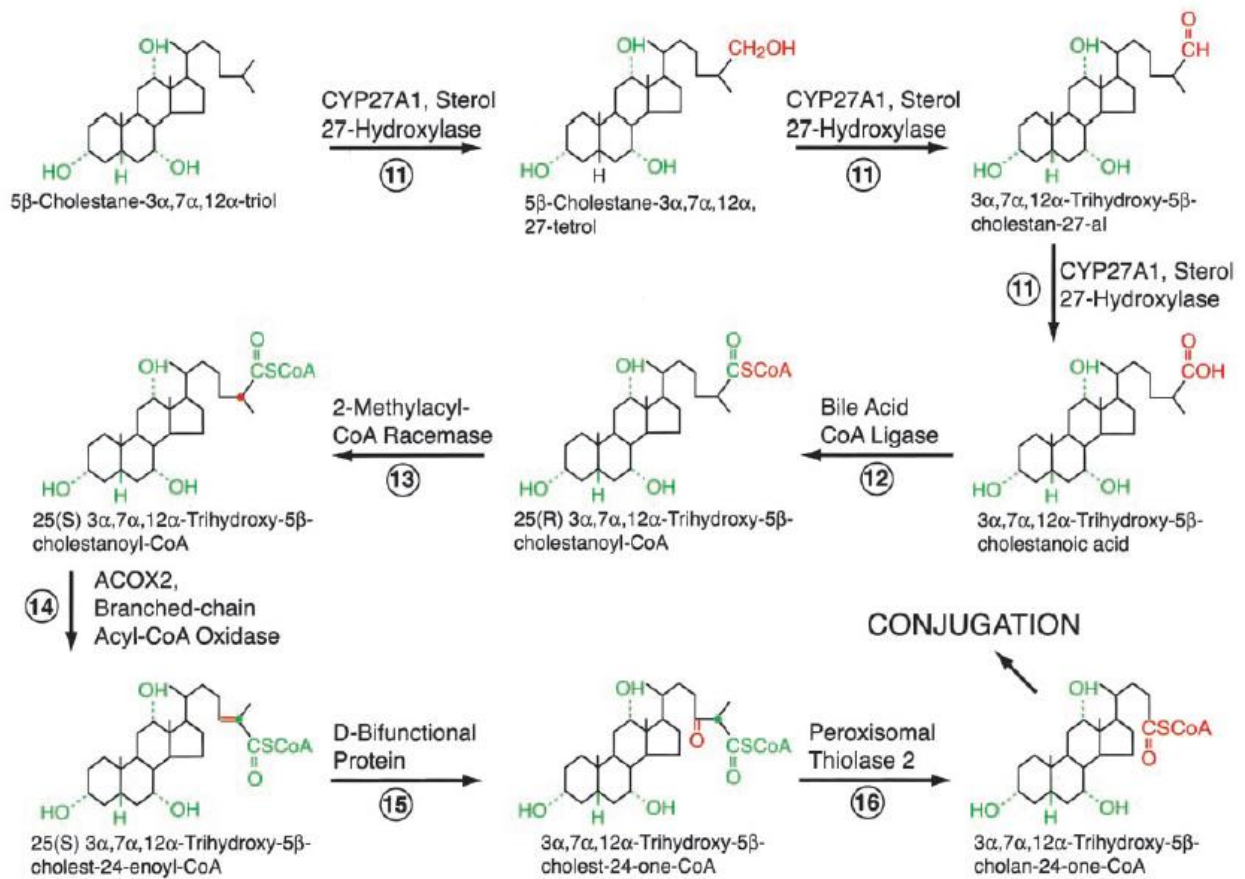


**Figure 1.9:** Oxidation and side chain shortening. First, a hydroxyl group is introduced at C27, hereby oxidizing this group to an aldehyde and then carboxylic acid. Then, side chain shortening occurs by a series of reactions.

(adapted from Russell, 2003).

### Conjugation

The final step in bile acid synthesis involves the addition of an amino acid, glycine or taurine, in amide linkage to carbon 24 (Figure 1.10, reaction 17). This reaction is catalyzed by the bile acid coenzyme A:amino acid N-acyltransferase enzyme.

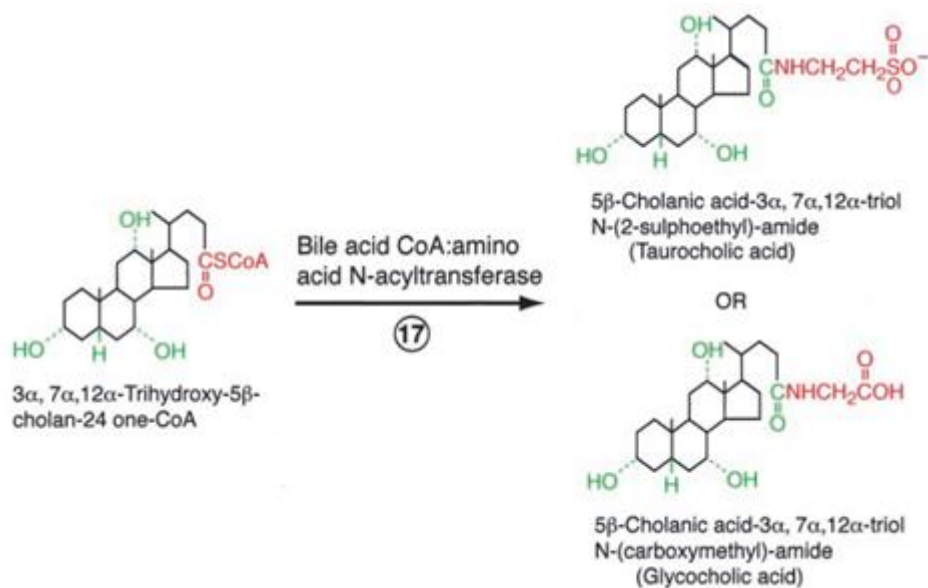


**Figure 1.10:** Conjugation (adapted from Russell, 2003).

Conjugation of bile acids increases the amphipathicity and enhances the solubility of the molecules, which makes them impermeable to cell membranes. Sulphonic acid group of taurocholic acid and the carboxyl group of glycocholic acid are ionized at physiological pH, which renders the bile salt (the ionized form of the bile acid) very amphipathic, together with the planar structure of the bile acid and the hydroxyl groups on the ring. For example, conjugation of cholic acid with glycine reduces the  $pK_a$  from 6.4 to 4.4 ensuring that the bile acid is completely ionized and highly soluble (Russell *et al.*, 2003).

Additionally, besides conjugation with amino acids, there are four more types of conjugation (Hofmann *et al.*, 2008):

- 1) Sulfation
- 2) Ester glucuronidation at C24
- 3) Ethereal conjugation at C3
- 4) N-acetylglucosamination at C7 in bile acids with a  $\beta$ -hydroxyl group

Because conjugated and free bile acids do not cross cell membranes, dedicated transport systems are required to move bile acids in and out of cells.



Secondary bile acids

During the enterohepatic cycle, bile acids are exposed to bacterial enzymes. When primary bile acids are modified by these enzymes, the resulting bile acid is called a secondary bile acid. Figure 1.11 shows the chemical structure of the major bile acids present in human bile.

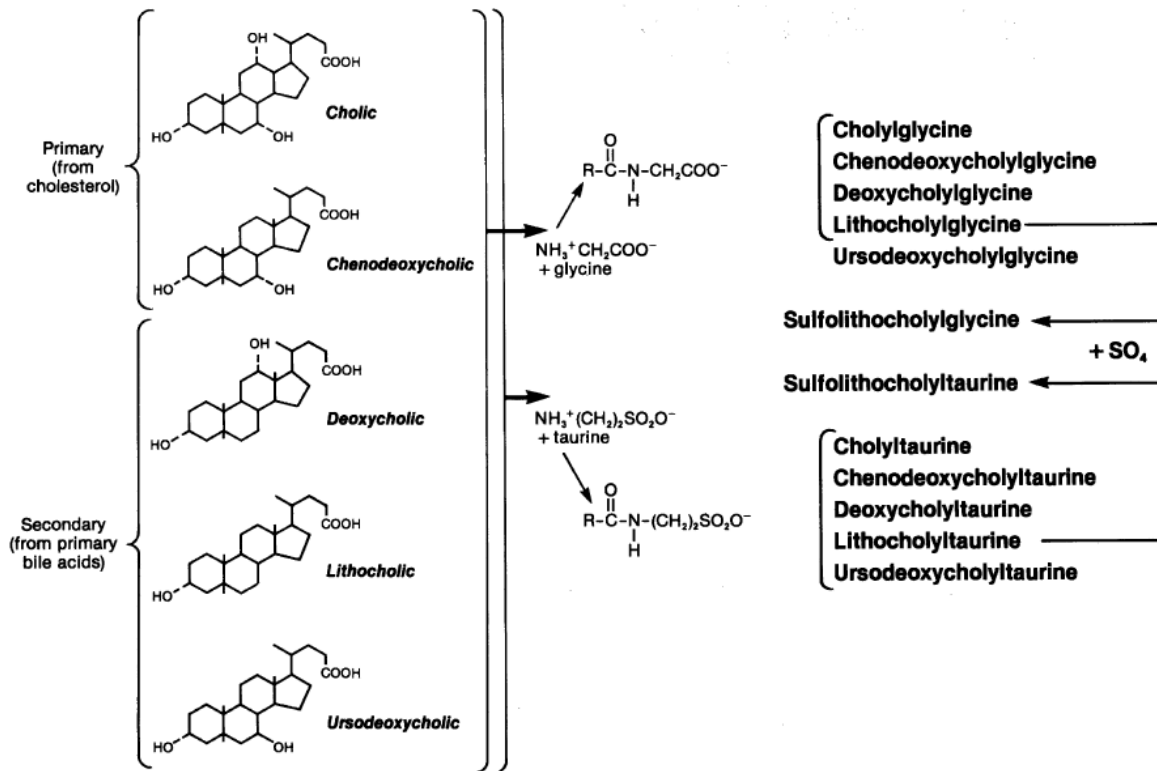


Figure 1.11: Chemical structure of the major bile acids present in human bile (Hofmann et al., 2008).

In the colon of animals with a cecum, anaerobic bacteria remove the hydroxyl group at C7 to form a new class of bile acids termed 7-deoxy bile acids.

**Bile acid transporters of the enterohepatic cycle**

To maintain bile acid homeostasis, transport proteins that make the enterohepatic cycle possible are needed (Figure 1.5). Approximately 95% of the bile acids that are excreted in the bile derive from the recirculating pool. Therefore, hepatocytes must transport bile acids efficiently from the portal blood into the bile. This vectorial trans-hepatocellular movement of bile acids is a concentrative transport process that is driven by a distinct set of transport systems at the sinusoidal and canalicular plasma membranes (Table 1.1). Three different groups can be distinguished (Dawson et al., 2009):

- 1) Primary (adenosine triphosphate (ATP)-dependent) transport systems
- 2) Secondary (Na<sup>+</sup> gradient dependent) transport systems
- 3) Tertiary (OH<sup>-</sup> or HCO<sub>3</sub><sup>-</sup> dependent anion exchange) transport systems

**Table 1.1:** Overview of bile acid transporters. (adapted from Marin et al., 2016)

Energy	Gene	Protein	Cell	Membrane
Active Primary Transporters (Pumps)	<i>ABCB11</i>	BSEP	Hepatocyte	Apical
	<i>ABCC1</i>	MRP1	Hepatocyte	Basal
	<i>ABCC2</i>	MRP2	Hepatocyte Renal epithelium	Apical
	<i>ABCC3</i>	MRP3	Hepatocyte Cholangiocyte Renal epithelium Intestinal epithelium	Basal
	<i>ABCC4</i>	MRP4	Hepatocyte Renal epithelium	Basal
	<i>ABCG2</i>	BCRP	Hepatocyte Trophoblast Renal epithelium Intestinal epithelium	Apical
Active Secondary Cotransporters	<i>SLC10A1</i>	NTCP	Hepatocyte	Basal
	<i>SLC10A2</i>	ASBT	Cholangiocyte Ileal epithelium Renal epithelium	Apical
Active Secondary Antiporters	<i>SLCO1B1</i>	OATP1B1	Hepatocyte	Basal
	<i>SLCO1B3</i>	OATP1B3	Hepatocyte	Basal
Facilitative transporters	<i>SLC51A</i>	OST $\alpha$	Cholangiocyte Ileal epithelium Renal epithelium	Basal
	<i>SLC51B</i>	OST $\beta$	Cholangiocyte Ileal epithelium Renal epithelium	Basal

Next, an overview of the transport proteins is given.

### Sinusoidal (basolateral) uptake

Bile acids are 100- to 1000-fold concentrated in bile compared to plasma. Therefore, hepatocellular secretion of bile acids (and their precursors) occurs against a steep concentration gradient and necessitates active transport (Pellicoro et al., 2007). Uptake is initiated at the basolateral membrane that is in direct contact with portal blood plasma, via sodium-dependent and independent mechanisms. The uptake of conjugated bile acids is predominantly mediated (>75%) by Na<sup>+</sup>-dependent transport using NTCP. In contrast,

unconjugated bile acids are taken up predominantly via Na<sup>+</sup>-independent transport using OATPs (Kullak-Ublick *et al.*, 2000).

### NTCP

The Na<sup>+</sup>/taurocholate cotransporting polypeptide (NTCP) is a member of the solute carrier (SLC) family 10 (*SLC10*) of sodium/bile salt cotransporters and the NTCP gene has been mapped to chromosome 14q24 (Hagenbuch *et al.*, 2004). In man, the family includes two bile acid carriers (*SLC10A1/NTCP*; *SLC10A2/ASBT*, see later). NTCP was the first bile acid carrier identified at both the molecular and functional levels (Alrefai *et al.*, 2007; Hagenbuch *et al.*, 1994; Hallen *et al.*, 2002). It is expressed exclusively in hepatocytes and is localized at the basolateral membrane (St-Pierre *et al.*, 2001). The transporter is distributed homogeneously throughout the liver lobule (Trauner *et al.*, 2003). NTCP consists of 349 amino acids with a mass of 56 kDa (Dawson *et al.*, 2009). The transporter has been cloned from rat, human, mouse and rabbit liver (Claro da Silva *et al.*, 2013).

NTCP is a secondary transport system. The transport is unidirectional and has two important driving forces for hepatic uptake: 1) an inwards chemical Na<sup>+</sup> gradient that is a result of the Na efflux out of the cell by the Na/K ATPase pump, where 3 Na<sup>+</sup> ions are exchanged for 2 K<sup>+</sup> ions and 2) an intracellular negative electrical gradient of about -35 to -40 mV. The outward conductance of K<sup>+</sup> via K<sup>+</sup> channels in the basolateral membrane further contributes to the regulation of this negative membrane potential. Together, the chemical and electrical gradients produced by the sodium pump are able to move solutes into the hepatocytes against their concentration gradients, with a 2:1 stoichiometry (Na<sup>+</sup>:bile acids = 2:1) (Boyer, 2013; Meier *et al.*, 2002).

NTCP transport activity is highest for glycine and taurine conjugated dihydroxy and trihydroxy bile acids. Conjugated taurocholate is taken up for more than 80% via NTCP, unconjugated cholate for less than 50% (Trauner *et al.*, 2003). However, most bile acids are conjugated and therefore, uptake of bile acids into the hepatocytes occurs predominantly by NTCP (Anwer *et al.*, 2014). The high level of NTCP expression at the sinusoidal membrane of hepatocytes and the high affinity for conjugated bile acids promotes their efficient extraction from portal blood. Thus, NTCP functions to maintain the enterohepatic cycle of bile acids and keeps plasma concentrations at a minimum (Dawson *et al.*, 2009). Although, bile acids are the major physiological substrate for NTCP, other compounds can be transported like estrogen conjugates, bromosulphothalein, thyroid hormones and

dehydroepiandrosteron (DHEA) (*Kosters et al., 2008*). In addition, NTCP also mediates uptake of drugs such as rosuvastatin and micafungin and drugs that are covalently bound to taurocholate such as chorambucil-taurocholate (*Trauner et al., 2003*).

### OATPs

Uptake of bile acids into the hepatocytes occurs predominantly by NTCP, and to a lesser extent by organic anion-transporting polypeptides (OATPs). OATPs are members of the solute carrier organic anion transporter (*SLCO*) superfamily. This OATP superfamily consists of 6 different families, which can be further subdivided into subfamilies based on their amino acid sequence identity. Currently, 11 human OATPs have been identified (*van de Steeg et al., 2010; Iusuf et al., 2011*). The OATP genes of the OATPs expressed in liver can be found on chromosome 12q12 (*Alrefai et al., 2007*). OATP1A2, OATP1B1 and OATP1B3 consist of 670, 691 and 702 amino acids and a weight of 85, 84 and 120 kDa, respectively.

OATPs are tertiary transport systems and function as electroneutral anion exchanges. They are thought to transport bile acids and other solutes in exchange for intracellular anions, such as glutathione and bicarbonate (*Boyer et al., 2013*). Four OATPs have been functionally identified in human liver (OATP1A2, OATP1B1, OATP1B3, OATP2B1) and many are also expressed in other tissues like the blood-brain barrier, kidney, choroid plexus, lung, heart, intestine, placenta and testis (*Kullak-Ublick, 2001; Tamai et al., 2001*). OATP1B1 and 1B3 are hepatocyte specific and functionally most important. OATP1B1 is expressed on the basolateral membrane throughout the hepatic lobule in human liver, while OATP1B3 is most strongly expressed in pericentral regions of the hepatic lobule. The highest expression in liver is found for OATP1B1 and has 80% sequence homology with OATP1B3 (*Hagenbuch et al., 2004; Boyer et al., 2013; Pauli-Magnus et al., 2005*).

OATPs mediate the sodium-independent cellular uptake of a wide variety of organic endogenous and exogenous compounds, such as bile acids, bilirubin, steroid and thyroid hormones and their conjugates, and numerous drugs, xenobiotics and environmental toxins. Most OATP substrates are organic anions with molecular weights greater than 300 Da, but they can also transport cations and neutral compounds (*Boyer et al., 2013*). In contrast to NTCP, unconjugated bile acids can be efficiently taken up by the liver by OATPs. Because of this broad substrate specificity and due to their expression in pharmacokinetically important tissues (liver, small intestine, kidney), OATPs of the 1A/1B subfamilies are thought to play an

important role in drug disposition (*van de Steeg et al., 2010; Tamai et al., 2001; Kullak-Ublick et al., 2001*).

### Alternative basolateral bile acid efflux

Under normal physiological conditions, bile acid uptake is the predominant transport across the basolateral membrane of hepatocytes and the basolateral efflux into the sinusoids is negligible. However, under cholestatic conditions (see later), basolateral bile acid efflux can be upregulated and can in part compensate for the disturbed canalicular bile acid secretory pathway (*Meier et al., 2002*) to protect the liver (*Halilbasic et al., 2013*). This alternative basolateral bile acid efflux is mediated by members of the ATP-binding cassette (ABC) superfamily of transporters, namely the multidrug resistance proteins (MRPs) family. This subfamily of transporters consists of at least six members (MRP1-6) with four of them expressed in the liver. MRP3 and MRP4 are expressed in the basolateral membrane of the hepatocyte, whereas MRP2 is localized on the canalicular membrane (see later) (*Alrefai et al., 2007*). MRP1 is almost absent in the liver. In cholestatic conditions, an upregulation of MRP3 and MRP4 can be observed. These transporters are expressed at extremely low levels in normal hepatocytes. Both are ATP-dependent pumps with a wide range of substrates (*Alrefai et al., 2007; Sievänen, 2007*). Additionally, the heterodimeric Organic Solute Transporters  $\alpha$  and  $\beta$  (OST $\alpha/\beta$ ) participate in this basolateral efflux (*Halilbasic et al., 2013*).

### Canalicular excretion

After uptake in the hepatocytes, bile acids and other organic solutes move across the cell to the canalicular membrane, where they can be excreted into bile. This can occur by rapid diffusion in association with cytosolic proteins, in association with intracellular membranes, or by transcytosis in membrane vesicles associated with microtubules. The hydrophobicity of the compounds influences which pathway the solute will take. The more hydrophobic the solute, the more it will associate with intracellular membranes rather than the cytosolic proteins (*Boyer et al., 2012; Trauner et al., 2003*).

Canalicular bile acid transport is a critical component of their enterohepatic circulation and represents the rate-limiting step in hepatic excretion and bile formation. Additionally, it is the main generator of bile flow (*Kosters et al., 2008*). Secretion of bile acids into bile across the

canalicular membrane occurs against a steep concentration gradient that ranges between 100-1000 fold. Therefore, the canalicular excretion of bile acids occurs via direct transporter systems whose function depends on ATP hydrolysis. The most important efflux transporters are BSEP, which is responsible for the transport of monovalent bile acids, and MRP2, which is the main transporter of divalent bile acids. (Alrefai *et al.*, 2007; Trauner *et al.*, 2003)

### **BSEP**

The Bile Salt Export Pump (BSEP) is the predominant efflux transporter on the canalicular membrane. BSEP is a member of the multidrug resistance P-glycoprotein family that belongs to the ABC superfamily (*ABCB11*) (Noé *et al.*, 2002). Human BSEP can be found on chromosomes 2q24. It has been cloned from pig, human, rabbit, rat and mouse (Alrefai *et al.*, 2007). BSEP is a direct transport system that requires ATP. It consists of 1321 amino acids and it has a mass of 150-170 kDa. BSEP was also found in human testis (Stieger *et al.*, 2007).

BSEP mediates the transport of mainly monovalent bile acids. BSEP has a poor affinity for unconjugated bile acids, and a high affinity for conjugated bile acids (Kosters *et al.*, 2008). Whereas bile acids are the major physiological substrates, BSEP is also able to transport a limited number of drugs, such as pravastatin. Other drugs like cyclosporine, rifamycin, troglitazone and glibenclamide are no substrates but interact with BSEP and inhibit bile acid export (Dawson *et al.*, 2009).

### **MRP2**

The Multidrug Resistance Protein 2 (MRP2) is another transporter of the ABC transporter superfamily (Nies *et al.*, 2007) and is a unidirectional ATP-dependent efflux pump. Human MRP2 gene (*ABCC2*) is mapped on chromosome 10q24.

The gene has been cloned from six mammalian species including human, rhesus monkey, rat, rabbit, mouse and dog and three other vertebrates. (Fardel *et al.*, 2005).

In the liver, it is predominantly localized in the canalicular membrane of the hepatocytes. Additionally, this protein can be found in the kidneys and enterocytes of the duodenum and jejunum. MRP2 mediates the transport of divalent bile acids and it does not have the capacity to transport monovalent bile acids. It has a wide range of organic substrates (mainly organic anions), such as glutathione, glucuronide and sulfate conjugates and also some unconjugated drugs (Alrefai *et al.*, 2007).

### Intestinal bile acid uptake

Bile acids are reabsorbed in the intestines through a combination of passive absorption in the proximal small intestine, active transport in the distal ileum, and passive absorption in the colon. Bile acids are actively transported into the distal ileum by the Apical Sodium Dependent Bile Acid Transporter (ASBT). (*Dawson et al., 2009*)

#### **ASBT**

ASBT, the ileal counterpart of hepatic NTCP, is also a member of the *SLC10* family of sodium/bile salt cotransporters. The ASBT gene is localized on chromosome 13q33 in human. NTCP and ASBT are phylogenetically related.

ASBT is, just like NTCP, a secondary transporter system that is driven by sodium and a negative intracellular potential to move bile acids from the lumen of the small intestine across the apical brush border. The ASBT mediated transport is electrogenic with 2:1 Na<sup>+</sup>/bile acid coupling stoichiometry. It consists of 348 amino acids and has a mass of 48 kDa. It has been cloned from hamster, human, rat, rabbit and mouse ileum (*Alrefai et al., 2007; Dawson et al., 2009*).

ASBT is expressed in the apical membrane of ileal enterocytes, proximal renal convoluted tubule cells, epithelial cells lining the biliary tract (cholangiocytes) and gallbladder epithelial cells.

Human ASBT transports both conjugated and unconjugated bile acids with preference for conjugated. ASBT has a higher affinity for dihydroxy bile acids that are more hydrophobic than trihydroxy bile acids.

### Intestinal bile acid efflux

#### **OST $\alpha/\beta$**

Organic solute transporter  $\alpha/\beta$  (OST $\alpha/\beta$ ) is a unique heteromeric sterol transporter. Both subunits are required for the functional expression of this transporter. It was cloned from human and mice. It is located on chromosome 16B13 (*Alrefai et al., 2007; Boyer et al., 2013; Dawson et al., 2009; Kusters et al., 2008*).

OST $\alpha/\beta$  is Na<sup>+</sup>-independent facilitated diffusion transporter. Therefore, in contrast with other bile acid transporters, substrates can be driven bidirectionally (uptake or efflux) across the

membrane of the cell depending on the electrical chemical gradient. The transporters can only function as heterodimers, secreting bile acids back into the circulation, both in the intestine and hepatocytes (*Kosters et al., 2008*).

Human OST $\alpha/\beta$  is expressed in a variety of tissues with the highest levels in liver, small intestine, colon, kidney, adrenal gland, testes and ovary (*Kosters et al., 2008*). It is also expressed at lower levels in other tissues like heart, lung, brain, ... OST $\alpha$  is built up of 340 amino acids, while OST $\beta$  is 128 amino acids in size.

Substrates include conjugated bile acids. In addition, OST $\alpha/\beta$  transports sterols conjugated with sulphate or glucuronic acid, including DHEAs, estrone-3-sulfate, digoxin, and prostaglandin E2 (*Ballatori et al., 2013*).

### **Bile acid transporters in cholangiocytes and renal epithelial cells**

Besides the expression in cells of the enterohepatic cycle, bile acid transporters are also expressed in other epithelial cells, such as cholangiocytes and renal proximal tubule cells (*Xia et al., 2006*). Between the cholangiocytes and hepatocytes, there is a cholehepatic shunt (Figure 1.12) in which bile acids are actively absorbed by cholangiocytes lining bile ducts and then, these bile acids cycle back to the hepatocytes for resecretion (*Alrefai et al., 2007*). The exact physiological relevance of this shunt is not clear, but this pathway may play a role in the modification of bile in the bile ductules and may become important under cholestatic conditions, providing a mechanism to avoid high levels of intracellular bile acids, or help improve bile flow within the liver (*Kosters et al., 2008*). Transport of bile acids in and out the cholangiocytes is mediated by a similar set of transporters found in the terminal ileum. ASBT mediates the Na<sup>+</sup>-dependent uptake of bile acids across the apical membrane (*de Lima Toccafonda Vieira et al., 2014*), and OST $\alpha/\beta$ , MRP3 or t-ASBT (truncated ASBT) are potentially responsible for efflux of bile acids through the basolateral membrane into the blood. The bile acids enter the peribiliary plexus adjacent to intrahepatic bile ducts, and are then forwarded to the hepatic sinusoids for reuptake in the hepatocytes (*Xia et al., 2006*).



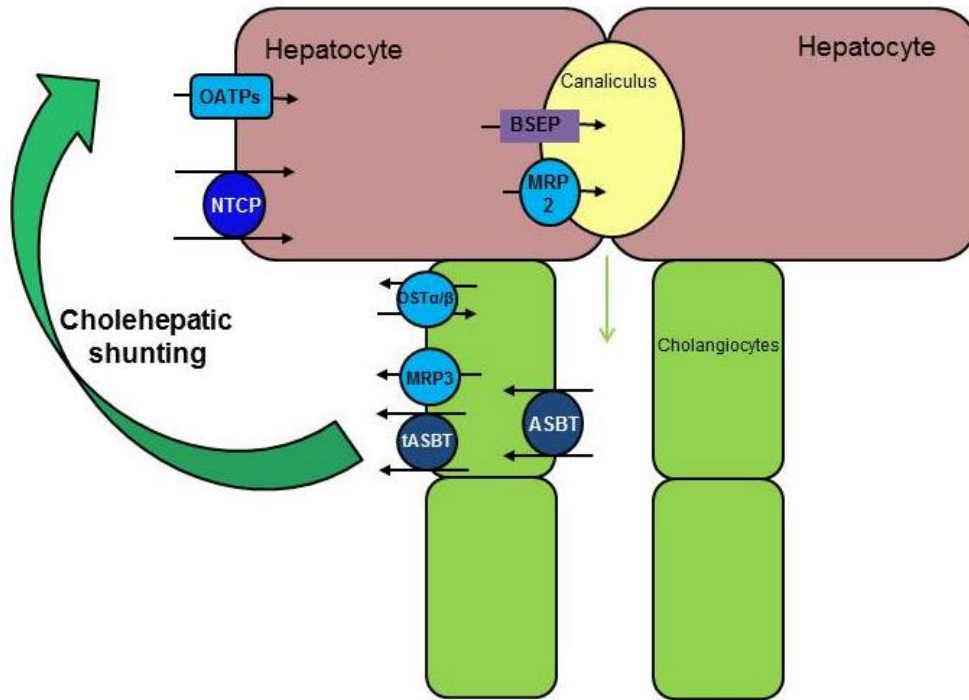


**Figure 1.12:** Cholehepatic shunting.

Active bile acid transport has also been reported in renal proximal tubule (Figure 1.13) (Trauner *et al.*, 2003). Reabsorption of bile acids from the glomerular filtrate ensures the conservation of bile acids that escape hepatic clearance. Under normal conditions, urinary excretion of bile acids is smaller compared to the amount of bile acids in the glomerular filtrate due to almost complete renal reabsorption. ASBT, MRP4 and MRP2 were found to be localized on the apical membrane of renal epithelial cells. Additionally, OST $\alpha/\beta$  is also expressed on the basolateral membrane of proximal tubule suggesting its involvement in bile acid efflux from renal epithelial cells (Alrefai *et al.*, 2007).

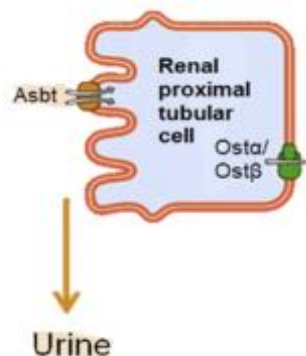


**Figure 1.13:** Bile acid transporters in the renal proximal tubular cell. (adapted from: Gai *et al.*, 2013)

## Drug-induced liver injury

Drug-induced liver injury (DILI) is a leading cause for the withdrawal of drugs from the market. A variety of clinical presentations can be seen in patients, ranging from asymptomatic mild biochemical abnormalities to an acute illness with jaundice that resembles viral hepatitis (Pauli-Magnus *et al.*, 2006). Drugs can cause liver injury via different and overlapping pathologic mechanisms (de Lima Toccafondo Vieira *et al.*, 2014).

DILI can be classified as hepatocellular, cholestatic and mixed type liver injury, depending on the serum biochemistry markers (Schadt *et al.*, 2016). Hepatocellular injury is mainly characterized by the elevation of serum aminotransferases, while cholestatic liver damage is reflected in increased levels of alkaline phosphatase,  $\gamma$ -glutamyltranspeptidase and conjugated bilirubin in serum. On the one hand, in most hepatocellular forms, most cases are attributed to idiosyncratic reactions, where immunoallergic mechanisms resulting from hypersensitivity and unusual metabolism of the drug are the predominant pathophysiological pathways. On the other hand, cholestatic drug induced injury (also referred to as drug induced cholestasis) results from a drug- or metabolite-mediated inhibition of hepatobiliary transporters. Basolateral uptake transporters are important in controlling hepatic drug and toxin exposure, canalicular (apical) transporters are responsible for drug clearance from the liver as well as for the secretion of bile acids and other bile constituents. Among 784 DILI cases reported between 1970 and 2004, almost one-half of the cases had either cholestatic or mixed cholestatic hepatic toxicity (Yang *et al.*, 2013).

Cholestatic drugs may disturb bile acid homeostasis by direct inhibition of bile acid transport, or by indirect processes, such as regulation of transporter localization or expression (Yang *et al.*, 2013). The interactions of drugs with transporters can lead to toxic concentrations of bile acids, bilirubin or substrate drugs in blood or liver (Figure 1.14) (Pauli Magnus *et al.*, 2006; Padda *et al.*, 2011), leading to drug-drug interactions, hypercholanemia, hyperbilirubinemia and cholestasis. (Vaz *et al.*, 2014; Shneider *et al.*, 1997; Keppler *et al.*, 2014; Marin *et al.*, 2016; Perez *et al.*, 2009). Several transport proteins have been identified as potential targets of drug-induced cholestasis. These include the basolateral uptake transporters (NTCP and OATPs), canalicular efflux transporters (BSEP, MRP2) and basolateral efflux transporters (MRP3 and MRP4). Since hepatic accumulation of compounds is regulated by both uptake and efflux processes, inhibition of uptake can also exert a protective effect by preventing the hepatic accumulation.

Many drugs can inhibit OATPs. Inhibition of OATPs can lead to drug induced benign isolated hyperbilirubinemia. This transient jaundice may arise due to inadequate bilirubin clearance from the body via OATP1B1 and OATP1B3. Drug interference with MRP2 may also be correlated to clinical hyperbilirubinemia, since MRP2 directly regulates bilirubin elimination via excretion of glucuronide metabolites into the bile (*de Lima Toccafonda Vieira et al., 2014*). Although the inhibition of OATPs and MRP2 in itself possess a moderate risk, it can increase the concentration of substrate drugs to elevated and toxic levels (e.g. statins) (*Maddrey et al., 2005*). Consequently, it can cause drug-drug interactions that result in altered pharmacokinetics (*Maddrey et al., 2005*).

Drugs may also inhibit the hepatic uptake and/or efflux of bile acids resulting in an increase in intracellular concentrations leading to hepatotoxicity. To predict the hepatic exposure to bile acids, inhibitory effects of drugs on each transport protein, as well as drug concentrations at the interaction site should be considered. Inhibition of NTCP or BSEP can lead to bile acid retention that may lead to hypercholanemia and severe cholestasis, resulting in liver failure (*Alrefai et al., 2007; Stieger et al., 2011*). Prior to their interference with bile secretion, drugs with intrahepatic cholestatic potential need to be taken up in the liver cells, which can be modulated by OATPs or NTCP (*de Lima Toccafonda Vieira, 2014*). During cholestasis, a 20- to 100-fold increase in systemic bile acid concentrations have been reported, which is associated with morbidity (*Greupink et al., 2012*). Drug-induced cholestasis may mimic other intrahepatic and extrahepatic cholestatic diseases. Not recognizing a drug as a triggering factor for cholestasis extends the exposure, which may lead to worse liver injury (*Padda et al., 2011*). Basolateral efflux transporters, like MRP3 and MRP4, play a minor role in bile acid transport in normal conditions. However, in cholestatic conditions, they can be upregulated to compensate for impaired biliary excretion. Impaired function of these transporters can thus lead to accumulation of toxic bile acids in hepatocytes and is therefore also a risk factor for the development of drug-induced cholestasis (*Yang et al. 2013*).

Given the overlap in substrate specificity of uptake and efflux transporters involved in vectorial transport of bile acids, it is not unexpected that compounds may modulate multiple hepatobiliary transport mechanisms. The relative effect of compounds on several processes should be considered to predict the potential clinical consequences (*de Lima Toccafonda Vieira, 2014*).

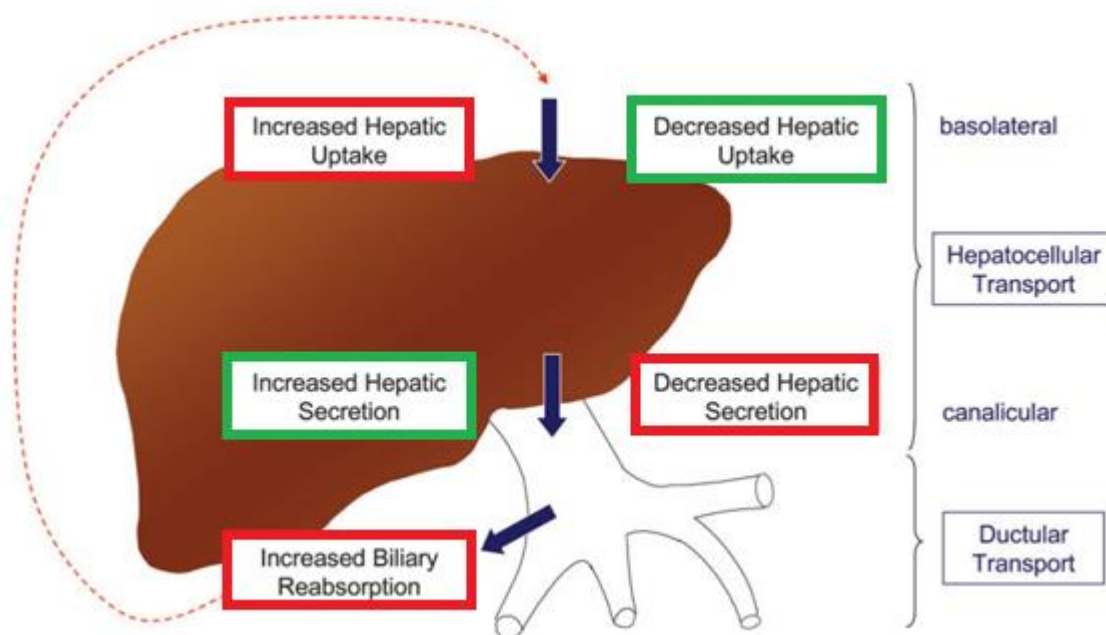


**Figure 1.14:** Transporter-related mechanisms in the development of liver injury. Red and green rectangles designate potentially harmful (red) or protective (green) transporter-related mechanisms, respectively (*adapted from Pauli-Magnus et al., 2006*).

Rifampicin for example, is one of the most commonly used anti-tubercular drugs and is known to be hepatotoxic. Several studies showed that rifampicin caused a direct toxic injury to the hepatocytes and that it significantly increases the level of serum conjugated bilirubin and total bile acids in man (*Chen et al., 2009*). Rifampicin is known as an OATP1, BSEP and MRP2 inhibitor (*Stieger et al., 2000; Mita et al., 2006; Lengyel et al., 2008; Van de Steeg et al., 2010*).

As previously mentioned, DILI is a major cause of attrition during drug development and is responsible for drug withdrawals from the market. Additionally, hepatotoxicity is the most common single adverse drug event leading to refusal for drug approval. DILI also poses a significant burden to patient safety and to the costs of health care systems. Therefore, it is important to improve the understanding and characterization, and to develop better prediction methods to identify possible interactions (*de Lima Toccafonda Vieira et al., 2014*).

Currently, this possible inhibition of transport proteins by new candidate drugs is investigated by means of *in vitro* and invasive, time-consuming and expensive preclinical *in vivo* tests. In *in vitro* tests, mainly BSEP inhibition was investigated, since it can lead to severe cholestasis (*Stieger et al., 2000; Kis et al., 2012*). To study transporter activity, two different types of *in*

*vitro* assay systems can be distinguished: membrane-based and cell-based assays. The two most commonly used membrane-based assays, which are suitable to investigate hepatobiliary transporters are the vesicular transport and the ATPase assay (Stieger *et al.*, 2000). Transfected cell lines can be used to assess the uptake and efflux transporters separately. In cell-based assays, sandwich-cultured hepatocytes are widely used to assess drug-induced cholestasis, as they reflect *in vivo* properties (Annaert *et al.*, 2005; Wolf *et al.*, 2010; Nakanishi *et al.*, 2011; De Bruyn *et al.*, 2014; Chatterjee *et al.*, 2014; Oorts *et al.*, 2016). In *in vivo* toxicity studies, increasing amounts of potential new drugs are administered to animals. Blood and bile samples are subsequently taken to measure bile acid and bilirubin concentrations in blood and bile (Bergman *et al.*, 2010). Another approach to study transporter activity is by using fluorescein conjugated bile acid analogues and fluorescence microscopy for *in vitro* (Yamaguchi *et al.*, 2006) and invasive *in vivo* studies (Milkiewicz *et al.*, 2001). These *in vivo* experiments require liver tissue and bile samples and are therefore very invasive. In addition, these studies cannot distinguish between influx or efflux interactions. Besides *in vitro* and *in vivo* experiments, *in silico* modeling was used to predict drug interactions with bile acid transport proteins. These models rely on a series of experimentally measured interactions of small molecules with membrane transporters and employ statistical learning approaches, such as quantitative structure-activity relationship. However, the quantitative models are limited to small sets of compounds (Warner *et al.*, 2012; Saito *et al.*, 2009; Greupink *et al.*, 2012).

## Part II: Molecular Imaging

### Medical Imaging

Medical imaging began in 1895 when the German physicist Wilhelm Conrad Roentgen discovered X-rays, an achievement that earned him the first Nobel Prize in Physics in 1901. While working with a cathode ray tube, he noticed that invisible rays were able to penetrate some solids better than others. This difference in penetration can be explained by the difference in density between several materials or tissues. X-rays can be detected on a photographic plate, providing a two dimensional image that is in accordance with the density of the material or tissue. In medical imaging, X-ray detection on a photographic plate is especially useful for the detection of structural skeletal disorders due to the higher density of bone compared to surrounding soft tissues. (Bradley WG *et al.*, 2008) Consequently, X-ray imaging can be classified as a structural imaging technique. Nowadays, different imaging techniques are available that can be divided into two main categories: structural (or anatomical) and functional imaging.

Structural imaging modalities visualize non-invasively the anatomy of the patient. The best known modalities are X-ray radiography (Figure 1.15, A), computed tomography (CT) (Figure 1.15, B), magnetic resonance imaging (MRI) (Figure 1.15, C) and ultrasound imaging (US) (Figure 1.15, D). These techniques were developed to visualize nonspecific macroscopic physical and physiological changes in tissues. These techniques were not able to identify the specific molecular events responsible for disease, although image spatial resolution has been constantly improved (Tian, 2012).



**Figure 1.15:** Medical X-ray of the pelvis (A), CT of the head (B), MRI of the brain (C) and ultrasound image of a fetus (D) (Image obtained from <http://commons.wikimedia.org>, used under a Creative Commons Attribution-ShareAlike license: <http://creativecommons.org/licenses/by-sa/3.0/>)

Functional imaging modalities, such as planar scintigraphy, single photon emission computed tomography (SPECT), positron emission tomography (PET) and optical imaging (OI) focus on the study of molecular events in living subjects and are regarded as functional metabolic or

molecular imaging. The targets in functional imaging can include transporters, cell surface receptors, intracellular enzymes, etc.

Nowadays, the traditional distinction between structural and functional imaging has become a little blurred with the introduction of functional MRI that can provide functional information as well. Moreover, the introduction of micro-bubbles enables functional imaging in US. Peptides, antibodies, etc. can be attached to the surface of microbubbles to target specific biochemical processes.

An overview of the most commonly used preclinical imaging modalities with their main characteristics is shown in Table 1.2.

### Multi-modality

Since none of the imaging modalities is perfect (Table 1.2), these imaging modalities are often combined into a single imaging device, called multi-modality imaging. For example, because the molecular imaging modalities SPECT and PET do not provide detailed anatomical information, they are often combined with CT or MRI. CT and MRI have a high spatial resolution and serve to identify morphological changes in small structures, however, they have lower sensitivity compared to SPECT and PET. So when these imaging modalities are combined into one imaging device, we combine ‘the best of both worlds’ (Khalil *et al.*, 2011).

## Molecular imaging

Molecular imaging (MI) has its roots in functional imaging and is defined by Weissleder and Mahmood (Weissleder and Mahmood, 2001) as:

“Molecular imaging is the *in vivo* characterization and measurement of biologic processes on the cellular and molecular level. In contradistinction to ‘classical’ diagnostic imaging, it sets forth to probe such molecular abnormalities that are the basis of disease rather than to image the end results of these molecular alterations”

In other words, it is a non-invasive, real-time visualization of biochemical events at the cellular and molecular level within living cells, tissues, and/or intact subjects (James *et al.*,

2012). These events can be as simple as location(s) of a specific population of cells or levels of a given protein receptor on the surface of cells. In addition, it is possible to study more complex events, such as interaction of two intracellular proteins, cellular metabolic flux, etc. (Weissleder *et al.*, 2010; Massoud *et al.*, 2003).

The reason for monitoring/imaging/quantifying various molecular targets are related to characterizing a disease process that may correlate with concentrations of one or more of these molecular targets. MI allows detection of functional alterations even before anatomical changes can be observed. Additionally, molecular imaging helps to dissect complex biology. Another important application is in the process of drug discovery and validation, as well as in predicting and monitoring response to various types of therapy.

MI modalities include optical imaging that mainly records bioluminescent and fluorescent light, SPECT and PET that detect  $\gamma$ - and  $\beta^+$  radiation, functional MRI that detects differences in relaxation time, and US that detects sound waves reflected back from ligand-targeted acoustic particles (micro-bubbles) (Tian *et al.*, 2012).



## Chapter 1: General introduction

**Table 1.2:** Characteristics of preclinical imaging modalities (*adapted from Massoud et al., 2003*).

	PET	SPECT	OI	MRI	CT	US
<b>Radiation type</b>	high-energy $\gamma$ rays	lower-energy $\gamma$ rays	visible light or near infrared	radiowaves	X-rays	high-frequency sound
<b>Spatial resolution</b>	1-2 mm	< 1 mm	2-5 mm	25-100 $\mu$ m	50-200 $\mu$ m	50-500 $\mu$ m
<b>Depth</b>	no limit	no limit	1-2 cm	no limit	no limit	millimeters to centimeters
<b>Temporal resolution</b>	seconds to minutes	seconds to minutes	seconds to minutes	minutes to hours	minutes	seconds to minutes
<b>Contrast agent administration</b>	$10^{-11}$ - $10^{-12}$ M	$10^{-10}$ - $10^{-11}$ M	not well-characterized	$10^{-3}$ - $10^{-5}$ M	not well characterized	not well characterized
<b>Amount of probe used</b>	nanograms	nanograms	micrograms to milligrams	micrograms to milligrams	not applicable	micrograms to milligrams
<b>Quantitative degree</b>	+++	++	+ to ++	++	++	+
<b>Principle use</b>	metabolic, reporter/gene expression, enzyme targeting	reporter/gene expression, receptor/ligand	reporter/gene expression, cell trafficking	morphological reporter/gene expression, receptor/ligand if many receptors	morphological	morphological
<b>Advantages</b>	high sensitivity, Isotopes can substitute naturally occurring atoms, quantitative translational research	many molecular probes available, can image multiple probes simultaneously	quick, easy, low cost, relative high-throughput	highest spatial resolution, combines morphological and functional imaging	bone, tumor and anatomical imaging	real-time, low cost
<b>Disadvantages</b>	cyclotron needed, relatively low spatial resolution, radiation	relatively low spatial resolution, collimation, radiation	low spatial resolution, 2D imaging only, relatively surface-weighted	relatively low sensitivity, long scan and postprocessing time, mass quantity of probe may be needed	limited “molecular” applications, limited soft tissue resolution, radiation	limited spatial resolution, mostly morphological
<b>Cost</b>	\$\$\$\$	\$\$\$	\$-\$	\$\$\$\$	\$\$	\$\$

MI uses specific molecules as the source of image contrast. To obtain successful images of specific molecules *in vivo* at the molecular level, the following criteria should be met (Massoud *et al.*, 2003):

- (1) availability of high affinity probes with reasonable pharmacodynamics;
- (2) the ability of these probes to overcome biological delivery barriers;
- (3) use of chemical or biological amplification strategies;
- (4) availability of sensitive, fast, high resolution imaging techniques

Consequently, one of the key prerequisites for molecular imaging is the ability to design the perfect cell or tissue-specific probe. The MI research chain, i.e. the process of developing new probes/strategies/assays for MI is shown in Figure 1.16. However, not all research in the field is intended for clinical translation and then, the chain stops at step 10. It is an iterative process, based on lessons learned in a given application.

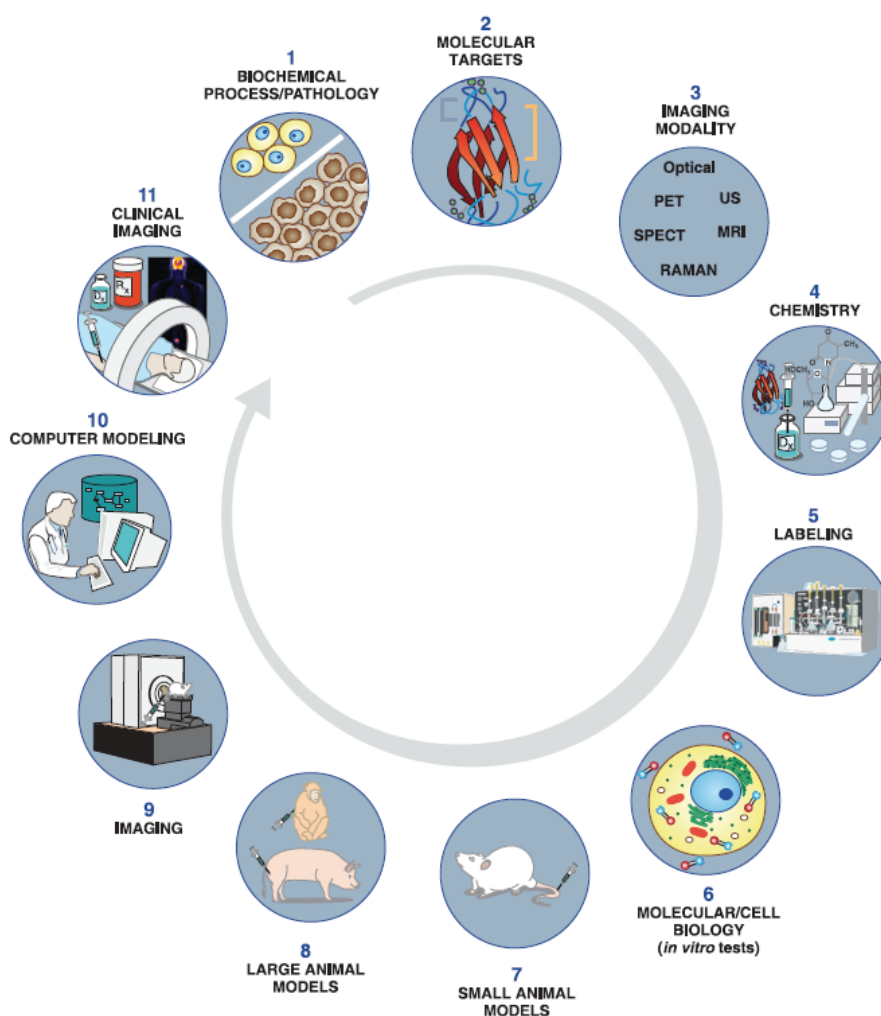


Figure 1.16: Molecular imaging research chain. (adapted from James *et al.*, 2012)

## Molecular imaging and nuclear medicine

Nuclear medicine, in the field of molecular imaging, offers important advantages over other MI modalities (Zanzonico, 2012):

- (1) The specific activity (i.e., activity per unit mass) of radiopharmaceuticals and the detection sensitivity of the imaging instruments are generally high. In contrast to CT and MRI, far lower mass doses are administered during nuclear medicine imaging. These sub-nmol doses correspond to nonpharmacological, non-perturbing mass doses of the radiopharmaceutical.
- (2) Nuclear medicine imaging is non-invasive, hereby allowing serial imaging to characterize the longitudinal time course of some processes.
- (3) Nuclear medicine images are (semi)-quantitative and may be parameterized.
- (4) A large number of targeted radiopharmaceuticals have been developed and will be developed in the future.

However, there are also several drawbacks:

- (1) Nuclear imaging techniques have a poorer spatial resolution compared to CT and MRI (Table 1.2).
- (2) Nuclear imaging modalities deliver radiation doses for patients, with effective doses and maximal organ-absorbed doses per study in the order of ten mSv and up to several cGy, respectively (Stabin MG et al., 2008).
- (3) Only limited anatomical information can be obtained. This drawback is largely overcome with the introduction of multi-modality devices (e.g. PET-CT, SPECT-CT, PET-MRI). Here, functional information, obtained from PET or SPECT, is inherently co-registered with anatomical images.

### PET

The principles of PET imaging are summarized in Figure 1.17. PET imaging requires the use of a cyclotron to generate short-living radionuclides such as  $^{18}\text{F}$ ,  $^{11}\text{C}$ ,  $^{13}\text{N}$ ,  $^{15}\text{O}$ . PET uses the unique properties of these radioisotopes that decay via positron emission, also called  $\beta^+$  decay. An overview of the most common PET isotopes is listed in Table 1.3. Positron emitters are neutron-deficient isotopes that achieve stability through the nuclear transmutation of a proton into a neutron. As shown in the right part of Figure 1.17, this process involves the

emission of a positive electron (positron) and an electron neutrino. The energy spectrum of the emitted positron depends on the specific isotope. After emission, the positron will travel a certain distance that is dependent on the energy of the positron, called the positron range, in the surrounding tissue and will lose its energy through interactions with the surrounding tissue until it annihilates with an electron in the tissue. Annihilation is a process in which the combined energy of the positron and electron will result in the emission of two gamma photons with an energy of 511 keV that are emitted in opposite directions (180°) and since they are highly energetic, they are able to leave the subject's body and can be detected externally by detectors (Tian *et al.*, 2012). PET detectors take the form of a closed ring, or set of rings, surrounding the subject to be imaged. This circular configuration of the PET scanner and its scintillation detectors and photo multiplier tubes (amplifiers) allows simultaneous detection of these two photons. This detection of a coincidence event allows localization of an annihilation event somewhere along the line between the two detectors, which received a signal. A large number of such coincidence lines form the data set. Then, this raw data is reconstructed in 3D images that allow accurate positioning of the radioisotope in the body. (James and Gambhir, 2012)

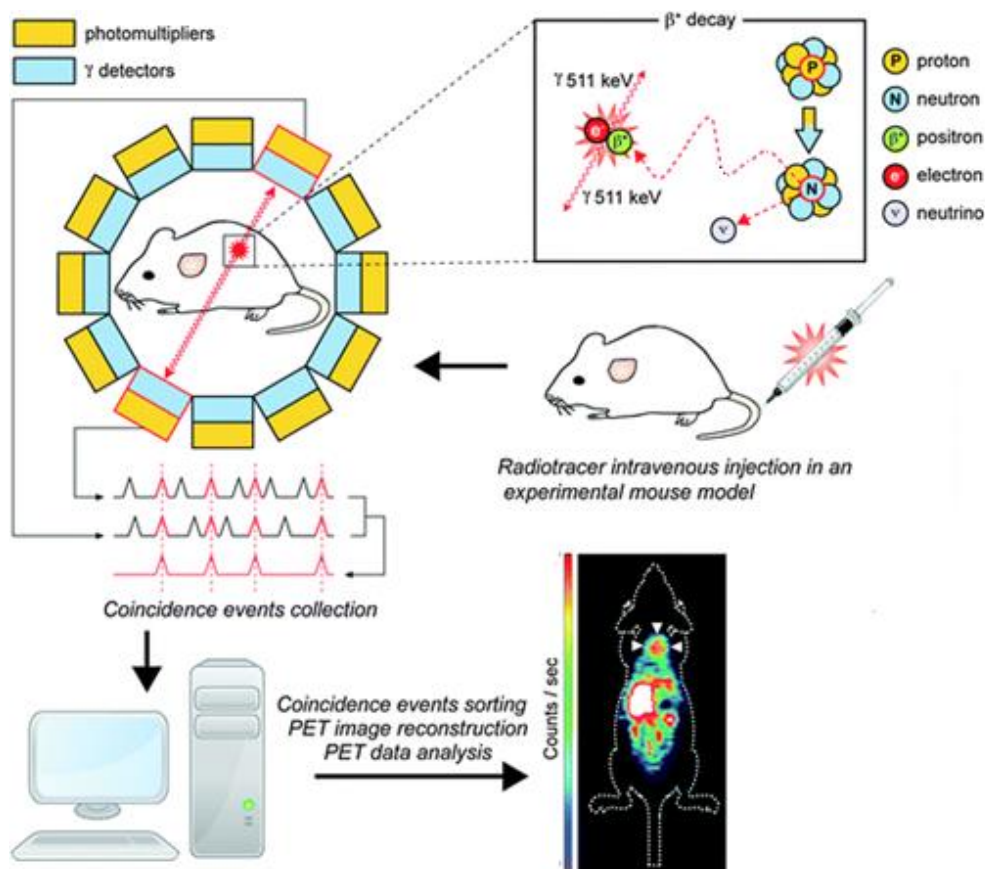


Figure 1.17: Basic principle of PET imaging (adapted from Nguyen *et al.*, 2010).

In practice, a specific probe to visualize a specific molecular process is labeled with a positron-emitting radionuclide that is administered (mostly intravenously) to the subject that is then positioned into the PET scanner.

**Table 1.3:** Commonly used radionuclides in PET and SPECT. EC= electron capture; IT= internal transition (adapted from Lee *et al.*, 2010; Rowland and Cherry, 2008).

Radionuclide	Decay Mode	Half-Life	Modality
<sup>11</sup> C	β <sup>+</sup> (100%)	20.39 min	PET
<sup>18</sup> F	β <sup>+</sup> (96.7%) EC (3%)	109.77 min	PET
<sup>15</sup> O	β <sup>+</sup> (100%)	2.04 min	PET
<sup>13</sup> N	β <sup>+</sup> (100%)	9.97 min	PET
<sup>64</sup> Cu	β <sup>+</sup> (17.6%) EC (43.4%) β <sup>-</sup> (39.0%)	12.70 h	PET/therapy
<sup>124</sup> I	β <sup>+</sup> (23%) EC (77%)	4.20 days	PET
<sup>68</sup> Ga	β <sup>+</sup> (89%) EC (11%)	67.71 min	PET
<sup>89</sup> Zr	β <sup>+</sup> (23%) EC (77%)	3.30 days	PET
<sup>99m</sup> Tc	IT (100%)	6.02 h	SPECT
<sup>111</sup> In	EC (100%)	2.80 days	SPECT
<sup>123</sup> I	EC (100%)	13.22 h	SPECT
<sup>125</sup> I	EC (100%)	60 days	SPECT
<sup>131</sup> I	β <sup>-</sup> (100%)	8.03 days	SPECT/therapy
<sup>201</sup> Tl	EC	3.04 days	SPECT

### SPECT

SPECT imaging is based on the detection of nuclides that decay via the emission of gamma photons, called single-photon emitters. The most commonly used radioisotopes for SPECT imaging are displayed in Table 1.3. The unstable nucleus decays by isomeric transition (IT), β<sup>-</sup> decay, or electron capture (EC) into a stable nucleus, hereby emitting photons. A typical clinical SPECT camera is composed of one or more rotating gamma cameras to obtain multiple projections around the patient and to eventually obtain a tomographic reconstruction.

Since position detection of these photons in SPECT does not provide adequate information about the origin of the photon, it is not possible to determine a “line of response”, as done with PET. Therefore, to allow origin determination of the detected signal, a lead or tungsten collimator is added to the modality, where only photons that travel into a certain direction can pass through the holes of the collimator. The disadvantage of this is the fact that the collimator rejects most of the photons that are not traveling at right angles to the detector. Consequently, the sensitivity is typically two orders of magnitude lower than PET. In clinical cameras, mostly parallel-hole collimators are used (Figure 1.18), whereas in small-animal imaging systems, (multi)pinhole collimators are most often used (see later). The photons are converted into visible light by the NaI(Tl) crystal, and then the light is converted into an electrical signal by the photomultiplier tubes.

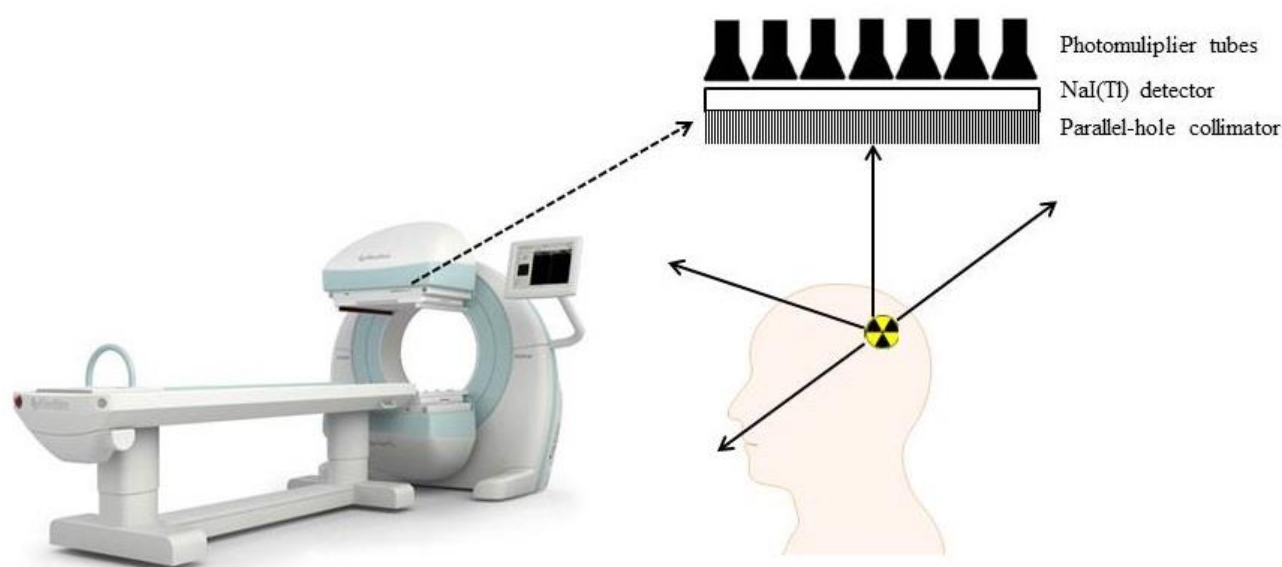
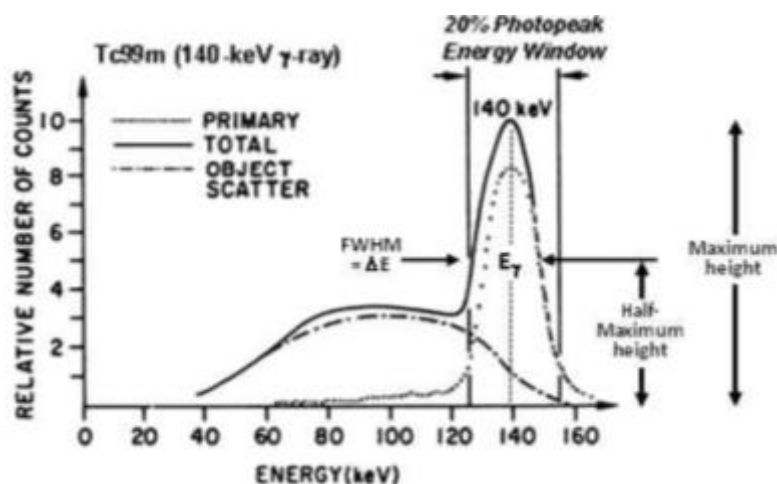


Figure 1.18: Basic principles SPECT imaging.

The gamma photons of SPECT radioisotopes have different energies, in contrast to PET isotopes where two gamma photons of 511 keV originate after annihilation. During SPECT image reconstruction, an energy window is determined that is typically 10-20% around the photon energy peak. A narrow window is chosen to avoid reconstruction of Compton scatter and to improve energy resolution to allow simultaneous imaging of multiple radionuclides (Zanzonico *et al.*, 2012). For  $^{99m}\text{Tc}$ , the energy window is displayed in Figure 1.19. When the energy window is carefully chosen, multi-radionuclide studies can be performed, in contrast

to PET imaging. After reconstruction, 2D and 3D images can be obtained. (*James and Gambhir, 2012; Khalil et al., 2011; Zanzonico, 2012*)



**Figure 1.19:** Energy window of  $^{99m}\text{Tc}$ . (*adapted from Zanzonico., 2012*)

In practice, similar to PET, a specific probe to visualize a specific molecular process is labeled with a single-photon emitter that is administered to the subject that is then positioned into the SPECT scanner for imaging.

### Small animal imaging

Small animal imaging has become an integral part of molecular medicine. Translation of ideas from bench to the clinic needs a verification and validation step where molecular diagnostic modalities are important tools in developing new tracers, drug design and therapeutics (*Khalil et al., 2011*) (see Figure 1.16). Small-animal imaging investigates biological function and structure *in vivo* in a non-invasive manner, to obtain quantitative, spatial and temporal information about a specific normal or diseased animal or tissue. Because of its non-invasive nature, it allows serial investigation of the same animal hereby obtaining information from the inception to progression of a certain disease state. It also allows monitoring of the effectiveness of treatment, with each animal serving as its own control and thereby reducing biological variability. Imaging also reduces the number of animals required for a study. Additionally, the same imaging modalities are used in the clinic and therefore, the findings of small-animal imaging can be translated into patients. Summarized, small animal imaging is clinically translatable, non-invasive and has a quantitative nature. Therefore, it is an important component of modern biomedical research (*Zanzonico, 2012*).

Since more than 75% of animals used for preclinical research are rodents (mostly rats and mice), the spatial resolution of preclinical imaging devices has to be improved because these rodents are typically 100 to 1000 times smaller than humans. Table 1.4 gives an overview of the characteristics of both clinical and preclinical SPECT ( $\mu$ SPECT) and PET ( $\mu$ PET) cameras. The improvement of spatial resolution is achieved at a substantial cost in terms of longer data acquisition times and/or higher administered activities and radiation dose. (Vanhove et al., 2015)

**Table 1.4:** Characteristics of clinical and preclinical cameras (adapted from Khalil et al., 2011; Rowland and Cherry, 2008).

	Clinical SPECT	Clinical PET	Preclinical PET	Preclinical SPECT
<b>Spatial resolution</b>	8-12 mm	4-6 mm	1-2 mm	$\leq 1$ mm
<b>Sensitivity</b>	0.01-0.03%	1-3%	2-4%	0.3%
<b>Field of view</b>	50 cm	50 cm	7 cm	8 cm

### $\mu$ PET

In case of  $\mu$ PET, this superior resolution is achieved by the application of smaller detector elements. Sensitivity can be improved by using a smaller detector ring diameter, by increasing the length of the detector ring, by using novel detector geometries that improve the photon absorption efficiency and by using detectors with better timing resolution and faster decay (de Kemp et al., 2010).

### $\mu$ SPECT

In case of  $\mu$ SPECT, better spatial resolutions can be achieved by the use of pinhole collimation, which magnifies the acquired projection images. Pinhole imaging with gamma rays is based on the same geometric principle as the optical pinhole camera (Figure 1.20). A scintillation detector is used instead of a film. Figure 1.21 shows a mouse that is projected through a parallel-hole collimator (left side) and a pinhole collimator (right side). In the case of an “ideal” parallel-hole collimator, the projection of the object is blurred only by the intrinsic gamma camera resolution,  $R_i$ . The value of  $R_i$ , which is typically 3-4 mm, is a measure for the width of the blob that appears when a pencil gamma beam is used to irradiate the crystal.



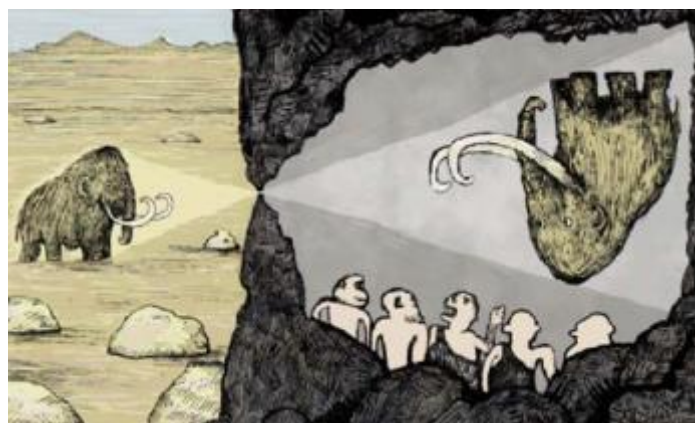


Figure 1.20: Early pinhole imaging.

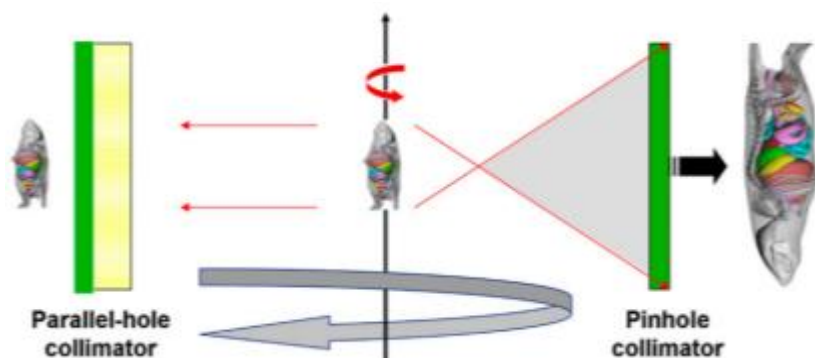


Figure 1.21: Parallel-hole versus pinhole collimator in small-animal imaging. Through magnification of a small object at short distance onto a large detector area, pinhole collimation geometry offers substantial increase in detection efficiency over that of parallel hole collimation geometry. Spatial resolution is determined by size of pinhole aperture (adapted from de Kemp *et al.*, 2010).

The spatial resolution  $R_s$  of a pinhole camera is approximated by the following formula:

$$R_s = \sqrt{\left[ d_e \left( 1 + \frac{1}{M} \right) \right]^2 + \left[ \frac{R_i}{M} \right]^2}$$

$$\text{with } M = \frac{t}{b}$$

$d_e$  is the effective diameter of the pinhole,  $R_i$  is the intrinsic spatial resolution of the gamma detector,  $M$  is the pinhole magnification,  $t$  is the distance between the pinhole opening and the detector and  $b$  is the distance between the object and the pinhole (Figure 1.22). So when the distance between the mouse and the pinhole is 7 cm and the distance between the pinhole and the detector is 35 cm, the magnification of the mouse amounts 5. Therefore, when the size of

the projection of the mouse is reduced to its original size, it is not smoothed with an amount corresponding to  $R_i$ , but is smoothed only with  $R_i/5$ , thus improving spatial resolution. The smaller the object, the closer it can be placed to the pinhole and the higher the magnification can be.

A consequent challenge is to acquire a sufficient number of counts in each individual voxel to support the high spatial resolution and to obtain a sufficient signal-to-noise ratio. The sensitivity of a pinhole system is approximated by:

$$S = \left( \frac{d_e^2}{16b^2} \right) N$$

Where N represents the number of gamma detectors. The sensitivity can be improved by increasing the diameter of the pinhole opening to allow more gamma photons to pass. However, this will be at the cost of a poorer spatial resolution. The sensitivity can also be improved by bringing the object closer to the pinhole opening, however, this will be at the cost of the size of the field of view.

In conclusion, the choices between spatial resolution, sensitivity and size of the field of view need to be carefully examined before performing a preclinical animal SPECT experiment. (Vanhove *et al.*, 2015; Beekman and van der Have, 2006; Nuyts *et al.*, 2009; Franc *et al.*, 2008; de Kemp *et al.*, 2010)

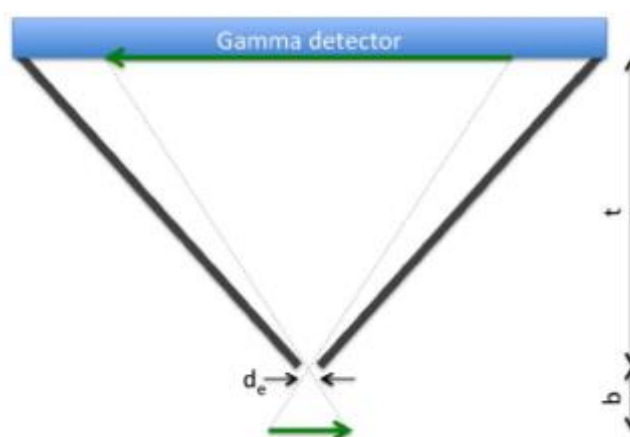


**Figure 1.22:** Principle of pinhole collimation.  $b$  represents the distance between the object and the pinhole and  $t$  represents the distance between the pinhole opening and the gamma detector.  $d_e$ = effective diameter of the pinhole opening (adapted from Vanhove *et al.*, 2016).

When carefully designed, the use of multiple detectors in combination with multi-pinhole collimators can improve the spatial resolution and sensitivity with one order of magnitude,

compared to clinical systems (Figure 1.23). The use of multipinhole collimators and detectors (and resulting higher sensitivity) also allows dynamic imaging, in contrast to clinical systems.

Today, all commercial  $\mu$ SPECT systems are equipped with multi-detector and multi-pinhole geometry. In this thesis, an USPECT-II/CT device (MILabs, The Netherlands) was used (Figure 1.24). The detectors are stationary and the animal bed is moving (*van der Have F, 2009*).

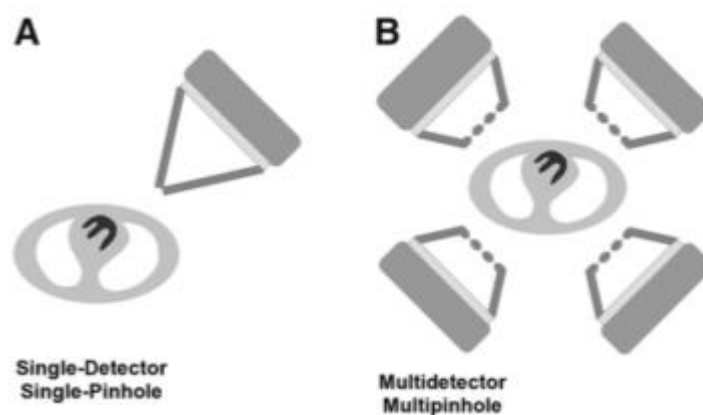


**Figure 1.23:** Early small-animal SPECT systems were developed using single scintillation camera with single-pinhole collimator (A). Modern small-animal SPECT systems use multiple detectors, each with multipinhole collimators (B). (*adapted from Franc et al., 2008*)



**Figure 1.24:** USPECT-II/CT.

After imaging, the acquired projection data need to be reconstructed. In multi-detector multipinhole  $\mu$ SPECT imaging, iterative reconstruction algorithms are routinely used that can take into account the complex system geometry .

### Dynamic imaging and kinetic modeling

After injection into the blood stream, the radiotracer is transported to several organs and is taken up by these organs. Dynamic imaging is an imaging procedure that follows the distribution of the radiotracer in function of time in different organs of interest: clearance from the blood, uptake in several tissues, secretion, possible trapping, etc. Both, PET and SPECT, have the potential to perform dynamic imaging studies.

The uptake of the radiotracer depends on the affinity for the particular compound in the organ. Additionally, the uptake also depends on delivery of the tracer, which is reflected in the time course of activity in the blood. Therefore, it is very important to measure the arterial blood curve during the acquisition. Blood sampling is the gold standard to obtain arterial input functions. This can be achieved by manual sampling or continuous blood withdrawal and detection. However, for small animal imaging, this is a problem since the maximal sampling volume in a mouse of 25g is 0.015 mL (1%) for repeated measures within 24 hours. Therefore, image derived methods were introduced, where a region of interest (ROI) is drawn around the heart or an artery (*Lammertsma, 2002; Gullberg et al., 2010; Vanhove et al., 2015*). To determine the ROI around the heart, radiotracers can be used that can visualize the left ventricular cavity. This was demonstrated in a PET study of Moerman et al. (2011), where [ $^{18}\text{F}$ ] fluoro-2-deoxy-D-glucose ([ $^{18}\text{F}$ ]FDG) was used to visualize the myocardium of the left ventricle. After the dynamic scan with the tracer of interest, [ $^{18}\text{F}$ ]FDG was administered to the mice and an additional static scan was done. A ROI around the left ventricle could be drawn based on the static FDG scan, and this ROI could be easily pasted on the dynamic tracer data, since the animal was not moved between the dynamic tracer acquisition and the static FDG scan.

Besides the determination of the arterial input curve, the time course of the tracer in the organs of interest have to be determined. ROIs are drawn around the organs of interest and the tracer distributions in function of time are obtained as time activity curves (TACs).

Tracer kinetic or compartmental modeling of these dynamic PET or SPECT measurements allow calculation of physiological parameters by fitting a mathematical compartmental model of tracer distribution and metabolism to the data. An example of a general two-tissue compartment model is given in Figure 1.25.

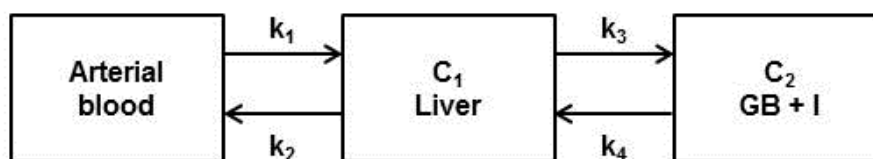


**Figure 1.25:** General two tissue compartment model. This model consist of a blood compartment, two tissue compartments and 4 rate constants. GB+I: gallbladder + intestines.

A compartmental model is divided in physiologically separate entities in which the tracer is distributed. These entities are also called compartments that represent different organs or different states of the tracer within an organ, for example the bound and unbound fraction of the tracer. Between these compartments, there can be movements of the tracer, influx and efflux, which are expressed by means of rate constants, denoted with lower case  $k$ . For example, in Figure 1.25, the first compartment is the arterial blood. From the arterial blood, the tracer passes into a second compartment, namely the first tissue compartment  $C_1$ , for example the liver. Then, the radiotracer can be transported into a second tissue compartment,  $C_2$ , for example the gallbladder and intestines. This transport can be an indication of, for example, functioning hepatobiliary transport proteins. The influx in tissue compartment  $C_1$  (liver) is represented by  $k_1$  and is an indicator of the blood clearance of the tracer, in this case from the liver sinusoids into the hepatocytes.  $k_2$  then represents the transport of the tracer from the liver back into the blood.  $k_3$  then represents efflux from the liver to the gallbladder and intestines. No transport from gallbladder and intestines to the liver is observed and therefore,  $k_4$  equals 0 in this specific example. All rate constants ( $k$ -values) are expressed as 1/sec or 1/min.

The kinetics of compartmental models can be described by a set of first-order linear differential equations. We are dealing with first order processes under the assumptions. Tracer kinetic modeling requires several assumptions: the physiological process of interest is not influenced by administration of the radiotracer, the physiological process has to remain constant during the acquisition and each compartment is homogeneous and the tracer is immediately mixed in the compartment (*Watabe et al., 2006; Acton et al., 2004; Innis et al., 2007; Kutner, 2014*).

When the first order kinetics are applied to the model depicted in Figure 1.25, the concentration of the tracer in compartments  $C_1$  and  $C_2$  in function of time can be described by two differential equations:

$$\frac{dC_1(t)}{dt} = k_1 C_a(t) - (k_2 + k_3) C_1(t) + k_4 C_2(t)$$

$$\frac{dC_2(t)}{dt} = k_3 C_1(t) - k_4 C_2(t)$$

$C_a$  is the time course of the tracer in the arterial plasma, also referred as the arterial input curve. When the TACs, the arterial input function and a proposed model configuration are given, the underlying rate constants ( $k_1$ - $k_4$ ) can be calculated by solving the differential equations using for example least square methods.

## References

- Acton PD, Zhuang H, Alavi A. Quantification in PET. *Radiol Clin N Am* 2004;42:1055-1062.
- Alrefai WA, Gill RK. Bile acid transporters: structure, function, regulation and pathophysiological implications. *Pharm Res* 2007;24:1803-1823.
- Annaert PP, Brouwer KL. Assessment of drug interactions in hepatobiliary transport using rhodamine 123 in sandwich-cultured rat hepatocytes. *Drug Metab Dispos* 2005;33:388-394.
- Anwer MS, Stieger B. Sodium-dependent bile salt transporters of the SLC10A transporter family: more than solute transporters. *Eur J Physiol* 2014;466:77-89.
- Arrese M, Ananthanarayanan M, Suchy FJ. Hepatobiliary transport: molecular mechanisms of development and cholestasis. *Ped Res* 1998;44:141-147.
- Ballatori N, Christian WV, Wheeler SG, Hammond CL. The heteromeric organic solute transporter, OST $\alpha$ -OST $\beta$ /SLC51: a transporter for steroid-derived molecules. *Mol Aspects Med* 2013;34:683-692.
- Beekman F, van der Have F. The pinhole: gateway to ultra-high-resolution three-dimensional radionuclide imaging. *Eur J Nucl Med Mol Imaging* 2007;34:151-161.
- Bergman E, Hedeland M, Bondesson U, Lennernas H. The effect of acute administration of rifampicin and imatinib on the enterohepatic transport of rosuvastatin *in vivo*. *Xenobiotica* 2010;40:558-568.
- Bernal JD. Crystal structures of vitamin D and related compounds. *Nature* 1932;129:277-278.
- Boyer JL. Bile formation and secretion. *Compr Physiol* 2013;3:1035-1078.
- Bradley WG. History of medical imaging. *Proc Am Philos Soc* 2008;152:349-361.
- Claro da Silva T, Polli JE, Swaan PW. The solute carrier family 10 (SLC10): beyond bile acid transport. *Mol Aspects Med* 2013;34:252-269.
- Chatterjee S, Richert L, Augustijns P, Annaert P. Hepatocyte-based *in vitro* model for assessment of drug-induced cholestasis. *Toxicol Appl Pharmacol* 2014;274:124-136.
- Dawson PA, Lan T, Rao A. Bile acid transporters. *J Lipid Res* 2009;50:2340-2357.
- De Bruyn T, Sempels W, Snoeys J, Holmstock N, Chatterjee S, Stieger B, et al. Confocal imaging with a fluorescent bile acid analogue closely mimicking hepatic taurocholate disposition. *J Pharm Sci* 2014;103:1872-1881.
- de Graaf W, Häusler S, Heger M, van Ginhoven TM, van Cappellen G, Bennink RJ, et al. Transporters involved in the hepatic uptake <sup>99m</sup>Tc-mebrofenin and indocyanine green. *J Hepatol* 2011;54:738-745.

De Kemp RA, Epstein FH, Catana C, Tsui BMW, Ritman EL. Small-animal molecular imaging methods. *J Nucl Med* 2010;51:18S-32S.

de Lima Toccafonda Vieira M, Tagliati CA. Hepatobiliary transporters in drug-induced cholestasis: a perspective on the current identifying tools. *Expert Opin Drug Metab Toxicol* 2014;10:581-597.

Dietschy JM, Turley SD, Spady DK. Role of the liver in the maintenance of cholesterol and low density lipoprotein homeostasis in different animal species, including humans. *J Lipid Res* 1993;34:1637-1659.

Dietschy JM, Turley SD. Control of cholesterol turnover in the mouse. *J Biol Chem* 2002;277:3801-3804.

Erlinger S. New insights into the mechanisms of hepatic transport and bile secretion. *J Gastroenterol Hepatol* 1996;11:575-579.

Esteller A. Physiology of bile secretion. *World J Gastroenterol* 2008;14:5641-5649.

Fardel O, Jigorel E, Le Vee M, Payen L. Physiological, pharmacological and clinical features of the multidrug resistance protein 2. *Biomed Pharmacother* 2005;59:104-114.

Franc BL, Acton PD, Mari C, Hasegawa BH. Small-animal SPECT and SPECT/CT: important tools for preclinical investigation. *J Nucl Med* 2008;49:1651-1663.

Frevert U. Sneaking in through the back entrance: the biology of malaria liver stages. *Trends Parasitol* 2004;20:417-424.

Gai Z, Chu L, Hiller C, Arsenijevic D, Penno CA, Montani JP, Odermatt A, et al. Effect on chronic renal failure on the hepatic, intestinal, and renal expression of bile acid transporters. *Am J Physiol Renal Physiol* 2014;306:F130-F137.

Greupink R, Nabuurs SB, Zarzycka B, Verweij V, Monshouwer M, Huisman MT, et al. In silico identification of potential cholestasis-inducing agents via modeling of Na<sup>+</sup>-dependent taurocholate cotransporting polypeptide substrate specificity. *Toxicol Sci* 2012;129:35-48.

Hagenbuch B, Dawson P. The sodium bile salt cotransport family SLC10. *Eur J Physiol* 2004;447:566-570.

Hagenbuch B, Meier PJ. Molecular cloning, chromosomal localization, and functional characterization of a human liver Na<sup>+</sup>/bile acid cotransporter. *J Clin Invest* 1994;93:1326-1331.

Hagenbuch B, Meier PJ. Organic anion transporting polypeptides of the OATP/SLC21 family: phylogenetic classification as OATP/SLCO superfamily, new nomenclature and molecular/functional properties. *Eur J Physiol* 2004;447:653-665.

Halilbasic E, Claudel T, Trauner M. Bile acid transporters and regulatory nuclear receptors in the liver and beyond. *J Hepatol* 2013;58:155-168.

Hallen S, Mareninova O, Branden M, Sachs G. Organization of the membrane domain of the human liver sodium/bile acid cotransporter. *Biochemistry* 2002;41:7253-7266.



Hofmann AF, Hagey LR. Bile acids: chemistry, pathochemistry, biology, pathobiology, and therapeutics. *Cell Mol Life Sci* 2008;65:2461-2483.

Hofmann AF, Hagey LR. Key discoveries in bile acid chemistry and biology and their clinical applications: history of the last eight decades. *J Lipid Res* 2014;55:1553-1595.

Hofmann AF, Molino G, Milanese M, Belforte G. Description and simulation of a physiological pharmacokinetic model for the metabolism and enterohepatic circulation of bile acids in man. *J Clin Invest* 1983;71:1003-1022.

Hulzebos CV, Renfurm L, Bandsma RH, Verkade HJ, Boer T, Boverhof R. Measurement of parameters of cholic acid kinetics in plasma using a microscale stable isotope dilution technique: application to rodents and humans. *J Lipid Res* 2001;42:1923-1929.

Innis RB, Cunningham VJ, Delforge J, Fujita M, Gjedde A, Gunn RN, et al. Consensus nomenclature for *in vivo* imaging of reversibly binding radioligands. *J Cereb Blood Flow Metab* 2007;27:1533-1539.

Iusuf D, van de Steeg E, Schinkel AH. Functions of OATP1A and 1B transporters *in vivo*: insights from mouse models. *Trends Pharmacol Sci* 2012;33:100-108.

James ML, Gambhir SS. A molecular imaging primer: modalities, imaging agents and applications. *Physiol Rev* 2012;92:897-965.

Keppler D. The roles of MRP2, MRP3, OATP1B1, and OATP1B3 in conjugated hyperbilirubinemia. *Drug Metab Dispos* 2014;42:561-565.

Khalil MM, Tremoleda JL, Bayomy TB, Gsell W. Molecular SPECT imaging: an overview. *Int J Mol Imaging* 2011:Epub 2011.

King MA, Pretorius PH, Farncombe T, Beekman FJ. Introduction to the physics of molecular imaging with radioactive tracers in small animals. *J Cell Biochem Suppl* 2002;39:332-230.

Kis E, Ioja E, Rajnai Z, et al. BSEP inhibition - *In vitro* screens to assess cholestatic potential of drugs. *Toxicol In vitro* 2012;26:1294-1299.

Kosters A, Karpen J. Bile acid transporters in health and disease. *Xenobiotica* 2008;38:1043-1071.

Kullak-Ublick GA, Ismail MG, Stieger B, Landmann L, Huber R, Pizzagalli F, et al. Organic anion-transporting polypeptide B (OATP-B) and its functional comparison with three other OATPs of human liver. *Gastroenterology* 2001;120:525-533.

Kullak-Ublick GA, Stieger B, Hagenbuch B, Meier PJ. Hepatic transport of bile salts. *Semin Liver Dis* 2000;20:273-292.

Kutner C. Kinetic modeling in pre-clinical positron emission tomography. *Z Med Phys* 2014;24:274-285.

Lammertsma AA. Radioligand studies: imaging and quantitative analysis. *Eur Neuropsychopharmacol* 2002;12:513-516.

Lee YS. Radiopharmaceuticals for molecular imaging. *The Open Nuclear Medicine Journal* 2010;2:178-185.

Lengyel G, Veres Z, Tugyi R, et al. Modulation of sinusoidal and canalicular elimination of bilirubin-glucuronides by rifampicin and other cholestatic drugs in a sandwich culture of rat hepatocytes. *Hepatol Res.* 2008;38:300-309.

Maddrey WC. Drug-induced hepatotoxicity. *J Clin Gastroenterol.* 2005;39:S83-S89.

Mareninova O, Shin JM, Vagin O, Turdikulova S, Hallen S, Sachs G. Topography of the membrane domain of the liver Na<sup>+</sup>-dependent bile acid transporter. *Biochemistry* 2005;44:13702-13712.

Marin JJG, Macias RIR, Briz O, Banales JM, Monte MJ. Bile acids in physiology, pathology and pharmacology. *Curr Drug Metab* 2016;17:4-29.

Massoud TE, Gambhir SS. Molecular imaging in living subjects: seeing fundamental biological processes in a new light. *Genes Dev* 2003;17:545-580.

Meier PJ, Eckhardt U, Schroeder A, Hagenbuch B, Stieger B. Substrate specificity of sinusoidal bile acid and organic anion uptake systems in rat and human liver. *Hepatology* 1997;26:1667-1677.

Meier PJ, Stieger B. Bile salt transporters. *Annu Rev Physiol* 2002;64:635-661.

Mita S, Suzuki H, Akita H, Hayashi H, Onuki R, Hofmann AF, et al. Inhibition of bile acid transport across Na<sup>+</sup>/taurocholate cotransporting polypeptide (SLC10A1) and bile salt export pump (ABCB 11)-coexpressing LLC-PK1 cells by cholestasis-inducing drugs. *Drug Metab Dispos.* 2006;34:1575-1581.

Moerman L, De Naeyer D, Boon P, De Vos F. Kinetic modeling with <sup>11</sup>C-desmethyloperamide to visualize P-glycoprotein in brain. *EJNMMI Research* 2011;1:12-20.

Nakanishi T, Shibue Y, Fukuyama Y, Yoshida K, Fukuda H, Shirasaka Y, et al. Quantitative time-lapse imaging-based analysis of drug-drug interaction mediated by hepatobiliary transporter, multidrug resistance-associated protein 2, in sandwich-cultured rat hepatocytes. *Drug Metab Dispos.* 2011;39:984-991.

Nguyen QD, Aboagye EO. Imaging the life and death of tumors in living subjects: preclinical PET imaging of proliferation and apoptosis. *Integr Biol (Camb)* 2010;2:483-495.

Nies AT, Keppler D. The apical conjugate efflux pump ABCC2 (MRP2). *Eur J Physiol* 2007;463:643-659.

Noé J, Stieger B, Meier PJ. Functional expression of the canalicular bile salt export pump of human liver. *Gastroenterology* 2002;123:1659-1666.

Nuyts J, Vunckx K, Defrise M, Vanhove C. Small animal imaging with multi-pinhole SPECT. *Methods* 2009;48:83-91.

- Oorts M, Baze A, Bachelier P, Heyd B, Zacharias T, Annaert P, et al. Drug-induced cholestasis risk assessment in sandwich-cultured human hepatocytes. *Toxicol in vitro* 2016;34:179-186.
- Padda MS, Sanchez M, Akhtar AJ, Boyer JL. Drug-induced cholestasis. *Hepatology*. 2011;53:1377-1387.
- Pauli-Magnus C, Meier PJ. Hepatobiliary transporters and drug-induced cholestasis. *Hepatology* 2006;44:778-787.
- Pellicoro A, Faber KN. The function and regulation of proteins involved in bile salt biosynthesis and transport. *Aliment Pharmacol Ther* 26:149-160.
- Perez MJ, Briz O. Bile-acid-induced cell injury and protection. *World J Gastroenterol* 2009;15:1677-1689.
- Roberts MS, Magnusson BM, Burczynski FJ, Weiss M. Enterohepatic circulation. *Clin Pharmacokinet* 2002;41:751-790.
- Rosenheim O, King H. The chemistry of the sterols, bile acids, and other cyclic constituents of natural fats and oils. *Annu Rev Biochem* 1934;3:87-110.
- Rowland DJ, Cherry SR. Small-animal preclinical nuclear medicine instrumentation and methodology. *Semin Nucl Med* 2008;38:209-222.
- Russell DW. The enzymes, regulation, and genetics of bile acid synthesis. *Annu Rev Biochem* 2003;72:137-174.
- Saito H, Osumi M, Hirano H, Shin W, Nakamura R, Ishikawa T. Technical pitfalls and improvements for high-speed screening and QSAR analysis to predict inhibitors of the human bile salt export pump. *AAPS J* 2009;11:581-589.
- Schadt HS, Wolf A, Pognan F, Chibout SD, Merz M, Kullak-Ublick GA. Bile acids in drug induced liver injury: key players and surrogate markers. *Clin Res Hepatol Gastroenterol* 2016; in press.
- Shneider BL, Fox VL, Schwarz KB, Watson CL, Ananthanarayanan M, Thevananther S, et al. Hepatic basolateral sodium-dependent-bile acid transporter expression in two unusual cases of hypercholanemia and in extrahepatic biliary atresia. *Hepatology* 1997;25:1176-1183.
- Stabin MG, Brill AB. Radiation dosimetry and exposure in nuclear medicine. *Semin Nucl Med* 2008;38:306-307.
- Stenvall A, Larsson E, Strand SE, Jönsson BA. A small-scale anatomical dosimetry model of the liver. *Phys Med Biol* 2014;59:3353-3371.
- Stieger B, Fattinger K, Madon J, Kullak-Ublick GA, Meier PJ. Drug-and Estrogen-Induced Cholestasis Through Inhibition of the Hepatocellular Bile Salt Export Pump (Bsep) of Rat Liver. *Gastroenterology*. 2000;118:422-430.
- Stieger B, Geier A. Genetic variations of bile salt transporters as predisposing factors for drug-induced cholestasis, intrahepatic cholestasis of pregnancy and therapeutic response of viral hepatitis. *Expert Opin Drug Metab Toxicol*. 2011;7:411-425.

Stieger B, Meier Y, Meier PJ. The bile salt export pump. *Eur J Physiol* 2007;453:611-620.

St-Pierre M, Kullak-Ublick GA, Hagenbuch B, Meier PJ. Transport of bile acids in hepatic and non-hepatic tissues. *J Exp Biol* 2001;204:1673-1686.

Strazzabosco M, Fabris L. Functional anatomy of normal bile ducts. *Anat Rec* 2008;291:653-660.

Tamai I, Nozawa T, Koshida M, Nezu J, Sai Y, Tsuji A. Functional characterization of human organic anion transporting polypeptide B (OATP-B) in comparison with liver-specific OATP-C. *Pharm Res* 2001;18:1262-1269.

Thomas C, Pellicciari R, Pruzanski M, Auwerx J, Schoonjans K. Targeting bile-acid signaling for metabolic diseases. *Nat Rev Drug Discov* 2008;7:678-669.

Tian J. *Molecular imaging: Fundamentals and applications*. Elsevier 2012. E-book.

Trauner M, Boyer JL. Bile salt transporters: molecular characterization, function and regulation. *Physiol Rev* 2003;83:633-671.

Treyer A, Müsch A. Hepatocyte polarity. *Compr Physiol* 2013;3:243-287.

Van de Steeg E, Wagenaar E, van der Kruijssen CMM, Burggraaff JEC, de Waart DR, Oude Elferink RPJ, et al. Organic anion transporting polypeptide 1a/1b-knockout mice provide insights into hepatic handling of bilirubin, bile acids, and drugs. *J Clin Invest* 2010;120:2942-2952.

Van der Have F, Vastenhouw B, Ramakers RM, Branderhorst W, Krah JO, Ji C, Staelens SG, Beekman FJ. U-SPECT-II: an ultra-high-resolution device for molecular small-animal imaging. *J Nucl Med* 2009;50:599-605.

Vanhove C, Bankstahl JP, Krämer SD, Visser E, Belcari N, Vandenberghe S. Accurate molecular imaging of small animals taking into account animal models, handling, anaesthesia, quality control and imaging system performance. *EJNMMI Physics* 2015;2:EPub.

Vaz FM, Paulusma CC, Huidekoper H, de Ru M, Lim C, Koster J, Ho-Mok K, et al. Sodium taurocholate cotransporting polypeptide (SLC10A1) deficiency: conjugated hypercholanemia without a clear clinical phenotype. *Hepatology* 2015;61:260-267.

Warner DJ, Chen H, Cantin LD, Kenna JG, Stahl S, Walker CL, et al. Mitigating the inhibition of human bile salt export pump by drugs: opportunities provided by physicochemical property modulation, in silico modeling, and structural modifications. *Drug Metab Dispos* 2012;40:2332-2341.

Watabe H, Ikoma Y, Kimura Y, Naganawa M, Shidahara M. PET kinetic analysis – compartmental model. *Ann Nucl Med* 2006;20:583-588.

Weissleder R, Ross BD, Rehemtulla A, Gambhir SS. 2010. *Molecular imaging: principles and practice*. People's Medical Publishing House – USA

Wieland H. 1928. The chemistry of the bile acids. In Nobel Lectures, Chemistry 1922–1941. Elsevier Publishing Company, Amsterdam, The Netherlands. 94–102.

Windaus A. 192 . Constitution of sterols and their connection with other substances occurring nature. In Nobel Lectures, Chemistry 1922–1941. Elsevier Publishing Company, Amsterdam, The Netherlands. 105–121.

Wolf KK, Vora S, Webster LO, Generaux GT, Polli JW, Brouwer KLR. Use of cassette dosing in sandwich-cultured rat and human hepatocytes to identify drugs that inhibit bile acid transport *Toxicol In vitro*. 2010;24:297-309.

Wolkoff, AW, DE Cohen. Bile acid regulation of hepatic physiology: Hepatocyte transport of bile acids. *Am J Physiol Gastrointest Liver Physiol*. 2003;284:G175-G179.

Xia X, Francis H, Glaser S, Alpini G, LeSage G. Bile acid interactions with cholangiocytes. *World J Gastroenterol* 2006;12:3553-3563.

Yamaguchi H, Okada M, Akitaya S, et al. Transport of fluorescent chenodeoxycholic acid via the human organic anion transporters OATP1B1 and OATP1B3. *J Lipid Res*. 2006;47:1196-1202.

Yang K, Köck K, Sedykh A, Tropsha A, Brouwer KLR. An updated review on drug-induced cholestasis: mechanisms and investigation of physiochemical properties and pharmacokinetic parameters. *J Pharm Sci* 2013;102:3037-3057.

Zanzonico P. Principles of nuclear medicine imaging: planar, SPECT, PET, multi-modality, and autoradiography systems. *Radiat Res* 2012;177:349-364.

Zwicker BL, Agellon LB. Transport and biological activities of bile acids. *Int J Biochem Cell Biol* 2013;42:1389-1398

# Chapter 2. Functional hepatobiliary imaging



## Introduction

Functional liver assessment is of great importance and the determination of clearance of hepatobiliary transport proteins substrates could be used as a measure for liver function. There are three factors that can modify the transport of hepatobiliary imaging agents through hepatocytes:

- 1) Interindividual variability of transporters in the normal liver
- 2) Modifications of transporter expression in diseased liver tissue and focal lesions
- 3) Drug interactions.

Prognostic tools are also important for the management of patients with severe chronic liver disease or liver failure, which is the major cause of mortality and morbidity after partial liver resection and is a result of insufficient functional remnant liver mass. Additionally, the investigation of liver function is important in the development of new drug candidates, the inhibition of hepatobiliary transporters, for example, can lead to drug induced liver injury (see Chapter 1). Several liver function tests have been developed. In this chapter, we will focus on molecular imaging techniques as useful tool to investigate hepatobiliary function in which measurement of hepatobiliary compounds in the liver may serve as biomarkers. An overview on the molecular imaging techniques and specific hepatobiliary contrast agents for the assessment of hepatobiliary function will be given (*Hoekstra et al., 2013; Sakka, 2007; Stieger et al., 2012*).



# Hepatobiliary contrast agents in magnetic resonance imaging

Magnetic resonance imaging (MRI) is a technique that uses a powerful magnet to align the nuclei of atoms (mainly H) inside the body, and a variable magnetic field that causes the atoms to resonate. Two relaxation times, the longitudinal relaxation T1 and spin-spin relaxation T2 (caused by interactions between neighbouring protons), can be used for image reconstruction.

MRI of the liver is used for the characterization of masses, detection of primary and metastatic lesions, assessment of vascular structures, investigation of lesion vascularity and evaluation of the biliary tree. In MRI of the liver, several classes of contrast agents can be distinguished:

- 1) Extracellular or nonspecific contrast agents
- 2) Reticuloendothelial contrast agents
- 3) Blood pool agents
- 4) Hepatobiliary contrast agents

A short description of the first three groups will be given, but the focus will be on the last group, since this group allows functional imaging of hepatobiliary transport because these agents are taken up by the hepatocytes.

Most contrast agents are composed of gadolinium bound within an organic chelate, which makes them paramagnetic substances that can induce changes in the local magnetic field. The T1 shortening property of gadolinium based contrast agents (GBCAs) is the most useful and the contrast enhancement is used to detect the presence of the GBCAs. Other types of contrast agents are manganese and iron based (*Bashir, 2014; Gandhi et al., 2006*).

## Extracellular contrast agents

Extracellular contrast agents, for example gadobutrol, are GBCAs that are distributed within the extracellular interstitial space. After intravenous injection, these contrast agents reach the liver via the hepatic arteries, which results in mild enhancement of the hepatic parenchyma. Solid liver lesions with an arterial-dominant vascular supply will have an arterial

hyperenhancement which is important for lesion detection and characterization. Additionally, the arterial hyperenhancement is important for the delineation of normal and variant hepatic arterial anatomy. After the arterial phase, further hepatic enhancement can be observed due to additional contrast medium that arrives in the liver via the portal vein, called the portal venous phase which occurs 60 to 70 seconds after intravenous injection of the contrast agent. In this phase, a washout appearance can be observed in liver lesions, since there is a weak additional enhancement of these lesions from the portal venous supply. After the portal venous phase, the equilibrium phase can be observed after 90 seconds, in which the contrast agent equilibrates between the arterial and venous distributions, as well as the extravascular and extracellular interstitium.

### **Reticuloendothelial contrast agents**

These contrast agents target the reticuloendothelial system, particularly the liver and spleen. The uptake is a measure for the number of functioning macrophages. Examples of reticuloendothelial contrast agents are superparamagnetic iron oxide (SPIO) particles, which are phagocytosed by macrophages, and preferentially by Kupfer cells, which line the liver sinusoids. The reason for this affinity is unclear, but it may be related to particle size. SPIOs are negative contrast agents that reduce signal intensity, particularly on T2 and T2\*. Most liver tumors (benign and malignant, primary or metastatic) are deficient in Kupffer cells and do not exhibit SPIO uptake, so tumors appear relatively hyperintense compared to normal tissue (*Gandhi et al., 2006*).

### **Bloodpool contrast agents**

The blood pool agents, for example gadofosveset trisodium, remain longer in the intravascular space than extracellular agents. Because of strong binding to serum albumin, they are cleared slowly and there is little leakage into the interstitial compartment. Due to the long serum half-lives, there is only little parenchymal enhancement and therefore, they can be used for imaging vascular abnormalities in the equilibrium phase. There are three main categories: ultrasmall SPIO particles, agents that reversibly bind to plasma proteins and macromolecules (*Gandhi et al., 2006; Bashir, 2014*).

## Hepatobiliary contrast agents

### *Hepatobiliary contrast agents used in the clinic – transporter substrates*

There are two hepatobiliary contrast agents available in the clinic: Gadobenate dimeglumine (Gd-BOPTA, MultiHance, Bracco Diagnostics), which shows 5% uptake in a normal human liver, and Gadoxetate disodium (Gd-EOB-DTPA, Eovist, Bayer Healthcare), which shows 50% uptake in normal liver, via OATPs and MRP2 (*Ulloa et al., 2013; Nassif et al., 2012; Leonhardt et al., 2010; de Haën et al., 1995*).

Figure 2.1 displays representative images of the different phases from a liver MRI examination with gadoxetate disodium as contrast agent. Initially, these contrast agents distribute in a similar manner compared to extracellular contrast agents. There is both an arterial phase with enhancement (Figure 2.1, A), followed by a portal venous phase (Figure 2.1, B) with washout features of liver lesions. Additionally, after the dynamic phase, hepatocyte uptake and biliary excretion can be observed (Figure 2.1, C). The contrast agents are taken up by the hepatocytes and are excreted to the gallbladder and intestines, reaching the hepatobiliary phase (Figure 2.1, D). In this phase, the liver and bile ducts are enhanced on T1-weighted images, due to accumulation of the contrast agents, and the blood vessels are dark. The hepatobiliary phase is typically reached between 20 and 120 minutes for gadoxetate disodium, and between 45 and 120 minutes for gadobenate dimeglumine and has an optimal uptake into hepatocytes and excretion into bile to allow visualization of both the biliary system and liver.

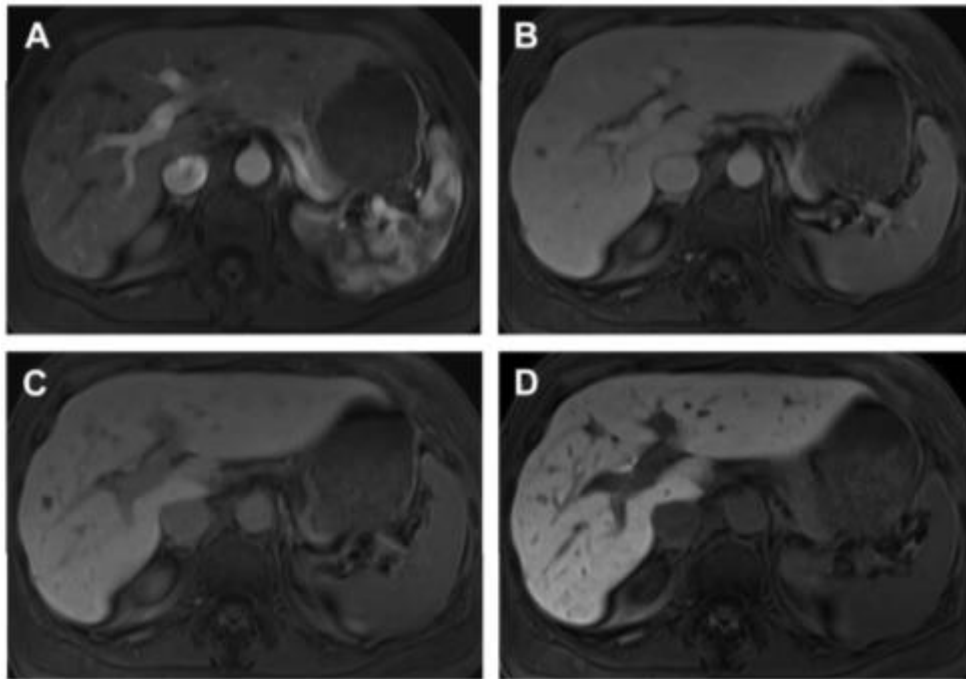


**Figure 2.1:** MRI images of the different phases from a liver MRI examination with gadoxetate disodium as contrast agent. A: late hepatic arterial phase with enhancement of the hepatic artery and early enhancement of the portal vein. B: portal venous phase with enhancement of the portal and hepatic veins, and also a strong enhancement of the hepatic parenchyma, due to early hepatocyte uptake of the contrast agent. C: late dynamic phase with strong enhancement of the liver with relative washout in the vessels. The liver enhancement is caused by a combination of residual intravascular enhancement, leakage to the extravascular extracellular interstitial space and active hepatocyte uptake by OATPs. D: Hepatobiliary phase with strong enhancement of liver, washout of the blood vessels and excretion into the bile ducts (*adapted from Bashir, 2014*).

Additionally, hepatocyte-containing lesions will also be enhanced. This contrast enhancement pattern depends on:

- 1) the presence of functioning hepatocytes
- 2) vascular supply of the lesion
- 3) characteristics of the biliary structures within the lesions.

These hepatobiliary imaging agents can be used as biomarker of hepatobiliary transporter function in a noninvasive manner. The majority of the liver function tests measures the global function of the liver, with no consideration for segmental variations in function or dysfunction. Liver-specific MR contrast agents can assess liver function at segmental level, with an excellent anatomical resolution. This can be important in the treatment planning before liver resection for example in liver cirrhosis and hepatocellular carcinomas (HCC), which do not have a normal liver parenchyma. However, further technical development and clinical validation of this method is needed (*Serlin et al., 2014; Pastor et al., 2014*).

In the clinic, hepatobiliary imaging agents are mostly used for the characterization of liver lesions of hepatocellular origin (HCC, focal nodular hyperplasia (FNH), hepatocellular adenoma (HCA)) and of nonhepatocellular origin (cavernous hemangioma, cysts, metastases). FNH and HCA are often difficult to differentiate by conventional MRI. However, the distinction is important since FNH needs no therapeutic intervention but HCA does, due to its potential for malignant transformation and bleeding. Hepatobiliary contrast agents accumulate differently in these lesions: in FNHs, there is an accumulation of the contrast agents, since the bile ducts are not connected to the biliary tree.

Additionally, biliary tree imaging can be performed in the hepatobiliary phase to give both anatomical and functional information, which can be useful for identifying sites of bile duct injury and bile leakage. For example, cholestasis can be detected by a decrease, delay or total lack of contrast excretion into the biliary track (*Frydrychowicz et al., 2012; Gandhi et al., 2006; Bashir et al., 2014; Pascolo et al., 1999; Zech et al., 2007; Choi et al., 2014*).

### *Bile acid analogues*

In addition to the two hepatobiliary contrast agents used in the clinic, several experimental liver-specific MR contrast agents were developed. In the scope of this thesis, the focus will be on bile acid analogues.

In 2004, Anelli et al. (*Anelli et al., 2004*) published 12 bile acid analogues (Figure 2.2) that formed a complex with gadolinium in order to become contrast agents that were actively taken up by the hepatocytes at higher rates compared to Gd-EOB-DTPA and Gd-BOPTA. All agents showed biliary and renal excretion in different ratios. Different configurations were investigated and the extent of biliary excretion depends on several structural features such as the nature of the bile acid, the site of conjugation of the gadolinium complex and the global charge of the conjugate. One conjugate, compound 1j (Figure 2.2), was identified as possible NTCP substrate.

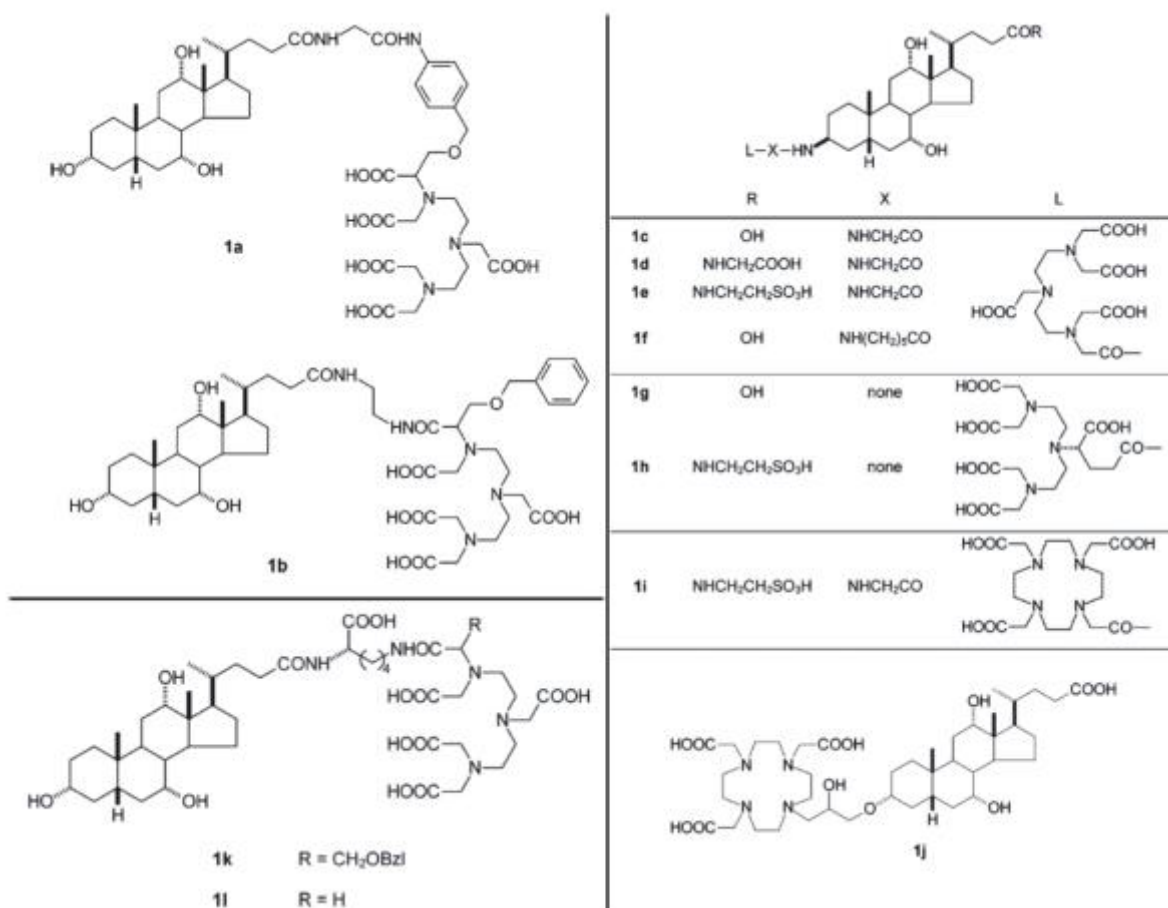


**Figure 2.2:** Bile acid analogues synthesized by Anelli et al. Bile acid analogues are indicated by the numbers 1a-1j (adapted from Anelli et al., 2004).

Gadocoletic acid trisodium salt (B22956/1; compound 1g in Figure 2.2), used as blood pool agent, was investigated by Libra et al. (Libra et al., 2006) as hepatobiliary imaging agent. The aim of the incorporation of a bile acid in the structure of B22956/1 was to increase plasma protein binding and so increasing the blood half-life. Biliary excretion is the primary elimination route of this compound, in contrast to Gd-BOPTA and Gd-EOB-DTPA. Libra et al. revealed that OATPs and MRP2 are involved in the uptake and efflux of B22956/1.

Vivian et al. published trifluorinated bile acid analogues for <sup>19</sup>F magnetic resonance imaging in the context of diagnosing bile acid malabsorption (Figure 2.3). First, cholic acid-trifluoroacetyl lysine (CA-lys-TFA) was synthesized and NTCP and ASBT were identified as the involved transport proteins (Vivian et al., 2013). A limitation of this imaging probe is that the molecule is deconjugated by gut bacterial enzymes (Vivian et al., 2014). Therefore, an additional bile acid analogue was synthesized to diminish the potential for differences in intestinal microbiota to alter probe concentrations and also increase the probe half-life (Vivian et al., 2014). In this context, CA-sar-TFMA was synthesized, a compound that is structurally

similar to choly sarcosine. NTCP and ASBT were also identified as the involved transporters and no bacterial metabolism was observed *in vitro*.

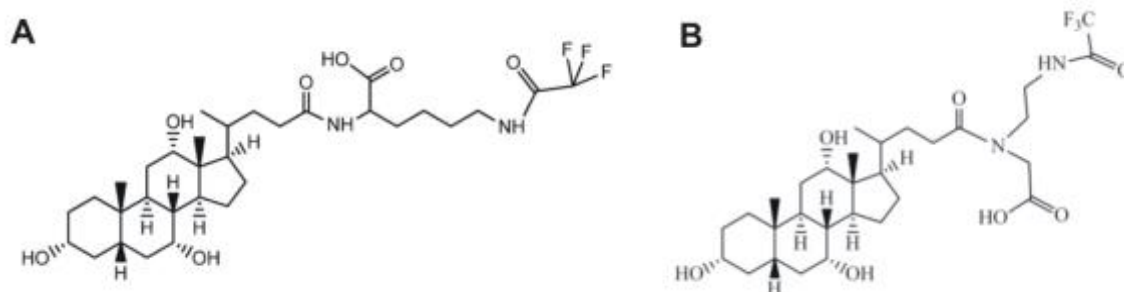


**Figure 2.3:** Structures of CA-lys-TFA (A) and CA-sar-TFMA(B) (*adapted from Vivian et al., 2013; Vivian et al., 2014*).

## Fluorescent hepatobiliary contrast agents

Fluorescent indocyanine green (ICG) imaging is used in the operating room to assess the function of liver segments. ICG is transported via OATPs, NTCP and MRP2. The vascular clearance of ICG over time is a measure for hepatic function. ICG clearance was mostly measured by blood sampling after intravenous injection. Today, ICG plasma clearance can be measured noninvasively at the bedside. It is for example used in the operating room to visualize the resection limits of HCCs by using a fluorescence camera. However, ICG is of concern for patients with iodine allergy (*Sakka et al., 2007*).

Besides ICG, mainly bile acid analogues were developed as fluorescent hepatobiliary agents. Plasma clearance of bile acids is a quantitative measure of liver function and is based on the principle that bile acid uptake and metabolism is a liver specific function. Two main classes can be distinguished: 1) (amino)fluorescein coupled to the carboxylic group of a bile acid and 2) nitrobenzoxdiazolyl (NBD) coupled to the  $\epsilon$ -amino group of a conjugated bile acid (*Holzinger et al., 1997*).

A first group, fluorescein conjugated bile acid analogues (Figure 2.4), express several physicochemical and biological properties similar to endogenous bile acids, including rapid secretion into bile. These imaging agents have been used in several studies to investigate the (patho)physiology of bile acid transport both *in vitro* and *in vivo*. Milkiewicz et al. (*Milkiewicz et al., 2000*), for example, performed a pilot study that revealed that there was a reduced clearance of cholesteryl-lysyl-fluorescein (CLF) in patients with liver cirrhosis. CLF is an OATP1B1, weak OATP1B3, MRP2 and MRP3 substrate (*de Waart et al., 2010*). Therefore, CLF was suggested as imaging agent for the assessment of liver function. Additionally, aminofluorescein (amF) bile acid analogues are used to assess liver function. Holzinger et al. (*Holzinger et al., 1997*) proposed amF conjugated cholesteryl-glycine, cholesteryl-glycylamidofluorescein (CGamF) as characterizing agent for hepatocyte transport function in health and disease. This contrast agent is mainly used in *in vitro* studies.



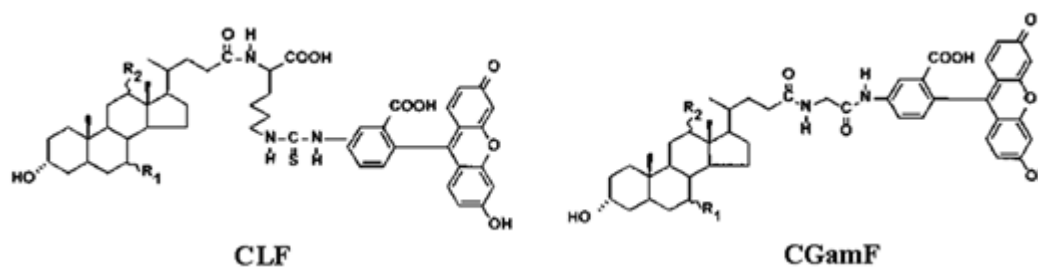


**Figure 2.4:** Structure of CLF and CGamF (adapted from de Waart et al., 2010).

Secondly, an NBD amino-group was used as fluorophore and was introduced in different positions of the steroid nucleus. 3-, 7-, and 12- $\alpha$  and - $\beta$  NBD analogues of cholic acid and its tauro conjugates (Figure 2.5) have been synthesized and were evaluated *in vitro* and in invasive *in vivo* studies (Schramm et al., 1991; Schneider et al., 1991; Schramm et al., 1993).

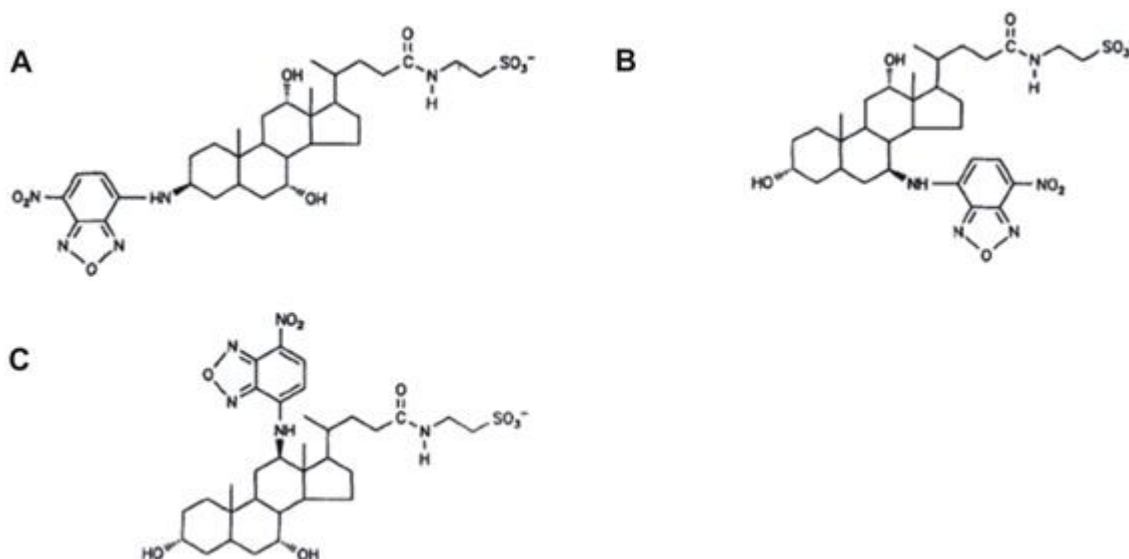


**Figure 2.5:** Structures of taurine-conjugated bile salt derivatives 3 $\beta$ -NBD-NCT (A), 7 $\beta$ -NBD-NCT and 12 $\beta$ -NBD-NCT (adapted from Schneider et al., 1991).

NBD labeled 24-lysyl conjugates have been studied as substrates for hepatic and intestinal transport proteins (Holzinger et al., 1996; Maglova et al., 1995) (Figure 2.6). Yamaguchi et al. (Yamaguchi et al., 2006) identified OATP1B1 and OATP1B3 as the involved uptake transporters of chenodeoxycholyl-NBD-lysine (CDC-NBD-L).

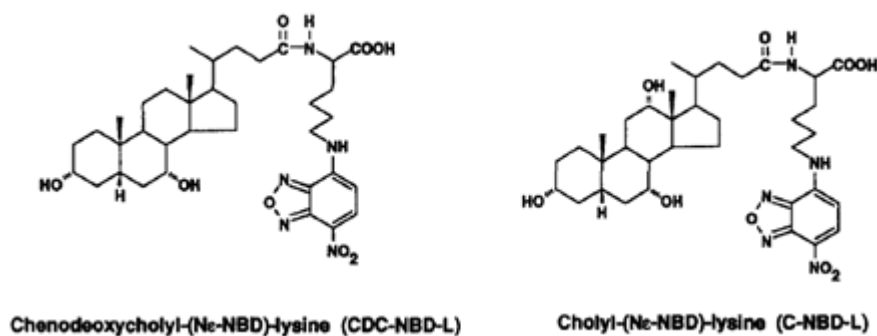


**Figure 2.6:** Structures of chenodeoxycholyl-NBD-lysine (CDC-NBD-L) and cholyl-NBD-lysine (C-NBD-L) (adapted from Maglova et al., 1995).

In 2012, Májer et al. (Májer et al., 2012) reported two new isomeric 3-deoxy 3-NBD-amino derivatives of UDCA and DCA (Figure 2.7).

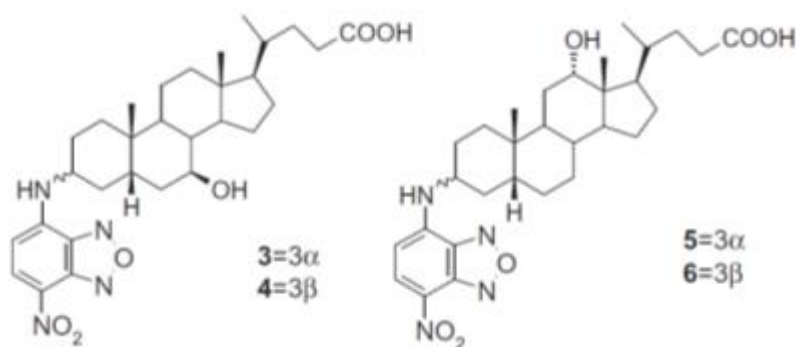


**Figure 2.7:** Structures of 3-deoxy 3-NBD-amino deoxycholic (left) and ursodeoxycholic acid (right) (adapted from Májer et al., 2012).

Additionally, Tauro-nor-THCA-24-DBD, a synthetic fluorescent bile acid analogue with a fluorophore at the side chain of the taurine conjugated bile acid (Figure 2.8), was synthesized by Yamaguchi et al. (Yamaguchi et al., 2010) and was used by De Bruyn et al. (De Bruyn et al., 2014) to study interference of drugs with NTCP and BSEP in a fluorescence-based *in vitro* assay. However, to the best of our knowledge, none of these agents were used in humans.

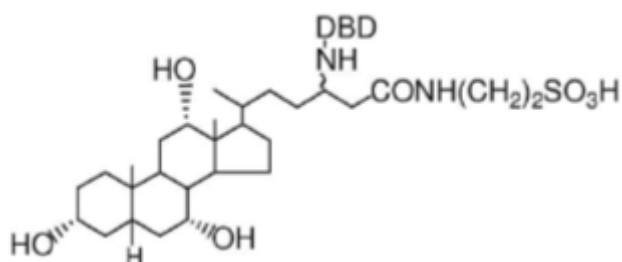


**Figure 2.8:** Structure of tauro-nor-THCA-24-NBD (adapted from Yamaguchi et al., 2010).

## PET tracers

Several PET tracers were developed to study hepatic bile acid transporters (*Testa et al., 2015*). Table 2.1 displays an overview of these tracers. The bile acid analogues are indicated in underlined italic font.

**Table 2.1:** Hepatobiliary PET tracers (*adapted from Testa et al., 2015*).

PET tracer	Bile acid transporters studied	Preclinically/clinically	References
[ <sup>11</sup> C]dehydropravastatin	OATPs, MRP2	Preclinical	<i>Shingaki et al., 2013</i>
[ <sup>11</sup> C]rosuvastatin	OATPs, NTCP, MRP2	Preclinical	<i>He et al., 2014</i>
[ <sup>11</sup> C]TIC-Me	OATP1B1, OATP1B3, MRP2	Preclinical Clinical	<i>Takashima et al., 2010</i> <i>Takashima et al., 2014</i>
[ <sup>11</sup> C]glyburide	OATPs	Preclinical	<i>Tournier et al., 2013</i>
[ <sup>11</sup> C]telmisartan	OATP1B3	Preclinical Clinical	<i>Shimizu et al., 2012; Iimori et al., 2011</i>
<u>[<sup>11</sup>C]cholylsarcosine</u>	Bile acid transporters	Preclinical Clinical	<i>Frisch et al., 2012</i>
<u>[<sup>18</sup>F]CDCA</u>	Bile acid transporters	Preclinical	<i>Jia et al., 2014</i>
<u>[<sup>11</sup>C]MTC</u>	Bile acid transporters	Preclinical	<i>Schacht et al., 2016</i>
<u>[<sup>11</sup>C]MTCDC</u>			
<u>[<sup>11</sup>C]MTDC</u>			
<u>[<sup>11</sup>C]MTUDC</u>			
<u>[<sup>11</sup>C]MTLCA</u>			

## Transporter substrates

[<sup>11</sup>C]dehydropravastatin is a pravastatin analogue and is taken up into the hepatocytes by OATPs and excreted into the biliary system via MRP2. This compound was investigated *in vitro*, in cryopreserved rat and human hepatocytes and also in control, rifampicin-treated and MRP2 knock-out rats (*Shingaki et al., 2013*).

Rosuvastatin is a known OATPs, NTCP and MRP2 substrate. Therefore, its [<sup>11</sup>C]-analogue was synthesized as imaging agent of hepatobiliary rosuvastatin transport. In rats, [<sup>11</sup>C]rosuvastatin was transported by Oatps, but not by Ntcp. It is then metabolized in the liver and/or excreted by Mrp2 and Bcrp. The inhibitory effect of rifampicin was also demonstrated. It was suggested as a useful PET probe for human hepatic transporters (*He et al., 2014*).

[<sup>11</sup>C]tetraiso-carbacyclin methyl ester ([<sup>11</sup>C]TIC-Me) is a prostaglandin E2 analogue and is taken up in the liver via OATP1B1 and OATP1B3 and excreted via MRP2. The metabolite profile and biliary clearance of this tracer was determined *in vitro* and *in vivo* in normal rats, Mrp2 knock-out rats and in humans. Additionally, the effects of rifampicin on hepatobiliary functionality were assessed in humans (Takashima *et al.*, 2010; Takashima *et al.*, 2012; Testa *et al.*, 2015).

Glyburide is an antidiabetic agent, used in the treatment of type 2 diabetes. It is a substrate of several ABC transporters but it is also a substrate of OATP1B1, OATP2B1 and OATP1A2. Its [<sup>11</sup>C]-labeled form (Tournier *et al.*, 2013) demonstrated the pharmacological consequences of the interaction between glyburide and inhibitors of OATP and ABC transporters *in vivo*.

[<sup>11</sup>C]telmisartan is a radiolabeled angiotensin receptor antagonist. It is transported into the liver mainly by OATP1B3. Its transport was investigated in normal and rifampicin-treated rats and then in healthy volunteers. Uptake in the liver was observed with gradual elimination to the gallbladder and intestine and the tracer was found to be safe and promising in order to study OATP1B3 in humans (Shimizu *et al.*, 2012; Imori *et al.*, 2011).

### Bile acid analogues

Cholylsarcosine is an analogue of the conjugated bile acid cholyl-glycine and is formed by cholic acid and the amino acid N-methylglycine (sarcosine). Frisch *et al.* (Frisch *et al.*, 2012) introduced [<sup>11</sup>C]cholylsarcosine (Figure 2.9) as an imaging agent for the visualization and quantification of normal and pathologic hepatic excretory functions. NTCP and BSEP are the expected transporters, because of the high similarity between cholylsarcosine and cholylglycine. However, no *in vitro* transporter characterization was performed. This radiotracer was investigated in pigs and hepatic uptake and biliary excretion was observed. After administration of cholyltaurine, both hepatic uptake and biliary excretion were inhibited *in vivo*.

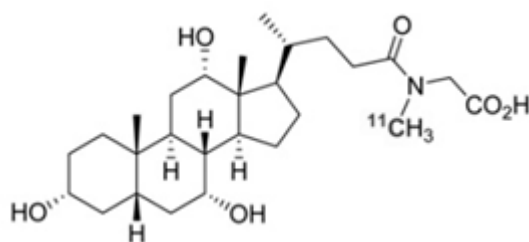


**Figure 2.9:** Structure of [ $^{11}\text{C}$ ]-cholylsarcosine (adapted from Frisch et al., 2012).

An  $^{18}\text{F}$  labeled chenodeoxycholic acid analogue was proposed by Jia et al. (Jia et al., 2014). No characterization of the involved uptake and efflux transporters was done, but *in vivo* evaluation in mice showed that this tracer had a similar uptake and efflux pattern as [ $^{11}\text{C}$ ]cholylsarcosine. This tracer was proposed as PET tracer FXR in related disease.

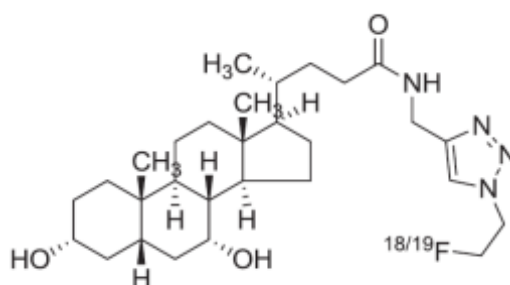


**Figure 2.10:** Structure of [ $^{18}\text{F}$ ]CDCA (adapted from Jia et al., 2014).

Recently, Schacht et al. (Schacht et al., 2016), inspired by the research of Frisch et al. (Frisch et al., 2012), proposed five methyl-aurine-conjugated bile acids. *In vivo* studies in pigs revealed that these tracers behave in a similar manner as endogenous taurine-conjugated bile acids, and therefore, they identified these agents as promising tracers for functional PET imaging of patients with cholestatic liver disease. However, no *in vitro* experiments were performed to identify the involved uptake and efflux transporters.

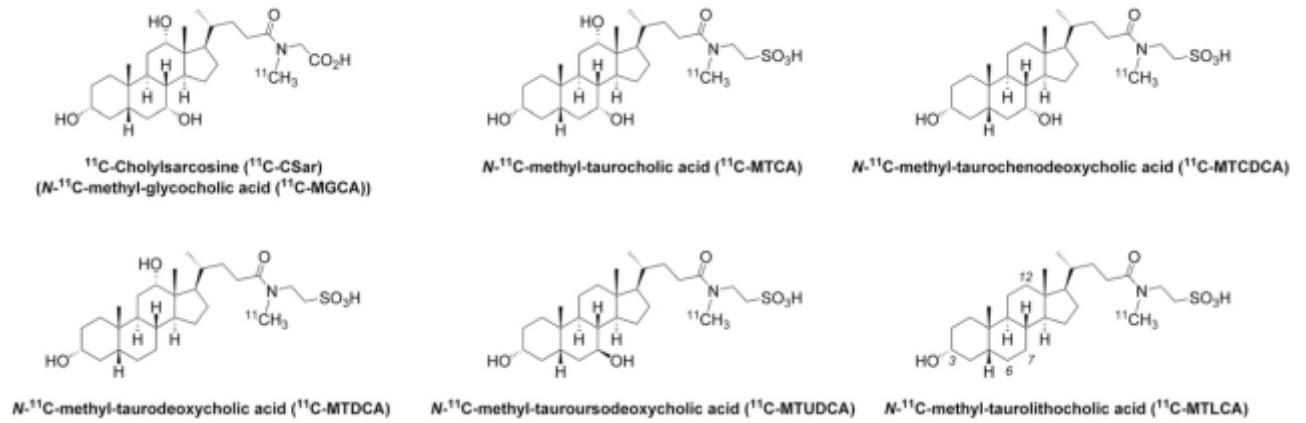
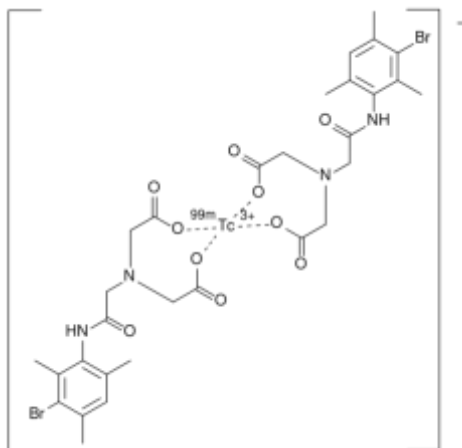


Figure 2.11: Structures of [<sup>18</sup>F] bile acid analogues (adapted from Schacht et al., 2014).

## SPECT tracers

### [<sup>99m</sup>Tc]mebrofenin

[<sup>99m</sup>Tc]mebrofenin ([<sup>99m</sup>Tc]MEB) is a second-generation hepatic imino diacetic acid (HIDA) derivative and lidocaine analogue (Figure 2.12).



**Figure 2.12:** Structure of [<sup>99m</sup>Tc]mebrofenin.

After intravenous injection, this ionic tracer binds to plasma proteins (mainly albumin) and circulates to the liver, where it dissociates in the space of Disse and is taken up by the hepatocytes via OATP1 (Morandi *et al.*, 2005; Ghibellini *et al.*, 2008). Subsequently, [<sup>99m</sup>Tc]MEB is transported through the hepatocytes, and is then secreted in the gallbladder through MRP2 (Nies *et al.*, 2007). Finally, [<sup>99m</sup>Tc]MEB is eliminated into the small intestine. In the clinic, it is used to assess many clinical indications, for example acute cholecystitis, biliary leak, complications after liver transplantation, prediction of remnant liver function, differential diagnosis of hepatic tumors, ... (Ziessman, 2014; Lambie *et al.*, 2011). Because of the high hepatic clearance rate via the biliary system, mainly dynamic assessment of [<sup>99m</sup>Tc]MEB is performed using planar scintigraphy. To measure global liver function, regions of interest are drawn around the heart, liver and total field of view. Out of these measures, the total uptake rate corrected for the patient's body surface area (%/min/m<sup>2</sup>) can be calculated. Remnant liver function can also be calculated by dividing the summed counts within the delineated functional remnant liver by the total liver counts within the same time frame and multiplying this factor with total liver uptake rate (Erdogan *et al.*, 2004).

Figure 2.13 shows an example of [ $^{99m}\text{Tc}$ ]MEB hepatobiliary dynamic scintigraphy. Figure 2.13 A depicts [ $^{99m}\text{Tc}$ ]MEB uptake in a superimposed image of the dynamic scintigraphy. A region of interest can be drawn around the entire liver (dark grey line), the heart (white line), the future remnant liver (light grey line) and the total field of view (not shown). The corresponding time activity curves are shown in Figure 2.13 B. The region of interest around the heart can be obtained from the first time frames after injection of the radiotracer (Figure 2.13 C). The uptake of [ $^{99m}\text{Tc}$ ]-MEB by the liver (slope, D) is calculated as an increase in [ $^{99m}\text{Tc}$ ]MEB uptake (y), over a predefined time interval (x), usually 200 seconds.

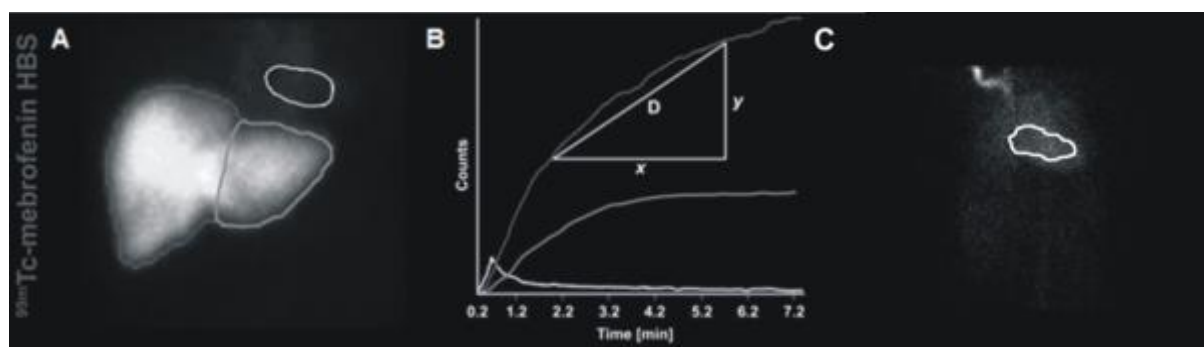


Figure 2.13: [ $^{99m}\text{Tc}$ ]MEB hepatobiliary scintigraphy (adapted from Hoekstra et al., 2013).

### [ $^{99m}\text{Tc}$ ]Galactosyl serum albumin

[ $^{99m}\text{Tc}$ ]diethylenetriamine-pentaacetic acid-galactosyl human serum albumin ([ $^{99m}\text{Tc}$ ]GSA) is an asialoglycoprotein analogue that binds to the asialoglycoprotein receptors on the hepatocyte and is then exclusively taken up in the hepatocytes via receptor-mediated endocytosis. This tracer is used for functional liver scintigraphy, however, it is not suitable for the evaluation of the biliary tract, since there is no biliary excretion. Evaluation of liver function via [ $^{99m}\text{Tc}$ ]GSA shows a good relationship with conventional liver function tests (e.g. total and direct bilirubin, antithrombin, prothrombin time, etc.). After dynamic [ $^{99m}\text{Tc}$ ]GSA scintigraphy with the gamma camera positioned over the heart and liver region, regions of interest are drawn around the heart and liver and blood clearance ratio (ratio of the heart uptake after 15 minutes and heart uptake after 3 minutes;  $\text{HH15}=\text{H15}/\text{H3}$ ) and hepatic uptake ratio ( $\text{LHL15}=\text{L15}/(\text{L15}+\text{H15})$ ; liver uptake after 15 min divided by the sum of the liver and heart uptake after 15 minutes) values are calculated, which are the two most commonly used parameters in planar [ $^{99m}\text{Tc}$ ]GSA scintigraphy. In the clinic, the preoperative hepatic uptake ratio is used as reliable indicator for predicting postoperative complications in patients with



HCC and chronic liver disease that have a significantly lower LHL15. However, postoperative liver failure was also observed in patients with normal LHL15 values. This can be explained by the fact that LHL15 only measures total liver function and not the function of the functional remnant liver.

To overcome this shortcoming, static and dynamic SPECT imaging can be performed to measure segmental liver function and functional liver volume. Planar scintigraphy images are two dimensional reconstructions of the tracer distribution in a field of view leading to superposition of tissue or tissue segments. SPECT imaging, in contrast, offers three dimensional tomographic images that allow measurements of radioactivity in volumes of interest, for example liver segments. Therefore, [ $^{99m}\text{Tc}$ ]GSA SPECT can be used to assess specifically the functional remnant liver. In cirrhotic patients for example, advanced fibrosis is accompanied by a reduction in functional hepatocytes (Hoekstra et al., 2013).

## Bile acid analogues

Huang et al. (Huang et al., 2009) synthesized rhenium and technetium labeled bile acid tricarbonyl complexes (Figure 2.14). However, no *in vitro* or *in vivo* evaluation of these compounds was done. To the best of our knowledge, these were the only technetium labeled bile acids reported to date.

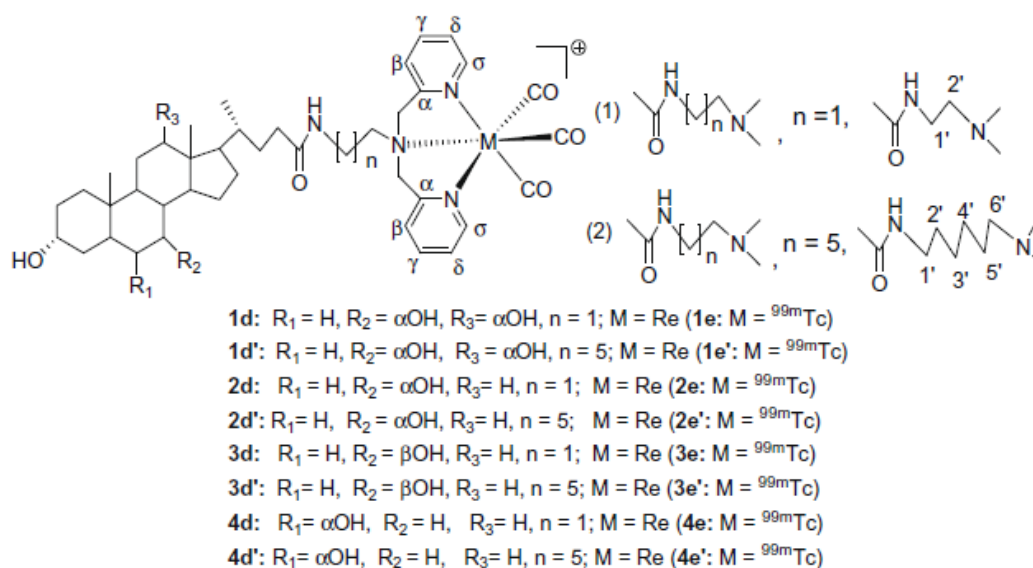


Figure 2.14: Structures of technetium labeled bile acid analogues (adapted from Huang et al., 2009).

## References

- Anelli PL, Lattuada L, Lorusso V, Lux G, Morisetti A, Morosini P, et al. Conjugates of gadolinium complexes to bile acids as hepatocyte-directed contrast agents for magnetic resonance imaging. *J Med Chem* 2004;27:3629-3641.
- Bashir MR. Magnetic resonance contrast agents for liver imaging. *Magn Reson Clin N Am* 2014;22:283-293.
- Burke C, Grant LA, Goh V, Griffin N. The role of hepatocyte-specific contrast agents in hepatobiliary magnetic resonance imaging. *Semin Ultrasound CT MRI* 2013;34:44-53.
- Choi SH, Byun JH, Kwon HJ, Ha HI, Lee SJ, Kim SY, et al. The usefulness of gadoxetic acid-enhanced dynamic magnetic resonance imaging in hepatocellular carcinoma: toward improving staging. *Ann Surg Oncol* 2014;ePub.
- De Bruyn T, Sempels W, Snoeys J, Holmstock N, Chatterjee S, Stieger B, et al. Confocal imaging with a fluorescent bile acid analogue closely mimicking hepatic taurocholate disposition. *J Pharm Sci* 2014;103:1872-1881.
- de Haën C, Lorusso V, Luzzani F, Tirone P. Hepatic transport of the magnetic resonance imaging contrast agent gadobenate dimeglumine in the rat. *Acad Radiol* 1995;2:232-238.
- De Waart DR, Häusler S, Vlaming ML, Kunne C, Hänggi E, Gruss HJ, Oude Elferink RP, Stieger B. Hepatic transport mechanisms of cholyl-L-lysyl-fluorescein. *J Pharmacol Exp Ther* 2010;334:78-86.
- Frisch K, Jakobsen S, Sorenson M, Munk OL, Alstrup AKO, Ott P, et al. [N-methyl-11C]cholylsarcosine, a novel bile acid tracer for PET/CT of hepatic excretory function: radiosynthesis and proof-of-concept studies in pigs. *J Nucl Med* 2012;53:772-778.
- Frydrychowicz A, Lubner MG, Brown JJ, Merkle EM, Nagle SK, Rofsky NM, et al. Hepatobiliary MR imaging with gadolinium-based contrast agents. *J Magn Reson Imaging* 2012;35:492-511.
- Gandhi SN, Brown MA, Wong JG, Aguirre DA, Sirlin CB. MR contrast agents for liver imaging: what, when, how. *Radiographics* 2006;26:1621-1637.
- Ghibellini G, Leslie EM, Pollack GM, Brouwer KLR. Use of Tc-99m Mebrofenin as a Clinical Probe to Assess Altered Hepatobiliary Transport: Integration of In Vitro, Pharmacokinetic Modeling, and Simulation Studies. *Pharm Res*. 2008;25:1851-60.
- He J, Yu Y, Prasad B, Link J, Miyaoka RS, Chen X, et al. PET imaging of Oatp-mediated hepatobiliary transport of [<sup>11</sup>C]-rosuvastatin in the rat. *Mol Pharm* 2014;11:2745-2754.
- Hoekstra LT, de Graaf W, Nibourg GAA, Heger M, Bennink RJ, Stieger B, et al. Physiological and biochemical basis of clinical liver function tests. *Ann Surg* 2013;257:27-36.

Holzinger F, Schteingart CD, Ton-Nu HT, Eming SA, Monte MJ, Hagey LR, Hofmann AF. Fluorescent bile acid derivatives: relationship between chemical structure and hepatic and intestinal transport in the rat. *Hepatology* 1997;26:1263-1271.

Imori H, Hashizume Y, Sasaki M, Kajiwara Y, Sugimoto Y, Sugiyama Y, et al. First automatic radiosynthesis of <sup>11</sup>C labeled telmisartan using a multipurpose synthesizer for clinical research use. *Ann Nucl Med* 2011;25:333-337.

Jia L, Jiang D, Hu P, Li X, Shi H, Cheng D, et al. Synthesis and evaluation of <sup>18</sup>F-labeled bile acid compound: a potential PET imaging agent for FXR-related diseases. *Nucl Med Biol* 2014;41:495-500.

Lambie H, Cook AM, Scarsbrook AF, Lodge JPA, Robinson PJ, Chowdhury FU. <sup>99m</sup>Tc-hepatobiliary iminodiacetic acid (HIDA) scintigraphy in clinical practice. *Clin Radiol* 2011;66:1094-1105.

Leonhardt M, Keiser M, Oswald S, Kühn J, Jia J, Grube M, et al. Hepatic uptake of the magnetic resonance imaging contrast agent Gd-EOB-DTPA: role of human organic anion transporters. *Drug Metab Dispos* 2010;38:1024-1028.

Libra A, Ferneti C, Lorusso V, Visigalli M, Anelli PL, Staud F, et al. Molecular determinants in the transport of a bile acid-derived diagnostic agent in tumoral and nontumoral cell lines of human liver. *J Pharmacol Exp Ther* 2006;319:809-817.

Maglova LM, Jackson AM, Meng XJ, Carruth MW, Schteingart CD, Ton-Nu HT, Hofmann AF, Weinman SA. Transport characteristics of three fluorescent conjugated bile acid analogs in isolated rat hepatocytes and couplets. *Hepatology* 1995;22:637-647.

Májér F, Salomon JJ, Sharma R, Eitzbach SV, Nadzri Mohd Jajib M, Keaveny R, et al. New fluorescent bile acids: synthesis, chemical characterization, and diastereoselective uptake by Caco-2 cells of 3-deoxy-3-NBD-amino deoxycholic and ursodeoxycholic acid. *Bioorg Med Chem* 2012;20:1767-1778.

Milkiewicz P, Saksena S, Cardenas T, Mills CO, Elias E. Plasma elimination of cholestyramine-fluorescein (CLF): a pilot study in patients with liver cirrhosis. *Liver* 2000;20:330-334.

Morandi F, Frank N, Avenell J, Daniel GB. Quantitative assessment of hepatic function by means of <sup>99m</sup>Tc-Mebrofenin in healthy horses. *J Vet Intern Med.* 2005;19:751-5.

Nassif A, Jia J, Keiser M, Oswald S, Modess C, Nagel S, et al. Visualization of hepatic uptake transporter function in healthy subjects by using gadoxetic acid-enhanced MR imaging. *Radiology* 2012;264:741-750.

Nies AT, Keppler D. The apical conjugate efflux pump ABCC2 (MRP2). *Pflugers Arch.* 2007;453:643-59.

Pascolo L, Cupelli F, Anelli PL, Lorusso V, Visigalli M, Uggeri F, et al. Molecular mechanisms for the hepatic uptake of magnetic resonance imaging contrast agents. *Biochem Biophys Res Commun* 1999;257:746-752.

Pastor CM, Müllhaupt B and Stieger B. The role of organic anion transporters in diagnosing liver diseases by magnetic resonance imaging. *Drug Metab Dispos* 2014;42:675-684.

Sakka SG. Assessing liver function. *Curr Opin Crit Care* 2007;13:207-214.

Schacht C, Sorensen M, Munk OL, Frisch. Radiosynthesis of N-<sup>11</sup>C-methyl-aurine-conjugated bile acids and biodistribution studies in pigs by PET/CT. *J Nucl Med* 2016;57:628-633.

Schneider S, Schramm U, Schreyer A, Buscher HP, Gerok W, Kurz G. Fluorescent derivatives of bile salts. I. Synthesis and properties of NBD-amino derivatives of bile salts. *J Lipid Res* 1991;32:1755-1767.

Schramm U, Dietrich A, Schneider S, Buscher HP, Gerok W, Kurz G. Fluorescent derivatives of bile salts. II. Suitability of NBD-amino derivatives of bile salts for the study of biological transport. *J Lipid Res* 1991;32:1769-1779.

Schramm U, Fricker G, Buscher HP, Gerok W, Kurz G. Fluorescent derivatives of bile salts. III. Uptake of 7 $\beta$ -NBD-NCT into isolated hepatocytes by the transport systems for cholytaurine. *J Lipid Res* 1993;34:741-757.

Serlin CB, Hussain HK, Jonas E, Kanematsu M, Lee JM, Merkle EH, et al. Consensus report from the 6th international forum for liver MRI using gadoxetic acid. *J Magn Reson Imaging* 2014;40:516-529.

Shimizu K, Takashima T, Yamane T, Sasaki M, Kageyama H, Hashizume Y, et al. Whole-body distribution and radiation dosimetry of [<sup>11</sup>C]telmisartan as a biomarker for hepatic organic anion transporting polypeptide (OATP) 1B3. *Nucl Med Biol* 2012;39:847-853.

Shingaki T, Takashima T, Ijuin R, Zhang X, Onoue T, Katayama Y, et al. Evaluation of Oatp and Mrp2 activities in hepatobiliary excretion using newly developed positron emission tomography tracer [<sup>11</sup>C]-dehydropravastatin in rats. *J Pharmacol Exp Ther* 2013; 347:193-202.

Stieger B, Heger M, de Graaf W, Paumgartner G, van Gulik T. The emerging role of transport systems in liver function tests. *Eur J Pharmacol* 2012;675:1-5.

Takashima T, Kitamura S, Wada Y, Tanaka M, Shigihara Y, Ishii H, Ijuin R, et al. PET imaging-based evaluation of hepatobiliary transport in humans with (<sup>15</sup>R)-<sup>11</sup>C-TIC-Me. *J Nucl Med* 2012;53:741-748.

Takashima T, Nagata H, Nakae T, Cui Y, Wada Y, Kitamura S, et al. Positron emission tomography studies using (<sup>15</sup>R)-<sup>16</sup>m-[<sup>11</sup>C]tolyl-17,18,19,20-tetranorisocarbacyclin methyl ester for the evaluation of hepatobiliary transport. *J Pharmacol Exp Ther* 2010;335:314-323.

Testa A, Zando M, Elmore CS, Sharma P. PET tracers to study clinically relevant hepatic transporters. *Mol Pharmaceutics* 2015;12:2203-2216.

Tournier N, Saba W, Cisternino S, Peyronneau MA, Damont A, Goutal S, et al. Effects of selected OATP and/or ABC transporter inhibitors on the brain and whole-body distribution of glyburide. *AAPS J* 2013;15:1082-1090.

Ulloa JL, Stahl S, Yates J, Woodhouse N, Kenna JG, Jones HB, et al. Assessment of gadoxetate DCE-MRI as a biomarker of hepatobiliary transporter inhibition. *NMR Biomed* 2013;26:1258-1270.

Vivian D, Cheng K, Khurana S, Xu S, Dawson PA, Raufman JP, et al. Design and evaluation of a novel trifluorinated imaging agent for assessment of bile acid transport using fluorine magnetic resonance imaging. *J Pharm Sci* 2014;103:3782-3792.

Vivian D, Cheng K, Khurana S, Xu S, Kriel EH, Dawson PA, et al. In vivo performance of a novel fluorinated magnetic resonance imaging agent for functional analysis of bile acid transport. *Mol Pharm* 2014;11:1575-1582.

Vivian D, Cheng K, Khurana S, Xu S, Whiterock V, Witter D, et al. Design and characterization of a novel fluorinated magnetic resonance imaging agent for functional analysis of bile acid transporter activity. *Pharm Res* 2013;30:1240-1251.

Yamaguchi H, Okada M, Akitaya S, Ohara H, Mikkaichi T, Ishikawa H, et al. Transport of fluorescent chenodeoxycholic acid via the human organic anion transporters OATP1B1 and OATP1B3. *J Lipid Res* 2006;47:1196-1202.

Yamaguchi K, Murai T, Yabuuchi H, Hui SP, Kurosawa T. Measurements of bile salt export pump transport activities using a fluorescent bile acid derivative. *Drug Metab Pharmacokinet* 2010;25:214-219.

Zech CJ, Hermann KA, Reiser MF, Schoenberg SO. MR imaging in patients with suspected liver metastases: value of liver-specific contrast agent Gd-EOB-DTPA. *Magn Reson Med Sci* 2007;6:43-52.

Ziessman HA. Hepatobiliary scintigraphy in 2014. *J Nucl Med* 2014;55:967-975.

# Chapter 3.

## Scope and aims



Drug induced liver injury (DILI) is responsible for up to 15% of cases of acute liver failure in Europe and US, and is a one of the leading causes of drug withdrawal from the market and attrition in the development process of new drug candidates. Therefore, it is important to understand, characterize, and develop prediction methods to identify possible interactions. One of the involved causes of DILI is drug induced cholestasis and many cases are caused by inhibition of hepatic transporters by drugs. Clinically relevant hepatic transport systems include the Organic Anion Transporting Polypeptides (OATPs), sodium Taurocholate Cotransporting Protein (NTCP), Multidrug Resistance-associated Protein-2 (MRP2) and bile salt export pump (BSEP). Cholestatic drugs may disturb bile acid homeostasis by direct inhibition of bile acid transport, or by indirect processes, such as regulation of transporter localization or expression. Inhibition of these transporters for example, can lead to toxic concentrations of bile acids, bilirubin or substrate drugs in blood or liver, which can lead to hypercholanemia, hyperbilirubinemia, cholestatic liver injury and drug-drug interactions.

Currently, these interactions are investigated by *in vitro* and invasive, time consuming, and expensive preclinical *in vivo* experiments. Therefore, the overall aim of this thesis is the development of non-invasive predictive methods to visualize and quantify disturbed hepatobiliary transport by drugs in preclinical animal species as an alternative to the invasive methods. An additional advantage is that the number of sacrificed animals can be reduced. This overall aim can be subdivided in four research questions.

<p><b>Question 1: Is it possible to visualize and quantify altered hepatobiliary transport in mice? (Chapter 5)</b></p>
---

[<sup>99m</sup>Tc]mebrofenin ([<sup>99m</sup>Tc]MEB) is a second-generation hepatic imino diacetic acid (HIDA) derivative, which is commonly used in hepatobiliary scintigraphy to investigate the function and dysfunction of the liver. After intravenous injection, this ionic tracer binds to plasma proteins (mainly albumin) and circulates to the liver, where it dissociates and is taken up by the hepatocytes, through a carrier-mediated, sodium-independent transport mechanism, the organic anion transport protein 1 (OATP1/Oatp1). Subsequently, [<sup>99m</sup>Tc]MEB is transported through the hepatocytes, and is then secreted in the gallbladder through MRP2/Mrp2. Finally, [<sup>99m</sup>Tc]MEB is eliminated into the small intestine. Therefore, this radiotracer was chosen as biomarker to study hepatobiliary transporter function *in vivo* and will be evaluated in a non-invasive manner by dynamic SPECT imaging in mice. Wild type mice will be evaluated to



determine the coefficient of variation of the measurements. As proof-of-principle, a bile duct ligated animal (mechanical inhibition of hepatobiliary efflux) will be investigated. In addition, transporter knock-out (KO) mice models will be used to study altered uptake and efflux transporter function. *Slco1a/1b* and *Abcc2* KO mice will be evaluated. These mice lack the Oatp1a/1b and Mrp2 transporters, respectively. Lastly, rifampicin will be used as model drug to visualize and quantify pharmacological inhibition of transporters. It has been shown that rifampicin mediates the inhibition of OATP1B1 *in vitro*, mouse Oatp1a/1b *in vivo* and Mrp2 *in vitro*.

**Question 2: Can this quantification be further refined by kinetic modeling of [<sup>99m</sup>Tc]MEB? (Chapter 6)**

Tracer kinetic or compartmental modeling of dynamic SPECT measurements allows calculation of physiological parameters by fitting a mathematical compartmental model of tracer distribution and metabolism to the data. We will investigate if tracer kinetic modeling can be used to absolutely quantify altered hepatobiliary transport in Mrp2 KO and rifampicin treated mice. A two-tissue compartmental model will be proposed. Additionally, a non-invasive method to obtain the blood input function will be evaluated.

**Question 3: Is a humanized mouse model useful for the prediction of disturbed human-type hepatobiliary transport? (Chapter 7)**

Due to species differences, many hepatotoxicants remain undetected in preclinical safety studies. Therefore, a chimeric mouse model with a humanized liver will be evaluated to study human-type hepatobiliary transport. [<sup>99m</sup>Tc]MEB transport will be assessed to characterize the chimeric “humanized” model.

**Question 4: Can bile acid analogues serve as biomarkers for DILI? (Chapter 8)**

To investigate non-invasively the effect of inhibition of hepatobiliary transporters on the transport of bile acids, there is a need for labeled bile acid analogues since [<sup>99m</sup>Tc]MEB has no chemical similarities with endogenous bile acids. Therefore, radiolabeled primary bile acid

analogues will be synthesized. We will investigate a technetium labeled chenodeoxycholic and cholic acid analogue: technetium labeled diethylene triamine pentaacetic acid chenodeoxycholic acid ( $[^{99m}\text{Tc}]$ DTPA-CDCA) and technetium labeled diethylene triamine pentaacetic acid cholic acid, ( $[^{99m}\text{Tc}]$ DTPA-CA), respectively. Technetium will be used as radioisotope since it is easily produced (it can be eluted from a generator), its suitable half-life (6 hours) and its limitless depth of penetration. Additionally, *in vitro* assays will be performed to identify the involved uptake and efflux transporters. Lastly, *in vivo* SPECT evaluation of normal and disturbed hepatobiliary transport will be performed to illustrate the ability of these agents to visualize and quantify (altered) hepatobiliary transport *in vivo*.



# **Chapter 4.**

# **Calibration curves**



## NaI(Tl) scintillation detector

10 samples with 100  $\mu\text{L}$  [ $^{99\text{m}}\text{Tc}$ ]TcO $_4^-$  ranging from 0.37 to 45 kBq and determined with a conventional CRC-15R dose calibrator (Capintec, Ramsay, NJ) are measured with the NaI(Tl) scintillation detector (in cps) (Perkin Elmer, Waltham, USA) to obtain a calibration curve from cps to MBq/mL with the following equation:

$$\text{Radioactivity in kBq} = 0.00013 * (\text{counts}/30\text{sec}) \quad R^2 = 0.9983$$

This calibration curve will be used in Chapter 5 to measure the exact amount of radioactivity in the manual blood samples.

## $\mu\text{SPECT}$

To obtain quantitative measurements from the  $\mu\text{SPECT}$  camera (USPECT-II, MILabs, Utrecht, The Netherlands), 8 samples with predetermined amounts of [ $^{99\text{m}}\text{Tc}$ ]TcO $_4^-$  ranging from 0.37 MBq to 74 MBq, measured with a CRC-15R dose calibrator were acquired during 10 minutes. The field of view was determined by means of a 30 seconds CT acquisition. ROIs were manually drawn around the content of the syringe (approximately 1 mL), to determine the total amount of radioactivity and in the middle of the syringe, to determine the activity concentration (Figure 4.1). The resulting output, measured in counts or counts/mL, was expressed as a function of the true activity (MBq or MBq/mL) as measured by the dose calibrator. The resulting calibration curve was used to quantify the amount of radioactivity in MBq or concentration of radioactivity in MBq/mL in specific organs (Chapter 5, 6, 7 and 8).

The calibration curves were obtained with the following equations:

$$\text{Total amount of radioactivity (MBq)} = 1095 * \text{counts} \quad R^2 = 0.9986$$

$$\text{Concentration of radioactivity (MBq/mL)} = 2.646 * 10^6 * \text{counts/mL} \quad R^2 = 0.9987$$

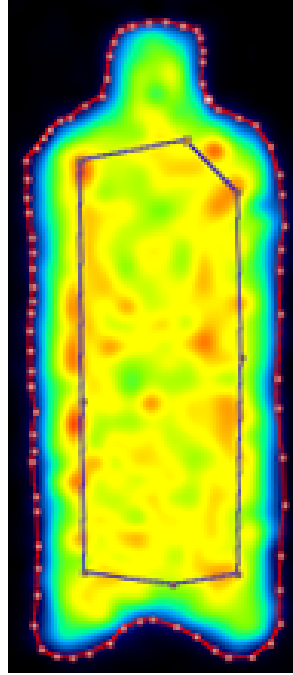


**Figure 4.1:** ROIs around syringe which is used for the calibration curve of the USPECT-II imaging system. Red: ROI that is used for determination of total amount of radioactivity (in MBq). Blue: ROI that is used for the determination of the radioactivity concentration (in MBq/mL).

# Chapter 5.

## *In vivo* visualization and quantification of normal and disturbed hepatobiliary transport by means of [<sup>99m</sup>Tc]mebrofenin

*Parts have been adapted from*

Neyt S<sup>1</sup>, Huisman MT<sup>2</sup>, Vanhove C<sup>3</sup>, De Man H<sup>2</sup>, Vliegen M<sup>2</sup>, Moerman L<sup>1</sup>, Dumolyn C<sup>1</sup>, Mannens G<sup>2</sup>, De Vos F<sup>1</sup>. *Journal of Nuclear Medicine* **2013**; 54 (4): 624-630.

<sup>1</sup>Laboratory of Radiopharmacy, Ottergemsesteenweg 460, Ghent University, Ghent, Belgium

<sup>2</sup>Preclinical Development & Safety, Janssen Pharmaceutical Companies of Johnson & Johnson, Beerse, Belgium

<sup>3</sup>iMinds Medical IT-IBITech-MEDISIP-INFINITY, Ghent University, Ghent, Belgium





## Introduction

As outlined in Chapter 1, the liver is an important organ for homeostasis. Hepatobiliary transport processes are essential for these key functions and therefore, hepatocytes express several transport systems (Kullak-Ublick *et al.*, 2000; Wolkoff *et al.*, 2003).

Clinically relevant hepatic transport systems include the organic anion transport pumps (OATPs), sodium taurocholate cotransporting protein (NTCP), multidrug resistance protein 2 (MRP2) and bile salt export pump (BSEP) (Kosters *et al.*, 2008; Kullak-Ublick *et al.*, 2000; Meier *et al.*, 2002; Trauner *et al.*, 2003). Numerous drugs are substrates or inhibitors of these hepatic transporters and therefore, unexpected and unwanted interactions are frequently observed as stated in Chapter 1 (Shitara *et al.*, 2005; Maddrey, 2005). Therefore, in drug research, it is important to assess the inhibition of hepatic transporters at an early developmental phase. Currently, this possible inhibition is investigated by means of *in vitro* and invasive, time-consuming and expensive preclinical *in vivo* tests (Chapter 1).

The current study, in contrast, describes a non-invasive *in vivo* method to assess the effect of drugs on the hepatobiliary transport mechanisms in mice as an alternative for invasive methods. Consequently, the number of sacrificed animals and costs can be reduced. In addition, the proposed method can be used in both preclinical and clinical settings. We aim to introduce a radioactive labeled substrate for the hepatic transporters, which can be used to visualize the hepatic uptake, efflux and possible inhibition of these processes with molecular imaging techniques, such as Single Photon Emission Computed Tomography (SPECT). In this context, we propose the second-generation hepatic imino diacetic acid (HIDA) derivative mebrofenin (MEB), which is commonly used in hepatobiliary scintigraphy to investigate the function and dysfunction of the liver as outlined in Chapter 2 (Bujanover *et al.*, 1983; Newell *et al.*, 2000; Morandi *et al.*, 2005; Ghibellini *et al.*, 2008). Normal transport of [<sup>99m</sup>Tc]MEB is shown in Figure 5.1, A.

First, we will evaluate the possibility of visualizing and quantifying normal hepatobiliary transport in mice. The interanimal and intra-animal variability of the dynamic imaging procedure will be evaluated.

Following the study of [<sup>99m</sup>Tc]MEB as a suitable SPECT tracer for the evaluation of hepatobiliary transport, the effect of altered hepatobiliary transport on [<sup>99m</sup>Tc]MEB kinetics

will be investigated in mice. Based on the results, a non-invasive *in vivo* method is proposed to assess disturbances in the transport of [<sup>99m</sup>Tc]MEB in mice.

As proof-of-principle, mechanical inhibition will be obtained by placing a ligation around the bile duct. Pharmacological inhibition will be achieved by administration of rifampicin, an antibiotic that is often used to treat tuberculosis and other bactericidal infections. Rifampicin is known to mediate the inhibition of OATP1B1, OATP1B3 *in vitro* (de Graaf et al., 2011; Ghibellini et al., 2008), mouse Oatp1a/1b *in vivo* (Van de Steeg et al., 2010) and Mrp2 in sandwich-cultured rat hepatocytes (Lengyel et al., 2008). However, less is known about the effects of rifampicin on the function of hepatic MRP2 in humans, as these may be hard to detect in circulating blood, since inhibition of MRP2 leads to an accumulation of substrates in the liver. Thus, rifampicin provided an ideal test compound for this study. We hypothesized that rifampicin inhibits Oatp1a/1b as well as Mrp2, with inhibition reflected in altered time-activity curves (TACs) for the blood, liver, and gallbladder+intestines (Figure 5.1 D) (Kosters et al., 2008; Kullak-Ublick et al., 2000). As a reference, and to investigate *in vivo* the relative contributions of uptake and efflux transporters in [<sup>99m</sup>Tc]MEB handling, dynamic  $\mu$ SPECT imaging was used to characterize the behavior of [<sup>99m</sup>Tc]MEB in mice unable to express the uptake transporters Oatp1a/1b (*Slc1a1b*<sup>-/-</sup>, Oatp1a/1b knock-out (KO)) (Van de Steeg et al., 2010) or the efflux transporter Mrp2 (*Abcc2*<sup>-/-</sup>, Mrp2 KO) (Vlaming et al., 2006). It was further hypothesized that elevated concentrations of [<sup>99m</sup>Tc]MEB would be detected in the blood of Oatp1a/1b KO mice and in the liver of Mrp2 KO mice (Figure 5.1 B and C, respectively).

Critical for the interpretation and translation of the data in such experiments is a comprehensive mechanistic understanding of the hepatic handling of [<sup>99m</sup>Tc]MEB. [<sup>99m</sup>Tc]MEB is an *in vitro* substrate of OATP1B1, OATP1B3, MRP2, and MRP3, but not of OATP2B1 and NTCP (Ghibellini et al., 2008, de Graaf et al., 2011). Although unlikely, it is not yet known whether [<sup>99m</sup>Tc]MEB (an anion) is a substrate for OCT1 (organic cation transporter 1). Considering the high-level expression of OCT1 in the sinusoidal membrane, in the present work it was also important to formally exclude OCT1-mediated [<sup>99m</sup>Tc]MEB transport.

In summary, the possibility of non-invasive visualizing and quantifying transporter activity in a reproducible manner will be examined. Furthermore, we will examine whether we can quantify altered hepatobiliary transport and whether we can distinct the effect on the

sinusoidal uptake into the liver and efflux into the bile. If these aims will be fulfilled, one will have a possible model to predict the effects of drugs in a (pre-)clinical setting. Since this method could be used in preclinical and clinical research, the translation from animal to human could be made more easily.

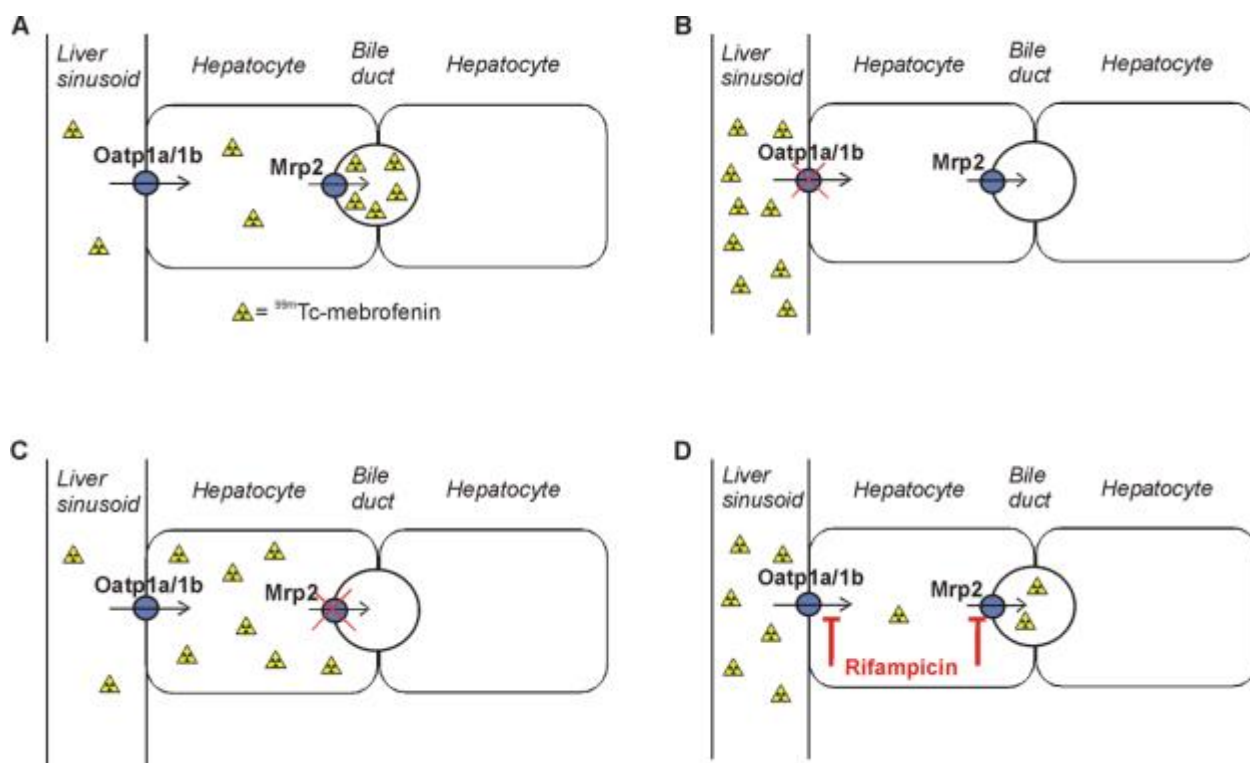


**Figure 5.1:** Study hypothesis for [ $^{99m}\text{Tc}$ ]MEB transport in wild-type (A), Oatp1a/1b KO (B), BDL and Mrp2 KO (C) and rifampicin-treated (D) mice. In wild-type mice, rapid uptake in the liver and efflux to the gallbladder and intestines are expected, in contrast to Oatp1a/1b KO mice, in which no noteworthy uptake is anticipated. In Mrp2 KO mice, normal uptake in the liver and the absence of efflux to the gallbladder and intestines is hypothesized whereas in rifampicin-treated mice, decreased uptake and efflux are assumed.

## Materials and methods

### *In vitro* assays

Chinese hamster ovary (CHO) cells, CHO-OCT, Human Embryonic Kidney (HEK), HEK293-OATP1B3 cells were purchased from Solvo Biotechnologies (Hungary); CHO-NTCP and HEK293-OATP1B1 cells were a kind gift from the same company. The cells were stably transfected with genes encoding human NTCP (*SLC10A1*), OATP1B1 (*SLCO1B1*), OATP1B3 (*SLCO1B3*) and OCT1 (*SLC22A1*). The cell lines were cultured in a humidified atmosphere at 37°C in the presence of 5% CO<sub>2</sub>. The culture medium of the CHO cells consisted of Dulbecco's modified Eagle's medium (DMEM)/F12, supplemented with 10% fetal calf serum, 2 mM L-glutamine, 0.3 mM L-proline, and antibiotics (Penicillin/Streptomycin; 50 U/mL; 50 µg/mL). The culture medium of the HEK293 cells consisted of DMEM glutamax; high glucose; pyruvate supplemented with 10% fetal calf serum, 5 mL MEM-non essential amino acid solution, and antibiotics (Penicillin/Streptomycin; 50 U/mL; 50 µg/mL).

For transport experiments, all CHO and HEK cells were seeded in 24-well plates (6.0×10<sup>5</sup> cells/well) in 1 mL of culture medium. After 18–24 h, the medium was removed and the cells were washed twice with washing buffer (1.25 mL sterile HBSS+/+ (HBSS with Ca<sup>2+</sup> and Mg<sup>2+</sup>), 10 mM HEPES, pH=7.4, 37°C). Incubation buffers (500 µL/well) were obtained by adding the (radiolabeled) compounds to the washing buffer. Final concentrations were 1 µM <sup>3</sup>H-estradiol-17β-glucuronide (E17βG, for OATP1B1), 1 µM <sup>3</sup>H-taurocholic acid (TCA, for NTCP), 1 µM <sup>14</sup>C-tetra-ethyl-ammonium (TEA, for OCT1), and 100 µM [<sup>99m</sup>Tc]MEB (for all cell lines). The plates were incubated at 37°C and 5% CO<sub>2</sub>. The incubation was stopped by adding 1.5 mL of ice-cold HBSS+/+ (1% BSA) after which the wells, containing the cells, were washed twice more with HBSS+/+. Next, the cells were lysed with 200 µL mammalian protein extraction reagent (MPer, Invitrogen, Belgium) and the plates were shaken for 10 min at 120 rpm. A 150 µL aliquot of this solution was used for NaI(Tl) scintillation counting and liquid scintillation counting.

## Murine models

FVB wild-type (WT) mice (♀, 5 weeks, 20–25 g) were from Janvier (France) and *Slco1a1b-/-/-* (♂, 5 weeks, 25–30 g; *Oatp1a/1b* KO mice) and *Abcc2-/-* (♀, 5 weeks, 20–25 g; *Mrp2* KO mice) animals were from Taconic Farms (USA). The mice were housed and handled according to guidelines approved by the European Ethics Committee and acclimatized for at least one week before the experiments. All of the animals were kept under environmentally controlled conditions (12 h normal light/dark cycles, 20–22°C and 60% relative humidity) with food and water ad libitum. The study protocol was approved by the Animal Experimental Ethical Committee of Ghent University (ECD10/39).

## Radionuclides, radiopharmaceuticals and chemicals

Mebrofenin (N-(3-bromo-2,4,6 trimethylphenylcarbamoylmethyl)-iminodiacetic acid) was obtained as a commercial kit from GE Healthcare (Bridatec®, Belgium) in a preparation containing 40 mg of mebrofenin and 0.3 mg of tin(II)chloride-dihydrate. [<sup>99m</sup>Tc]TcO<sub>4</sub><sup>-</sup> was eluted from a sterile <sup>99m</sup>Tc-generator (Drytec™, GE Healthcare). The Bridatec kit was reconstituted according to the manufacturer's recommendations with 1480 MBq [<sup>99m</sup>Tc]TcO<sub>4</sub><sup>-</sup> in 4 mL saline. Radiochemical purity was determined according to Billingham et al. (Billinghurst et al., 2004). The formulations employed had a radiochemical purity of ≥ 95%. Rifampicin and polyethyleneglycol 400 (PEG400) were obtained from Sigma Aldrich (Belgium), and dimethyl sulfoxide (DMSO) from Acros Organics (Belgium).

## Molecular imaging

Dynamic μSPECT/CT acquisitions were acquired on a USPECT-II/CT device (MILabs, Utrecht, The Netherlands) (van der Have et al., 2009) equipped with a cylindrical collimator containing 75 pinholes of 1 mm diameter (rat whole-body collimator; spatial resolution, 0.8 mm). All acquisitions were acquired in list mode.

After an overnight fast (minimum 6 h), the WT, *Oatp1a/1b* KO and *Mrp2* KO mice were anesthetized with a mixture of isoflurane (1.5%) and medical O<sub>2</sub> to allow placement of an intravenous needle (30G) and polyethylene (PE10) tubing (Becton Dickinson, Belgium) in a lateral tail vein. The mice were placed in a prone position on the mouse scan bed. 200 μL (37-

74 MBq; 2 mg MEB) [<sup>99m</sup>Tc]MEB was injected via the intravenous PE10 tubing, directly after scan initiation (IV, intravenous).

One hour before tracer injection, rifampicin-treated mice were pre-treated with five different rifampicin doses (100, 50, 37.5, 25, or 12.5 mg/kg in 100  $\mu$ L DMSO, intraperitoneal (IP)) and the vehicle-control mice with vehicle (100  $\mu$ L DMSO, IP). Then, the mice were anesthetized and a PE10 tubing was placed intravenously. 200  $\mu$ L (37-74 MBq; 2 mg MEB) [<sup>99m</sup>Tc]MEB was injected directly after scan initiation. During tracer injection, a second dose of rifampicin (25, 12.5, 9.37, 6.25, or 3.12 mg/kg in 100  $\mu$ L PEG400:saline, 30:70, v:v) or vehicle (100  $\mu$ L PEG400:saline, 30:70, v:v) was intravenously co-administered.

In one WT animal, after anesthesia, bile duct ligatures (BDL) were placed posterior and anterior to the gallbladder to obstruct bile flow completely (Figure 5.2). Immediately after surgery, a PE10 tubing was placed in a lateral tail vein and the bile duct-ligated mouse was placed in a supine position on the mouse scan bed. [<sup>99m</sup>Tc]MEB was injected via the intravenous PE10 tubing, directly after scan initiation.

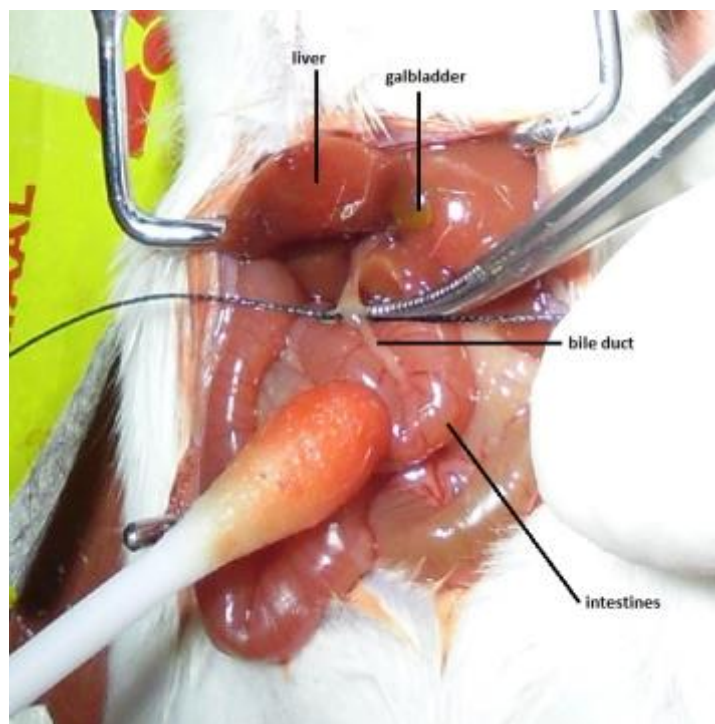


**Figure 5.2:** Placement of a bile duct ligature in a mouse. The ligature is placed around the bile duct.

All the mice were imaged while anesthetized, with their body temperature was maintained during imaging using a heated bed. The axial field of view required for the SPECT scan was chosen based on 3 planar X-ray images (Figure 5.3). Subsequently, a 15 min dynamic SPECT acquisition using 60 time frames of 15 s was initiated 5 s before the injection of [ $^{99m}\text{Tc}$ ]MEB. Lastly, a CT acquisition (5 min; tube current, 612  $\mu\text{A}$ ; tube voltage, 50 kV) was performed for anatomical correlation. The resultant CT scan is inherently co-registered with the corresponding  $\mu\text{SPECT}$  acquisition.

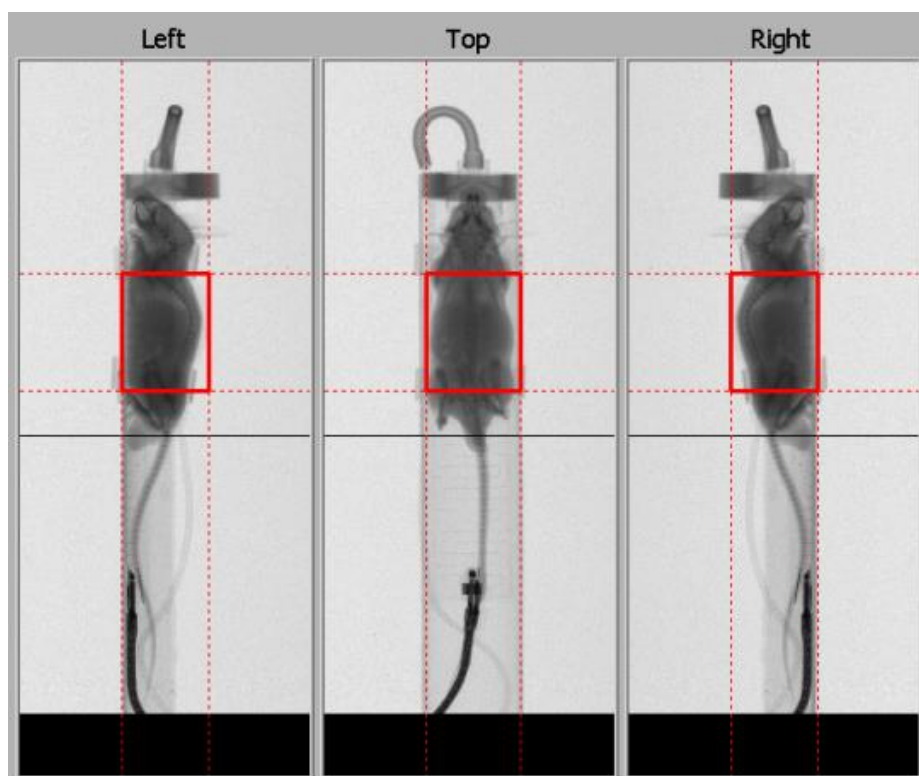


**Figure 5.3:** Field of view determination by means of 3 planar X-ray images (~ 30 seconds acquisition time).

The dynamic SPECT scans were iteratively reconstructed using an ordered subsets expectation maximization algorithm (3 iterations; 16 subsets; 0.75 mm voxel size; decay correction), including only those photons from the acquired list-mode data with an energy range of  $140 \pm 20$  %. After reconstruction, three regions of interest (ROIs) were manually drawn over the liver, the gallbladder+intestines and the urinary bladder using PMod software (PMod Technologies, Zürich, Switzerland) to obtain a time activity curve (TAC) for each ROI. ROI volumes varied between 67 and 1578  $\text{mm}^3$  (Figure 5.4). Additionally, reconstructions of different phases (frame 1-4, frame 5-12, frame 13-20 and frame 21-60) were performed to visualize the distribution of [ $^{99m}\text{Tc}$ ]MEB as function of time. Three-



dimensional projection images of the co-registered CT and  $\mu$ SPECT images were performed using ImageJ software.

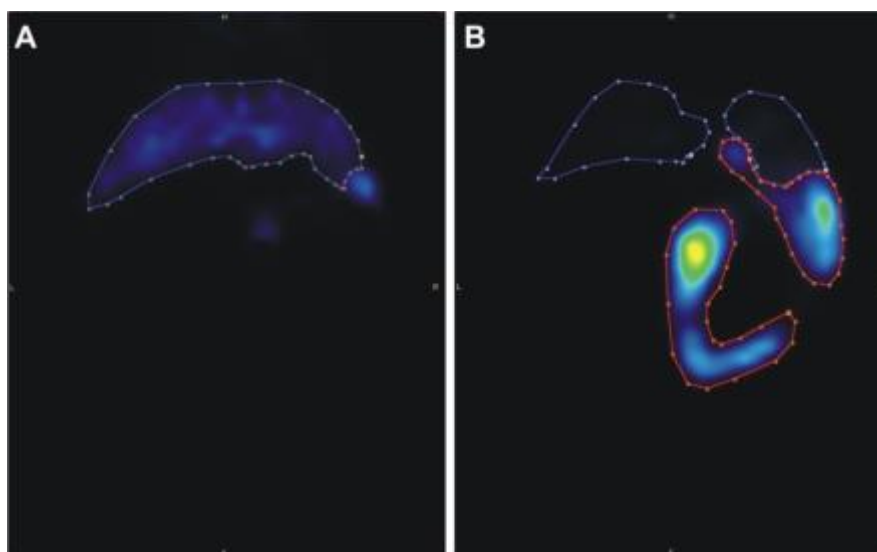


**Figure 5.4:** ROI determination using the PMOD software. Coronal views of the sum of the 10 first frames (2.5 minutes; A) and all 60 frames (0-15minutes; B). The sum of the first 10 frames can be used to draw the ROI around the liver (blue), the sum of all the frames can be used to draw the ROI around the gallbladder and intestines (red).

For WT mice, the interanimal and intra-animal variation was investigated, to determine the reproducibility of the imaging experiments.

The total activity in each organ, expressed in MBq (normalized to an injection of 37 MBq and a mouse weight of 20 g), was expressed as a function of time (in seconds).

### **Determination of the [<sup>99m</sup>Tc]mebrofenin blood curve**

After an overnight fast, the mice were injected with 200  $\mu$ L of [<sup>99m</sup>Tc]MEB (2.7 mg, 74 MBq) through a lateral tail vein. Blood samples (30  $\mu$ L) were taken by intravenous puncture in the contralateral tail vein at 1, 2, 5, 7, 10, and 15 min post-injection. The radioactivity in these samples was counted in a calibrated NaI(Tl) scintillation counter (Perkin Elmer, Belgium). A calibration curve was used to determine the activity in MBq.

To determine the blood curve of rifampicin-treated mice, the animals were pre-treated with the drug (100, 50, 37.5, 25, or 12.5 mg/kg in 100  $\mu$ L DMSO, IP) or with vehicle (100  $\mu$ L DMSO). Rifampicin (25, 12.5, 9.37, 6.25, or 3.12 mg/kg in 100  $\mu$ L PEG400:saline, 30:70,

v.v) or vehicle was also co-injected with the tracer. Blood samples were then taken as described above and used to determine the % injected dose per gram blood (%ID/g) in function of time, to calculate the area under the blood curve (AUC<sub>blood curve</sub>) and the T<sub>1/2</sub> values of the distribution and elimination phases, T<sub>1/2,α</sub> and T<sub>1/2,β</sub>, respectively.

### Statistical and kinetic analysis

Statistical analysis was performed using Prism, version 3.00 (GraphPad), and SPSS, version 19, for Windows (Microsoft). The TACs were described by calculating the maximal activity in liver and gallbladder, time-to-peak of the liver (i.e. the time point at which the maximal tracer amount or plateau was reached), and AUC<sub>liver</sub> and AUC<sub>gallbladder+intestines</sub>. Additionally, as a measure of Mrp2 transport, the tracer emergence time in the gallbladder was determined, defined as the time point when radioactivity in the gallbladder appeared in the dynamic SPECT data. AUCs were calculated using the trapezoidal method. To obtain rifampicin dose–response curves, time-to-peak of the liver and AUC<sub>gallbladder+intestines</sub> were expressed as a function of the administered doses. Time-to-peak of the liver was a measure of [<sup>99m</sup>Tc]MEB uptake and AUC<sub>gallbladder+intestines</sub> a measure of [<sup>99m</sup>Tc]MEB efflux. Bi-exponential curve fitting was applied to generate the blood curves. T<sub>1/2</sub> values were computed using the method of least squares.

$$C_p = C_1 e^{-\alpha t} + C_2 e^{-\beta t}$$

Clearance values were calculated according to Ghibellini et al. (Ghibellini et al., 2004; Ghibellini et al., 2008).

$$\text{Total clearance} = \frac{\text{Dose}}{\text{AUC}_{\text{blood}, 0 \rightarrow \infty}}$$

$$\text{Hepatic clearance} = \frac{\text{Cumulative amount in liver}}{\text{AUC}_{\text{blood}, 0 \rightarrow 180}}$$

$$\text{Biliary clearance} = \frac{\text{Cumulative amount in GB + I}}{\text{AUC}_{\text{blood}, 0 \rightarrow 180}}$$

Differences between two groups were tested for significance using the nonparametric Mann–Whitney test for two groups. All experiments were performed at  $n=3$  (unless stated otherwise);  $P \leq 0.05$  was considered significant.

## Results

### *In vitro* assessment of the potential role of OCT1

Small-scale *in vitro* experiments using stably transfected cells and parental or mock-transfected controls confirmed the OATP1B1- and OATP1B3-mediated transport of [<sup>99m</sup>Tc]MEB and a lack of detectable transport by NTCP (Figure 5.6) (Ghibellini *et al.*, 2008; Lengyel *et al.*, 2008). Not unexpectedly, in the transfected cells OCT1-mediated transport of [<sup>99m</sup>Tc]MEB could not be demonstrated, whereas <sup>14</sup>C-TEA uptake was 33 ± 6.0-fold higher than in the parental controls (Figure 5.5).

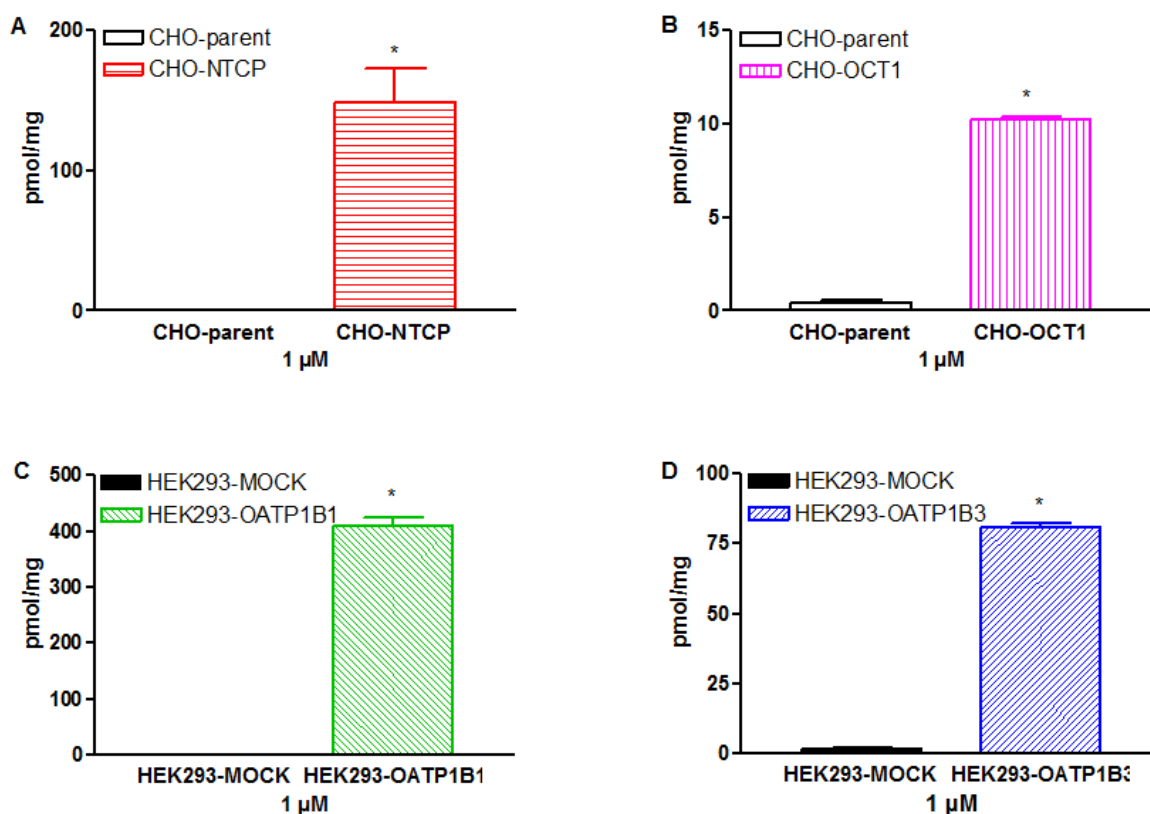


**Figure 5.5:** Positive controls: (A) <sup>3</sup>H-taurocholate uptake (A), <sup>14</sup>C-tetra-ethyl-ammonium uptake (B) and <sup>3</sup>H-estradiol-17β-glucuronide uptake (C, D) (n=3).

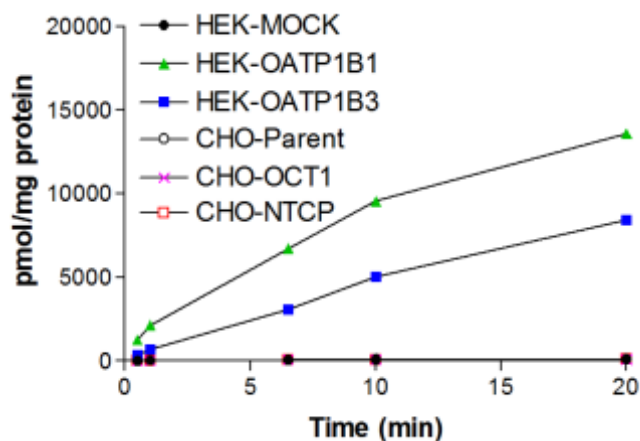


Figure 5.6: [<sup>99m</sup>Tc]MEB uptake in function of time. The tracer is only transported through OATP1B1 and OATP1B3. Data are mean±SD (n=3).

## Interanimal and intra-animal variation of the dynamic $\mu$ SPECT acquisitions

### Interanimal variation

In order to investigate the variation between several animals; we imaged 3 WT animals on the same day. The time activity curves are displayed in Figure 5.7, and the corresponding metrics with their mean, standard deviation (SD) and coefficient of variation (% CV) are shown in Table 5.1. The coefficient of variation was maximally 11.5%.

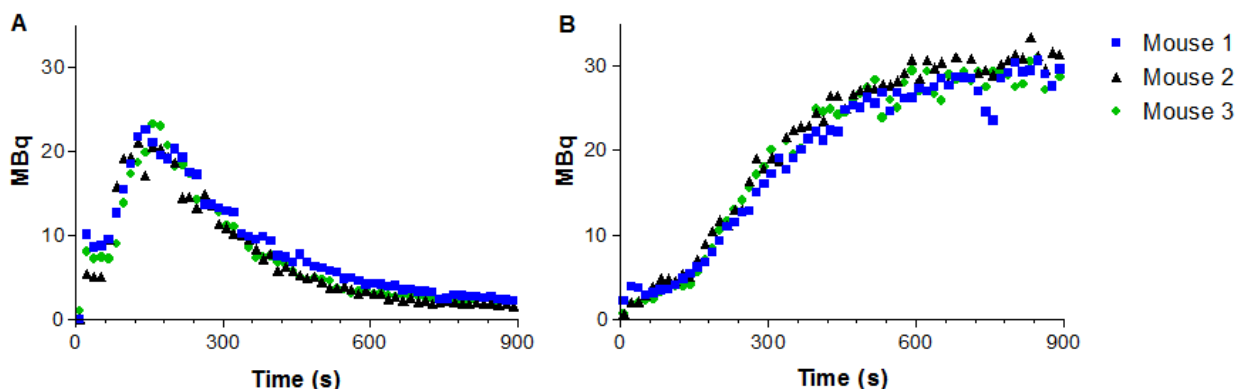


Figure 5.7: TACs of [<sup>99m</sup>Tc]MEB in the liver (A) and gallbladder and intestines (B) of 3 wild type FVB mice. Mice were imaged on the same day.

**Table 5.1:** Metrics of the time activity curves of [<sup>99m</sup>Tc]MEB of 3 wild type mice

	Mouse 1	Mouse 2	Mouse 3	Mean	SD	% CV
Maximal activity liver (MBq)	22.61	21.14	23.26	22.34	1.09	4.87
Time to peak liver (seconds)	143	128	157	143	15	10.5
AUC liver (MBq*sec)	7786	6718	6920	7141	821	11.5
Maximal activity gallbladder+intestines (MBq)	30.59	31.16	30.91	30.90	0.30	1.00
AUC gallbladder+intestines (MBq*sec)	17290	18900	17810	18000	821	4.56

***Intra-animal variation of the dynamic  $\mu$ SPECT acquisitions***

In order to investigate the variation within one animal; we imaged one animal on 3 different days. The time activity curves and corresponding metrics are shown in Figure 5.8 and Table 5.2, respectively. The coefficient of variance was maximally 12.6%.

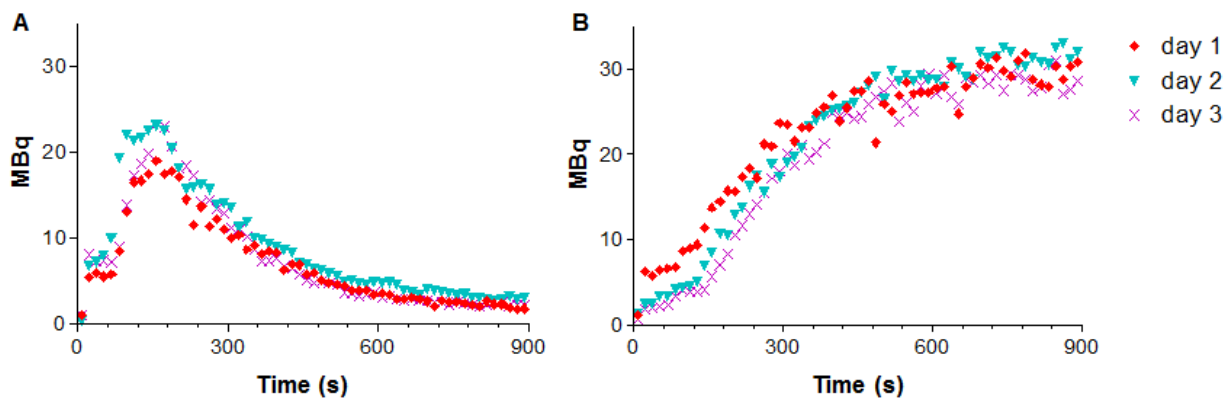


**Figure 5.8:** TACs of [<sup>99m</sup>Tc]MEB in the liver (A) and gallbladder and intestines (B) of one mouse (Mouse 3) on three different days.

**Table 5.2:** Metrics of the time activity curves of [<sup>99m</sup>Tc]MEB of one WT mouse (Mouse 3) on three different days

	Day 1	Day 2	Day 3	Mean	SD	% CV
Maximal activity liver (MBq)	18.96	23.17	23.26	21.80	2.46	11.28
Time to peak liver (seconds)	158	158	158	158	0	0
AUC liver (MBq × sec)	6344	8128	6920	7130	910	12.6
Maximal activity gallbladder+intestines (MBq)	31.37	32.46	30.91	31.58	0.80	2.5
AUC gallbladder+intestines (MBq × sec)	19960	19480	17810	19083	1128	5.9

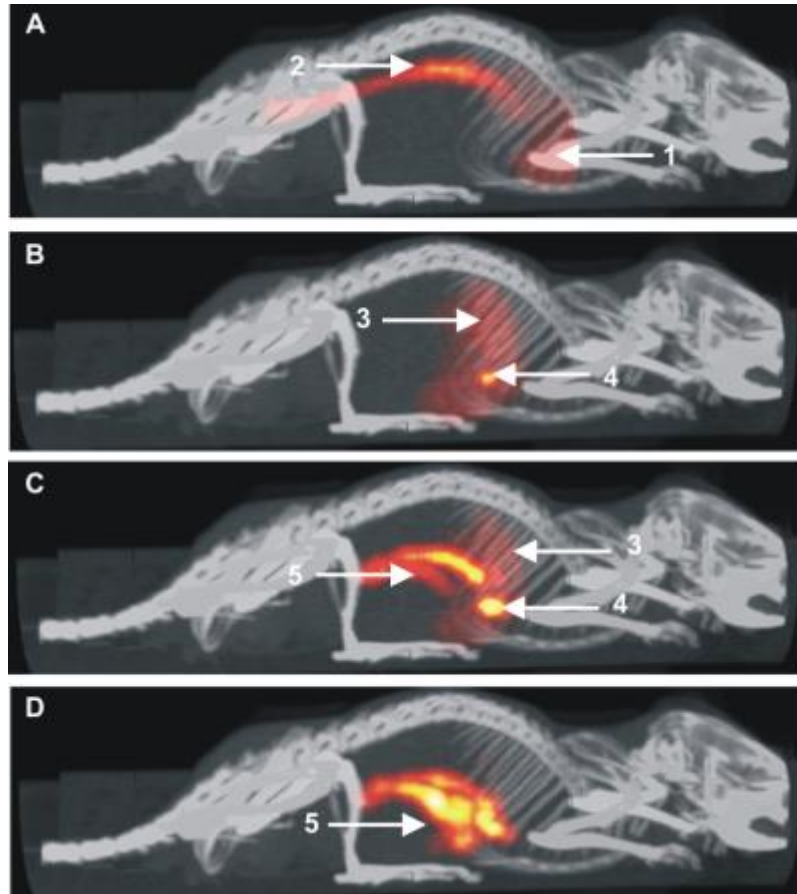
## Wild-type FVB mice

Figure 5.9 shows the projection images of the co-registered CT and SPECT images of the first four time frames (Figure 5.9 A, 0-1 minutes), frame 5-12 (Figure 5.9 B, 1-3 minutes), frame 13-20 (Figure 5.9 C, 3-5 minutes) and frame 21-60 (Figure 5.9 D, 5-15 minutes). In the first minute, after injection, mainly the blood pool is visible, including the abdominal aorta and the heart. In the next phase (1-3 minutes), mainly the liver is visible, which can be explained by the fact that [<sup>99m</sup>Tc]MEB is taken up from the blood into the hepatocytes. Additionally, the gallbladder can be observed, indicating that the efflux is already initiated. Then (3-5 minutes), the liver, gallbladder and intestines are visible, indicating efflux. In the last phase (5-15 minutes), only the intestines are visible, indicating that all the radioactivity is transported to the intestines.

Figure 5.10 depicts the mean TACs of [<sup>99m</sup>Tc]MEB of 3 WT FVB mice. Corresponding metrics are shown in Table 5.3. The maximal activity in the liver ( $19.2 \pm 2.4$  MBq) was reached after  $134 \pm 41$  s (time-to-peak<sub>liver</sub>) and was followed by a rapid exponential decrease to the background level within 15 min (900 s). According to the dynamic SPECT data, the mean appearance time of [<sup>99m</sup>Tc]MEB in the gallbladder was  $147 \pm 26$  s (Table 5.3). At the end of the acquisition, the majority of [<sup>99m</sup>Tc]MEB was found in the intestines.

The venous blood curve was consistent with a two-phase model, characterized by an initial rapid decline of the radiopharmaceutical from the blood (distribution phase), with a  $T_{1/2,\alpha}$  of  $17 \pm 2$  s, due to its distribution within the vascular space and the high extraction rate of

[<sup>99m</sup>Tc]MEB by the liver. This initial decline was followed by a slower decline (elimination phase) with a  $T_{1/2,\beta}$  of  $332 \pm 121$  s (Table 5.3).



**Figure 5.9:** Projection images of co-registered CT and  $\mu$ SPECT images of [<sup>99m</sup>Tc]MEB of WT mouse of the first minute (A, frame 1-4); 1-3 minutes (B, frame 5-12), 3-5 minutes (C, frame 13-20); and the last 10 minutes (D, frame 21-60). 1= heart; 2= abdominal aorta; 3= liver; 4= gallbladder; 5= intestines.

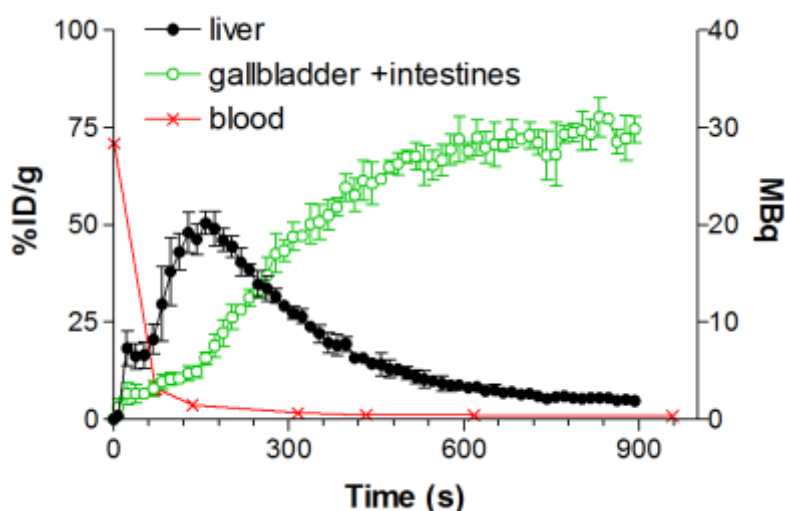


**Figure 5.10:** Mean TACs  $\pm$ SD (n=3) of [<sup>99m</sup>Tc]MEB in wild type mice. TAC<sub>liver</sub> and TAC<sub>gallbladder+intestines</sub> are expressed in MBq. Blood curves are expressed in %ID/g.

### Bile duct ligation: proof-of-principle

Next, we investigated the effect of complete obstructive cholestasis, induced by BDL in a WT animal, on [<sup>99m</sup>Tc]MEB transport (Figure 5.11, Figure 5.12).

The effect of BDL, i.e., obstructive cholestasis and thus a higher concentration of [<sup>99m</sup>Tc]MEB in the liver, is clearly seen by comparing Figure 5.10 with Figure 5.12. While in the TAC of WT mice a peak in the liver was followed by a rapid decrease to background levels, in the TAC of the BDL animal there was a continuous increase of [<sup>99m</sup>Tc]MEB uptake in the liver, with a maximum of 28.39 MBq. The tracer was not subsequently cleared but instead remained in the liver until the end of the SPECT scan. Expressed as AUC<sub>liver</sub> (MBq  $\times$  s), the activity in the liver of the BDL animal was 3.5-fold higher than that in non-treated animals (non-BDL and BDL: 6417 MBq  $\times$  s and 22202 MBq  $\times$  s, respectively). The AUC<sub>gallbladder+intestines</sub> was 17808 MBq  $\times$  s in the non-treated animal and undetectable in the BDL animal. Taken together, the total activity in the liver and gallbladder+intestines was nearly identical in the two treatment groups (non-BDL 24225 MBq  $\times$  s versus BDL 22202 MBq  $\times$  s).



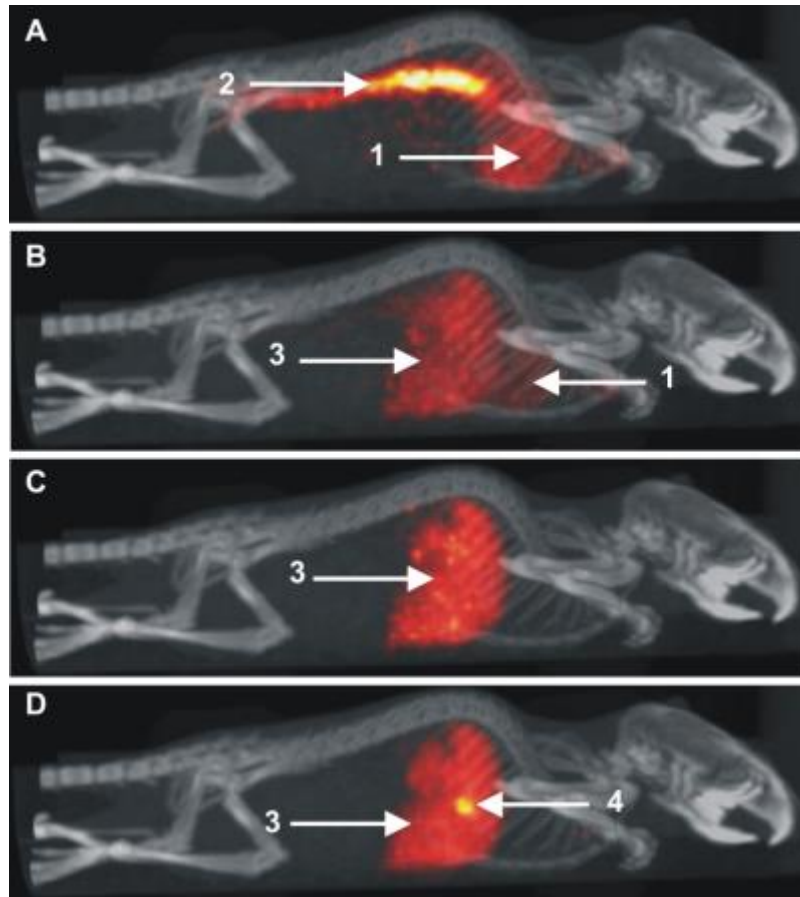


**Figure 5.11:** Projection images of co-registered CT and  $\mu$ SPECT images of [ $^{99m}\text{Tc}$ ]MEB of a mouse with a bile duct ligation of the first minute (A, frame 1-4); 1-3 minutes (B, frame 5-12), 3-5 minutes (C, frame 13-20); and the last 10 minutes (D, frame 21-60). 1= heart; 2= abdominal aorta; 3= liver; 4= gallbladder; 5= intestines.

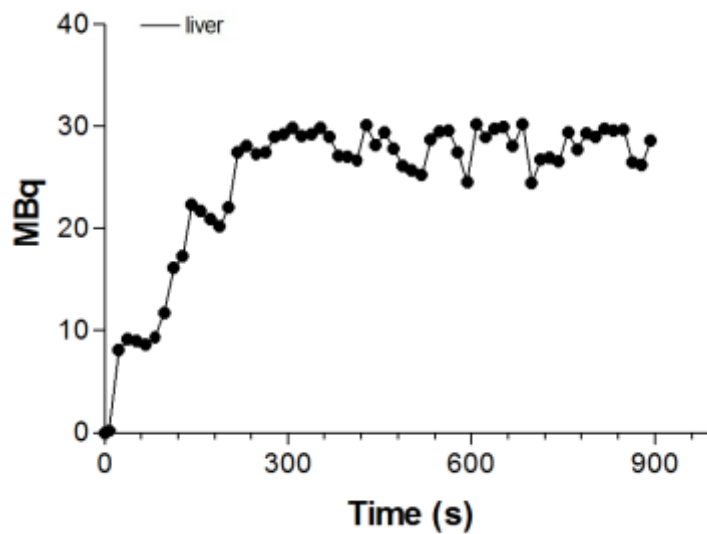


**Figure 5.12:** Proof of principle: TAC (n=1) of [ $^{99m}\text{Tc}$ ]MEB in 1 bile duct ligated mouse. TAC<sub>liver</sub> is expressed in MBq.

## Role of Oatp1a/1b transporters in the hepatic transport of [<sup>99m</sup>Tc]mebrofenin

Subsequently, the relative role of the uptake transporter family *Slc01a/1b* on the hepatic handling of [<sup>99m</sup>Tc]MEB was determined. The projection images of the different phases are shown in Figure 5.13. The majority of the tracers remains in the blood pool. The mean TACs of the Oatp1a/1b KO animals are shown in Figure 5.14.

The majority of [<sup>99m</sup>Tc]MEB activity was located in the blood and urinary bladder, with only a small amount of activity detected in the liver. [<sup>99m</sup>Tc]MEB levels in the gallbladder+intestines did not exceed the limit of quantification. This was in contrast to the WT mice, in which the majority of the [<sup>99m</sup>Tc]MEB was found in the gallbladder+intestines.

Specifically, the mean TAC<sub>liver</sub> of the Oatp1a/1b KO mice did not exceed baseline levels. The AUC<sub>liver</sub> was 3.4-fold lower in Oatp1a/1b KO mice than in WT animals ( $p=0.014$ ) (Table 5.3). At the final time point,  $3.6\pm 1.5\%$  of the injected dose was present in the urinary bladder. In the blood, the mean AUC in the Oatp1a/1b KO mice was 5.1-fold larger than in their WT counterparts ( $p\leq 0.05$ ) (Figure 5.14, Table 5.3). Hepatic clearance was lower compared to WT mice.

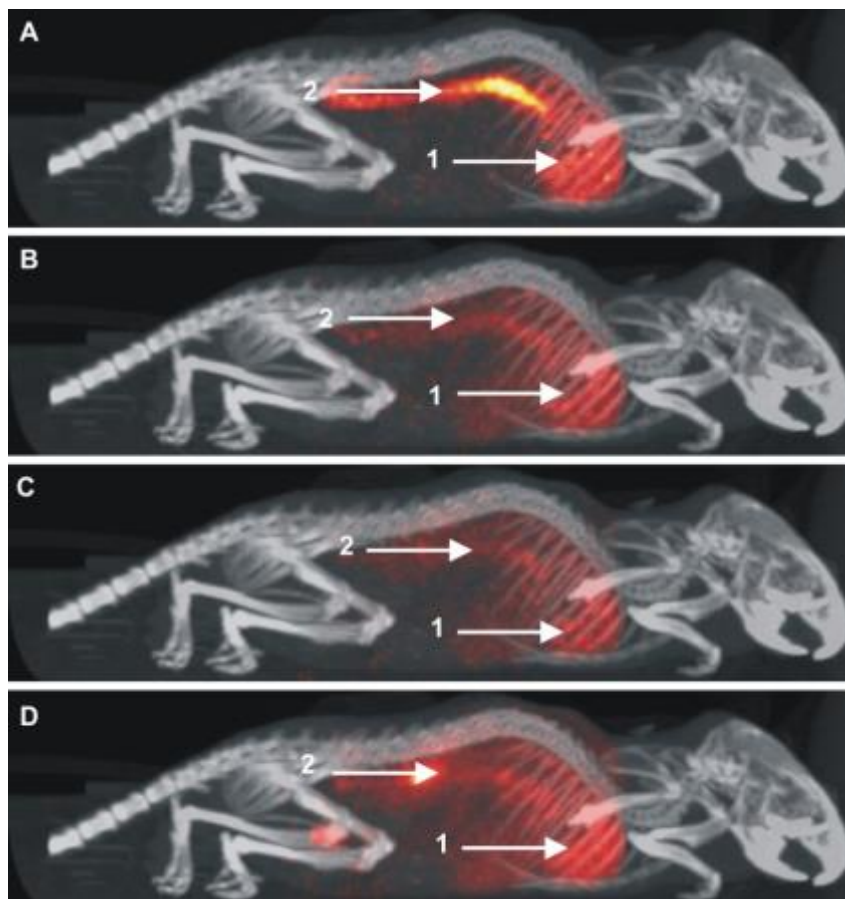


**Figure 5.13:** Projection images of co-registered CT and  $\mu$ SPECT images of [ $^{99m}\text{Tc}$ ]MEB of an Oatp1a/1b KO mouse of the first minute (A, frame 1-4); 1-3 minutes (B, frame 5-12), 3-5 minutes (C, frame 13-20); and the last 10 minutes (D, frame 21-60). 1= heart; 2= abdominal aorta.

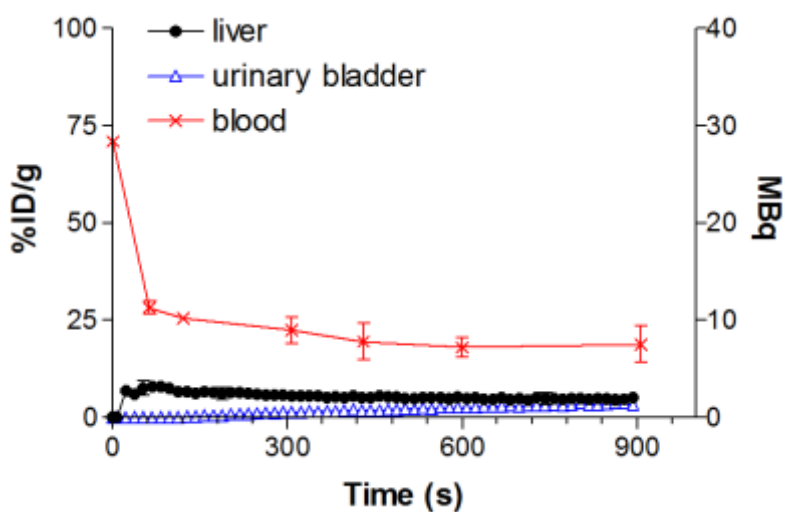


**Figure 5.14:** Mean TACs  $\pm$  SD (n=3) of [ $^{99m}\text{Tc}$ ]MEB in Oatp1a/1b KO mice.  $\text{TAC}_{\text{liver}}$  and  $\text{TAC}_{\text{urinary bladder}}$  are expressed in MBq. Blood curves are expressed in %ID/g.

## Role of the Mrp2 transporter in the hepatic transport of [ $^{99m}\text{Tc}$ ]mefenofen

The distribution of [ $^{99m}\text{Tc}$ ]MEB to the livers of Mrp2 KO mice was similar to that observed in WT mice (Figure 5.15, Figure 5.16, Table 5.3). This observation was supported by similar maximal activity in the liver ( $p > 0.05$ ) values between the two genotypes. Overall, the  $\text{AUC}_{\text{liver}}$  of Mrp2 KO mice was 2.3-fold higher than that of WT mice ( $p \leq 0.05$ ) (Table 5.3), mainly due to the impaired hepatic clearance. In line with the observations from WT animals, the activity in the urinary bladder was too low to be quantified.

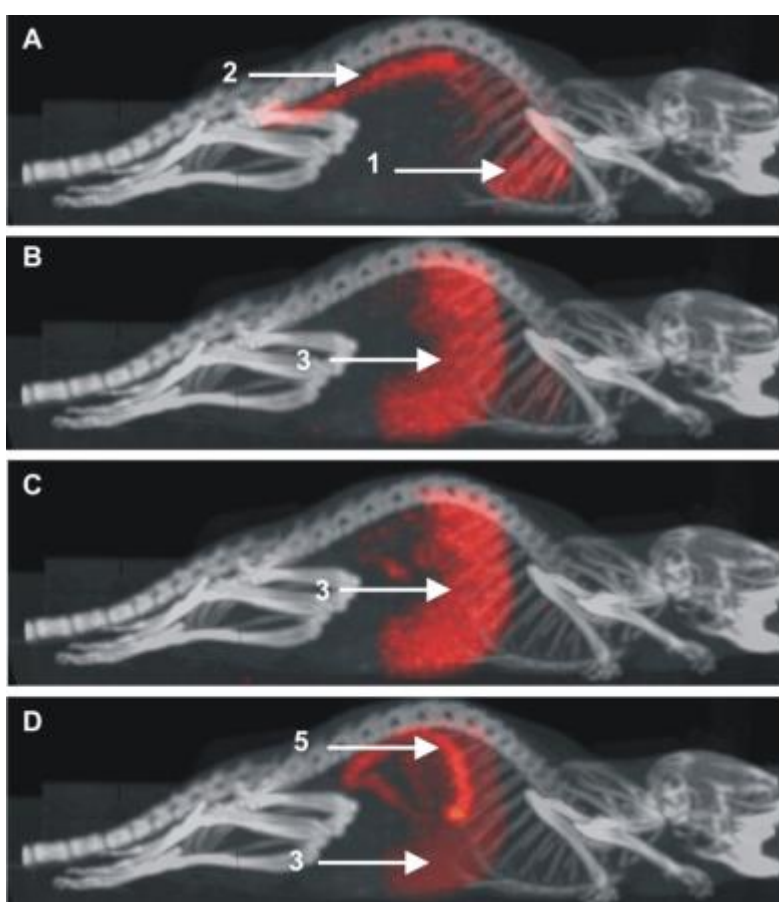


**Figure 5.15:** Projection images of co-registered CT and  $\mu\text{SPECT}$  images of [ $^{99m}\text{Tc}$ ]MEB of Mrp2 KO mouse of the first minute (A, frame 1-4); 1-3 minutes (B, frame 5-12), 3-5 minutes (C, frame 13-20); and the last 10 minutes (D, frame 21-60). 1= heart; 2= abdominal aorta; 3= liver; 5= intestines.

As shown in Table 5.3, activity in the gallbladder was observed after  $375 \pm 63$  s in Mrp2 KO mice compared to  $147 \pm 26$  s in their WT counterparts ( $p \leq 0.05$ ). The  $\text{AUC}_{\text{gallbladder+intestines}}$  in

the Mrp2 KO mice was 4.7-fold lower than in the WT mice ( $p \leq 0.05$ ). Total clearance and hepatic clearance was similar compared to WT mice. However, biliary clearance was lower.

The blood curve and corresponding metrics of the Mrp2 KO mice were comparable to those of the WT mice ( $p > 0.05$ ).

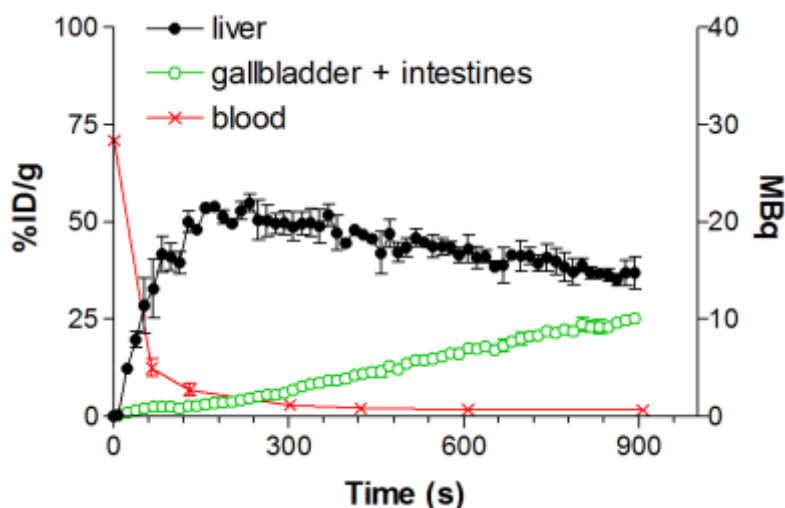


Figure 5.16: Mean TACs  $\pm$  SD ( $n=3$ ) of [<sup>99m</sup>Tc]-MEB in Mrp2 KO mice.  $TAC_{liver}$ ,  $TAC_{gallbladder+intestines}$  and  $TAC_{urinary\ bladder}$  are expressed in MBq. Blood curves are expressed in %ID/g.

## The effect of different rifampicin doses on the hepatic transport of [<sup>99m</sup>Tc]mebrofenin

The data generated thus far allowed us to investigate mechanistically the role of uptake and efflux transporters in the *in vivo* disposition of [<sup>99m</sup>Tc]MEB. With this framework established, we aimed to determine whether it was possible to discriminate dose-dependently between the inhibition of hepatic uptake transporters and that of efflux transporters. Since rifampicin is both a substrate and an inhibitor of OATPs/Oatps and MRP2/Mrp2, it was selected as the test agent.

In Figure 5.17, the projection images of the co-registered CT and  $\mu$ SPECT acquisitions are shown. Again, divided in different phases.

The mean TACs of the vehicle-control and rifampicin-treated (highest dose, 100 mg/kg IP, 25 mg/kg IV) mice are shown in Figure 5.18A and Figure 5.18B, respectively. In the control

mice, the TACs were similar to those of the untreated WT mice. The metrics of the different rifampicin doses are shown in Table 5.3.

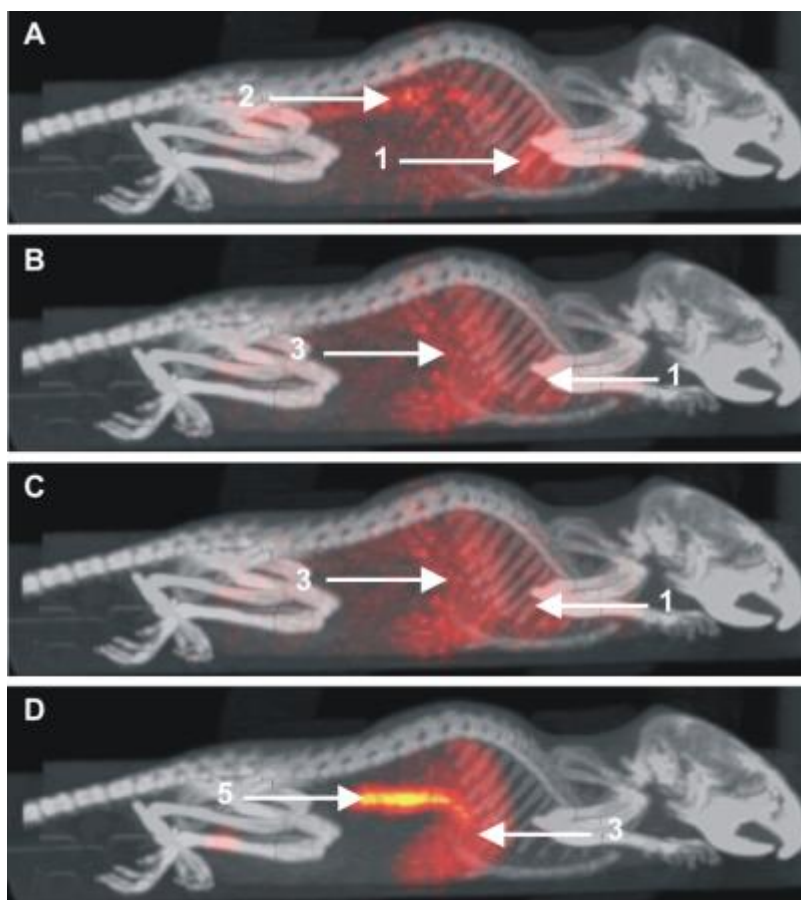


**Figure 5.17:** Projection images of co-registered CT and  $\mu$ SPECT image of [<sup>99m</sup>Tc]MEB of a rifampicin treated mouse of the first minute (A, frame 1-4); 1-3 minutes (B, frame 5-12), 3-5 minutes (C, frame 13-20); and the last 10 minutes (D, frame 21-60). 1= heart; 2= abdominal aorta; 3= liver; 5= intestines.

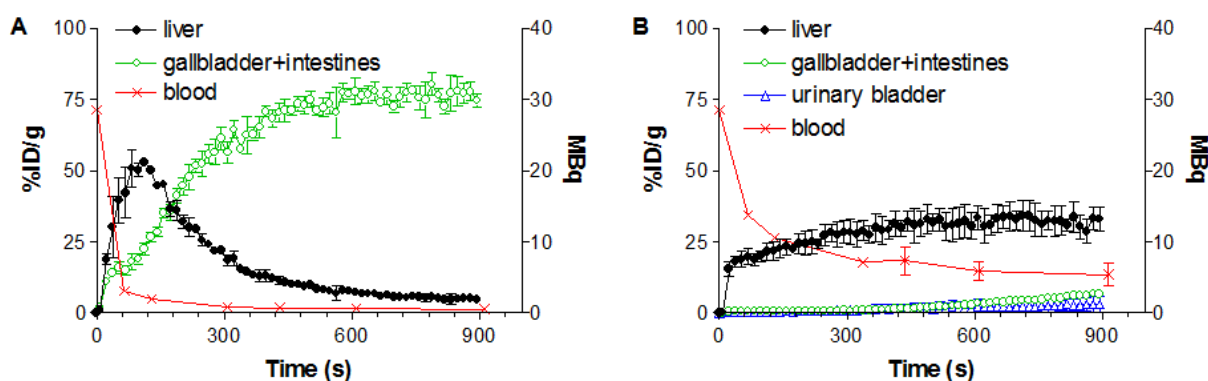


**Figure 5.18:** Mean TACs  $\pm$ SD in the vehicle-control mice (n=3) (A) and in rifampicin-treated mice (n=3) (B). TAC<sub>liver</sub>, TAC<sub>gallbladder+intestines</sub>, and TAC<sub>urinary bladder</sub> are expressed in MBq. Blood curves are expressed in %ID/g.

The time-to-peak in the liver of mice treated with the highest dose of rifampicin was 5.1-fold higher than that of vehicle-control mice ( $p \leq 0.05$ ) while the  $AUC_{\text{liver}}$  was 1.6-fold higher ( $p = 0.034$ ). Moreover, the mean emergence time of tracer activity in the gallbladder was prolonged 4.0-fold in rifampicin-treated mice ( $p \leq 0.05$ ) whereas the  $AUC_{\text{gallbladder+intestines}}$  decreased by a factor of 10 ( $p \leq 0.05$ ). A  $TAC_{\text{urinary bladder}}$  could be determined in the rifampicin-treated mice but not in the vehicle-control mice.

The mean  $AUC_{\text{blood}}$  in mice treated with the highest dose of rifampicin was 4.3-fold greater than that of their WT counterparts ( $p \leq 0.05$ ). Additionally,  $T_{1/2}$  values were 2.8-fold higher ( $p \leq 0.05$ ). All clearance values were lower compared to vehicle controlled mice.

In order to investigate if mild alterations can be detected with the proposed method, we administered 5 different rifampicin doses (100 mg/kg IP + 25 mg/kg IV; 50 mg/kg IP + 12.5 mg/kg IV; 37.5 mg/kg IP + 9.37 mg/kg IV; 25 mg/kg IP + 6.25 mg/kg IV; 12.5 mg/kg IP + 3.12 mg/kg IV), or vehicle in wild type mice ( $n=3$  for each dose), to obtain a dose response curve (Figure 5.19, Table 5.3). The time-to-peak in the liver and the area under the gallbladder+intestines curve are expressed in function of the administered dose in Figure 5.19A and Figure 5.19B, respectively (only the i.p. dose is displayed. Note that 1h after each i.p. dose, a second i.v. dose was given, co-injected with [<sup>99m</sup>Tc]MEB). The curves demonstrate a dose-dependent effect on the uptake and efflux of [<sup>99m</sup>Tc]MEB. Higher doses of rifampicin delayed the time-to-peak and caused a smaller  $AUC_{\text{gallbladder+intestines}}$ , representing decreases in hepatic uptake and in efflux to the gallbladder and intestines, respectively.

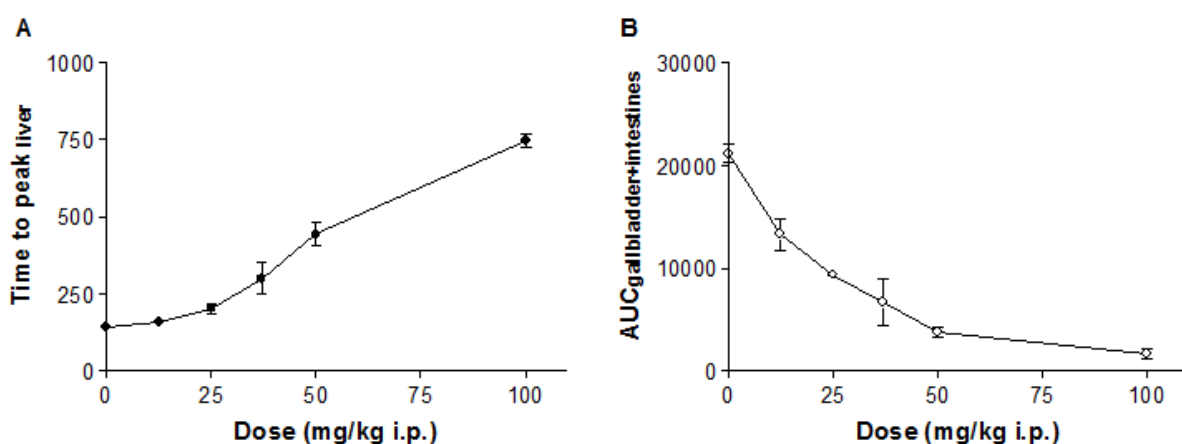


**Figure 5.19:** Mean dose response curves of rifampicin  $\pm$ SD ( $n=3$ ). Time to peak<sub>liver</sub> was expressed in seconds,  $AUC_{\text{gallbladder+intestines}}$  was expressed as MBq\*s. Note that only the i.p. dose is displayed. However, 1h after each i.p. dose, a second i.v. dose was given (co-injected with [<sup>99m</sup>Tc]-MEB).

**Table 5.3** Metrics of the time-activity curves of [<sup>99m</sup>Tc]MEB in wild type, *Slco1a1b*<sup>-/-</sup>, *Abcc2*<sup>-/-</sup> and rifampicin treated mice.

		Maximal activity liver (MBq)	Time to peak liver (s)	AUC liver (MBq × s)	Maximal activity gallbladder + intestines (MBq)	Emergence time gallbladder (s)	AUC gallbladder + intestines (MBq × s)	AUC blood curve (MBq/ml × s)	T <sub>1/2,α</sub> (s)	T <sub>1/2,β</sub> (s)	Total clearance (mL/min)	Hepatic clearance (mL/min)	Biliary clearance (mL/min)	
Wild type mice		19.17±2.39	134±41	6507±820	28.9 ± 1.00	147 ± 26	18269±4349	1411 ± 157	17±2	332±121	1.82±0.12	0.82	1.22	
Oatp1a/1b KO mice		3.44±0.51	77.5±23	1926±264	*	*	*	6771 ± 839	29±7	*	*	0.03	n/a	
Mrp2 KO mice		22.12±1.71	212±23	15010±1382	‡	375 ± 63	3916±475	1769 ± 212	18 ± 3	375 ± 63	1.63±0.61	0.75	0.33	
	Dose (mg/kg)													
Rifampicin treated wild type mice	IP													
	IV													
	100	25	12.7 ± 3.00	747±37	10048±2355	‡	555 ± 65	1639±776	6411 ± 544	40±4	853±273	0.19±0.064	0.12	0.14
	50	12.5	16.32±0.76	442±65	11297±436	‡	385 ± 31	3736±858	†	†	†	†	†	†
	37.5	9.37	14.50±0.71	300±47	9700±1655	‡	457 ± 53	6742±3201	†	†	†	†	†	†
	25	6.25	17.13±0.40	235±26	9686±606	‡	240 ± 15	937 ± 411	†	†	†	†	†	†
	12.5	3.12	16.40±0.42	157±12	6282±846	‡	240 ± 42	13300±2149	†	†	†	†	†	†
Vehicle controlled mice		18.69±3.82	145±31	6120±124	29.16±0.51	140 ± 20	17752±688	1514 ± 140	15 ± 2	300±21	1.90±0.29	0.74	1.16	

Data are mean (n=3) ± standard deviation

\* could not be observed

† not investigated

‡ linear increase, no maximal activity



## Discussion

Drug-induced liver injury is one of the leading causes for the withdrawal of approved drugs from the market (Maddrey *et al.*, 2005), highlighting the importance of assessing this effect early on in drug research. One of the underlying causes of drug-induced liver injury is an altered functional activity of hepatic uptake or efflux transporters. In this study, we investigated [<sup>99m</sup>Tc]MEB transport through Oatp and Mrp2. Based on the results, we were able to propose a non-invasive method to visualize and quantify altered hepatobiliary transporter activity. Moreover, the proposed method enables the differentiation between altered influx and efflux. By using dynamic SPECT measurements to calculate TACs of [<sup>99m</sup>Tc]MEB that quantify transport via the liver to the gallbladder and intestines, our method offers a novel approach, as thus far it has not been possible either to visualize or quantify *in vivo* hepatic drug interactions and the differentiation between uptake and efflux alterations.

First, the specificity for [<sup>99m</sup>Tc]MEB for the human transport proteins was investigated by means of CHO cell lines expressing these human transporters. Our data confirmed the results of Ghibellini *et al.* that identified OATP1B1 and OATP1B3 as uptake transporters of [<sup>99m</sup>Tc]MEB (Ghibellini *et al.*; 2008). Additionally, the current study was able to exclude OCT1 as a [<sup>99m</sup>Tc]MEB transporter.

Then, we clearly demonstrated the possibility to non-invasively visualize and quantify the *in vivo* hepatobiliary transport in a reproducible manner. Repeated measurements were performed in different animals and on different days. Out of these measurements, TACs were calculated to quantify the transport over the liver or in the gallbladder and intestines. The ROIs of the gallbladder and intestines were considered together as one ROI. The rationale behind this is the common bile duct, forming a direct connection between the liver and intestines. As a consequence, not all the bile flow to the gallbladder for temporary storage, but some bile flow directly to the intestines. The interanimal and the intra-animal measurements of the maximal activity in the liver and areas under the curve were not significantly different. Furthermore, the coefficient of variation did not exceed 13%. Consequently, these results indicate that it is possible to visualize and quantify the activity of hepatic transporters with [<sup>99m</sup>Tc]MEB in a reproducible manner. Secondly, we set out a mean TAC of the liver and gallbladder+intestines in wild type FVB mice. Significant differences in the following experiments will be due to altered hepatobiliary transport.

The primary aim of our study was the visualization of disturbed hepatobiliary transporter function. As proof-of-principle, a BDL was placed so as to simulate extrahepatic cholestasis. This mechanical inhibition caused the complete obstruction of bile flow and subsequently the accumulation of [<sup>99m</sup>Tc]MEB in the liver, thus demonstrating the ability of the proposed method to visualize and quantify disturbances in hepatobiliary transport.

To examine the possibility of distinguishing between uptake and efflux transporter alterations, Oatp1a/1b KO and Mrp2 KO mice were investigated. Experiments in the Oatp1a/1b KO mice confirmed the critical role played by transporters of the Oatp1a/1b family in the hepatic uptake of [<sup>99m</sup>Tc]MEB, consistent with the findings of Van de Steeg et al. (*Van de Steeg et al., 2010*). The liver TACs of Oatp1a/1b KO mice did not exceed baseline levels, due to the impaired hepatic uptake of [<sup>99m</sup>Tc]MEB. Consequently, blood concentrations remained elevated in comparison with WT mice, due to absence of Oatp1a/1b.

We were also able to demonstrate *in vivo* that the biliary efflux transporter Mrp2 is involved in [<sup>99m</sup>Tc]MEB transport. Specifically, in Mrp2 KO mice the absence of the efflux transporter led to the hepatic accumulation of [<sup>99m</sup>Tc]MEB, reflected in a higher AUC<sub>liver</sub>. Consequently, less [<sup>99m</sup>Tc]MEB reached the gallbladder and intestines, resulting in a lower AUC<sub>gallbladder+intestines</sub> and a delayed tracer emergence time. The corresponding blood concentrations were comparable to those of the WT animals, since hepatic uptake was not disturbed.

To assess the effect of pharmacological inhibition on transporter activity, rifampicin was administered to WT mice, by both the IP and the IV routes. This double administration led to the impaired uptake and efflux of [<sup>99m</sup>Tc]MEB. Inhibition of [<sup>99m</sup>Tc]MEB uptake occurs at the level of the basolateral (sinusoidal) Oatps, with rifampicin acting as a competitive inhibitor of the transporters (*Vavricka et al., 2002*). Since hepatic uptake was impaired, the time-to-peak in the liver of [<sup>99m</sup>Tc]MEB was delayed and blood concentrations of the tracer were elevated. Additionally, urinary elimination of [<sup>99m</sup>Tc]MEB was increased in rifampicin-treated mice. This increase in renal excretion reflected the decreased uptake of [<sup>99m</sup>Tc]MEB through Oatp1a/1b and the increased blood concentrations (higher AUC<sub>blood</sub>). Rifampicin is both a substrate and an inhibitor of Oatps. Therefore, a certain amount of rifampicin is able to enter the hepatocytes, where it inhibits the Mrp2 transporter at the level of the canalicular membrane. Consequently, an accumulation of [<sup>99m</sup>Tc]MEB in the liver (higher AUC<sub>liver</sub>) can be detected whereas the decreased amounts of [<sup>99m</sup>Tc]MEB in the intestines are due to a

combination of Oatp and Mrp2 inhibition (lower AUC<sub>gallbladder+intestines</sub>). These observations suggest that the impaired liver uptake and efflux is caused by a combination of rifampicin-mediated Oatp1a/1b and Mrp2 inhibition (Lengyel *et al.*, 2008; Mita *et al.*, 2006). To the best of our knowledge, Mrp2 inhibition has not been previously shown *in vivo*. Our study demonstrates the feasibility of visualizing and quantifying the effect of Oatp1a/1b and Mrp2 modulation by various drugs *in vivo*, with rifampicin as a model drug, and confirms the findings of Van de Steeg *et al.* (Van de Steeg *et al.*, 2010) with methotrexate and tritium-labeled fexofenadine.

Additionally, we were able to show that slight alterations in transporter activity can be detected with the proposed imaging method. Using five different rifampicin doses, a dose-response curve of the rifampicin-mediated inhibition of [<sup>99m</sup>Tc]MEB transport was obtained. The data demonstrated a dose-dependent effect on the uptake and efflux of [<sup>99m</sup>Tc]MEB. Higher doses of rifampicin delayed time-to-peak in the liver and caused a smaller AUC<sub>gallbladder+intestines</sub>, representing decreases in hepatic uptake and in efflux to the gallbladder and intestines, respectively. While Mrp2 inhibition occurred at low rifampicin concentrations (12.5 mg/kg IP, 6.25 mg/kg IV), Oatp inhibition was seen at higher concentrations of the drug (37.5 mg/kg IP, 9.37 mg/kg IV).

In summary, this study shows that it is possible to quantitatively discriminate between the lack of functional activity of sinusoidal uptake and that of biliary efflux transporters. Therefore, the method described in this chapter offers a promising approach to investigate the interaction between new chemical entities and hepatobiliary transporters.

## References

- Billingham MW, Eckert K, Mang'era K. Alternative quality control for technetium-99m IDA complexes. *Appl Radiat Isot* 2004;61:1151-1155.
- Bujanover Y, Bar-Meir S, Hayman I, Baron J. <sup>99m</sup>Tc-HIDA cholescintigraphy in children with Dubin-Johnson syndrome. *J Pediatr Gastroenterol Nutr* 1983;2:311-2.
- de Graaf W, Häusler S, Heger M, et al. Transporters involved in the hepatic uptake <sup>99m</sup>Tc-mebrofenin and indocyanine green. *J Hepatol* 2011;54:738-745.
- Ghibellini G, Leslie EM, Pollack GM, Brouwer KLR. Use of Tc-<sup>99m</sup> Mebrofenin as a Clinical Probe to Assess Altered Hepatobiliary Transport: Integration of *In vitro*, Pharmacokinetic Modeling, and Simulation Studies. *Pharm Res* 2008;25:1851-60.
- Kosters, A, Karpen SJ. Bile acid transporters in health and disease. *Xenobiotica* 2008;38:1043-1071.
- Kullak-Ublick G, Beuers U, Paumgartner G. Hepatobiliary transport. *J Hepatol* 2000;32:3-18.
- Kullak-Ublick GA, Stieger B, Hagenbuch B, Meier PJ. Hepatic transport of bile salts. *Semin Liver Dis* 2000;273-92.
- Lengyel G, Veres Z, Tugyi R, et al. Modulation of sinusoidal and canalicular elimination of bilirubin-glucuronides by rifampicin and other cholestatic drugs in a sandwich culture of rat hepatocytes. *Hepatol Res* 2008;38:300-309.
- Maddrey WC. Drug-induced hepatotoxicity. *J Clin Gastroenterol* 2005;39:S83-S89.
- Meier PJ, Stieger B. Bile salt transporters. *Annu Rev Physiol* 2002;64:635-61.
- Mita S, Suzuki H, Akita H, Hayashi H, Onuki R, Hofmann AF, et al. Inhibition of bile acid transport across Na<sup>+</sup>/taurocholate cotransporting polypeptide (SLC10A1) and bile salt export pump (ABCB 11)-coexpressing LLC-PK1 cells by cholestasis-inducing drugs. *Drug Metab Dispos* 2006;34:1575-81.
- Morandi F, Frank N, Avenell J, Daniel GB. Quantitative assessment of hepatic function by means of <sup>99m</sup>Tc-Mebrofenin in healthy horses. *J Vet Intern Med* 2005;19:751-5.
- Newell SM, Graham JP, Roberts GD, et al. Quantitative hepatobiliary scintigraphy in normal cats and in cats with experimental cholangiohepatitis. *Vet Radiol Ultrasound* 2000;42:70-6.
- Padda MS, Sanchez M, Akhtar AJ, Boyer JL. Drug-induced cholestasis. *Hepatology* 2011;53:1377-87.
- Shitara Y, Sato H, Sugiyama Y. Evaluation of Drug-Drug Interaction in the Hepatobiliary and Renal Transport of Drugs. *Annu Rev Pharmacol Toxicol* 2005;45:689-723.
- Trauner M, Boyer JL. Bile salt transporters: molecular characterization, function and regulation. *Physiol Rev* 2003;83:633-71.

## Chapter 5: *In vivo* visualization and quantification of normal and disturbed hepatobiliary transport by means of [<sup>99m</sup>Tc]mebrofenin

---

Van de Steeg E, Wagenaar E, van der Kruijssen CMM, et al. Organic anion transporting polypeptide 1a/1b-knockout mice provide insights into hepatic handling of bilirubin, bile acids, and drugs. *J Clin Invest* 2010;120:2942-2952.

Vavricka SR, Van Montfoort J, Riem Ha H, Meier PJ, Fattinger K. Interactions of rifamycin SV and rifampicin with organic anion uptake systems of human liver. *Hepatology* 2002;36:164-172.

Vlaming ML, Mohrmann K, Wagenaar E, et al. Carcinogen and anticancer drug transport by Mrp2 in vivo: studies using Mrp2 (Abcc2) knockout mice. *J Pharmacol Exp Ther* 2006;318:319-327.

Wolkoff, AW, DE Cohen. Bile acid regulation of hepatic physiology: Hepatocyte transport of bile acids. *Am J Physiol Gastrointest Liver Physiol* 2003;284:G175-G179.

van der Have F, Vanstenhouw B, Ramakers R, Branderhorst W, Krah JO, Ji C, et al. U-SPECT-II: An ultra-high-resolution device for molecular small-animal imaging. *J Nucl Med* 2009;50:599-605.

# Chapter 6.

## Kinetic modeling of [<sup>99m</sup>Tc]mebrofenin as a tool to quantify altered hepatobiliary transport

*Parts have been adapted from*

Neyt S<sup>1</sup>, Vanhove C<sup>2</sup>, De Lombaerde S<sup>1</sup>, Deblaere K<sup>3</sup>, De Vos F<sup>1</sup>. Submitted to Contrast Media Mol Imaging 2016.

<sup>1</sup>Laboratory of Radiopharmacy, Ottergemsesteenweg 460, Ghent University, Ghent, Belgium

<sup>2</sup>iMinds Medical IT-IBITech-MEDISIP-INFINITY, Ghent University, Ghent, Belgium

<sup>3</sup> Department of Radiology, Ghent University Hospital, Ghent, Belgium



## Introduction

As outlined in Chapter 5, identification of possible interactions of new candidate drugs with hepatobiliary transport mechanisms is important early during drug development (*Cuperus et al., 2014; de Lima Toccafondo Vieira et al., 2014; Ho et al., 2005; Schuetz et al., 2014*). In Chapter 5, a non-invasive *in vivo* method to visualize and semi-quantify (disturbed) hepatic transport by means of dynamic  $\mu$ SPECT imaging of [<sup>99m</sup>Tc]-mebrofenin ([<sup>99m</sup>Tc]MEB) was proposed (*Neyt et al., 2013*). Quantification was done using a calibration curve based on a known standard. Impaired uptake was reflected in elevated blood concentrations, a lower maximal liver uptake and a decreased  $AUC_{\text{gallbladder+intestines}}$ . Impaired efflux was shown in a higher  $AUC_{\text{liver}}$  value and a decreased  $AUC_{\text{gallbladder+intestines}}$ .

In this chapter, we will further optimize the quantification of the (disturbed) hepatobiliary transport by using tracer kinetic modeling. As outlined in Chapter 1, these models describe the tracer kinetics mathematically by using a number of compartments, representing distinct anatomical, physiological, or biochemical stages in the behavior of the tracer. The tracer kinetics are described by a set of differential equations that provide the link between activity levels measured on, for example, dynamic  $\mu$ SPECT images and physiologic parameters associated with the hepatobiliary transport. The goal is the implementation of a two-tissue compartment kinetic model of [<sup>99m</sup>Tc]MEB to describe impaired hepatobiliary uptake and/or efflux caused by drugs or genetic disorders.

Previously, Ghibellini et al. (*Ghibellini et al., 2008*) reported a pharmacokinetic model, based on human data, to simulate the effect of changes in hepatic uptake and/or secretion associated with disease states on [<sup>99m</sup>Tc]MEB disposition. Using a three-tissue compartment model including liver, gallbladder and urinary bladder, they concluded that [<sup>99m</sup>Tc]MEB could be a useful biomarker to assess the impact of altered hepatic function at the transport level, caused by drugs or genetic disorders. In the current study, we used a simplified version of the model proposed by Ghibellini et al. (two-tissue compartment model) in mice, since we observed almost no radioactivity in the urinary bladder and kidneys in mice (*Neyt et al., 2013*). In contrast to Ghibellini et al., who used the model to simulate the effect of altered hepatobiliary transport, we validated and implemented the model *in vivo*, before and after administration of the Oatp and Mrp2 inhibitor rifampicin, and in Mrp2 knock-out (KO) mice.



Kinetic parameters of wild type (WT), Mrp2 KO and rifampicin treated mice are compared. The kinetic parameters can offer a detailed quantitative description of altered hepatobiliary transport, in addition to the metrics of the time activity curves (TACs) as performed before (Neyt *et al.*, 2013).

Moreover, a novel non-invasive method was used to obtain an image derived input function of [<sup>99m</sup>Tc]MEB. As outlined in Chapter 1, the biggest challenge in preclinical kinetic modeling is the determination of the arterial input function. The “gold standard” in the clinic is arterial blood sampling. However, in rodents, invasive blood sampling is restricted to a small fraction of the total blood (Parasuraman, 2010). According to Diehl *et al.* (Diehl *et al.*, 2001), it is limited to 7.5% of the circulatory blood volume corresponding to 100  $\mu$ L for a 25g mouse. Apart from manual sampling, automated on-line blood sampling can be used during preclinical imaging. However, this technique only exists for tracers using positron emitters. To generate the arterial input function in a non-invasive way, image-derived methods were introduced that obtain the blood TACs from a region of interest (ROI) in the blood pool, such as the left ventricular cavity. However, the definition of the heart is sometimes challenging when no detailed anatomical information is present. Therefore, in the current study, [<sup>99m</sup>Tc]tetrafosmin was introduced as imaging agent to visualize the perfusion of the myocardium. On the static [<sup>99m</sup>Tc]tetrafosmin scan, a ROI can be drawn into the left ventricle and this ROI can be easily copy-pasted on the dynamic [<sup>99m</sup>Tc]MEB data, when [<sup>99m</sup>Tc]tetrafosmin and [<sup>99m</sup>Tc]MEB are acquired sequentially without changing the position of the animal between the two acquisitions.

## Materials and Methods

### Animal Model

FVB wild-type (WT) mice (♀, 5 weeks, 20–25 g) were from Janvier (France) and *Abcc2*<sup>-/-</sup> (♀, 5 weeks, 20–25 g; Mrp2 KO mice) mice were from Taconic Farms (USA). The mice were housed and handled according to guidelines approved by the European Ethics Committee and acclimatized for at least one week before the experiments. All of the animals were kept under environmentally controlled conditions (12 h normal light/dark cycles, 20–22°C and 60% relative humidity) with food and water ad libitum. The study protocol was approved by the Animal Experimental Ethical Committee of Ghent University (ECD10/39). n=5 per group.

### Molecular Imaging

Dynamic  $\mu$ SPECT/CT acquisitions were acquired on a USPECT-II/CT device (MILabs, Utrecht, The Netherlands) (*van der Have et al., 2009*) equipped with a cylindrical collimator containing 75 pinholes of 1 mm diameter (rat whole-body collimator; spatial resolution, 0.8 mm). All acquisitions were acquired in list mode.

After an overnight fast (minimum 6 h), the WT and Mrp2 KO mice were anesthetized with a mixture of isoflurane (1.5%) and medical O<sub>2</sub> to allow placement of an intravenous needle (30G) and polyethylene (PE10) tubing (Becton Dickinson, Belgium) in a lateral tail vein. The mice were placed in a prone position on the mouse scan bed. 200  $\mu$ L (37-74 MBq; 2 mg MEB) [<sup>99m</sup>Tc]MEB was injected via the intravenous PE10 tubing, directly after scan initiation.

One hour before tracer injection, rifampicin-treated mice were pre-treated with rifampicin (100 mg/kg in 100  $\mu$ L DMSO, IP). Then, the mice were anesthetized and a PE10 tubing was placed intravenously. 200  $\mu$ L (37-74 MBq; 2 mg MEB) [<sup>99m</sup>Tc]MEB was injected directly after scan initiation. During tracer injection, a second dose of rifampicin (25 mg/kg in 100  $\mu$ L PEG400:saline, 30:70, v:v) was intravenously co-administered.

All the mice were imaged while anesthetized, with their body temperature maintained during imaging using a heated bed. The axial field of view required for the SPECT scan was chosen based on 3 planar X-ray images. Subsequently, a 15 min dynamic SPECT acquisition using 60 time frames of 15 s was initiated 5 s before the injection of [<sup>99m</sup>Tc]MEB.

Immediately after dynamic scan termination and without repositioning the animal, 185 MBq of [ $^{99m}\text{Tc}$ ]tetrofosmin was injected. 20 minutes post-injection, with the animal still in the same position, a static SPECT scan of 30 minutes was performed. Lastly, a CT acquisition (5 min; tube current, 612  $\mu\text{A}$ ; tube voltage, 50 kV) was performed for anatomical correlation. The resultant CT scan is inherently co-registered with the corresponding  $\mu\text{SPECT}$  acquisition.

On the dynamic [ $^{99m}\text{Tc}$ ]MEB data, ROIs were manually drawn over the liver and gallbladder+intestines using PMOD software (PMOD technologies, Switzerland). On the static [ $^{99m}\text{Tc}$ ]tetrofosmin data, a ROI was manually drawn over the left ventricle of the heart. Since the position of the mice was unaffected between the two acquisitions, the ROI drawn around the left ventricle (Figure 6.1), was copied to the dynamic [ $^{99m}\text{Tc}$ ]MEB images to obtain an image derived input function (IDIF) (Figure 6.2). Using the changing activity levels measured in liver, gallbladder+intestines and blood pool, TACs were obtained.

The U-SPECT-II calibration curves (Chapter 4) were used to determine the total amount or concentration of the radiotracer. The total activity in each organ, expressed in MBq (normalized to an injection of 37 MBq), was expressed as a function of time (in seconds). The image derived blood function was expressed as MBq/mL as a function of time (in seconds).



**Figure 6.1:** Slice through the heart on the [ $^{99m}\text{Tc}$ ]tetrofosmin SPECT scan. ROI drawn around the left ventricle.

1: left ventricle; 2: right ventricle.

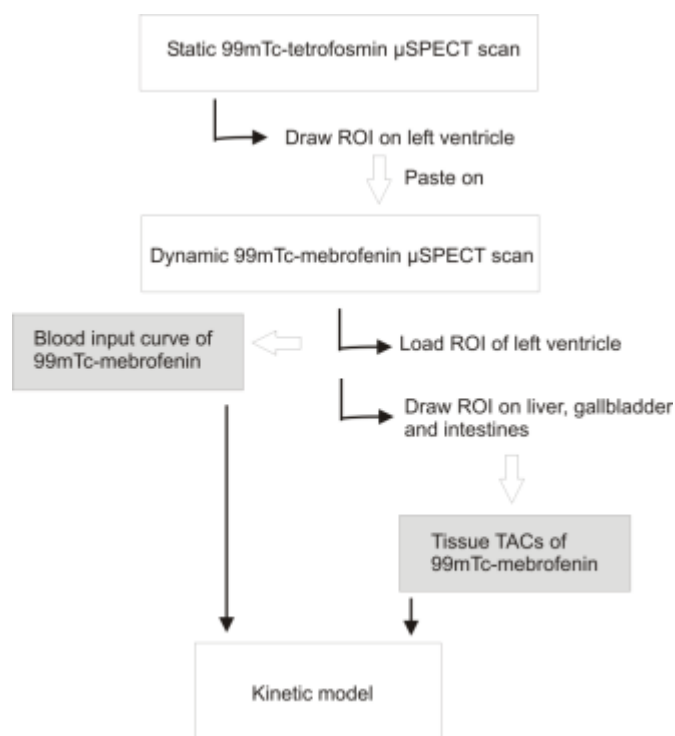


**Figure 6.2:** An overview of the processing used to obtain all the time activity curves that are needed to obtain a pharmacokinetic model of [ $^{99m}\text{Tc}$ ]MEB.

## Correlation of image derived blood function with manual blood samples

The image derived input functions were correlated with the blood curve obtained from manual samples (both expressed as MBq/mL).

## Kinetic modeling

A two-tissue compartment kinetic model of [ $^{99m}\text{Tc}$ ]MEB is used, based on the model presented by Ghibellini et al., (Ghibellini et al., 2008) to describe impaired hepatobiliary uptake and/or efflux caused by drugs or genetic disorders (Figure 6.3).

The differential equations of the model are shown below (Eq. 1-3).  $X_0$  represents the activity of the bolus injection of [ $^{99m}\text{Tc}$ ]MEB in MBq,  $V_c$  the volume of the central blood pool compartment in mL and  $C_c$  the activity concentration of [ $^{99m}\text{Tc}$ ]MEB (in MBq/mL) in the blood at a certain time point  $t$ . The activity level in the liver and gallbladder+intestines (in MBq), at a certain time point  $t$ , is represented by  $X_{liver}$  and  $X_{bile}$ , respectively.  $C_c^0$ ,  $X_{liver}^0$  and  $X_{bile}^0$  represent activity concentration and level directly after tracer injection (time point 0) for

the blood, liver and gallbladder+intestines, respectively. All rate constants were assumed to be first order:  $k_{12}$  represents hepatic basolateral uptake;  $k_{21}$  hepatic basolateral excretion and  $k_{20}$  hepatic canalicular efflux.

$$\frac{dC_c}{dt} = -k_{12} \times C_c + k_{21} \times \frac{X_{liver}}{V_c} \quad C_c^0 = \frac{X_0}{V_c} \text{ [Eq.1]}$$

$$\frac{dX_{liver}}{dt} = k_{12} \times V_c \times C_c - k_{20} \times X_{liver} - k_{21} \times X_{liver} \quad X_{liver}^0 = 0 \text{ [Eq.2]}$$

$$\frac{dX_{bile}}{dt} = k_{20} \times X_{liver} \quad X_{bile}^0 = 0 \text{ [Eq.3]}$$

The rate constants were obtained by solving the differential equations that were fit simultaneously to blood, liver and gallbladder+intestines TACs using nonlinear least-squares regression. Kinetic parameters of WT, rifampicin treated and Mrp2 KO mice are compared. Additionally, the model fit is investigated by fitting the measurements in blood pool and gallbladder+intestines to the calculated model curves. The model curves are calculated from the measurements in the liver.

Besides the kinetic rate constants, total clearance rates were calculated as described by Ghibellini et al. (Ghibellini et al., 2008).

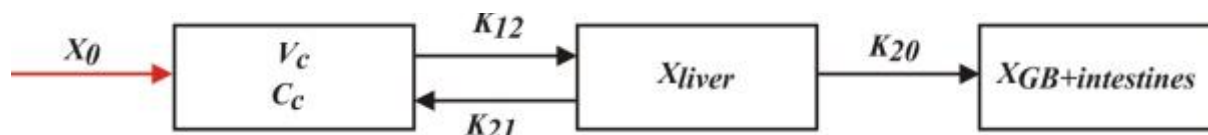


**Figure 6.3:** Scheme of the pharmacokinetic model describing the disposition and elimination of [<sup>99m</sup>Tc]MEB in mice.  $X_0$  represents the IV bolus of [<sup>99m</sup>Tc]MEB;  $C_c$  is the concentration of [<sup>99m</sup>Tc]MEB in the blood (MBq/mL) and  $V_c$  is the central compartment volume (mL). The activity levels in the liver and the gallbladder+intestines, expressed in MBq, is represented by  $X_{liver}$  and  $X_{bile}$ , respectively. All rate constants were assumed to be first order:  $k_{12}$  represents hepatic basolateral uptake;  $k_{21}$  represents hepatic basolateral excretion and  $k_{20}$  represents hepatic canalicular efflux.

## Statistical Analysis

Statistical analysis was performed using SPSS, version 22, for Windows (Microsoft). Differences between two groups were tested for significance using the nonparametric Mann–Whitney test for two groups. All experiments were performed at  $n=5$  (unless stated otherwise); a p-value of 0.05 or smaller was considered significant.

## Results

### Correlation of image derived blood function with manual blood samples

A comparison between the image derived input function and sampling blood curves (gold standard) showed acceptable agreement by graphical inspection (Figure 6.4). Additionally, AUC analysis showed similar AUCs ( $p > 0.05$ ). The AUC of WT mice was  $1355 \pm 158$  and  $1492 \pm 308$  MBq/mL x s for manual sampling and IDIF, respectively. The mean AUC of Mrp2 KO mice was  $1639 \pm 93$  and  $1478 \pm 258$  MBq/mL x s for manual sampling and IDIF, respectively. Lastly, the mean AUC of rifampicin treated mice was  $6340 \pm 535$  and  $6216 \pm 794$  MBq/mL x s for manual sampling and IDIF, respectively.

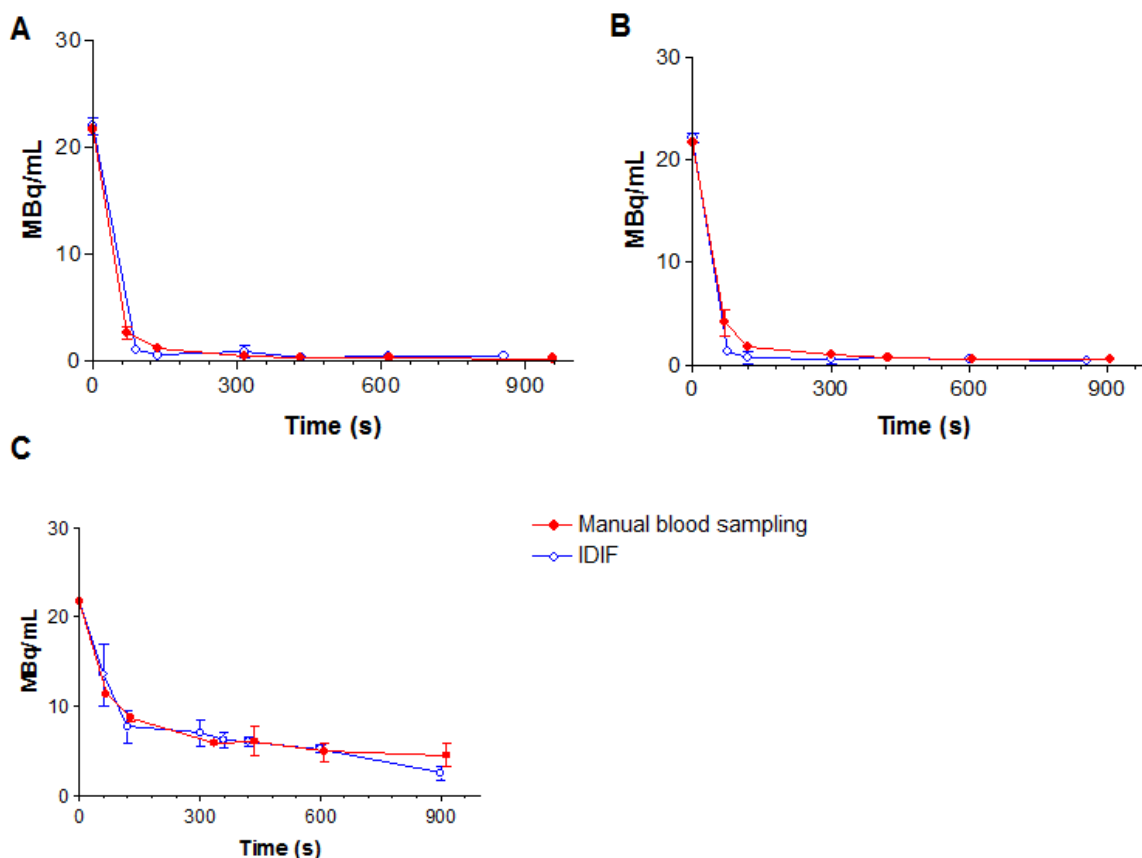


**Figure 6.4:** Visual inspection of the sampling blood curve (red, with standard deviations) and the image derived blood curve (blue, with standard deviations) clearly showed overlapping curves in WT (A;  $n=5$ ), rifampicin treated (B;  $n=5$ ) and Mrp2 knock-out (C;  $n=5$ ) mice.

## Kinetic Modeling

The model depicted in Figure 6.3 was suitable for describing [<sup>99m</sup>Tc]MEB disposition in all groups. The corresponding mean kinetic parameters,  $k_{12}$ ,  $k_{21}$  and  $k_{20}$  and standard deviations that were obtained per group are shown in Table 6.1.

$k_{12}$ , and  $k_{20}$  values were 3- and 9-fold smaller in rifampicin treated mice compared to vehicle controlled mice ( $p \leq 0.05$ ), respectively.  $k_{21}$  values were larger in rifampicin treated mice ( $p \leq 0.05$ ). In Mrp2 KO mice,  $k_{12}$  and  $k_{21}$  values were similar to those of WT mice. In contrast,  $k_{20}$  values were 8-fold lower compared to WT mice ( $p \leq 0.05$ ) (Table 6.1).

The goodness of fit of the model to three data sets is shown in Figure 6.5. Measurements are shown as symbols, the model is shown as solid lines. The cumulative amounts of [<sup>99m</sup>Tc]MEB in the liver are also depicted on the graph.

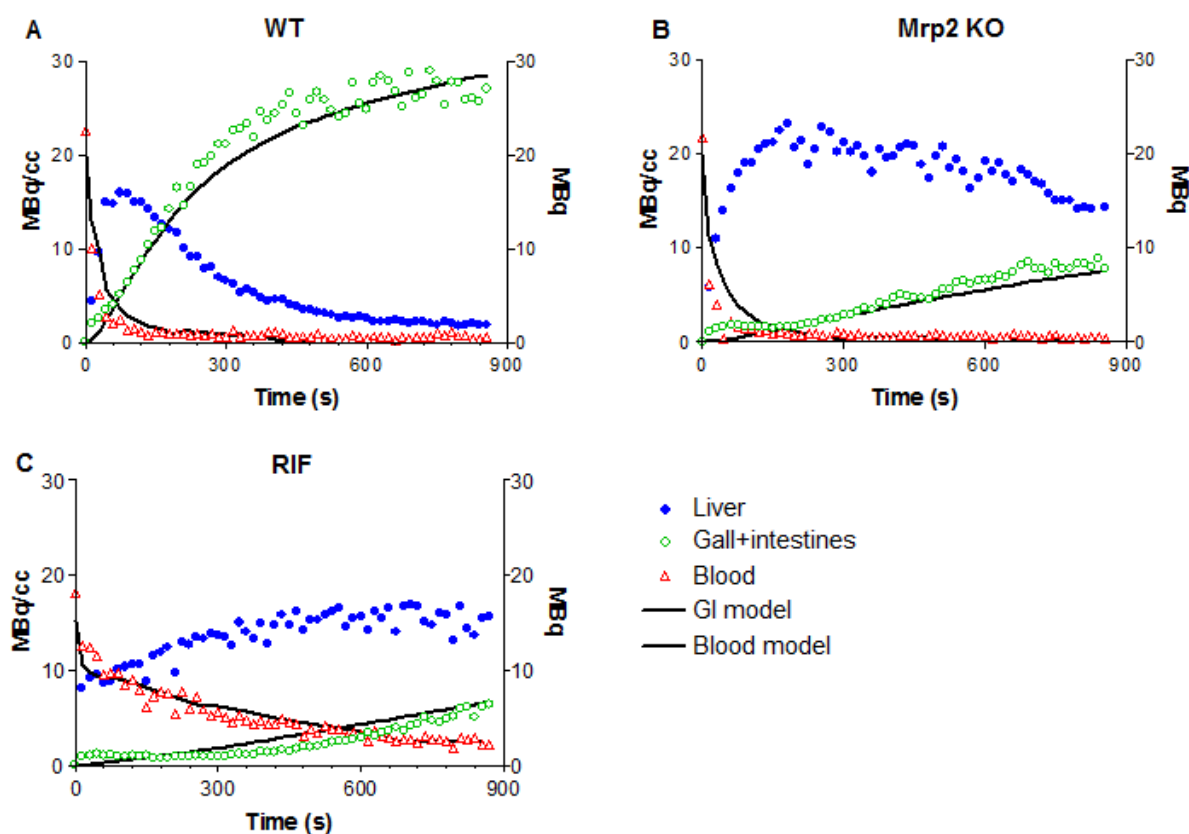


**Figure 6.5:** Goodness of fit. The kinetic model was fitted to the measured values in a WT (A), Mrp2 KO and rifampicin treated (C) mouse (n=1).

**Chapter 6: Kinetic modeling of [<sup>99m</sup>Tc]mebrofenin as a tool to quantify altered hepatobiliary transport**

**Table 6.1:** Mean kinetic parameters and standard deviations of WT, Mrp2 KO and rifampicin treated mice.\*:significantly different compared to WT ( $p \leq 0.05$ ) (n=5 per group).

	$k_{12}$ (1/min)	$k_{21}$ (1/min)	$k_{20}$ (1/min)	Total clearance (mL/min)
WT (n=5)	0.984±0.356	0.000±0.000	0.351±0.021	1.67±0.61
Mrp2 KO (n=5)	0.782±0.347	0.000±0.000	0.042±0.005*	1.32±0.55
RIF treated (n=5)	0.363±0.161*	0.119±0.086*	0.038±0.006*	0.17±0.039*



## Discussion

As stated in Chapter 5, numerous drugs can interact with hepatobiliary transport mechanisms and can lead to toxic concentrations of bile acids or substrate drugs in blood or liver (*Cuperus et al., 2014; Ho et al., 2005; Schuetz et al., 2014*). Therefore, it is important to detect these interactions from early on in drug research (*de Lima Toccafondo Vieira et al., 2014*). In Chapter 5, these interactions were visualized and quantified by means of metrics of the time activity curves. Impaired uptake was reflected in elevated blood concentrations, a lower maximal tracer uptake in the liver and decreased  $AUC_{\text{gallbladder+intestines}}$ . Impaired efflux was shown in a higher  $AUC_{\text{liver}}$  value and a decreased  $AUC_{\text{gallbladder+intestines}}$ . In addition to these metrics, the aim of the current study was to evaluate altered hepatobiliary transport by means of kinetic modeling of [<sup>99m</sup>Tc]MEB, based on the kinetic model of [<sup>99m</sup>Tc]MEB that was developed by Ghibellini et al. (*Ghibellini et al., 2008*).

A kinetic modeling approach requires bolus administration of a radiotracer immediately followed by dynamic recordings of the time activity curves of the radiotracer in tissues and blood pool. The gold standard to obtain dynamic recordings of the activity level in the blood pool is arterial blood sampling, however, this is very challenging in mice. Therefore, an image-derived method has been applied in the current study. [<sup>99m</sup>Tc]tetrafosmin was used as imaging agent to visualize the myocardium. After intravenous injection, [<sup>99m</sup>Tc]tetrafosmin is rapidly cleared from the blood and accumulates in the myocardium, skeletal muscle, spleen, liver and kidneys. Uptake in the myocardium is approximately 1% of the injected dose after 2 hours and is a consequence of passive diffusion of [<sup>99m</sup>Tc]tetrafosmin in the myocardial cells, followed by mitochondrial uptake and is proportional to the flow.

Application of this approach to the liver is very challenging, due to the dual input of the tracer from the portal vein and hepatic artery, compromising 75% and 25%, respectively (*Keiding et al., 2012; Winterdahl et al., 2011*). However, in the current study, our goal is not to obtain exact kinetic parameters of [<sup>99m</sup>Tc]MEB in mice, but to detect differences in kinetic parameters between wild type and rifampicin treated or Mrp2 KO mice. In this context, it is important to use the same input source in all subjects, i.e. blood pool in the heart, which is in line with the kinetic model of Ghibellini et al., where they performed blood sampling in the arm to obtain the input function (*Ghibellini et al., 2008*).

After generation of the TACs, physiological parameters can be calculated by fitting a mathematical model of tracer distribution and metabolism to the data. Previously, Ghibellini

et al. (Ghibellini et al., 2008) reported a pharmacokinetic model to simulate the effect of changes in hepatic uptake and/or secretion of [<sup>99m</sup>Tc]MEB associated with disease states in humans. In the current study, we used a simplified version of this model in mice by excluding the urine compartment, since no radioactivity was observed in the urinary bladder and kidneys in previous experiments. Additionally, an adjustment was done by evaluating the gallbladder and intestines as one compartment, in comparison with Ghibellini et al., who only used the gallbladder as second tissue compartment. The rationale behind this is outlined in Chapter 5. Disturbed hepatobiliary transport was investigated by means of pharmacological inhibition with rifampicin, a known Oatp and Mrp2 inhibitor and in Mrp2 KO mice, which lack the Mrp2 transporter.

In rifampicin treated mice, significantly decreased  $k_{12}$  and  $k_{20}$  values were observed, as expected, since rifampicin is an Oatp and Mrp2 inhibitor (Neyt et al., 2013). Additionally,  $k_{21}$  values were increased, which can be explained by a shortcoming of the proposed model. During the acquisition time used in this study, no urinary excretion was observed. However, due to inhibition of Oatp, urinary excretion will probably occur, but we were not able to detect this in the current study, due to the short acquisition time. Since we were not able to include the urinary bladder in the model, there is an overestimation of  $k_{21}$ .

Mrp2 KO mice show a similar uptake in comparison with WT mice, which is reflected in similar  $k_{12}$  and  $k_{21}$  values. In contrast, the efflux is as expected significantly decreased (lower  $k_{20}$  values).

In conclusion, kinetic parameters obtained using a two-tissue compartment model of [<sup>99m</sup>Tc]MEB can be used to quantify (altered) hepatobiliary transport, which can be suitable during drug development.

## References

- Chu X, Strauss JR, Mariano MA, Li J, Newton DJ, Cai X, et al. Characterization of mice lacking the multidrug resistance protein Mrp2 (Abcc2). *J Pharmacol Exp Ther* 2006;317:579-589.
- Cuperus FJC, Claudel T, Gautherot J, Halibasic E, Trauner M. The role of canalicular ABC transporters in cholestasis. *Drug Metab Dispos* 2014;42:546-560.
- De Lima Toccafondo Vieira M, Tagliati CA. Hepatobiliary transporters in drug-induced cholestasis: a perspective on the current identifying tools. *Expert Opin Drug Metab Toxicol* 2014;10:581-597.
- Diehl KH, Hull R, Morton D, Pfister R, Rabemampianina Y, Smith D, et al. A good practice guide to the administration of substances and removal of blood, including routes and volumes. *J Appl Toxicol* 2001;21:15-23.
- Ghibellini G, Leslie EM, Pollack GM, Brouwer KLR. Use of Tc-<sup>99m</sup> Mebrofenin as a Clinical Probe to Assess Altered Hepatobiliary Transport: Integration of *In vitro*, Pharmacokinetic Modeling, and Simulation Studies. *Pharm Res.* 2008;25:1851-60.
- Hendrikse NH, Kuipers F, Meijer C, Havinga R, Bijleveld CMA, van der Graaf WTA et al. In vivo imaging of hepatobiliary transport mediated by multidrug resistance associated protein and P-glycoprotein. *Cancer Chemother Pharmacol* 2004;54:131-138.
- Ho RH, Kim RB. Transporters and drug therapy: implications for drug disposition and disease. *Clin Pharmacol Ther* 2005;78:260-277.
- Keiding S. Bringing physiology into PET of the liver. *J Nucl Med* 2012;53:425-433.
- Kutner C. Kinetic modeling in pre-clinical PET. *Z Med Phys* 2014;24:274-285.
- Neyt S, Huisman MT, Vanhove C, De Man H, Vliegen M, Moerman L, et al. In vivo visualization and quantification of (disturbed) Oatp-mediated hepatic uptake and Mrp2-mediated biliary excretion of <sup>99m</sup>Tc-mebrofenin in mice. *J Nucl Med* 2013;54:624-630.
- Parasuraman S, Raveendran R, Kesavan R. Blood sample collection in small laboratory animals. *J Pharmacol Pharmacother* 2010;1:87-93.
- Schrenk D, Baus PR, Ermel N, Klein C, Vorderstemann B, Kauffmann HM. Up-regulation of transporters of the MRP family by drugs and toxins. *Toxicol Lett* 2001;120:51-57.
- Schuetz JD, Swaan PW, Tweedie DJ. The role of transporters in toxicity and disease. *Drug Metab Dispos* 2014;42:541-545.
- Winterdahl M, Keiding S, Sorensen M, Mortensen FV, Alstrup AKO, Munk OL. Tracer input for kinetic modelling of liver physiology determined without sampling portal venous blood in pigs. *Eur J Nucl Med Mol Imaging* 2011;38:263-270.

# Chapter 7.

## [<sup>99m</sup>Tc]mebrofenin transport in a humanized mouse model



## Introduction

One of the underlying causes of drug-induced liver cholestasis is an altered functional activity of hepatic uptake or efflux transporters. In chapter 5, we demonstrated that dynamic  $\mu$ SPECT imaging of [<sup>99m</sup>Tc]MEB is a useful method to discriminate quantitatively between the lack of functional activity of sinusoidal uptake and biliary efflux transporters. Therefore, this method can be used to investigate the interaction between new chemical entities and hepatobiliary transporters (Neyt *et al.*, 2013).

During drug development, the FDA requires *in vivo* toxicity studies conducted in at least two different animal species before human studies can be performed. In these preclinical toxicology studies, many hepatotoxicants remain undetected due to species differences, also known as the “preclinical species specificity issue”. There can be a difference in transporter expression, substrate affinity, physiological function, compensatory mechanisms and metabolic pathways, and this can lead to a difference in hepatotoxicant tolerance. Therefore, in the context of interpreting hepatotoxicity data from animal models, it is important to assess and understand the potential interspecies differences in mechanisms of drug toxicity. One of these mechanisms is hepatobiliary transport of drugs. Interspecies differences in transporter expression and substrate affinity can lead to interspecies differences in hepatic concentration of the drugs. For example, Wang *et al.* (Wang *et al.*, 2015) compared and quantified interspecies differences in expression of the hepatobiliary transporters in liver tissue and hepatocytes of beagle dogs, cynomolgus monkeys, Sprague-Dawley rats and Wistar rats. They found that there were notable interspecies differences in the relative abundance of hepatic transporters. Li *et al.* (Li *et al.*, 2008) also reported a 10-fold higher hepatic Mrp2 expression in rats compared to humans. Therefore, species differences should be considered carefully during the interpretation of preclinical data and in translating the preclinical findings to the clinic.

In Chapter 5 and 8, the effect on human transporters was tested by means of CHO- and HEK-cell lines that were transfected with the human transport proteins. However, there is a need for *in vivo* human-specific identification tools. Investigations of new drug candidates in human subjects is expensive, time-consuming and regulatory complex and therefore, there is a need for the development of preclinical methodologies and models that provide more predictive information about human drug metabolism or pharmacodynamic responses (de Lima Toccafondo Vieira and Tagliati, 2014; Xu *et al.*, 2014; Peltz *et al.*, 2013).

Consequently, chimeric mice models with a humanized liver were introduced to overcome this issue. In this chapter, we investigate human-type hepatobiliary transport of [<sup>99m</sup>Tc]mebrofenin ([<sup>99m</sup>Tc]MEB) *in vivo* in chimeric urokinase-type Plasminogen Activator SCID mice, since this model could offer a better understanding of interactions of drugs on [<sup>99m</sup>Tc]MEB transport via mainly human transporters *in vivo*.

The mice that were used in the current study were transplanted with human hepatocytes at the Center of Vaccinology at Ghent University. To allow successful repopulation of human primary hepatocytes into mice, rejection of the graft by the host's immune system must be avoided and an environment that promotes engraftment and expansion of liver cells must be created. (Meuleman *et al.*, 2005; Meuleman and Leroux-Roels, 2008) Therefore, urokinase-type plasminogen activator (uPA)-transgenic mice were created. The liver-specific (albumin-promoter) overexpression of the uPA-transgene causes a severe chronic liver disease, hereby creating an environment that favors hepatocyte engraftment. These mice were backcrossed with immunodeficient SCID mice, thereby avoiding rejection of the transplanted xenogeneic human hepatocytes (Yoshizato *et al.*, 2013). The success of human liver cell engraftment and expansion in the transplanted uPA<sup>+/+</sup> transgenic SCID mice can be evaluated by quantifying human albumin levels in mouse plasma (HuAlb, in mg/mL) at regular intervals. Several weeks after transplantation, a high proportion of diseased liver tissue, sometimes exceeding 90%, is replaced by human hepatocytes (Meuleman and Leroux-Roels, 2009).

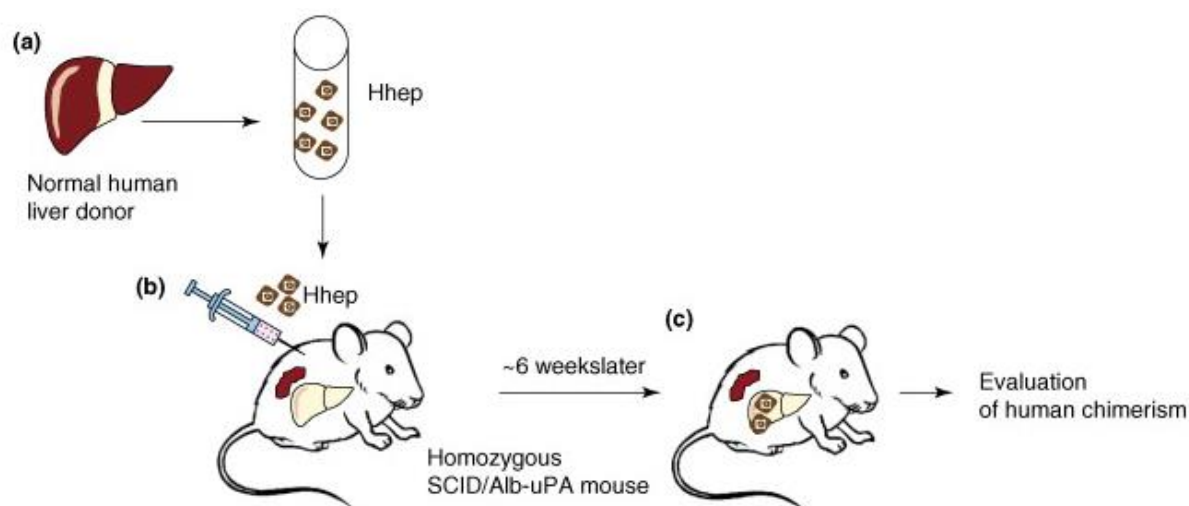


**Figure 7.1:** Generation of a humanized mouse model. (a) Human hepatocytes are obtained and isolated via the collagenase perfusion method. (b) intrasplenic transplant of the human hepatocytes in 10-14 day old mice (d) After transplantation, chimerism is evaluated by determination of human albumin in mouse serum samples (adapted from Moreno *et al.*, 2007).

In these humanized mice, normal [<sup>99m</sup>Tc]MEB transport was investigated to characterize the chimeric model. To study the effect of liver disease in itself, heterozygous mice of 5 and 8 weeks, which experience spontaneous somatic deletion of the transgene, thereby generating healthy mouse hepatocytes that can quickly repopulate the diseased liver, were used as controls.



## Materials and Methods

### Animal Model

Chimeric uPA<sup>+/+</sup> SCID (“humanized mice”, n= 11) and uPA<sup>+/-</sup> SCID (heterozygous) mice of 5 and 8 weeks (n=3 per group) were obtained from the Center of Vaccinology at Ghent University. The chimeric mice were produced as described previously (*Meuleman et al., 2005*). Briefly, uPA<sup>+/+</sup> SCID mice were transplanted with primary human hepatocytes within 2 weeks after birth. uPA<sup>+/-</sup> SCID mice were not transplanted and served as control animals. WT mice were obtained from Janvier (France). The mice were housed and handled according to guidelines approved by the European Ethics Committee and acclimatized for at least one week before the experiments. All the animals were kept under environmentally controlled conditions (12 h normal light/dark cycles, 20–22°C and 60% relative humidity) with food and water ad libitum. The study was approved by the Animal Experimental Ethical Committee of Ghent University (ECD13/01).

### Molecular Imaging

Dynamic  $\mu$ SPECT/CT acquisitions were acquired on a USPECT-II/CT device (MILabs, Utrecht, The Netherlands) equipped with a cylindrical collimator containing 75 pinholes of 1 mm diameter (rat whole-body collimator; spatial resolution, 0.8 mm). All acquisitions were acquired in list mode.

After an overnight fast (minimum 6 h), the mice were anesthetized with a mixture of isoflurane (1.5%) and medical O<sub>2</sub> to allow placement of an intravenous needle (30G) and polyethylene (PE10) tubing (Becton Dickinson, Belgium) in a lateral tail vein. The mice were placed in a prone position on the mouse scan bed. 200  $\mu$ L (37-74 MBq; 2 mg MEB) [<sup>99m</sup>Tc]MEB was injected via the intravenous PE10 tubing, directly after scan initiation.

Mice were imaged while anesthetized, with their body temperature maintained during imaging using a heated bed. The axial field of view required for the SPECT scan was chosen based on 3 planar X-ray images. Subsequently, a 15 min dynamic SPECT acquisition using 60 time frames of 15 s was initiated 5 s before the injection of [<sup>99m</sup>Tc]MEB. Lastly, a CT acquisition (5 min; tube current, 612  $\mu$ A; tube voltage, 50 kV) was performed for anatomical

correlation. The resultant CT scan is inherently co-registered with the corresponding  $\mu$ SPECT acquisition.

The dynamic SPECT scans were iteratively reconstructed using an ordered subsets expectation maximization algorithm (3 iterations; 16 subsets; 0.75 mm voxel size; decay correction), including only those photons from the acquired list-mode data with an energy range of  $140 \text{ keV} \pm 20 \%$ . After reconstruction, three regions of interest (ROIs) were manually drawn over the liver, the gallbladder+intestines and the urinary bladder using PMod software (PMod Technologies, Zürich, Switzerland) to obtain a time activity curve (TAC) for each ROI. The total activity in each organ, expressed in MBq (normalized to an injection of 37 MBq and a mouse weight of 20 g), was expressed as a function of time (in seconds).

## Statistical analysis

Statistical analysis was performed using Prism, version 3.00 (GraphPad, USA), and SPSS, version 22, for Windows (IBM, USA). The TACs were described by calculating the maximal activity in the liver and time-to-peak of the liver (i.e. the time point at which the maximal tracer amount or plateau was reached) as indicators of the uptake, and maximal activity in the gallbladder+intestines and area under the gallbladder and intestines curve ( $\text{AUC}_{\text{gallbladder+intestines}}$ ) as indicators of the efflux. AUCs were calculated using the trapezoidal method. The humanized mice were divided in 4 groups:

- 1) Human albumin level  $> 5 \text{ mg/mL}$ , weight  $\leq 11 \text{ g}$  (n=1)
- 2) Human albumin level  $> 5 \text{ mg/mL}$ , weight  $> 11 \text{ g}$  (n=2)
- 3) Human albumin level  $< 5 \text{ mg/mL}$ , weight  $\leq 11 \text{ g}$  (n=4)
- 4) Human albumin level  $< 5 \text{ mg/mL}$ , weight  $> 11 \text{ g}$  (n=4)

Differences between the groups were tested for significance using the nonparametric Mann-Whitney U or Kruskal-Wallis test. A p-value of 0.05 was considered as significant. Due to the small sample size in certain groups (n=2) in combination with the nonparametric test, a p-value between 0.05 and 0.1 was considered as marginally significant.

## Results

### [<sup>99m</sup>Tc]MEB disposition in mice with liver disease (heterozygous mice)

Figure 7.2 displays the time activity curves of [<sup>99m</sup>Tc]MEB of the liver (Figure 7.2, A) and gallbladder+intestines (Figure 7.2, B) in heterozygous mice (uPA<sup>+/-</sup> SCID) of 5 and 8 weeks, compared to that in WT mice. The corresponding metrics are shown in Table 7.1. A significant difference was found between the time-to-peak in the liver, maximal activity in the gallbladder and the AUC<sub>gallbladder+intestines</sub> between WT and heterozygous mice of 5 weeks (Mann Whitney U test,  $p \leq 0.05$ ), and between WT and heterozygous mice of 8 weeks (Mann Whitney U test,  $p \leq 0.05$ ). The boxplots are shown in Figure 7.3.

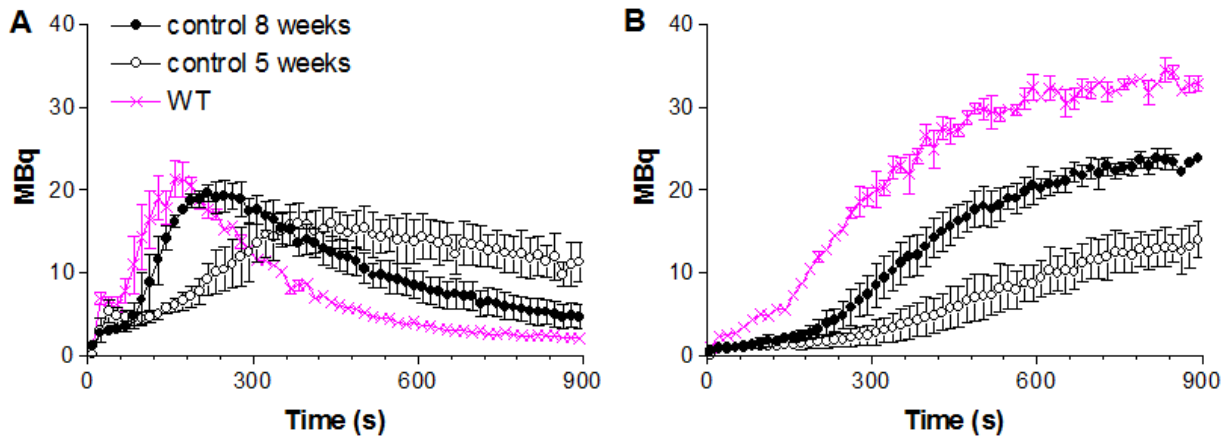


**Figure 7.2** Mean time activity curves + SD (n=3) of liver (A) and gallbladder + intestines (B) of wild type, 8-week-old heterozygous and 5-week-old heterozygous mice.

**Table 7.1:** Metrics of the TACs of heterozygous mice. Data are mean  $\pm$  SD (n=3).

	Maximal activity liver (MBq)	Time-to-peak liver (s)	Maximal activity gallbladder+intestines (MBq)	AUC <sub>gallbladder+intestines</sub> (MBq x s)
uPA <sup>+/-</sup> 8 weeks	20.19 $\pm$ 1.86	233 $\pm$ 15	24.74 $\pm$ 1.25	11957 $\pm$ 2053
uPA <sup>+/-</sup> 5 weeks	17.90 $\pm$ 4.22	413 $\pm$ 79	14.03 $\pm$ 3.95	5634 $\pm$ 2669
WT	21.88 $\pm$ 2.95	168 $\pm$ 17	35 $\pm$ 1.76	20100 $\pm$ 1028

In heterozygous mice of 5 weeks, the time-to-peak was 2.5 times later, the maximal activity in the gallbladder and intestines 2.5 times lower, and the AUC<sub>gallbladder+intestines</sub> 3.6 times smaller compared to WT mice (all p-values  $\leq 0.05$ ). In heterozygous mice of 8 weeks, the time to

peak was 1.4 times later, the maximal activity in the gallbladder and intestines 1.5 times lower, and the  $AUC_{\text{gallbladder+intestines}}$  1.7 times smaller compared to WT mice (all p-values  $\leq 0.05$ ).

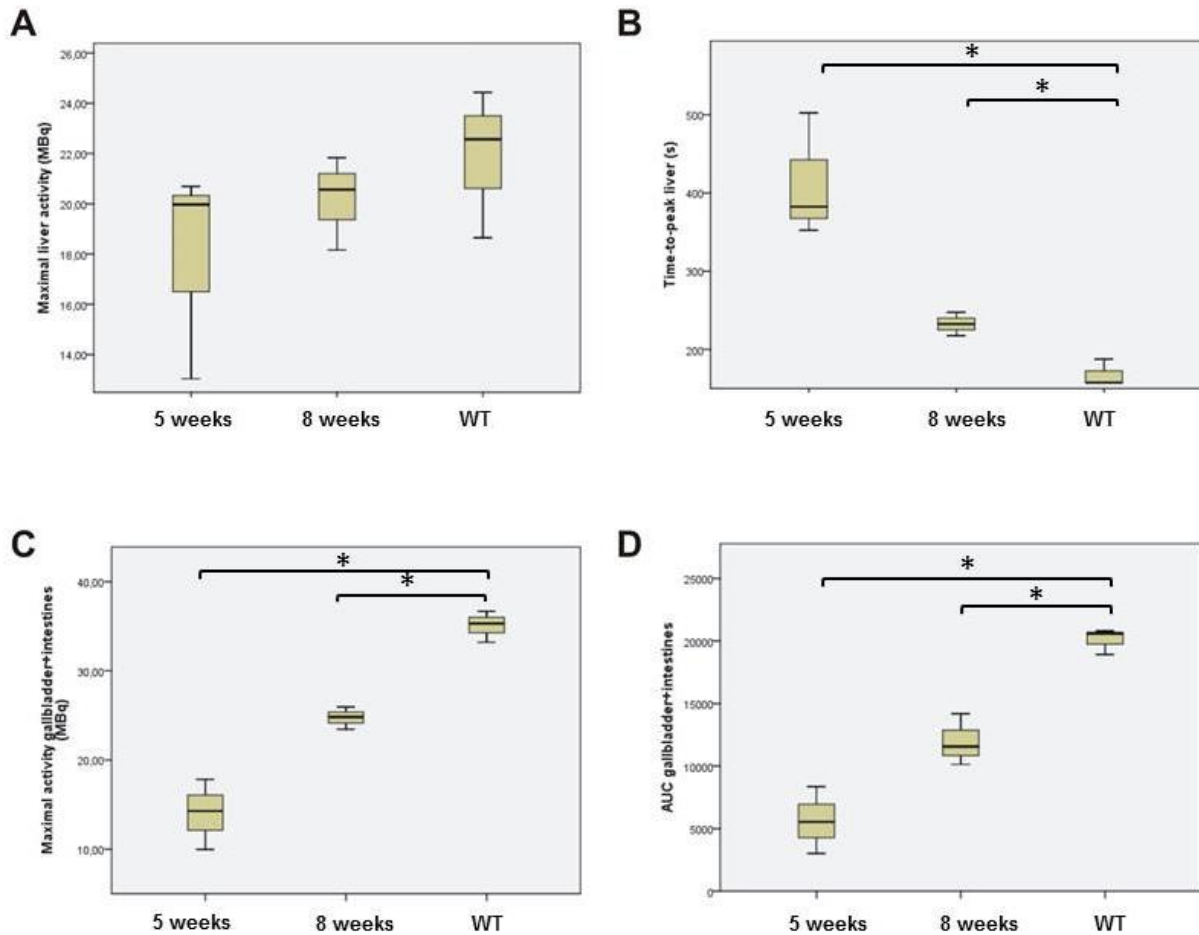


**Figure 7.3:** Boxplots of the maximal liver activity (A), time-to-peak in the liver (B), the maximal activity in gallbladder+intestines (C) and the AUC of gallbladder+intestines (D) in heterozygous mice (n=3 per group).

### [<sup>99m</sup>Tc]MEB disposition in chimeric (humanized) mice

Figure 7.4 displays the time activity curves of [<sup>99m</sup>Tc]MEB of the liver and gallbladder+intestines in chimeric “humanized” mice. The corresponding metrics are shown in Table 7.2. A significant difference was found in efflux metrics, namely the maximal activity in gallbladder+intestines, and the  $AUC_{\text{gallbladder+intestines}}$  (Kruskal-Wallis test;  $p \leq 0.05$ ). Boxplots are shown in Figure 7.5.

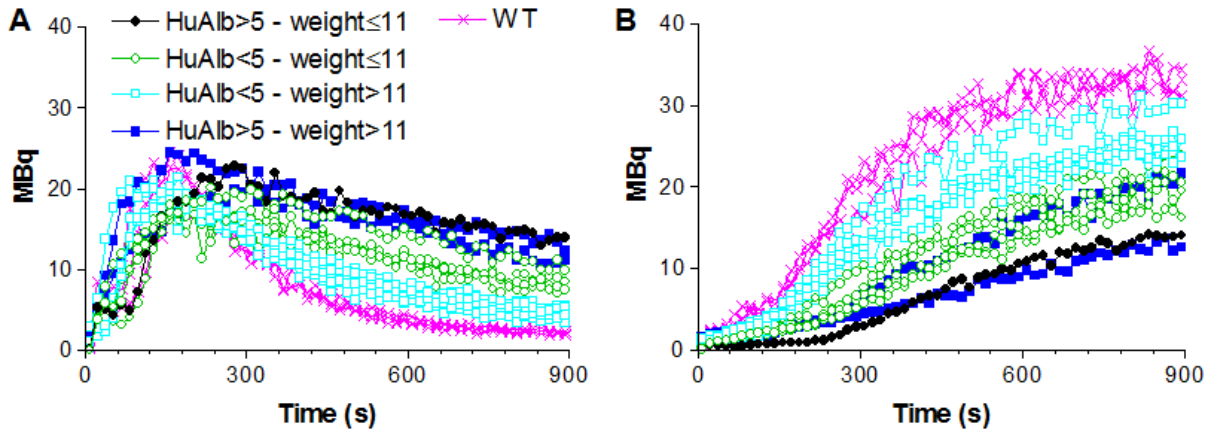


Figure 7.4: Time activity curves of liver (A) and gallbladder + intestines (B) of humanized mice.

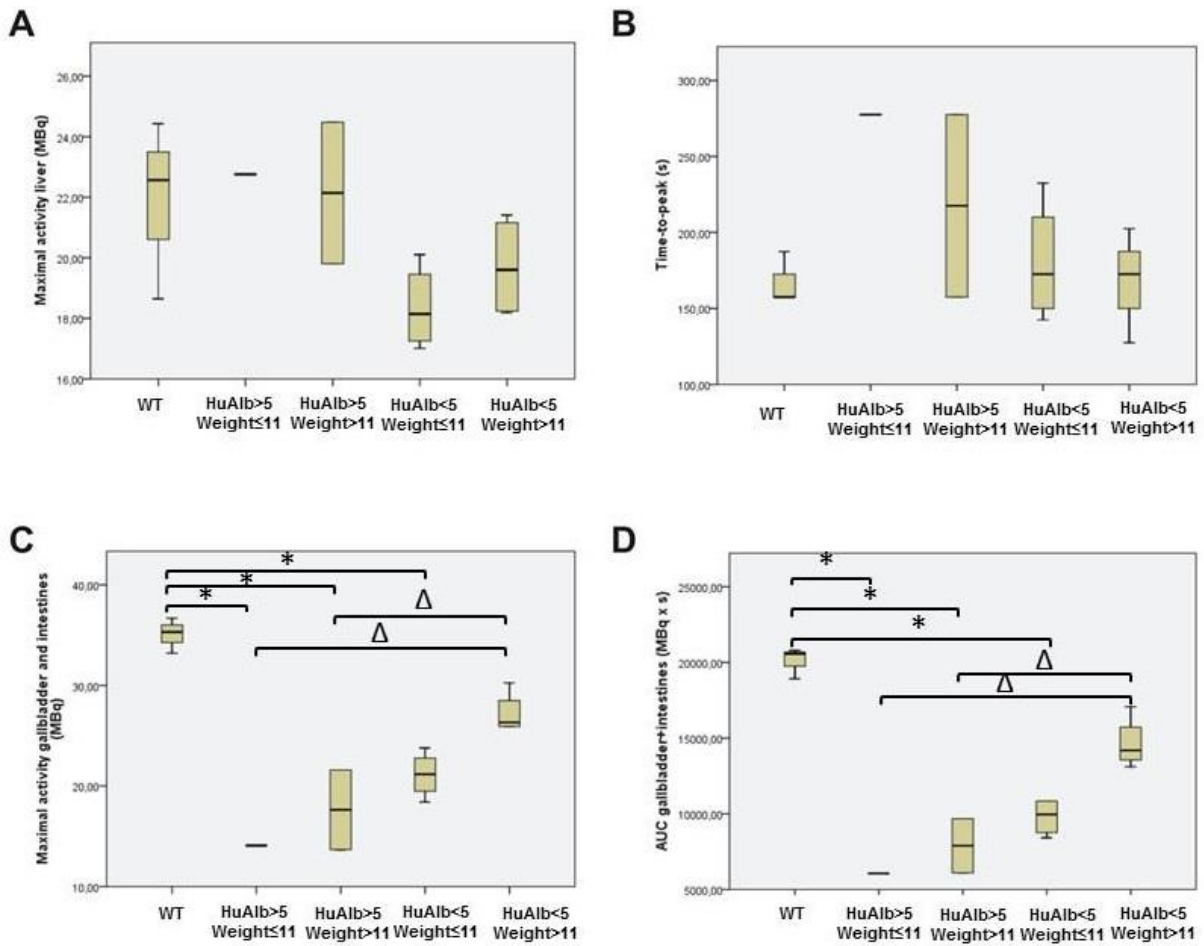


Figure 7.5: Boxplot of the maximal liver activity (A), time-to-peak in the liver (B), the maximal activity in gallbladder+intestines (C) and the AUC of the gallbladder+intestines (D) in humanized mice. Significant differences are indicated. \*:  $p \leq 0.05$ ;  $\Delta$ :  $0.05 < p < 0.1$ .

**Table 7.2:** Metrics of TACs of humanized mice.

	Maximal activity liver (MBq)	Time-to-peak liver (s)	Maximal activity gallbladder+intestines (MBq)	AUC <sub>gallbladder+intestines</sub> (MBq x s)
HuAlb>5 mg/mL, weight≤11g (n=1)	22.76*	278*	14.08*	6068*
HuAlb<5 mg/mL, weight≤11g (n=4)	18.36 ± 1.39	180 ± 40	21.13 ± 2.25	9799 ± 1234
HuAlb>5 mg/mL, weight>11g (n=2)	22.15 ± 3.30	218 ± 85	17.64 ± 5.59	7888 ± 2534
HuAlb<5 mg/mL, weight>11g (n=4)	19.70 ± 1.70	169 ± 31	27.20 ± 2.07	14642 ± 1704
WT (n=3)	21.88 ± 2.95	168 ± 17	35 ± 1.76	20100 ± 1028

After pairwise comparison of the significant different parameters (the efflux metrics: maximal activity in gallbladder+intestines, and AUC<sub>gallbladder+intestines</sub>), a significant lower maximal activity in gallbladder+intestines, and a significant lower AUC<sub>gallbladder+intestines</sub> was found for both parameters in 1) all the humanized mice (≤ 11g and > 11g) with human albumin levels larger than 5 mg/mL compared to WT mice and 2) mice with human albumin levels below 5 mg/mL and weight lower or equal than 11g, compared to WT mice (p≤0.05).

Additionally, a marginally significantly lower maximal activity in the gallbladder and intestines, and smaller AUC<sub>gallbladder+intestines</sub> (0.05<p<0.1) was found in mice with a weight larger than 11g and a high human albumin level, compared to mice with a weight larger than 11g and a low human albumin level. Lastly, a marginally significantly lower maximal uptake in liver and gallbladder+intestines, and smaller AUC<sub>gallbladder+intestines</sub> was found in mice with high human albumin level and low weight, compared to mice with a low human albumin level and high weight.

## Discussion

In the current study, the aim was to investigate human-type [<sup>99m</sup>Tc]MEB transport by means of SPECT imaging in mice with a humanized liver, expressing human OATPs and MRP2. Consequently, this model could offer a better understanding of interactions of drugs with human transporters, since species differences are avoided. Heterozygous mice were used as controls, to assess the effect of the liver disease in itself (Wang *et al.*, 2015; Yoshizato *et al.*, 2013; Peltz *et al.*, 2013; Xu *et al.*, 2015).

First, we demonstrated that the heterozygous mice have impaired liver function, which is reflected in decreased maximal uptake value in the liver, decreased AUC<sub>liver</sub> and decreased AUC<sub>gallbladder+intestines</sub>. Additionally, we demonstrated that the liver function improved in time. This can be explained by the fact that the heterozygous mice experience a spontaneous somatic deletion of the transgene, thereby generating healthy mouse hepatocytes that can quickly repopulate the diseased liver and that can restore liver function. Liver function can thus be followed in time by means of repeated SPECT imaging of [<sup>99m</sup>Tc]MEB.

Molecular SPECT imaging of the chimeric “humanized” mice demonstrated that the liver function, and more in particular liver efflux of [<sup>99m</sup>Tc]MEB, is dependent on the weight of the animal and the human albumin level in mouse plasma, since these mice exhibit different amounts of human and murine hepatocytes. uPA<sup>+/+</sup> SCID mice have high uPA activity, which leads to a lower weight. The lower the weight, the higher the uPA activity and the higher the effect of the liver disease in itself (cf. heterozygous mice) (Tateno *et al.*, 2015). Additionally, it has been demonstrated that mice with a high human serum albumin level have more functional human hepatocytes compared to mice with low human serum albumin levels. The repopulation indexed (RI%) is higher in mice with high human albumin levels (Tateno *et al.*, 2004; Okumura *et al.*, 2007; Tateno *et al.*, 2015). Normal hepatic uptake of [<sup>99m</sup>Tc]MEB was observed in all groups, and this was reflected in similar uptake metrics in all the “humanized” mice compared to WT mice. This indicates that there is a normal hepatic blood flow and functioning of the human hepatic uptake transporters, OATP1B1 and OATP1B3. However, efflux parameters are significantly decreased in “humanized” mice compared to WT mice. Additionally, marginally significant differences are found in the efflux parameters between several groups. This can be explained by differences in efflux between rodents and humans.

Arguments for this hypothesis can be found in the literature. In 2008, Li *et al.* (Li *et al.*, 2008) reported a fourfold higher elimination rate of Mrp substrates in rats compared to humans.

They used hepatocyte fluorescent dye efflux assays and demonstrated marked species differences on MRP/Mrp function between rat and human, with a higher elimination rate observed in rat hepatocytes. In 2009, Li et al. (Li et al., 2009) reported and even quantified the absolute species difference in Mrp2 expression. They found a 10-fold higher Mrp2 amount in the liver of rats compared to humans.

Wang et al. (Wang et al., 2015) also reported a lower MRP2 abundance in human hepatocytes compared to rat hepatocytes. They studied and quantified transporter abundances of hepatobiliary transporters in human, beagle dogs, cynomolgus monkeys, Sprague-Dawley rats and Wistar rats. They found interspecies differences in the transporter abundances. The findings of Li et al. and Wang et al. are in accordance with our findings: decreased efflux in mice with a humanized liver.

Ohtsuki et al. (Ohtsuki et al., 2014) determined the protein expression levels of transporters in the uPA/SCID “humanized” mouse model in order to validate the model. They found that protein expression levels in plasma membrane fractions of humanized mice were similar compared to protein expression levels in plasma membrane fraction of the corresponding human liver. However, they found a difference in expression level between several subjects and also found these differences in the corresponding transplanted mice. Consequently, differences between several humanized mice could be explained by inter-donor differences on the protein expression level. However, the humanized mice in the current study received hepatocytes from the same donor, so the inter-subject difference cannot be the cause of altered efflux.

Additionally, differences in Mrp2/MRP2 transporter affinities for numerous substrates were previously reported (Takekuma et al., 2007; Ishizuka et al., 1999; Ninomiya et al., 2005; Shilling et al., 2006). For example, Ishizuka et al. (Ishizuka et al., 1999) reported a 12.9-fold lower  $K_m$  value of 2,4-dinitrophenyl-S-glutathione into canalicular membrane vesicles of mice compared to humans, which is a measure for a higher affinity. Takekuma et al. (Takekuma et al., 2007) reported a 3.6-fold higher affinity for glucuronized mycophenolic acid of rat Mrp2 compared to humans.

The pronounced interspecies difference in the biliary excretion of Mrp2/MRP2 substrates can thus result from a combination of the protein expression level ( $V_{max}$ ) and the intrinsic transporter affinity ( $K_m$ ) for its substrates.



We can conclude that functional liver imaging in the current study revealed differences in liver functionality between WT and humanized uPA<sup>+/+</sup> SCID mice, and between the different groups of humanized mice. Consequently, the selection of mice for the mechanistic evaluation of new drug candidates or metabolism studies must be handled with care. Molecular SPECT imaging can thus be a useful screening method to carefully select a homogenous group of chimeric mice with similar liver function.

## References

- de Lima Toccafondo Vieira M, Tagliati CA. Hepatobiliary transporters in drug-induced cholestasis: a perspective on the current identifying tools. *Expert Opin Drug Metab Toxicol* 2014;10:581-597.
- Ghibellini G, Leslie EM, Pollack GM, Brouwer KLR. Use of Tc-99m mebrofenin as a clinical probe to assess altered hepatobiliary transport: integration of in vitro, pharmacokinetic modeling, and simulation studies. *Pharm Res*. 2008;25:1851–1860.
- Ishizuka H, Konno K, Shiina T, Naganuma H, Nishimura K, Ito K, et al. Species differences in the transport activity for organic anions across the bile canalicular membrane. *J Pharmacol Exp Ther* 1999;290:1324-1330.
- Li M, Yuan H, Li N, Song G, Zheng Y, Baratta M, Hua F, Thurston A, Wang J, Lai Y. Identification of interspecies difference in efflux transporters of hepatocytes from dog, rat, monkey and human. *Eur J Pharm Sci* 2008;35:114-126.
- Li N, Zhang Y, Hua F, Lai Y. Absolute difference of hepatobiliary transporter multidrug resistance-associated protein (MRP2/Mrp2) in liver tissues and isolated hepatocytes from rat, dog, monkey and human. *Drug Metab Dispos* 2009;37:66-73.
- Maddrey WC. Drug-induced hepatotoxicity. *J Clin Gastroenterol*. 2005;39:S83–S89.
- Meuleman P, Leroux-Roels G. HCV animal models: a journey of more than 30 years. *Viruses*. 2009;1:222-240.
- Meuleman P, Leroux-Roels G. The human liver-uPA-SCID mouse: A model for evaluation of antiviral compounds against HBV and HCV. *Antiviral research*. 2008;80:231-238.
- Meuleman P, Libbrecht L, De Vos R, de Hemptinne B, Gevaert K, Vandekerckhove J, Roskams T, Leroux-Roels G. Morphological and biochemical characterization of a human liver in a uPA-SCID mouse chimera. *Hepatology*. 2005;41:847-856.
- Moreno A, Pérignon JL, Morosan S, Mazier D, Benito A. Plasmodium falciparum-infected mice: more than a tour de force. *Trends Parasitol* 2007;23:254-259.
- Neyt S, Huisman MT, Vanhove C, De Man H, Vliegen M, Moerman L, Dumolyn C, Mannens G, De Vos F. In vivo visualization and quantification of (disturbed) Oatp-Mediated Hepatic Uptake and Mrp2-Mediated Biliary Excretion of <sup>99m</sup>Tc-mebrofenin in mice. *Journal of Nuclear Medicine*. 2013;54: 624-630.
- Ninomiya M, Ito K, Horie T. Functional analysis of dog multidrug resistance-associated protein 2 (MRP2) in comparison with rat Mrp2. *Drug Metab Dispos* 2005;33:225-232.
- Ohtsuki S, Kawakami H, Inoue T, Nakamura K, Tateno C, Katsukura Y, et al. Validation of uPA/SCID mouse with humanized liver as a human liver model: protein quantification of transporters, cytochromes P450, and UDP-glucuronosyltransferases by LC-MS/MS. *Drug Metab Dispos* 2014;42:1039-1043.

Okumura H, Katoh M, Sawada T, Nakajima M, Soeno Y, Yabuuchi H, et al. Humanization of excretory pathway in chimeric mice with humanized liver. *Toxicol Sci* 2007;97:533-538.

Padda MS, Sanchez M, Akhtar AJ, Boyer JL. Drug-induced cholestasis. *Hepatology*. 2011;53:1377–1387.

Peltz G. Can ‘humanized’ mice improve drug development in the 21<sup>st</sup> century? *Trends Pharmacol Sci* 2013;34:255-260.

Shilling AD, Azam , Leung L. Use of canalicular membrane vesicles (CMVs) from rats, dogs, monkeys and humans to assess drug transport across the canalicular membrane. *J Pharmacol Toxicol Methods* 2006;53:186-197.

Takekuma Y, Kakiuchi H, Yamazaki K, Miyauchi S, Kikukawa T, Kamo N, et al. Differences between pharmacokinetics of mycophenolic acid (MPA) in rats and that in humans is caused by different affinities of MRP2 to a glucuronized form. *J Pharm Pharm Sci* 2007;10:71-85.

Tateno C, Yoshizane Y, Saito N, Kataoka M, Utoh R, Yamasaki C, et al. Near completely humanized liver in mice shows human-type metabolic responses to drugs. *Am J Pathol* 2004;165:901-912.

Tateno C, Kawase Y, Tobita Y, Hamamura S, Ohshita H, Yokomichi H, et al. Generation of novel chimeric mice with humanized livers by using hemizygous cDNA-uPA/SCID mice. *Plos One* 2015;10:e0142145.

Wang L, Prasad B, Salphati L, Chu X, Gupta A, Hop CECA, et al. Interspecies variability in expression of hepatobiliary transporters across human, dog, monkey, and rat as determined by quantitative proteomics. *Drug Metab Dispos* 2015;43:367-374.

Xu D, Wu M, Nishimura S, Nishimura T, Michie SA, Zheng M, et al. Chimeric TK-NOG mice: a predictive model for cholestatic human liver toxicity. *J Pharmacol Exp Ther* 2015;352:274-280.

Yoshizato K, Tateno C. A mouse with humanized liver as an animal model for predicting drug effects and for studying viral infection: where to next? *Expert Opin. Metab. Toxicol.* 2013;9:1-17.

# Chapter 8.

## Synthesis, *in vitro* and *in vivo* evaluation of technetium labeled bile acid analogues

*Parts have been adapted from*

Neyt S<sup>1</sup>, Vliegen M<sup>2</sup>, Verreet B<sup>2</sup>, De Lombaerde S<sup>1</sup>, Braeckman K<sup>1,3</sup>, Vanhove C<sup>3</sup>, Huisman MT<sup>2</sup>, Dumolyn C<sup>1</sup>, Kersemans K<sup>1</sup>, Hulpia F<sup>4</sup>, Van Calenbergh S<sup>4</sup>, Mannens G<sup>2</sup>, De Vos F<sup>1</sup>. Nucl Med Biol 2016; 43:642-649.

<sup>1</sup>Laboratory of Radiopharmacy, Ottergemsesteenweg 460, Ghent University, Ghent, Belgium

<sup>2</sup>Preclinical Development & Safety, Janssen Pharmaceutical Companies of Johnson & Johnson, Beerse, Belgium

<sup>3</sup>iMinds Medical IT-IBITech-MEDISIP-INFINITY, Ghent University, Ghent, Belgium

<sup>4</sup>Laboratory for Medicinal Chemistry, Ottergemsesteenweg 460, Ghent University, Ghent, Belgium



## Introduction

As outlined in Chapter 1, bile acids play an essential role in the absorption of lipids, cholesterol and lipid-soluble vitamins in the intestinal lumen. The majority of the bile acids undergo efficient enterohepatic cycling, whereas only 5% of the bile acids enter the colon and are excreted from the body. Hepatobiliary transport proteins are essential for this enterohepatic cycling of bile acids. The most important bile acid transporters in the liver are OATPs, NTCP, BSEP and MRP2. A detailed discussion is given in Chapter 1.

Additionally, these hepatobiliary transport mechanisms are crucial for the overall excretion process of substrate toxic compounds, such as drugs, xenobiotics and toxins. This essential function makes the liver vulnerable to drug toxicity, since numerous drugs are substrates or inhibitors of hepatic transporters and hence, unexpected and unwanted interactions are frequently observed (*Maddrey, 2005; Shitara et al., 2005*). As stated in Chapter 1 and 5, it is important to assess the inhibition of hepatic transporters early in the development of new drug candidates. In Chapter 5, dynamic  $\mu$ SPECT scanning of [ $^{99m}\text{Tc}$ ]mebrofenin ([ $^{99m}\text{Tc}$ ]MEB) was proposed as non-invasive method to visualize and quantify normal and disturbed hepatobiliary transport in a non-invasive manner (*Neyt et al., 2013*). However, [ $^{99m}\text{Tc}$ ]MEB has no chemical similarities with endogenous bile acids. To assess non-invasively the effect of inhibition of hepatobiliary transporters on endogenous bile acids, there is a need for labeled bile acid analogues.

Previously, Gadolinium (Gd)(III), fluorescent,  $^{18}\text{F}$  and  $^{11}\text{C}$  labeled bile acid analogues were synthesized, as discussed in Chapter 2. Typically, these tracers have some shortcomings: Gd(III) labeled contrast agents do not allow dynamic imaging and larger amounts have to be administered. The fluorescently labeled bile acid analogues have a lower tissue depth, the radioactive tracers labeled with  $^{18}\text{F}$  and  $^{11}\text{C}$  are difficult to synthesize (e.g. need for cyclotron) and  $^{11}\text{C}$  tracers have a short half-life.

The aim of the current study is the (radio)synthesis of a technetium labeled chenodeoxycholic and cholic acid analogue: technetium labeled diethylene triamine pentaacetic acid chenodeoxycholic acid ([ $^{99m}\text{Tc}$ ]DTPA-CDCA) and technetium labeled diethylene triamine pentaacetic acid cholic acid, ([ $^{99m}\text{Tc}$ ]DTPA-CA), respectively. Technetium was used as radioisotope since it is easily produced (it can be eluted from a generator), its suitable half-life (6 hours) and its limitless depth of penetration. Additionally, *in vitro* assays have been performed to identify the involved uptake and efflux transporters. Lastly, *in vivo*  $\mu$ SPECT

**Chapter 8:** Synthesis, *in vitro* and *in vivo* evaluation of technetium labeled bile acid analogues

---

evaluation of normal and disturbed hepatobiliary transport have been performed to illustrate the ability of these agents to visualize and quantify (altered) hepatobiliary transport *in vivo*.

## Materials and methods

### General procedures and materials

Unless stated otherwise, all chemical reagents were obtained from commercial sources and used without further purification. Mebrofenin (N-(3-bromo-2,4,6-trimethylphenylcarbonylmethyl)-iminodiacetic acid) was obtained as a commercial kit from GE Healthcare (Bridatec®) in a preparation containing 40 mg of mebrofenin and 0.3 mg of tin(II)chloride-dihydrate. [<sup>99m</sup>Tc]TcO<sub>4</sub><sup>-</sup> was eluted from a sterile [<sup>99m</sup>Tc]-generator (Drytec; GE Healthcare). Exact mass measurements were performed on a Waters LCT Premier XETM Time of Flight (ToF) mass spectrometer equipped with a standard electrospray (ESI) and modular Lockspray TM interface. Samples were infused in a acetonitrile (MeCN) / water (1:1) + 0.1 % formic acid mixture at 100 μL/min. Where reversed phase flash purification was performed, Reveleris C18 RP 12g cartridges were used on a Reveleris X<sub>2</sub> device (Grace) with a flow rate of 20 mL/min and a water:acetonitrile gradient (from 10 to 95% acetonitrile in 20 minutes; with 0.1% formic acid added to the solvents). Radiochemical yield/purity was determined by means of RP-HPLC (Econosphere C18 10 μm, length 250 mm, ID 10.0 mm (Grace)) with radiodetection (Ludlum Measurements Inc., Model 2200). A 20 minutes gradient was used at a flow rate of 6 mL/min (from 10 to 95% acetonitrile in 20 minutes; 0.1% formic acid). Radioactivity in cell lysates was acquired on an automatic gamma counter (COBRA, Perkin Elmer).

### Animal models

FVB mice (female; age: 5 weeks; weight: 20–25 g) were purchased from Janvier, and were housed and handled according to guidelines approved by the European Ethics Committee and acclimatized for at least 1 week before the experiments. All animals were kept under environmentally controlled conditions (12-h normal light/dark cycles, 20°C–24°C, and 40–70% relative humidity) with food and water ad libitum. The study protocol was approved by the Animal Experimental Ethical Committee of Ghent University (ECD12/62).

### Chemistry

A summary of the (radio)synthesis is displayed in Figure 8.1.



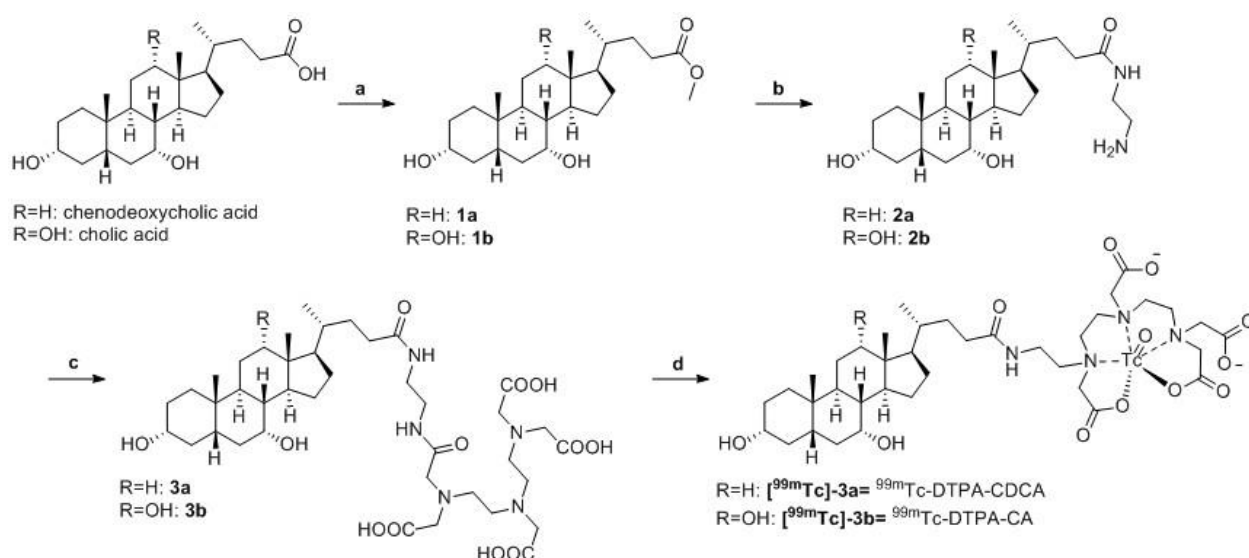


**Figure 8.1:** Overview of the (radio)synthesis of the technetium labeled chenodeoxycholic acid analogue, [<sup>99m</sup>Tc]DTPA-CDCA ([<sup>99m</sup>Tc]-3a) and cholic acid analogue, [<sup>99m</sup>Tc]DTPA-CA ([<sup>99m</sup>Tc]-3b). Reagents and conditions: (a) dimethoxypropane, methanol, hydrochloric acid, 91% (1a), 83% (1b); (b) ethylenediamine, methanol, 98% (2a), 98% (2b); (c) dimethylformamide, triethylamine, DTPA(bis)anhydride, 26% (3a) and 16% (3b); (d) stannous chloride, pertechnetate ([<sup>99m</sup>Tc]O<sub>4</sub><sup>-</sup>), radiochemical purity >95%.

*Synthesis of methyl (R)-4-((3R,5S,7R,8R,9S,10S,13R,14S,17R)-3,7-dihydroxy-10,13-dimethylhexadecahydro-1H-cyclopenta[a]phenanthren-17-yl)pentanoate (1a) and methyl (R)-4-((3R,5S,7R,8R,9S,10S,12S,13R,14S,17R)-3,7,12-trihydroxy-10,13-dimethylhexadecahydro-1H-cyclopenta[a]phenanthren-17-yl)pentanoate (1b)*

Chenodeoxycholic and cholic acid (1g, 2.55 and 2.45 mmol respectively) were dissolved in MeOH (5mL). 2,2-dimethoxypropane (2.5 mL) and 0.15 mL 12M hydrochloric acid were added. The resulting mixture was stirred at room temperature overnight and subsequently evaporated under reduced pressure (*Rohacova et al., 2009*). Next, the residue was dissolved in EtOAc, washed with saturated NaHCO<sub>3</sub>, brine, dried over MgSO<sub>4</sub>, filtered and evaporated under reduced pressure till dryness to obtain 1a and 1b (91% and 83% yield, respectively), which were used in the next step without further purification. MRMS (ESI) calculated for 1a [C<sub>25</sub>H<sub>42</sub>O<sub>4</sub>] [M+H]<sup>+</sup>: 407.3161, found: 407.3159; [2M+H]<sup>+</sup>: 813.6249, found: 813.6251. MRMS (ESI) for 1b [C<sub>25</sub>H<sub>42</sub>O<sub>5</sub>] [M+H]<sup>+</sup>: 423.3110, found: 423.3118; [2M+H]<sup>+</sup>: 845,6137, found: 845,6198.

*Synthesis of (R)-N-(2-aminoethyl)-4-((3R,5S,7R,8R,9S,10S,13R,14S,17R)-3,7-dihydroxy-10,13-dimethylhexadecahydro-1H-cyclopenta[a]phenanthren-17-yl)pentanamide (2a) and (R)-N-(2-aminoethyl)-4-((3R,5S,7R,8R,9S,10S,12S,13R,14S,17R)-3,7,12-trihydroxy-10,13-dimethylhexadecahydro-1H-cyclopenta[a]phenanthren-17-yl)pentanamide (2b)*

1a and 1b (300 mg, 0.738 mmols and 0.710 mmol respectively) were dissolved in 10 mL MeOH and an excess of ethylenediamine (0.45 mL, 6.711 mmol) was added (Pandey *et al.*, 2002). The reaction mixtures were stirred overnight at 50°C. The solvents were evaporated under reduced pressure and the crude products were purified by column chromatography (20% (NH<sub>3</sub> 7M in MeOH) in DCM (v/v)) to give 2a and 2b. Compounds containing fractions were pooled and evaporated under reduced pressure. The resulting residue was stirred in diisopropylether overnight, after which the materials were filtered and dried *in vacuo* to obtain 2a and 2b in 98% and 98% yield, respectively. MRMS (ESI) for 2a [C<sub>26</sub>H<sub>46</sub>N<sub>2</sub>O<sub>4</sub>] [M+H]<sup>+</sup>: 435.3581, found: 435.3585. MRMS (ESI) for 2b [C<sub>26</sub>H<sub>46</sub>N<sub>2</sub>O<sub>3</sub>] [M+H]<sup>+</sup>: 451.3531, found: 451.3488.

*Synthesis of (R)-3,6,9-tris(carboxymethyl)-19-((3R,5S,7R,8R,9S,10S,13R,14S,17R)-3,7-dihydroxy-10,13-dimethylhexadecahydro-1H-cyclopenta[a]phenanthren-17-yl)-11,16-dioxo-3,6,9,12,15-pentaazaicosanoic acid (3a) and (R)-3,6,9-tris(carboxymethyl)-11,16-dioxo-19-((3R,5S,7R,8R,9S,10S,12S,13R,14S,17R)-3,7,12-trihydroxy-10,13-dimethylhexadecahydro-1H-cyclopenta[a]phenanthren-17-yl)-3,6,9,12,15-pentaazaicosanoic acid (3b)*

2a and 2b (97 mg;0.450 mmol and 101 mg;0.450 mmol respectively) were coupled to DTPA-bis-anhydride (120 mg, 0.338 mmol) (Anelli *et al.*, 2004). Towards this end 5.5 µL (0.3 mmol) of water was added to a solution of DTPA-bis-anhydride and triethylamine (0.2 mL) in anhydrous DMF (10 mL). After 2 hours of stirring at room temperature, 2a or 2b was added and stirring continued for 72 hours. Then, the pH was adjusted to 7 with 6 M HCl. The solvent was evaporated under reduced pressure and the crude product was redissolved in 50:50 (v:v) MeCN:H<sub>2</sub>O. Subsequently, the products were purified by RP-flash chromatography (Reveleris X2; ELSD detection; column: Reveleris C18, 12g (Grace)) to give DTPA-CDCA (3a) and DTPA-CA (3b) in 26% and 16% yield, respectively. MRMS (ESI) for 3a [C<sub>40</sub>H<sub>67</sub>N<sub>5</sub>O<sub>12</sub>] [M+H]<sup>+</sup>: 810.4859, found: 810.4952. MRMS (ESI) for 3b [C<sub>40</sub>H<sub>67</sub>N<sub>5</sub>O<sub>13</sub>]

[M+H]<sup>+</sup>: 826.4808, found: 826.4789. The total yield was 23% and 13% yield for 3a and 3b, respectively.

### ***Radiosynthesis***

[<sup>99m</sup>Tc]-incorporation was done by a direct labeling method (*Sinha et al., 2009*) giving [<sup>99m</sup>Tc]DTPA-CDCA ([<sup>99m</sup>Tc]-3a) and [<sup>99m</sup>Tc]DTPA-CA ([<sup>99m</sup>Tc]-3b). To 2.25±0.25 mg of compound dissolved in 50 µL saline in a shielded lead vial, 60 µL of 10<sup>-2</sup> M SnCl<sub>2</sub>·2H<sub>2</sub>O solution (dissolved in N<sub>2</sub> purged 10% acetic acid) was added. Then, pH was adjusted to 6.5 with 0.2 M NaHCO<sub>3</sub>, followed by addition of freshly eluted saline solution of sodium pertechnetate (185 MBq, 50 µL). Subsequently, the pH was again adjusted to 6.5 with 0.2 M NaHCO<sub>3</sub>. The vial was allowed to incubate for 30 minutes at room temperature. Radiochemical purity was determined by means of RP-HPLC.

### ***In vitro* uptake assays**

Chinese hamster ovary (CHO) cells, CHO-OCT, Human Embryonic Kidney (HEK), HEK293-OATP1B3 cells were purchased from Solvo Biotechnologies (Hungary); CHO-NTCP and HEK293-OATP1B1 cells were a kind gift from the same company. CHO-NTCP, CHO-OCT1, HEK293-OATP1B1 and HEK293-OATP1B3 cells were stably transfected with genes encoding human NTCP (*SLC10A1*), OCT1 (*SLC22A1*), OATP1B1 (*SLCO1B1*), and OATP1B3 (*SLCO1B3*), respectively. The cell lines were cultured in a humidified atmosphere at 37°C in the presence of 5% CO<sub>2</sub>. The culture medium of the CHO cells consisted of Dulbecco's modified Eagle's medium (DMEM)/F12, supplemented with 10% fetal calf serum, 2 mM L-glutamine, 0.3 mM L-proline, and antibiotics (Penicillin/Streptomycin; 50 U/mL; 50 µg/mL). The culture medium of the HEK293 cells consisted of DMEM glutamax; high glucose; pyruvate supplemented with 10% fetal calf serum, 5 mL MEM-non essential amino acid solution, and antibiotics (Penicillin/Streptomycin; 50 U/mL; 50 µg/mL).

For transport experiments, all CHO and HEK cells were seeded in 24-well plates (4.0×10<sup>5</sup> cells/well; n=3/cell line) in 1 mL of the corresponding culture medium. After 18–24 h, medium was removed and cells were washed twice with washing buffer (1 mL sterile HBSS+/+ (HBSS with Ca<sup>2+</sup> and Mg<sup>2+</sup>), 10 mM HEPES, pH=7.4, 37°C). Incubation buffers (250 µL/well) were obtained by adding the radiolabeled compounds to the washing buffer.

Final concentrations of the positive controls were 1  $\mu\text{M}$  [ $^3\text{H}$ ]-estradiol-17 $\beta$ -glucuronide (E17 $\beta$ G, for OATP1B1), 1  $\mu\text{M}$  [ $^3\text{H}$ ]-taurocholic acid (TCA, for NTCP) and 1 $\mu\text{M}$  [ $^{14}\text{C}$ ]-tetraethyl-ammonium (TEA, for OCT1). Concentrations of the test compounds ([ $^{99\text{m}}\text{Tc}$ ]DTPA-CDCA and [ $^{99\text{m}}\text{Tc}$ ]DTPA-CA) were 1, 2, 5, 10, 20, 50, 100  $\mu\text{M}$  (for all cell lines). The plates were incubated at 4°C or 37°C and 5%  $\text{CO}_2$  for 5, 10, 20, 30, 60, 90, 120, 180 minutes. The incubation was stopped by placing the plates on ice and adding 1 ml of ice-cold HBSS+/+ with 1% BSA. Next, the cells were washed twice more with 2 mL HBSS+/+ and the supernatant was removed. The cells were lysed with 250  $\mu\text{L}$  mammalian protein extraction reagent and the plates were shaken for 10 minutes at 400 rpm at room temperature. A 150  $\mu\text{L}$  aliquot of this solution was used for gamma counting. Protein content was determined by means of a BCA kit (Thermo Scientific).

### ***In vitro* vesicular efflux assay**

HEK293-MRP2, HEK293-BSEP and HEK293-CTRL vesicles were purchased from PharmTox (The Netherlands). To determine the involved efflux transporters, ATP-binding cassette transporter vesicles transfected with human MRP2 or BSEP were used. Membrane vesicles (7.5  $\mu\text{g}$  of protein per well) were incubated at 37°C in a final volume of 30  $\mu\text{L}$ . The buffer used was Tris (10 mM)/sucrose (250 mM) with or without 4mM ATP,  $\text{MgCl}_2$  (10 mM) and [ $^{99\text{m}}\text{Tc}$ ]DTPA-CDCA or [ $^{99\text{m}}\text{Tc}$ ]DTPA-CA (20  $\mu\text{M}$ ) and incubated for 15, 30, 60 or 90 minutes. The reaction was stopped by addition of 150  $\mu\text{L}$  of ice-cold buffer and the well content was transferred to a glass fiber filter plate (Multiscreen HTS plates; Merck Millipore) and washed 3 times with buffer. Then, 100  $\mu\text{L}$  0.1 M NaOH was added and incubated at room temperature for 10 minutes to lyse the vesicles. An 80  $\mu\text{L}$  aliquot of this solution was used for gamma counting.

### **Molecular imaging**

Whole-body  $\mu\text{SPECT/CT}$  acquisitions were acquired on a USPECTII/CT device (MILabs) equipped with a cylindrical collimator containing 75 pinholes of 1 mm diameter (rat whole-body collimator; spatial resolution, 0.8 mm). All acquisitions were acquired in list mode.

After an overnight fast (minimum 6 hours), mice (n=6) were anesthetized with a mixture of 1.5% isoflurane and medical  $\text{O}_2$  to allow placement of intravenous needle (30G) and

polyethylene (PE10) tubing (Becton Dickinson) in a lateral tail vein. The mice were placed in a prone position on the mouse scan bed and were imaged while anesthetized, with their body temperature maintained during imaging using a heated bed. Subsequently, in untreated mice (n=3) a 120 minutes dynamic whole-body SPECT acquisition using 120 time frames of 1 minute was initiated 5 seconds before the injection of 200  $\mu\text{L}$  of [ $^{99\text{m}}\text{Tc}$ ]DTPA-CDCA or [ $^{99\text{m}}\text{Tc}$ ]DTPA-CA (37 MBq). Finally, a CT acquisition (5min; tube voltage, 50 kV; tube current, 612  $\mu\text{A}$ ) was performed for anatomical correlation. The resultant CT scan is inherently co-registered with the corresponding  $\mu\text{SPECT}$  acquisition. Additionally, an *in vivo* inhibition experiment was performed. Mice (n=3) were injected with rifampicin (100 mg/kg; IP) 60 minutes before tracer injection. Another dose of 25 mg/kg rifampicin was co-administered with the radiotracer (IV) and the same imaging protocol was performed.

All dynamic SPECT scans were iteratively reconstructed using an ordered subsets expectation maximization algorithm (3 iterations; 16 subsets; 0.75 mm voxel size; decay correction), including only those photons from the acquired list-mode data with an energy range of  $140 \text{ keV} \pm 20\%$ . After reconstruction, regions of interest (ROIs) were manually drawn over the heart, liver, gallbladder+intestines and urinary bladder using PMod software (PMod Technologies) to obtain a time activity curve (TAC) for each ROI. ROI volumes varied between 67 and 1578  $\text{mm}^3$ . Additionally, reconstructions of different phases (early phase: 0 - 10 minutes; late phase: 10 - 120 minutes) were performed to visualize the distribution of [ $^{99\text{m}}\text{Tc}$ ]MEB as function of time. Three-dimensional projection images of the co-registered CT and  $\mu\text{SPECT}$  images were performed using ImageJ software.

## Statistical analysis

Statistical analysis was performed using Prism, version 3.0 (GraphPad), and SPSS version 22, for Windows (Microsoft). For the *in vitro* uptake assays, uptake in function of time was determined. Additionally, Michaelis Menten constants and associated maximum transport rates were calculated by means of GraphPad Prism (nonlinear regression). The time–activity curves were described by calculating the maximal tracer amount in the liver and in the gallbladder and intestines, the time point at which tracer maximized (time to peak) in the liver, and the AUC in the blood, liver and gallbladder and intestines. AUCs were calculated using the trapezoidal method. Total, hepatic, biliary and urinary clearance rates were calculated.

$$\text{Total clearance} = \frac{\text{Dose}}{AUC_{\text{blood},0 \rightarrow \infty}}$$

$$\text{Hepatic clearance} = \frac{\text{Cumulative amount in liver}}{AUC_{\text{blood},0 \rightarrow 180}}$$

$$\text{Biliary clearance} = \frac{\text{Cumulative amount in GB + I}}{AUC_{\text{blood},0 \rightarrow 180}}$$

$$\text{Urinary clearance} = \frac{\text{Cumulative amount in urinary bladder}}{AUC_{\text{blood},0 \rightarrow 180}}$$

Differences between 2 groups were tested for significance using the nonparametric Mann–Whitney test for 2 groups. All experiments were performed on 3 wells per time point or concentration (unless stated otherwise); a p-value of 0.05 or smaller was considered significant.

## Results

### Radiosynthesis

Radiochemical purities were higher than 95% within 30 minutes. In its final formulation or dissolved in the appropriate buffer for the *in vitro* experiment, the tracers showed no alterations in radiochemical purity for up to 4h after the end of the synthesis.

### *In vitro* uptake assays

The transfected cell lines are fully functional, which is confirmed by the uptake of positive controls (cf. Figure 5.5, Chapter 5). The uptake of [<sup>3</sup>H]-TCA, [<sup>14</sup>C]-TEA and [<sup>3</sup>H]-E17-BG is respectively 255-, 11-, 256- and 50-fold higher in CHO-NTCP, CHO-OCT1, HEK293-OATP1B1 and HEK293-OATP1B3 compared to their parent/mock cell line.

Figure 8.2 shows the *in vitro* uptake of 20  $\mu$ M [<sup>99m</sup>Tc]DTPA-CDCA ([<sup>99m</sup>Tc]-3a) and [<sup>99m</sup>Tc]DTPA-CA ([<sup>99m</sup>Tc]-3b) after 60 minutes (Figure 8.2 A and C, respectively) and with or without rifampicin co-incubation (Figure 8.2 B and D, respectively). Without inhibitor, significantly higher uptake is observed for both tracers in HEK293-OATP1B1 and HEK293-OATP1B3 compared to their controls, HEK293-MOCK. After 60 minutes, the uptake of [<sup>99m</sup>Tc]DTPA-CDCA is  $534.2 \pm 6.0$  and  $316.8 \pm 8.1$  pmol/mg protein in OATP1B1 and OATP1B3 transfected cell lines, respectively. The uptake in the MOCK transfected cell lines was  $82.2 \pm 4.9$  pmol/mg protein. The uptake of [<sup>99m</sup>Tc]DTPA-CA was  $212 \pm 7.6$ ,  $110.9 \pm 2.1$  and  $50.8 \pm 1.7$  pmol/mg protein in OATP1B1, OATP1B3 and MOCK transfected cell lines, respectively. For both tracers, no significantly higher uptake was observed in NTCP and OCT1 transfected cell lines.

After co-incubation with 100  $\mu$ M rifampicin, a known OATP inhibitor, the uptake is significantly lower for both tracers in the OATP transfected cell lines. The uptake of [<sup>99m</sup>Tc]DTPA-CDCA after rifampicin administration amounts to  $100.2 \pm 13.9$  and  $87.9 \pm 13.4$  pmol/mg protein in OATP1B1 and OATP1B3 cell lines, respectively. The uptake of [<sup>99m</sup>Tc]DTPA-CA after rifampicin administration amounts to  $72.4 \pm 1.6$  and  $85.8 \pm 1.9$  pmol/mg protein in OATP1B1 and OATP1B3 cell lines, respectively.

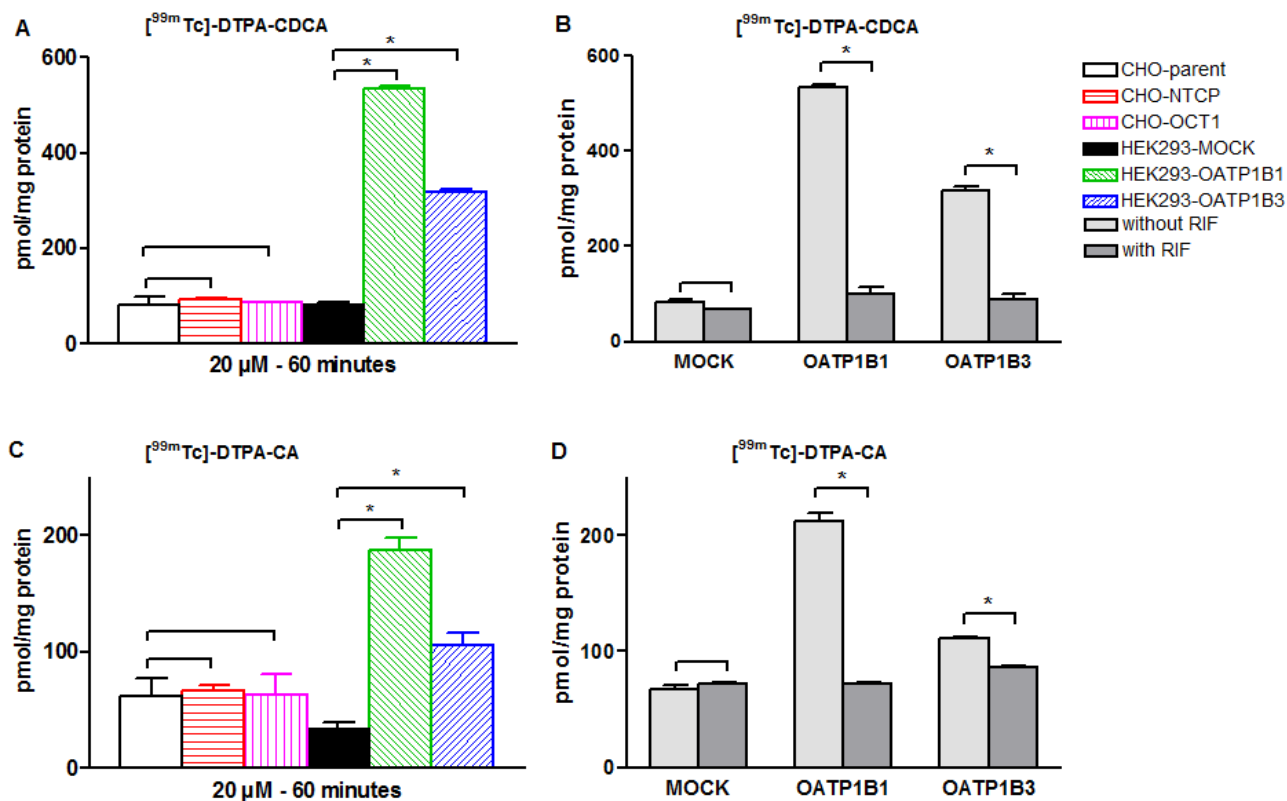


**Figure 8.2:** *In vitro* uptake of 20  $\mu\text{M}$   $[^{99m}\text{Tc}]$ DTPA-CDCA ( $[^{99m}\text{Tc}]$ -3a) (A) and  $[^{99m}\text{Tc}]$ DTPA-CA ( $[^{99m}\text{Tc}]$ -3b) (C) after 60 minutes. Uptake of 20  $\mu\text{M}$   $[^{99m}\text{Tc}]$ DTPA-CDCA ( $[^{99m}\text{Tc}]$ -3a) and  $[^{99m}\text{Tc}]$ DTPA-CA ( $[^{99m}\text{Tc}]$ -3b) after 60 minutes with or without co-incubation with 100  $\mu\text{M}$  rifampicin (B, D, respectively) (n=3). Data are mean  $\pm$  SD. \*= significant difference ( $p \leq 0.05$ ).

Figure 8.3 depicts uptake kinetics for  $[^{99m}\text{Tc}]$ DTPA-CDCA ( $[^{99m}\text{Tc}]$ -3a, Figure 8.3 A);  $[^{99m}\text{Tc}]$ DTPA-CA ( $[^{99m}\text{Tc}]$ -3a), Figure 8.3 B) and  $[^{99m}\text{Tc}]$ MEB (Figure 8.3 C). The uptake increased and saturated with increasing concentrations of substrate for all three tracers and for both cell lines (OATP1B1 and OATP1B3 transfected cell lines). The Michaelis-Menten constants ( $K_m$ ) with associated maximum transport rates ( $V_{max}$ ) were calculated (Table 8.1). Both tracers show a higher affinity compared to  $[^{99m}\text{Tc}]$ MEB. The lower  $K_m$  of  $[^{99m}\text{Tc}]$ DTPA-CDCA indicates a higher affinity for both OATP1B1 and OATP1B3 compared to  $[^{99m}\text{Tc}]$ DTPA-CA. The affinity for OATP1B1 is higher than the affinity for OATP1B3, for all the tracers.  $V_{max}$  values of  $[^{99m}\text{Tc}]$ DTPA-CDCA and  $[^{99m}\text{Tc}]$ DTPA-CA were lower compared to  $V_{max}$  value of  $[^{99m}\text{Tc}]$ MEB, indicating a lower transport capacity, which can also be concluded from the *in vitro* clearance values (Table 8.1).



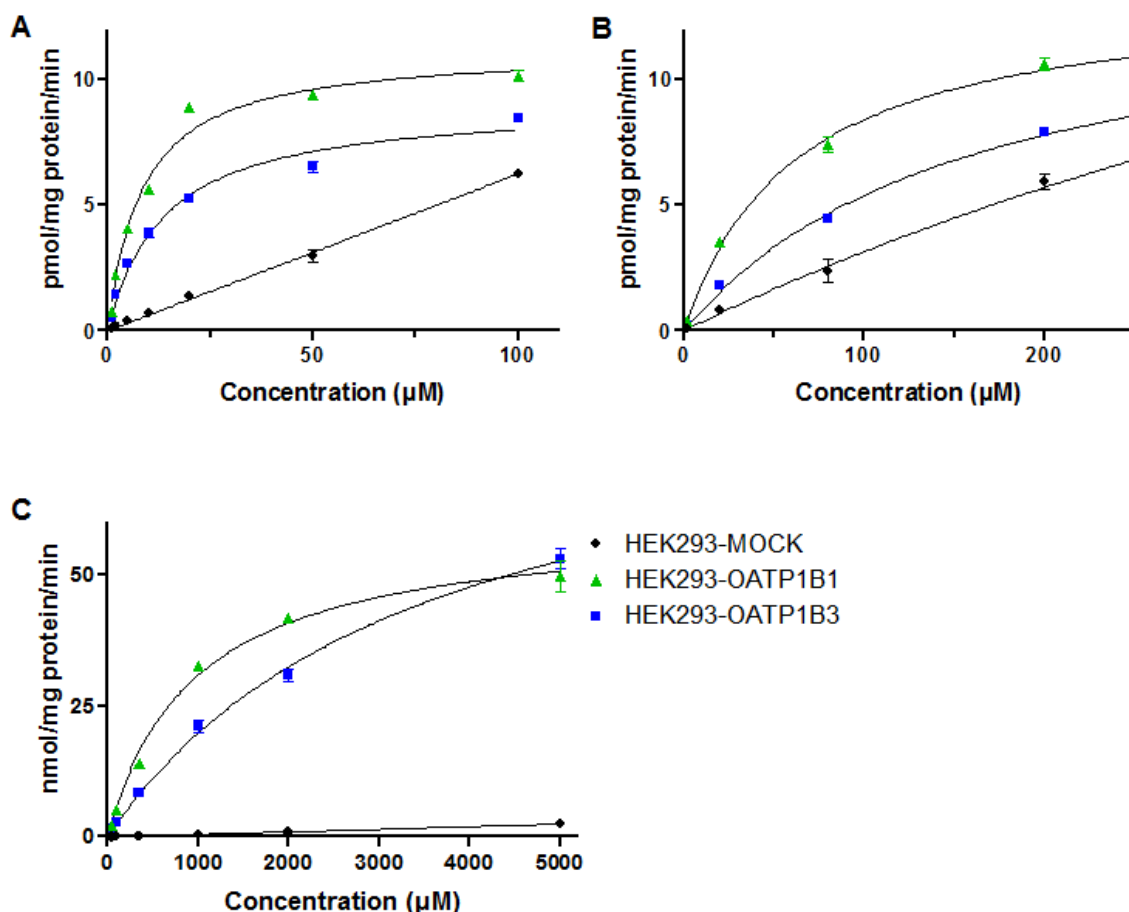


**Figure 8.3:** *In vitro* uptake of  $[^{99m}\text{Tc}]$ DTPA-CDCA ( $[^{99m}\text{Tc}]$ -3a, A),  $[^{99m}\text{Tc}]$ DTPA-CA ( $[^{99m}\text{Tc}]$ -3b, B) and  $[^{99m}\text{Tc}]$ MEB (C) (n=3). Data are mean  $\pm$  SD.

**Table 8.1:** Michaelis Menten constants and associated maximum transport rates of  $[^{99m}\text{Tc}]$ DTPA-CDCA ( $[^{99m}\text{Tc}]$ -3a) and  $[^{99m}\text{Tc}]$ DTPA-CA ( $[^{99m}\text{Tc}]$ -3b) and  $[^{99m}\text{Tc}]$ MEB. Data are mean  $\pm$  SD (n=3).

	Cell line	$K_m$ ( $\mu\text{M}$ )	$V_{max}$ (pmol/mg protein/min)	Clearance ( $V_{max}/K_m$ ; mL/mg/min)
$[^{99m}\text{Tc}]$ DTPA-CDCA	HEK293-OATP1B1	8.45 $\pm$ 0.75	11.3 $\pm$ 0.29	0.0013
	HEK293-OATP1B3	13.7 $\pm$ 1.24	9.10 $\pm$ 0.27	0.00066
$[^{99m}\text{Tc}]$ DTPA-CA	HEK293-OATP1B1	61.7 $\pm$ 5.25	13.6 $\pm$ 0.36	0.00022
	HEK293-OATP1B3	162 $\pm$ 16.9	14.1 $\pm$ 0.70	0.000087
$[^{99m}\text{Tc}]$ MEB	HEK293-OATP1B1	958 $\pm$ 78.8	(60.5 $\pm$ 1.70) $\times 10^3$	0.063
	HEK293-OATP1B3	3547 $\pm$ 294	(90.2 $\pm$ 3.97) $\times 10^3$	0.025

### *In vitro* vesicular efflux assay

To determine the involved efflux transporters, ATP-binding cassette transporter vesicles transfected with human MRP2 or BSEP were used. The ATP-dependent [<sup>99m</sup>Tc]DTPA-CDCA and [<sup>99m</sup>Tc]DTPA-CA uptake was determined in canalicular inside-out membrane vesicles by a rapid filtration method. A time dependent uptake of the tracers was observed in presence of ATP in MRP2 vesicles (Figure 8.4). We observed a significantly higher uptake in MRP2 vesicles in ATP+ conditions compared to ATP- conditions after 15, 30, 60 and 90 minutes for [<sup>99m</sup>Tc]DTPA-CDCA; and after 30, 60 and 90 minutes for [<sup>99m</sup>Tc]DTPA-CA ( $p \leq 0.05$ ). There was no difference in uptake in ATP+ and ATP- conditions for control and BSEP vesicles at all time points.

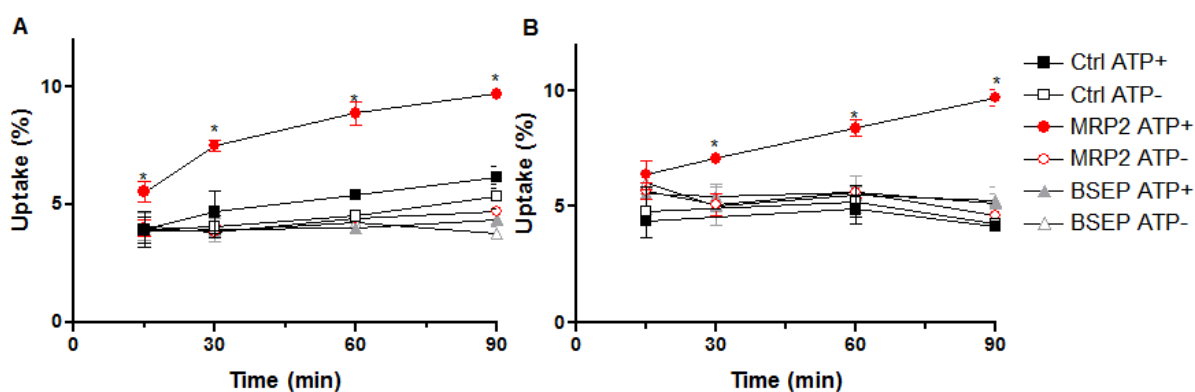


**Figure 8.4:** *In vitro* vesicular efflux assay. Uptake of 20  $\mu$ M [<sup>99m</sup>Tc]DTPA-CDCA ([<sup>99m</sup>Tc]-3a, A) and [<sup>99m</sup>Tc]DTPA-CA ([<sup>99m</sup>Tc]-3b, B) after 15, 30, 60 and 90 minutes. Data are mean  $\pm$  SD (n=3). \*= significant difference ( $p \leq 0.05$ ).

### Molecular imaging

*In vivo*  $\mu$ SPECT imaging of mice revealed uptake of both radiotracers in liver, gallbladder, intestines and urinary bladder. Figure 8.5 shows 3D projection images of co-registered CT and  $\mu$ SPECT images of [<sup>99m</sup>Tc]DTPA-CDCA (Figure 8.5 A, B) and [<sup>99m</sup>Tc]DTPA-CA (Figure 8.5 C, D) during the first 10 minutes (early phase, Figure 8.5 A and C) and during the last 110 minutes (late phase, Figure 8.5 B and D). In the early phase, [<sup>99m</sup>Tc]DTPA-CDCA is taken up in the liver, gallbladder and urinary bladder. [<sup>99m</sup>Tc]DTPA-CA is taken up in liver and urinary bladder. In the late phase, the mean distribution of the tracers show mainly uptake in the intestines and urinary bladder.

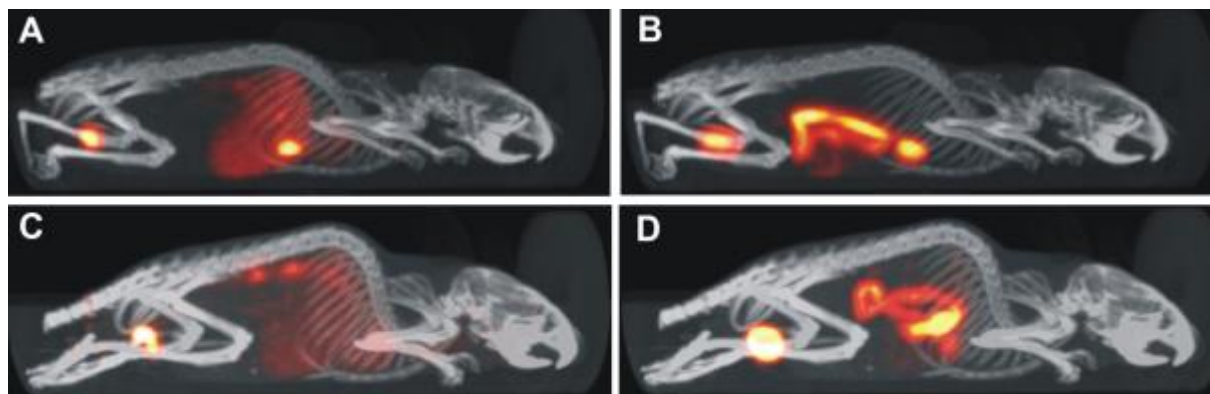


**Figure 8.5:** Projection images of co-registered CT and  $\mu$ SPECT images of 37 MBq of  $[^{99m}\text{Tc}]$ DTPA-CDCA ( $[^{99m}\text{Tc}]$ -3a) (A, B) and  $[^{99m}\text{Tc}]$ DTPA-CA ( $[^{99m}\text{Tc}]$ -3b) (C, D) in a WT mouse during the first 10 minutes (A, C) and during the last 110 minutes (B, D) of the dynamic  $\mu$ SPECT acquisition (120 frames, 1 minute/frame).

Time activity curves of  $[^{99m}\text{Tc}]$ DTPA-CDCA and  $[^{99m}\text{Tc}]$ DTPA-CA in WT and rifampicin treated mice are shown in Figure 8.7 and the corresponding metrics are shown in Table 8.2.

$[^{99m}\text{Tc}]$ DTPA-CDCA (Figure 8.7 A) and  $[^{99m}\text{Tc}]$ DTPA-CA (Figure 8.7 C) show a maximal liver uptake of respectively  $13.83 \pm 0.58$  MBq and  $9.50 \pm 1.45$  MBq after  $12.67 \pm 1.53$  and  $12.00 \pm 1.00$  minutes, followed by a decrease to baseline levels, indicating secretion.

A secretion maximum to gallbladder and intestine of  $23.00 \pm 2.00$  MBq and  $17.67 \pm 2.61$  MBq for  $[^{99m}\text{Tc}]$ DTPA-CDCA and  $[^{99m}\text{Tc}]$ DTPA-CA, respectively, indicates secretion of the radiotracer to gallbladder and intestines. Additionally, in the urinary bladder, an accumulation of activity was observed with a maximal uptake of respectively  $5.10 \pm 0.71$  and  $13.00 \pm 1.98$  MBq (Figure 8.7 A and B, Table 8.2). After 4 hours, the remaining radioactivity was located in the intestines and no activity was observed in the urinary bladder, since the urinary bladder was emptied.

Next, we investigated the effect of rifampicin administration on  $[^{99m}\text{Tc}]$ DTPA-CDCA and  $[^{99m}\text{Tc}]$ DTPA-CA transport. Rifampicin is both a substrate and an inhibitor of OATPs and MRP2, and therefore, it was selected as test agent. Figure 8.6 shows 3D projection images of co-registered CT and  $\mu$ SPECT images of  $[^{99m}\text{Tc}]$ DTPA-CDCA (Figure 8.6 A, B) and  $[^{99m}\text{Tc}]$ DTPA-CA (Figure 8.6 C and D) after rifampicin administration during the first 10 minutes (early phase, Figure 8.6 A and C) and during the last 110 minutes (late phase, Figure 8.6 B and D). In the early phase, less liver uptake of  $[^{99m}\text{Tc}]$ DTPA-CDCA and  $[^{99m}\text{Tc}]$ DTPA-CA is observed; mainly the blood pool and heart are visible. Additionally, the urinary bladder is visible. In the late phase, the mean distribution of the tracers shows mainly uptake in the urinary bladder, in contrast to the WT mouse (Figure 8.5).

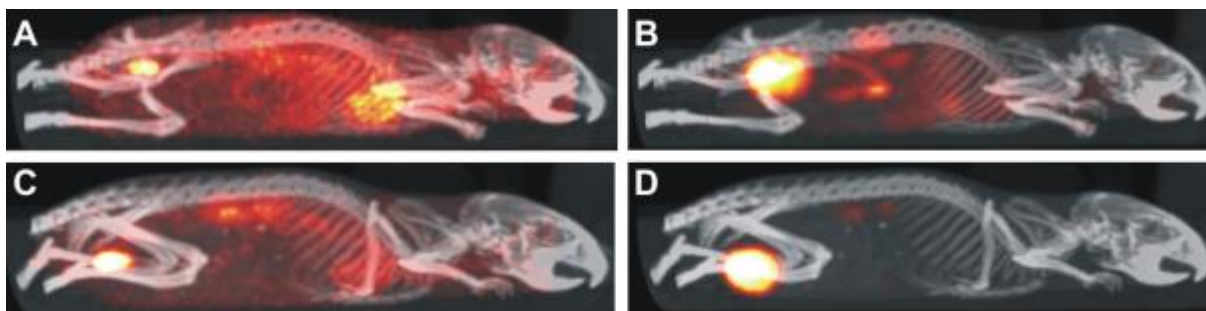


**Figure 8.6:** Projection images of co-registered CT and  $\mu$ SPECT images of 37 MBq of  $[^{99m}\text{Tc}]$ DTPA-CDCA ( $[^{99m}\text{Tc}]$ -3a) (A, B) and  $[^{99m}\text{Tc}]$ DTPA-CA ( $[^{99m}\text{Tc}]$ -3b) (C, D) in a rifampicin treated WT mouse during the first 10 minutes (A, C) and during the last 110 minutes (B, D) of the dynamic  $\mu$ SPECT acquisition (120 frames, 1 minute/frame).

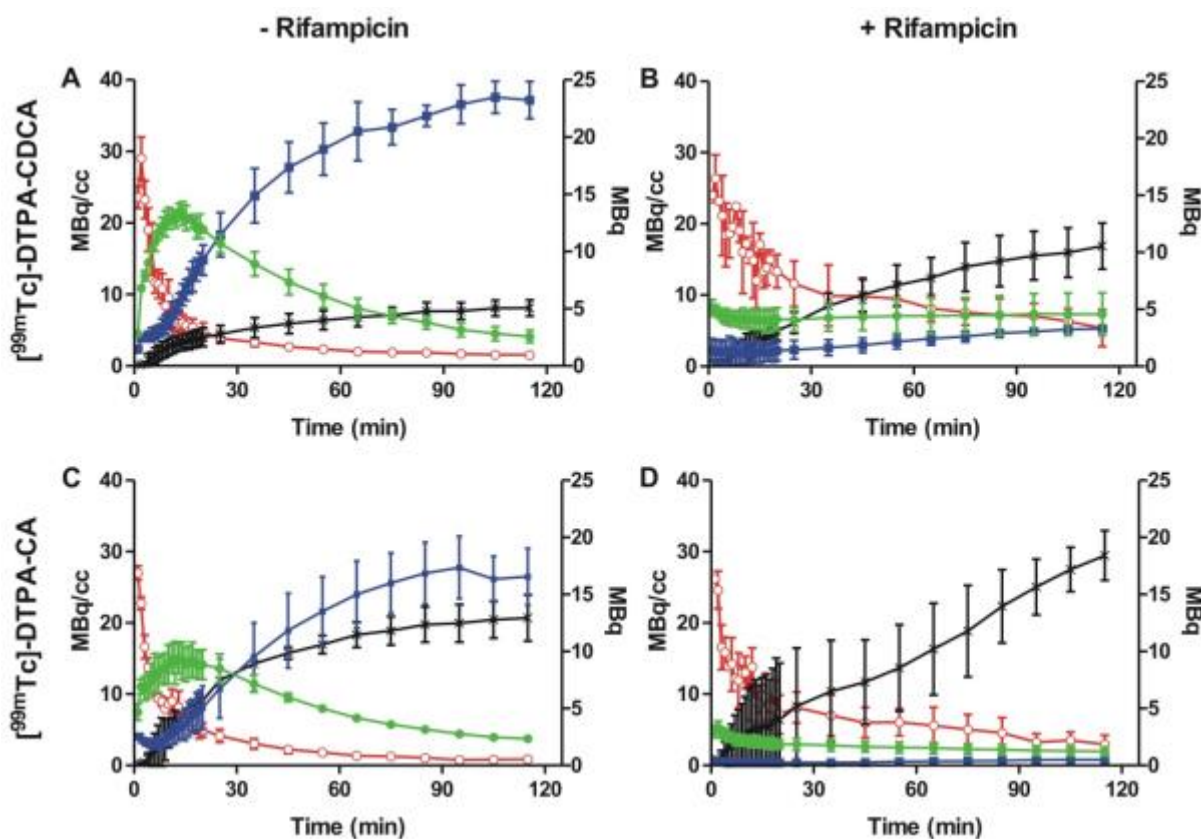


**Figure 8.7:** Time activity curves (TACs) of  $[^{99m}\text{Tc}]$ DTPA-CDCA ( $[^{99m}\text{Tc}]$ -3a) (A, B) and  $[^{99m}\text{Tc}]$ DTPA-CA ( $[^{99m}\text{Tc}]$ -3b) (C, D) in WT ( $n=3$ ) (A, C) and RIF treated ( $n=3$ ; 100 mg/kg IP, 60 minutes before imaging; 25 mg/kg IV, co-injected with tracer) (B, D) mice after intravenous injection of 37 MBq radiotracer and dynamic  $\mu$ SPECT imaging (120 frames; 1 minute/frame). TAC<sub>heart</sub> (blood) is expressed as MBq/mL (left y-axis); all other TACs are expressed as MBq (right y-axis). Data are mean $\pm$ SD. Green= liver, blue= gallbladder+intestines, black= urinary bladder, red= blood.

The time-activity curves of the rifampicin treated mice (100 mg/kg intraperitoneally, 25 mg/kg intravenously) are shown in Figure 8.7 B D. Corresponding metrics are shown in Table

8.2. Compared to control mice, the maximum liver uptake was 2.6- and 2.8-fold lower in rifampicin treated mice compared to control mice ( $p \leq 0.05$ ) for [ $^{99m}\text{Tc}$ ]DTPA-CDCA and [ $^{99m}\text{Tc}$ ]DTPA-CA, respectively. Additionally, the liver AUC was 1.5- and 3.1-fold lower in rifampicin treated mice for [ $^{99m}\text{Tc}$ ]DTPA-CDCA and [ $^{99m}\text{Tc}$ ]DTPA-CA, respectively. In rifampicin treated mice the AUC and the maximal tracer activity in the gallbladder and intestine for [ $^{99m}\text{Tc}$ ]DTPA-CDCA was 7.6 times lower compared to control animals. For [ $^{99m}\text{Tc}$ ]DTPA-CA, the maximal tracer activity in the gallbladder and intestine was 36 times lower and gallbladder/intestine AUC was 32 times lower, when rifampicin treated mice are compared to control animals. The mean blood AUC in RIF treated mice was 2.6-fold and 2.1-fold larger than in their control counterparts. There was no significant difference between urinary bladder  $C_{\text{max}}$  and AUC.

When clearance values are compared (Table 8.2), a significant lower total, hepatic and biliary clearance can be observed ( $p \leq 0.05$ ).

**Table 8.2:** Metrics of the time activity curves of the heart (blood pool), liver, gallbladder/intestines and urinary bladder after injection of 37 MBq of tracer. \*: 100 mg/kg intraperitoneal 60 minutes before tracer injection; 25 mg/kg intravenous, coinjected with tracer. (n=3 per group) Data are mean $\pm$ SD.

	[ $^{99m}\text{Tc}$ ]DTPA- CDCA	[ $^{99m}\text{Tc}$ ]DTPA- CDCA + RIF*	[ $^{99m}\text{Tc}$ ]DTPA-CA	[ $^{99m}\text{Tc}$ ]DTPA-CA + RIF*
<b>Maximum liver uptake (MBq)</b>	13.8 $\pm$ 0.58	5.2 $\pm$ 0.40	9.5 $\pm$ 1.45	3.37 $\pm$ 0.49
<b>Liver Time to peak (min)</b>	12.7 $\pm$ 1.53	N/A	12.0 $\pm$ 1.00	N/A
<b>Liver AUC (MBq x min)</b>	755 $\pm$ 81.1	499 $\pm$ 157	582 $\pm$ 21.5	185 $\pm$ 52.0
<b>Maximum secretion to gallbladder + intestines (MBq)</b>	23.0 $\pm$ 2.00	3.30 $\pm$ 0.28	17.7 $\pm$ 2.61	0.48 $\pm$ 0.8
<b>Gallbladder + intestines AUC (MBq x min)</b>	1926 $\pm$ 178	253 $\pm$ 67.9	1250 $\pm$ 171	39.0 $\pm$ 15.6
<b>Urinary bladder <math>C_{\text{max}}</math> (MBq)</b>	5.10 $\pm$ 0.71	10.6 $\pm$ 2.05	13.0 $\pm$ 1.98	18.5 $\pm$ 2.19
<b>Urinary bladder AUC (MBq x min)</b>	425 $\pm$ 85	758 $\pm$ 182	1093 $\pm$ 80.6	1098 $\pm$ 397
<b>Blood AUC (MBq/mL x min)</b>	426 $\pm$ 125	1138 $\pm$ 262	353 $\pm$ 58.3	742 $\pm$ 217
<b>Total clearance (mL/min)</b>	0.075 $\pm$ 0.023	0.015 $\pm$ 0.0025	0.10 $\pm$ 0.017	0.039 $\pm$ 0.017
<b>Hepatic clearance (mL/min)</b>	0.035 $\pm$ 0.014	0.0049 $\pm$ 0.0011	0.027 $\pm$ 0.0063	0.0047 $\pm$ 0.00098
<b>Biliary clearance (mL/min)</b>	0.057 $\pm$ 0.015	0.0030 $\pm$ 0.00094	0.049 $\pm$ 0.0039	0.00077 $\pm$ 0.000061
<b>Urinary clearance (mL/min)</b>	0.010 $\pm$ 0.0011	0.0093 $\pm$ 0.00033	0.034 $\pm$ 0.0058	0.030 $\pm$ 0.00062

## Discussion

[<sup>99m</sup>Tc]MEB is an OATP1 and MRP2 substrate that is used in nuclear medicine to investigate the (dys)function of liver and gallbladder. In Chapter 5, we demonstrated the ability of non-invasively visualizing and quantifying disturbed hepatic transport by drugs or genetic defects by means of  $\mu$ SPECT imaging of [<sup>99m</sup>Tc]MEB (Neyt *et al.*, 2013). However, [<sup>99m</sup>Tc]MEB is a lidocain analogue and has no similarities with endogenous bile acids. Therefore, in the current study, a procedure for the synthesis and radiolabeling of two bile acid analogues was developed, which resemble endogenous primary bile acids, for *in vitro* uptake and efflux experiment and *in vivo*  $\mu$ SPECT studies. These compounds can possibly be used to investigate the disturbances of hepatobiliary transport mechanisms by drugs *in vivo*. DTPA-chenodeoxycholic acid (DTPA-CDCA, 3a) and DTPA-cholic acid (DTPA-CA, 3b) were synthesized from respectively chenodeoxycholic and cholic acid by esterification with methanol, exchange of the methylester with ethylenediamine and subsequent coupling with DTPA-bis-anhydride as chelating agent. Finally, these bile acid analogues were successfully labeled by technetium incorporation.

*In vitro* evaluation of both compounds showed that the human uptake transporters OATP1B1 and OATP1B3 are involved in the uptake of both tracers. For [<sup>99m</sup>Tc]DTPA-CDCA,  $K_m$  values of  $8.45 \pm 0.75 \mu\text{M}$  and  $13.7 \pm 1.24 \mu\text{M}$  were obtained for OATP1B1 and OATP1B3, respectively, while for [<sup>99m</sup>Tc]DTPA-CA, these values were  $61.7 \pm 5.25 \mu\text{M}$  and  $162 \pm 16.9 \mu\text{M}$ , respectively. When these  $K_m$  values are compared to the  $K_m$  values of endogenous bile acids, values which were in the same range were observed ( $K_m$  OATP1B1 cholate:  $11.4 \pm 2.3 \mu\text{M}$  for OATP1B1 (Cui *et al.*, 2001);  $K_m$  Oatp1 taurocholic acid =  $19.4 \pm 3.3 \mu\text{M}$ ,  $K_m$  taurodeoxycholic acid:  $3.5 \pm 0.25 \mu\text{M}$  (Hata *et al.*, 2003)). Additionally, similar transport was observed of the previously reported fluorescent tracer cholyl-L-lysyl-fluorescein (CLF) (de Waart *et al.*, 2010; Milkiewicz *et al.*, 2001). Indeed, the structures of [<sup>99m</sup>Tc]DTPA-(CD)CA are comparable to that of CLF in that, all three structures are primary bile acids with modifications on the carboxyl moiety.  $K_m$  values of CLF were in the same range as [<sup>99m</sup>Tc]DTPA-(CD)CA ( $K_m$  for OATP1B3 of CLF:  $4.6 \pm 2.7 \mu\text{M}$ ; no  $K_m$  of OATP1B1 was reported). When the newly synthesized tracers were compared with the lidocain analogue [<sup>99m</sup>Tc]MEB, which is commonly used in nuclear medicine for hepatobiliary imaging, lower  $K_m$  values were observed ( $K_m$  values of [<sup>99m</sup>Tc]MEB of  $957 \pm 78.8 \mu\text{M}$  and  $3547 \pm 294 \mu\text{M}$ ; for OATP1B1 and OATP1B3, respectively).

$V_{\max}$  values of [ $^{99m}\text{Tc}$ ]DTPA-CDCA and [ $^{99m}\text{Tc}$ ]DTPA-CA were lower compared to that of [ $^{99m}\text{Tc}$ ]MEB, indicating that the efficiency of the active transport is much lower for the bile acid analogues (Table 8.1). However, the transport rates that are observed for [ $^{99m}\text{Tc}$ ]DTPA-CDCA and [ $^{99m}\text{Tc}$ ]DTPA-CA are in the same range as the transport rates of endogenous chenodeoxycholic acid and cholic acid ( $V_{\max}$  Oatp1 taurocholic acid:  $62 \pm 1.4$  pmol/mg protein/min;  $V_{\max}$  Oatp1 taurodeoxycholic acid:  $199 \pm 27$  pmol/mg protein/min (Hata *et al.*, 2003)). In conclusion, the synthesized bile acid analogues show more similarities with endogenous bile acid transport, in comparison with [ $^{99m}\text{Tc}$ ]MEB.

To summarize, the new tracers have a higher affinity ( $K_m$ ) and a lower transporter capacity ( $V_{\max}$ ). The clearance ( $V_{\max}/K_m$ ) is slower for both compounds compared to [ $^{99m}\text{Tc}$ ]MEB.

Additionally, our data confirm previous studies that the side chain of bile acids is essential for NTCP transport. Baringhaus *et al.* (Baringhaus *et al.*, 1999) determined the pharmacophore of both NTCP and ASBT (ASBT is the ileal counterpart, NTCP and ASBT are homologous bile salt transporters), and found that the 3-OH group is not essential for transport by these transporters, in contrast to the acidic side chain. Our data are completely in line with this model. In contrast to [ $^{99m}\text{Tc}$ ]DTPA-(CD)CA, a fluorescent bile salt conjugate, taurocholychlorambucil, was found to be a substrate for human NTCP (Kullak-Ublick *et al.*, 1997). This compound is conjugated at the 3-OH position of the bile acid, whereas our compounds are conjugated at the side chain. This confirms that the 3-OH position is not essential for transport, whereas the side chain is. The less specific bile salt transporters, OATP1B1 and OATP1B3, are more likely to be involved in uptake of [ $^{99m}\text{Tc}$ ]DTPA-(CD)CA into the hepatocyte, which is in line with the broad substrate specificity of these transporters (de Graaf *et al.*, 2011). After co-incubation with rifampicin, a known OATP inhibitor, uptake of [ $^{99m}\text{Tc}$ ]DTPA-CDCA in OATP1B1 and OATP1B3 transfected cell lines was 5- and 4- fold reduced, respectively. Uptake of [ $^{99m}\text{Tc}$ ]DTPA-(CD)CA was 2 and 1.3-fold reduced, respectively. Consequently, this also confirms that these two transporters are involved in the uptake of [ $^{99m}\text{Tc}$ ]DTPA-CDCA and [ $^{99m}\text{Tc}$ ]DTPA-CA, since rifampicin is a known OATP inhibitor (Neyt *et al.*, 2013).

Finally, a difference in *in vitro* uptake between the two analogues was observed, probably due to the presence or absence of the hydroxyl group at the C12 position. Our findings are in agreement with Hata *et al.* (Hata *et al.*, 2004), who stated that the transport of trihydroxy bile acids was below that of dihydroxy bile acids. Indeed, we also reported that the transport of the

trihydroxy analogue, [<sup>99m</sup>Tc]DTPA-CA is 2.5- and 3-fold lower in OATP1B1 and OATP1B3 transfected cell lines, respectively, compared to the transport of the dihydroxy analogue [<sup>99m</sup>Tc]DTPA-CDCA. This difference in transport was also reflected in the *in vivo* results.

Vesicular efflux experiments identified MRP2 as the involved efflux transporter, and not BSEP. Uptake in MRP2 transfected inside-out vesicles at 60 minutes was respectively 2- and 1.5-fold higher in presence of ATP, compared to conditions without ATP. This is in accordance with the findings of Gerloff et al. (*Gerloff et al., 1998*), who demonstrated that unconjugated cholates are not transported by rat Bsep. This is also supported by the observation that in patients with a defect in bile acid conjugation practically no unconjugated bile acids are found in bile (*Carlton et al., 2003*). Additionally, de Waart et al. (*de Waart et al., 2010*) stated that CLF is no BSEP substrate. There seems to be a negative correlation between BSEP substrates and molecular weight. MRP2, in contrast, can accommodate larger molecules than BSEP. Since the molecular weight of the bile acid analogues in this study was almost doubled due to DTPA coupling to the primary bile acid, efflux transport by MRP2 and not BSEP can be explained by the size of the analogues. Our findings are thus completely in line.

Preclinical *in vivo* evaluation revealed that both compounds showed uptake in the liver and efflux to gallbladder and intestines. [<sup>99m</sup>Tc]DTPA-CDCA showed more uptake in the liver and efflux to gallbladder and intestines compared to [<sup>99m</sup>Tc]DTPA-CA that is cleared to a higher extent by the kidneys. This is in line with the findings of Hata et al. (*Hata et al., 2003*), who stated that dihydroxy bile acids show better transport compared to trihydroxy bile acids. Additionally, our *in vitro* data also support these *in vivo* findings: uptake of [<sup>99m</sup>Tc]DTPA-CA was lower compared to [<sup>99m</sup>Tc]DTPA-CDCA in transfected OATP1B1 and OATP1B3 cells. No enterohepatic recirculation was observed for both compounds. Asbt is the ileal counterpart (homologous bile salt transporters) of Ntcp (*Dawson et al., 2009*), and consequently, these *in vivo* data, together with the finding that rifampicin can inhibit transport of both tracers, support the finding that Ntcp is not involved in transport of [<sup>99m</sup>Tc]DTPA-(CD)CA. Since there is no recirculation of these bile acids analogues, the radiation dose is reduced.

Our *in vitro* data also supports the *in vivo* findings of the current study and a previous study in which we investigated the hepatobiliary transport of [<sup>99m</sup>Tc]MEB (*Neyt et al., 2013*). We observed lower  $V_{max}$  values for [<sup>99m</sup>Tc]DTPA-(CD)CA compared to [<sup>99m</sup>Tc]MEB. *In vivo*, we also observed slower transport compared to [<sup>99m</sup>Tc]MEB. The time to peak in the liver was



2.5 minutes for [<sup>99m</sup>Tc]MEB, whereas the time to peak was 12.0 and 12.7 minutes for [<sup>99m</sup>Tc]DTPA-CDCA and [<sup>99m</sup>Tc]DTPA-CA, respectively.

Determination of the influence of newly synthesized drugs on liver transporters is important to detect possible pharmacological inhibition that can lead to hepatotoxicity. To assess the effect of pharmacological inhibition on transporter activity, rifampicin was administered as model drug, by both the intraperitoneal and the intravenous routes. This double administration led to impaired uptake of both tracers. This was reflected in a low maximum uptake value in the liver and elevated blood concentrations. These tracers allow the detection and quantification of impaired hepatobiliary transport.

To conclude, the current study showed that [<sup>99m</sup>Tc]DTPA-CDCA as an imaging probe shows better *in vitro* and *in vivo* characteristics compared to [<sup>99m</sup>Tc]DTPA-CA. It is mainly taken up in the hepatocytes by OATP1B1 and OATP1B3; and is secreted into bile canaliculi via MRP2. Dynamic  $\mu$ SPECT imaging can be a useful noninvasive method of visualizing and quantifying hepatobiliary transporter functionality and disturbances thereof *in vivo*, which could predict drug pharmacokinetics.

## References

- Anelli PL, Lattauda L, Lorusso V, Lox G, Morisetti A, Morosini P, et al. Conjugates of gadolinium complexes to bile acids as hepatocyte-directed contrast agents for magnetic resonance imaging. *J Med Chem* 2004;47:3629-2641.
- Baringhaus KH, Matter H, Stengelin S, Kramer W. Substrate specificity of the ileal and the hepatic Na<sup>+</sup>/bile acid cotransporters of the rabbit. II. A reliable 3D QSAR pharmacophore model for the ileal Na<sup>+</sup>/bile acid cotransporter. *J Lipid Res* 1999;40:2158-2168.
- Carlton VE, Harris BZ, Puffenberger EG, Batta AK, Knisely AS, Robinson DL, et al. Complex inheritance of familial hypercholanemia with associated mutations in TJP2 and BAAT1. *Nat Genet* 2003;34:91–96.
- Cui Y, König J, Leier I, Buchholz U, Keppler D. Hepatic uptake of bilirubin and its conjugates by the human organic anion transporter SLC21A6. *J Biol Chem* 2001;273:9626-9630.
- Dawson PA, Lan T, Rao A. Bile acid transporters. *J Lipid Res* 2009;50:2340–2357.
- de Graaf W, Häusler S, Heger M, van Ginhoven TM, van Cappellen G, Benink RJ, et al. Transporters involved in the hepatic uptake of [<sup>99m</sup>Tc]-mebrofenin and indocyanine green. *J Hepatol* 2011;54:738–745.
- de Waart DR, Häusler S, Vlaming MLH, Kunne C, Hänggi E, Gruss HJ, et al. Hepatic transport mechanisms of cholyl-L-lysyl-fluorescein. *Journal Pharmacol Exp Ther* 2010;334:78-86.
- Gerloff T, Stieger B, Hagenbuch B, Madon J, Landmann L, Roth J, et al. The sister of P-glycoprotein represents the canalicular bile salt export pump of mammalian liver. *J Biol Chem* 1998; 273:10046–10050.
- Hata S, Wang P, Eftychiou N, Ananthanarayanan M, Batta A, Salen G, et al. Substrate specificities of rat oatp1 and ntcp: implications for hepatic organic anion uptake. *Am J Physiol Gastrointest Liver Physiol* 2003;285:G829-G839.
- Kullak-Ublick GA, Glasa J, Böker C, Oswald M, Grützer U, Hagenbuch B, et al. Chlorambucil-taurocholate is transported by bile acid carriers expressed in human hepatocellular carcinomas. *Gastroenterology* 1997;113:1295-1305.
- Maddrey WC. Drug-induced hepatotoxicity. *J Clin Gastroenterol.* 2005;39:S83-S89.
- Milkiewicz P, Mills CO, Hubscher SG, Cardenas R, Cardenas T, Williams A, et al. Visualization of the transport of primary and secondary bile acids across liver tissue in rats: in vivo study with fluorescent bile acids. *J Hepatol* 2001;34:4-10.
- Neyt S, Huisman MT, Vanhove C, De Man H, Vliegen M, Moerman L et al. In vivo visualization and quantification of (disturbed) Oatp mediated hepatic uptake and Mrp2 mediated biliary excretion of [<sup>99m</sup>Tc]-mebrofenin in mice. *J Nucl Med* 2013;54:624-630.

## Chapter 8: Synthesis, *in vitro* and *in vivo* evaluation of technetium labeled bile acid analogues

Pandey PS, Rai R, Singh RB. Synthesis of cholic acid-based molecular receptors : head-to-head cholaphanes. J Chem Soc 2002;1:918-923.

Rohacova J, Marin ML, Martinez-Romero A, O'Connor JE, Gomez-Lechon MJ Donato MT et al. Synthesis of new, UV-photoactive dansyl derivatives for flow cytometric studies on bile acid uptake. Org Biomol Chem 2009;7:4973-4980.

Shitara Y, Sato H, Sugiyama Y. Evaluation of Drug-Drug Interaction in the Hepatobiliary and Renal Transport of Drugs. Annu Rev Pharmacol Toxicol. 2005;45:689-723.

Sinha D, Shukla S, Chuttani K, Chandra H, Mishra AK. Synthesis and biological evaluation of (99m)Tc-DTPA-bis(His) as a potential probe for tumor imaging with SPECT. Cancer Biother Radiopharm 2009, 24:615-620.

# **Chapter 9.**

# **General discussion**



Drug induced liver injury (DILI) is the most frequent single cause of safety-related withdrawal of drugs from the market (for example iproniazid, troglitazone, benoxaprofen, etc.). Additionally, it is a major cause of attrition in the drug development process. Therefore, it is important to assess these interactions early in the drug development process.

Drug-induced cholestasis is a type of DILI that can result from defects in bile formation in the hepatocytes or flow at the bile duct level and the retention of bile acids leads to liver injury. It presents as an acute or chronic illness that will fade out after termination of the medication. Many cases of drug-induced cholestasis are a result from functional inhibition of hepatobiliary transporter by the drug or its metabolites. When hepatobiliary uptake transporters are inhibited, it can cause drug-drug interactions, bilirubinemia or hypercholanemia. For example, OATPs mediate the uptake of antibiotics, statins, chemotherapeutic agents, which are associated with cholestatic liver injury. A significant increase in statin concentration in blood is observed after cyclosporine administration, due to OATP1B1 inhibition. Additionally, OATPs are associated with drug-induced hyperbilirubinemia, which causes transient jaundice due to impaired bilirubin clearance. Drugs that can cause hyperbilirubinemia are for example atazanavir, rifampicin, cyclosporine A, saquinavir, etc. Drug interference with MRP2 can cause hyperbilirubinemia. BSEP inhibition is also a major cause of drug-induced cholestasis: cyclosporine A, glibenclamide, troglitazone, rifampicin, etc. for example exhibit cis-inhibition of BSEP in a concentration dependent manner. Inhibition of NTCP can lead to hypercholanemia. As stated before, it is important to detect these interactions from early on.

Therefore, in this work our aim was to develop non-invasive predictive methods to visualize and quantify disturbed hepatobiliary transport by drugs in mice as an alternative to the existing invasive techniques. Rifampicin was used as model compound, since it is a known *in vitro* and *in vivo* OATPs/Oatps and *in vitro* Mrp2 inhibitor. Rifampicin is both substrate and inhibitor of OATP/Oatps. 1 oral dose of 10 mg/kg in mice ensures plasma and liver concentrations of 11,9 and 35  $\mu$ M, respectively. Double administration of rifampicin (100 mg/kg i.p. and 25 mg/kg i.v.), which was used in this work, ensures high rifampicin levels in blood and liver during the dynamic SPECT measurements, which in turn ensures Oatp and Mrp2 inhibition.

In this work, our goal was to answer four research questions.

**Question 1: Is it possible to visualize and quantify altered hepatobiliary transport in mice? (Chapter 5)**

We proposed a non-invasive method to visualize and quantify altered hepatobiliary transporter function by means of SPECT imaging of [<sup>99m</sup>Tc]MEB in mice. Out of dynamic SPECT measurements, time activity curves (TACs) of the liver, gallbladder+intestines and blood pool were calculated and several metrics were obtained derived from these curves. The maximal liver uptake, time-to-peak in the liver and the area under the blood curve (AUC<sub>blood</sub>) could be used to quantify normal and disturbed hepatic uptake of [<sup>99m</sup>Tc]MEB from the liver sinusoids into the hepatocytes via Oatp. The maximal activity in the gallbladder+intestines, emergence time of the gallbladder and AUC<sub>gallbladder+intestines</sub> could be used to describe and quantify normal and altered efflux from the hepatocytes to the gallbladder and intestines, via Mrp2. Repeated measurements were performed and interanimal and intra-animal variation was lower than 13% for all metrics. Experiments performed in Oatp1a/1b and Mrp2 knock-out (KO) mice showed the critical roles of Oatp1a/1b and Mrp2, respectively, in the hepatic handling of [<sup>99m</sup>Tc]MEB. Differences in metrics between Oatp1a/1b KO and Mrp2 KO mice on the one hand and WT mice on the other hand are shown in Table 9.1. Pharmacological inhibition was achieved by rifampicin administration, a known Oatp and Mrp2 inhibitor. Rifampicin is both a substrate and inhibitor of Oatp. Therefore, a certain amount of rifampicin is able to enter the hepatocytes, where it can inhibit Mrp2, which was demonstrated by an accumulation of [<sup>99m</sup>Tc]MEB in the liver. A comparison of the metrics of rifampicin treated mice with their vehicle controls is also shown in Table 9.1. To the best of our knowledge, we were the first to demonstrate *in vivo* Mrp2 inhibition. Our method offers a novel approach for *in vivo* visualizing and quantifying disturbed hepatobiliary transport, and the differentiation between uptake and efflux alterations. We demonstrated the feasibility of visualizing and quantifying the effect of Oatp1a/1b and Mrp2 modulation by various drugs *in vivo*, with rifampicin as model drugs. Additionally, we were able to show that slight alterations in transporter activity can be detected with the proposed imaging method. Therefore, this method offers a promising approach to investigate the interaction between new chemical entities and hepatobiliary transporters.

**Table 9.1:** Summary of results: comparison of Oatp1a/1b KO, Mrp2 KO and rifampicin treated mice with their control mice (vehicle controlled or WT mice). GB: gallbladder, GB+I: gallbladder+intestines, \*: could not be observed, nd: not determined.

	AUC <sub>blood</sub>	Maximal activity liver	Time-to-peak liver	AUC <sub>liver</sub>	Mean emergence time GB	Maximal activity GB+I	AUC <sub>GB+I</sub>	k <sub>12</sub>	k <sub>21</sub>	k <sub>20</sub>
Oatp1a/1b KO	↑	↓	*	↓	*	*	*	nd	nd	nd
Mrp2 KO	=	=	=	↑	↑	↓	↓	=	=	↓
Rifampicin treated	↑	↓	↓	↑	↑	↓	↓	↓	↑	↓

**Question 2: Can this quantification be further refined by kinetic modeling of [<sup>99m</sup>Tc]MEB? (Chapter 6)**

Normal and disturbed hepatobiliary transport of [<sup>99m</sup>Tc]MEB in mice were absolutely quantified by calculating kinetic parameters from a two-tissue compartmental model. Tracer kinetic modeling of [<sup>99m</sup>Tc]MEB was performed and the following kinetic parameters were calculated: k<sub>12</sub> that is a measure for the hepatic uptake of [<sup>99m</sup>Tc]MEB from the liver sinusoids into the hepatocytes via Oatp, k<sub>21</sub> that is a measure for the basolateral efflux of [<sup>99m</sup>Tc]MEB and k<sub>20</sub> that is a measure for the canalicular efflux of [<sup>99m</sup>Tc]MEB from the liver to the gallbladder and intestines via Mrp2. Discrimination on a quantitative level between pharmacological inhibition of uptake and efflux was possible. Similar results were obtained compared to the study in Chapter 5: Mrp2 KO mice showed normal uptake and decreased efflux of [<sup>99m</sup>Tc]MEB. Rifampicin treated mice showed decreased uptake and efflux of [<sup>99m</sup>Tc]MEB. A comparison of the k-values of Mrp2 KO and rifampicin treated mice with their controls is shown in Table 9.1. Kinetic modeling enables a more robust estimation of disturbed hepatobiliary transport and estimation of k<sub>21</sub>, which is a measure for basolateral efflux. Additionally, a non-invasive image derived method was evaluated to obtain the input function, using [<sup>99m</sup>Tc]tetrofosmin to visualize the left ventricle. A comparison between the image derived input function and the sampling blood curve showed similar curves. We can conclude that these kinetic parameters can also be used to describe disturbed hepatobiliary transport.



**Question 3: Is a humanized mouse model useful for the prediction of disturbed human-type hepatobiliary transport? (Chapter 7)**

It was demonstrated that the heterozygous mice, i.e. the mice that exhibit the liver disease caused by the uPA transgene, had an impaired Oatp and Mrp2 transporter function that was reflected in a lower maximal liver uptake, a decreased  $AUC_{liver}$  and a decreased  $AUC_{gallbladder+intestines}$ . The older the mice get, the better the liver function, due to a spontaneous somatic deletion of the transgene. Thus, the liver disease in itself causes an impaired liver function. Chimeric, “humanized” mice exhibited normal uptake values, indicating normal hepatic blood flow and functional human hepatic uptake transporters of [ $^{99m}Tc$ ]MEB, namely OATP1B1/3. However, impaired liver efflux of [ $^{99m}Tc$ ]MEB compared to WT mice was observed. The degree of impaired efflux was dependent on the human albumin level in mouse serum sample and the weight of the animal. The higher the human serum albumin level, the higher the repopulation index of the human hepatocytes and the more the efflux was impaired. This impaired efflux function can be caused by a pronounced interspecies difference in the biliary excretion of Mrp2/MRP2 at the level of the protein ( $V_{max}$ ) or at the level of the intrinsic transporter affinity ( $k_m$ ) of the substrates, or a combination of both factors. It was concluded that the chimeric “humanized” mouse model could be useful to study pharmacologically disturbed hepatobiliary transport. However, the selection of mice must be handled with care, due to differences between several groups of humanized mice. Molecular SPECT imaging can be a useful screening method to select a homogenous group of humanized mice.

**Question 4: Can bile acid analogues serve as biomarkers for DILI? (Chapter 8)**

Technetium labeled diethylene triamine pentaacetic acid chenodeoxycholic acid ([ $^{99m}Tc$ ]DTPA-CDCA) and technetium labeled diethylene triamine pentaacetic acid cholic acid ([ $^{99m}Tc$ ]DTPA-CA) were successfully synthesized and radiolabeled with radiochemical purities higher than 95% within 30 minutes. Both tracers remain stable in their final formulation or dissolved in the appropriate buffer for up to 4 hours. *In vitro* cellular uptake assays showed that OATP1B1 and OATP1B3 were involved in the uptake of both tracers.  $k_m$  values were in the same range of endogenous bile acids. When these bile acid analogues were compared to [ $^{99m}Tc$ ]MEB, lower  $k_m$  values were observed, indicating that the active

components are larger for the bile acid analogues compared to [ $^{99m}\text{Tc}$ ]MEB, resulting in a higher affinity.  $V_{\text{max}}$  values were lower compared to [ $^{99m}\text{Tc}$ ]MEB, which indicates that the efficiency of the active transport is much lower for the bile acid analogues. However, transport rates were in the same range as endogenous bile acids. When these bile acid analogues were compared to each other, less uptake was observed in the cholic acid analogue. This was also shown in the *in vivo* results and indicates that the transport of trihydroxy bile acids, like cholic acid, was below that of dihydroxy bile acids, like chenodeoxycholic acid. Vesicular efflux experiments identified MRP2 as the involved efflux transporter. *In vivo* evaluation in mice showed that both tracers are taken up in the liver and are then transported to gallbladder and intestines. Additionally, urinary clearance was observed and was larger in the cholic acid analogue, compared to the chenodeoxycholic acid analogue. After administration of rifampicin, almost no hepatic uptake and efflux was observed, due to Oatp and Mrp2 inhibition. Slower transport of both compounds compared to [ $^{99m}\text{Tc}$ ]MEB was also observed *in vivo* that was in line with the *in vitro* findings. To the best of our knowledge, these were the first radiolabeled bile acid analogues that were fully characterized both *in vitro* and *in vivo*.



**Chapter 10.**  
**Broader international context,**  
**relevance, and future**  
**perspectives**



The drug development process is lengthy, costly and takes about 14 years from synthesis to marketing approval (Figure 10.1). Therefore, new strategies that aid the early detection of promising candidates or early termination of candidates that are unlikely to be successful, could improve the drug development process.

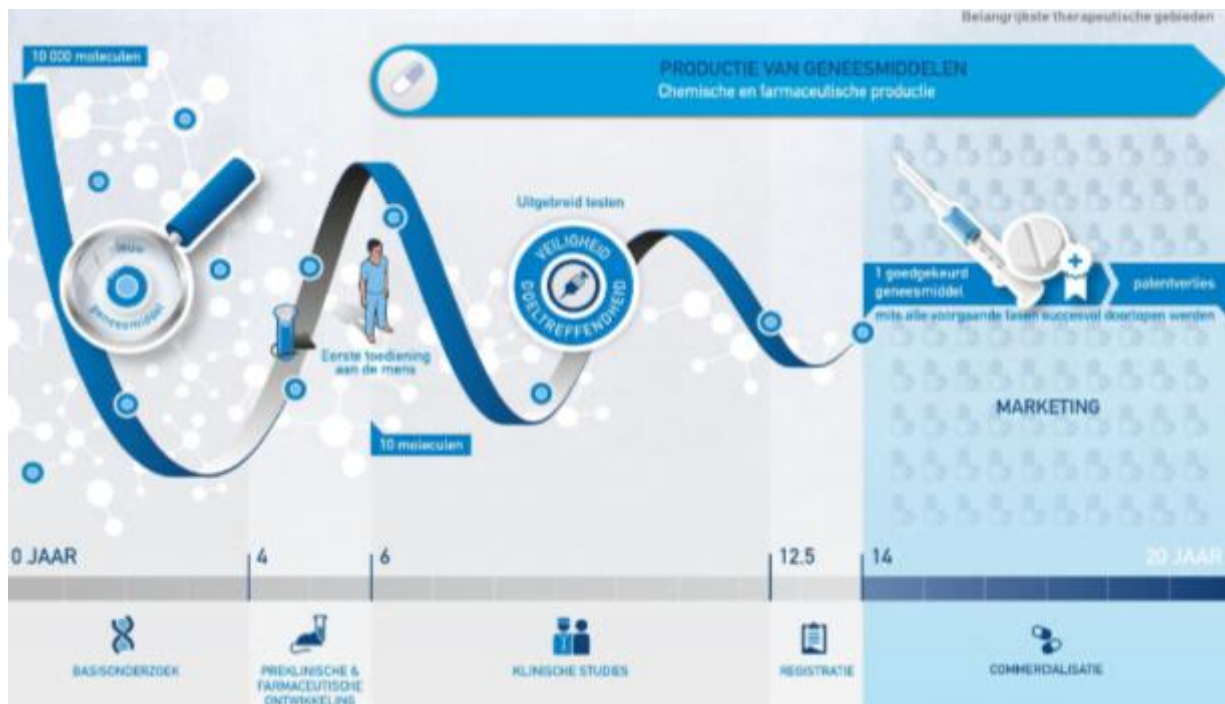
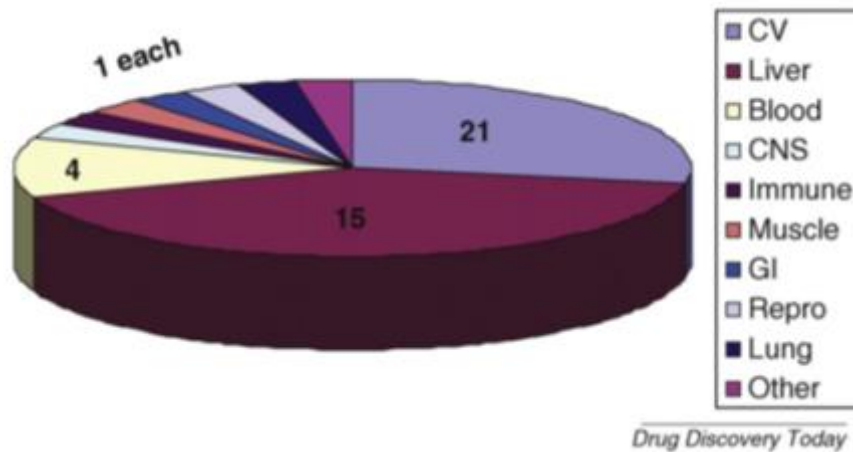


Figure 10.1: The drug development pipeline (source: Janssen Pharmaceutica)

Drug induced liver injury (DILI) is a form of acquired liver disease and is a major cause of safety-related withdrawal of drugs from the market (Figure 10.2). Additionally, it is a major cause of attrition during the drug development process. Although DILI is a rare event, it still represents a significant health problem because of its unpredictable nature, poorly understood pathogenesis and potential to cause a fatal outcome. Since DILI poses a significant burden to patient safety and to the cost of health care systems, it is crucial to assess the hepatotoxic potential of new candidate drugs early in the drug development process. It is important to improve the currently available prediction methods to identify and mitigate potential compound-related safety issues. This will result in safer drugs and a more efficient drug development process (Regev et al., 2014; Stevens et al., 2009).



**Figure 10.2:** Summary of target organ contributions to drug withdrawals from 1975-2007. Target organs were identified on the basis of the reasons for withdrawal. CV: cardiovascular; CNS: central nervous system; GI: gastrointestinal (adapted from Stevens et al., 2009).

Drug-induced cholestasis is one of the major mechanisms in DILI and many cases are a result from functional inhibition of hepatobiliary transporters by the drug or its metabolites. Cholestasis occurs when there is a disturbance, metabolic or mechanical, in bile acid homeostasis. The accumulation of bile acids in hepatocytes can become cytotoxic and cause liver injury. Table 10.1 provides an overview of drugs that are associated with induced cholestatic syndromes (de Lima Toccafondo Vieira et al., 2014; Schadt et al., 2016; Padra et al., 2011; Maddrey et al., 2005).

**Table 10.1:** Drugs associated with induced cholestatic syndromes. Listed drugs with at least 1000 reported cases of liver adverse events in the WHO database (adapted from de Lima Toccafondo Vieira et al., 2014).

Clinical manifestation	List of causative drugs
<b>Bland cholestasis</b>	Anabolic steroids, azathioprine, cetirizine, cyclosporine A, glimepiride, nevirapine, tamoxifen
<b>Cholestatic hepatitis</b>	Acitretin, amoxicillin-clavulanic acid, atorvastatin, azathioprine, bupropion, captopril, celecoxib, carbamazepine, chlorpromazine, fenofibrate, gabapentin, glimepiride, isoniazid, itraconazole, metformin, methyl dopa, macrolide antibiotics, orlistat, propafenone, propylthiouracil, risperidone, terbinafine, ticlopidine, tricyclic antidepressants, troglitazone
<b>Cholestatic hepatitis associated with bile duct injury</b>	Amoxicillin-clavulanic acid, dextropropoxyphene, flucoxacin, pioglitazone
<b>Vanishing bile duct syndrome</b>	Amitriptyline, amoxicillin/clavulanic acid, azathioprine, barbiturates, carbamazepine, chlorpromazine, cimetidine, ciprofloxacin, clindamycin,

diazepam, erythromycin, estradiolb, flucloxacillin, glibenclamide, haloperidol, ibuprofen, imipramine, methyltestosterone, phenytoin, terbinafine, tetracyclines, trimethoprim sulfamethoxazole

**Unconjugated hyperbilirubinemia**

Cyclosporine A, indinavir, rifampicin

Currently, interactions of candidate drugs with hepatic transporters are investigated by means of *in vitro*, *in silico* and invasive, expensive and time-consuming *in vivo* experiments. An overview of the available methods is given in Table 10.2.

**Table 10.2:** Current methods for the identification of drugs with cholestatic potential (*adapted from de Lima Toccafonda Vieira et al., 2014*).

<b><i>In vitro</i> methods</b>	<ul style="list-style-type: none"> <li>• Vesicular transport assay using membrane vesicles</li> <li>• Transfected cell lines</li> <li>• Suspended hepatocytes</li> <li>• In vitro biliary clearance technique using accumulation studies in sandwich-cultured hepatocytes (human and preclinical species)</li> <li>• Sandwich-cultured hepatocyte uptake and efflux assays</li> <li>• Ex vivo liver perfused technique</li> <li>• Xenobiotic metabolism</li> </ul>
<b><i>In vivo</i> based-methods</b>	<ul style="list-style-type: none"> <li>• Blood chemistry (bile acids, bilirubin, etc.)</li> <li>• Hepatobiliary transporters rodent wild-type and knock-out models</li> <li>• Bile duct-cannulated rodent models</li> </ul>
<b><i>In silico</i> methods</b>	<ul style="list-style-type: none"> <li>• Structure-activity relationship (SAR) and quantitative SAR modeling</li> <li>• 3D-pharmacophore modeling</li> <li>• Chemical category approach</li> <li>• Analogue/read-across approach</li> </ul>

*In vitro* methods are valuable to provide an efficient development of safer drugs by identifying hepatotoxic potential during early stages. Additionally, these assays contribute to the understanding of the pathogenic mechanisms, and can assist in the design and testing of alternative compounds. An ideal *in vitro* model resembles the *in vivo* situation with relevant liver functions and mechanisms of hepatotoxicity. *In vitro* high-throughput assays allow early estimation of the potential cytotoxic effect that might otherwise go undetected during preclinical development (*de Lima Toccafonda Vieira et al., 2014*).



Two different types of *in vitro* assay systems can be distinguished: membrane-based and cell-based assays. Membrane based assays use for example membranes isolated from baculovirus-infected cells overexpressing BSEP/Bsep. BSEP inhibition was considered as the major mechanism of drug induced cholestasis and therefore, the majority of the *in vitro* models rely on detection of BSEP inhibition. However, other mechanisms (for example inhibition of other bile acid transporters) are involved. Therefore, cell lines transfected with human hepatic transporters were widely used. Additionally, cell-based assays were introduced as *in vitro* model to assess drug-induced toxicity caused by bile acid accumulation as a result of disturbed bile acid homeostasis, such as suspended hepatocytes and sandwich-cultured human hepatocytes (SCHH). SCHH allow simultaneous evaluation of hepatic uptake and efflux transport at the basolateral membrane, as well as biliary secretion at the canalicular membrane (Oorts *et al.*, 2016; de Lima Toccafonda Vieira *et al.*, 2014; Annaert *et al.*, 2005; Wolf *et al.*, 2010; Nakanishi *et al.*, 2011).

*In silico* methods use computational modeling algorithms to gain insight into transporter-substrate interactions. These models can identify chemical components that are important for interaction with hepatic transporters.

During drug development, preclinical *in vivo* safety experiments are required. In these toxicity studies, increasing amounts of potential new drugs are administered to animals. Blood and bile samples are subsequently taken to measure bile acid and bilirubin concentrations in blood and bile (Bergman *et al.*, 2010). These *in vivo* experiments require liver tissue and bile samples and are therefore very invasive. In addition, these studies cannot distinguish between uptake or efflux interactions.

In this thesis, non-invasive *in vivo* methods were proposed as an alternative to the invasive, time-consuming and expensive *in vivo* models that are currently available to study drug induced cholestasis. The presented methods offer pharmaceutical companies a powerful non-invasive tool to visualize and quantify possible interactions of new candidate drugs with hepatic transporters and to identify drug-drug interactions by means of molecular SPECT imaging.

Our methods are innovative, since we are using a combination of dynamic SPECT imaging and biomarkers (mebrofenin and bile acid analogues, both labeled with technetium) for visualizing and quantifying normal and disturbed hepatobiliary transport. Additionally, we were able to quantitatively discriminate between uptake and efflux alterations. We identified several parameters that were able to quantify alterations in hepatic uptake and/or efflux using [<sup>99m</sup>Tc]MEB, [<sup>99m</sup>Tc]DTPA-CDCA and [<sup>99m</sup>Tc]DTPA-CA. Here, [<sup>99m</sup>Tc]DTPA-CDCA and [<sup>99m</sup>Tc]DTPA-CA were the first radiolabeled bile acid analogues that were completely characterized both *in vitro* and *in vivo*.

Previously, Frisch et al. (Frisch et al., 2013), Jia et al. (Jia et al., 2014) and Schacht et al. (Schacht et al., 2016) also developed radiolabeled bile acid analogues to study drug-induced cholestasis or FXR-related diseases. However, no inhibitors were evaluated and no *in vitro* characterization was done. In this context, our technetium labeled bile acid analogues are the first analogues that were fully evaluated.

The non-invasive SPECT imaging protocol of [<sup>99m</sup>Tc]MEB can also be applied for the screening of the chimeric, “humanized” mouse model to carefully select a homogenous group of mice that can be used for the assessment of new candidate drugs in pharmacokinetic and metabolism studies. To detect small alterations between two groups, it is important to have a homogenous group of mice (Sanoh et al., 2014; Jaiswal et al., 2014). This chimeric model also offers advantages compared to normal mice, due to the preclinical species specificity issue in which many hepatotoxicants remain undetected in preclinical toxicity studies.

Besides drug induced cholestasis, the bile acid analogues proposed in this thesis can also be used for other applications like functional liver assessment in cirrhosis, fibrosis, radiation induced liver injury, etc. Additionally, these analogues can be used to evaluate specific tumors. For example, OATP1B1 and OATP1B3 is downregulated in liver tumors, and OATP1B3 is frequently expressed in cancers of the gastrointestinal tract, breast, prostate and lung and may be associated with different clinical outcomes. For example, OATP expression in breast cancer is significantly associated with a hormone-dependent growth mechanism of the breast cancer, but patients expressing this OATP had a better prognosis. This can be explained by the fact that OATP also transports anticancer drugs, and this leads to a better response to anticancer therapy. Therefore, identification of OATP expression in these tumors can be beneficial and since [<sup>99m</sup>Tc]DTPA-CDCA and [<sup>99m</sup>Tc]DTPA-CA are substrates of

OATP1B1 and OATP1B3, these tracers can be used to visualize these tumors (*Yamaguchi et al., 2006; Abe et al., 2001; Buxohofer-Ausch et al., 2013*).

However, there is still a need to investigate drug-induced cholestasis that is caused by NTCP and/or BSEP inhibition. The bile acid analogues used in this thesis are OATP and MRP2 substrates, possibly due to large modifications that were done on the structure of the bile acids to allow  $^{99m}\text{Tc}$  labeling. Therefore,  $^{18}\text{F}$  labeled bile acid analogues that require only minor modification on the bile acid structure are currently in development at our laboratory by Stef De Lombaerde and are very promising. These tracers can be used to assess pharmacological inhibition of NTCP and BSEP. An additional advantage of these bile acid analogues is their applicability in PET imaging. Dynamic PET imaging is more feasible in humans compared to dynamic SPECT and absolute quantification can be easily achieved. A disadvantage is the need of a cyclotron and the shorter half-life of the  $^{18}\text{F}$  isotope.

To conclude, the future perspectives of this work are:

- (1) Mechanistic evaluation of new candidate drugs for OATP and/or MRP2 interactions by means of  $\mu\text{SPECT}$  imaging of  $[^{99m}\text{Tc}]\text{MEB}$ ,  $[^{99m}\text{Tc}]\text{DTPA-CDCA}$  or  $[^{99m}\text{Tc}]\text{DTPA-CA}$  in normal or “humanized” mice.
- (2) Screening of “humanized” mice to obtain a homogenous animal group for further studies.
- (3) Evaluation of  $[^{99m}\text{Tc}]\text{DTPA-CA}$  and  $[^{99m}\text{Tc}]\text{DTPA-CDCA}$  for cancers that have decreased or increased OATP1 expression.
- (4) Synthesis, *in vitro* and *in vivo* evaluation of  $^{18}\text{F}$  labeled bile acid analogues, in order to search for NTCP and BSEP biomarkers.
- (5) Evaluation of radiolabeled bile acid analogues for functional liver assessment in liver diseases.

## References

- Abe T, Unno M, Onogawa T, Tokui T, Kondo TN, Nakagomi R, et al. LST-2, a human liver-specific organic anion transporter, determines methotrexate sensitivity in gastrointestinal cancers. *Gastroenterology* 2001;120:1689-1699.
- Annaert PP, Brouwer KL. Assessment of drug interactions in hepatobiliary transport using rhodamine 123 in sandwich-cultured rat hepatocytes. *Drug Metab Dispos.* 2005;33:388-394.
- Buxhofer-Ausch V, Secky L, Wlcek K, Svoboda M, Kounnis V, Briasoulis E, et al. Tumor-specific expression of organic anion-transporting polypeptides: transporters as novel targets for cancer therapy. *J Drug Deliv* 2013;Epub.
- de Lima Toccafonda Vieira M, Tagliati CA. Hepatobiliary transporters in drug-induced cholestasis: a perspective on the current identifying tools. *Expert Opin Drug Metab Toxicol* 2014;10:581-597.
- Frisch K, Jakobsen S, Sorenson M, Munk OL, Alstrup AKO, Ott P, et al. [N-methyl-11C]choly sarcosine, a novel bile acid tracer for PET/CT of hepatic excretory function: radiosynthesis and proof-of-concept studies in pigs. *J Nucl Med* 2012;53:772-778.
- Jaiswal S, Sharma A, Shukla M, Vaghasiya K, Rangaraj N, Lal J. Novel pre-clinical methodologies for pharmacokinetic drug-drug interaction studies: spotlight on “humanized” animal models. *Drug Metab Rev* 2014;46:475-493.
- Jia L, Jiang D, Hu P, Li X, Shi H, Cheng D, et al. Synthesis and evaluation of 18F-labeled bile acid compound: a potential PET imaging agent for FXR-related diseases. *Nucl Med Biol* 2014;41:495-500.
- Maddrey WC. Drug-induced hepatotoxicity. *J Clin Gastroenterol.* 2005;39:S83-S89.
- Nakanishi T, Shibue Y, Fukuyama Y, et al. Quantitative time-lapse imaging-based analysis of drug-drug interaction mediated by hepatobiliary transporter, multidrug resistance-associated protein 2, in sandwich-cultured rat hepatocytes. *Drug Metab Dispos.* 2011;39:984-991.
- Oorts M, Baze A, Bachellier P, Heyd B, Zacharias T, Annaert P, et al. Drug-induced cholestasis risk assessment in sandwich-cultured human hepatocytes. *Tox in Vitro* 2016;34:179-186.
- Padda MS, Sanchez M, Akhtar AJ, Boyer JL. Drug-induced cholestasis. *Hepatology.* 2011;53:1377-1387.
- Regev A. Drug-induced liver injury and drug development: industry perspective. *Semin Liver Dis* 2014;34:227-239.
- Sanoh S, Ohta S. Chimeric mice transplanted with human hepatocytes as a model for prediction of human drug metabolism and pharmacokinetics. *Biopharm Drug Dispos* 2014;35:71-86.
- Schacht C, Sorensen M, Munk OL, Frisch. Radiosynthesis of N-11C-methyl-aurine-conjugated bile acids and biodistribution studies in pigs by PET/CT. *J Nucl Med* 2016;57:628-633.

Schadt HS, Wolf A, Pognan F, Chibout SD, Merz M, Kullak-Ublick GA. Bile acids in drug induced liver injury: key players and surrogate markers. *Clin Res Hepatol Gastroenterol* 2016; in press.

Stevens JL, Baker TK. The future of drug safety testing: expanding the view and narrowing the focus. *Drug Discov Today* 2009;14:163-167.

Wolf KK, Vora S, Webster LO, Generaux GT, Polli JW, Brouwer KLR. Use of cassette dosing in sandwich-cultured rat and human hepatocytes to identify drugs that inhibit bile acid transport *Toxicol In vitro*. 2010;24:297-309.

Yamaguchi H, Okada M, Akitaya S, Ohara H, Mikkaichi T, Ishikawa H, et al. Transport of fluorescent chenodeoxycholic acid via the human organic anion transporters OATP1B1 and OATP1B3. *J Lipid Res* 2006;47:1196-1202.

**Chapter 11.**  
**Summary – Samenvatting**  
**Curriculum Vitae**



## Summary

The liver is an important organ for homeostasis. Its most important functions include glycogen storage, production of plasma proteins and bile acids, elimination of endogenous substances and secretion of toxic compounds like drugs, carcinogens, etc. Drugs can interfere with these important functions, which can lead to drug induced liver injury. Drug induced liver injury is a major cause for the withdrawal of drugs from the market or for the termination of the development of a new candidate drug. Additionally, up to 15% of the cases of acute liver failure in Europe and the United States is caused by drug induced liver injury. An example of interference of new candidate drugs with liver functionality is inhibition of hepatic transporters. Therefore, new strategies are needed to identify and characterize interactions of new candidate drugs with hepatic transporters early in the developmental process. In this thesis, we propose non-invasive methods to assess altered transporter function, as an alternative of the invasive, time-consuming and expensive preclinical *in vivo* tests.

**Chapter 1** provided an overview of the function of the liver, with a focus on the enterohepatic cycling of bile acids and their biosynthesis, the most common bile acid transporters and an introduction on drug induced liver injury. Additionally, the main characteristics of molecular imaging, and more specifically, preclinical functional SPECT and PET imaging were given. Dynamic imaging and tracer kinetic modeling was also discussed. **Chapter 2** focused on functional liver imaging and hepatobiliary imaging agents for MR, optical imaging (fluorescence), PET and SPECT imaging. Bile acid analogues were discussed in detail. The scope and aims of this thesis were outlined in **Chapter 3**.

In **Chapter 4**, the calibration curves of the NaI(Tl) scintillation detector and SPECT camera were given. These calibration curves were used in the experimental sections to calculate exact radioactivity amounts and concentrations from the output of these two devices.

**Chapter 5** proposed a non-invasive *in vivo* method to visualize and quantify normal and disturbed hepatobiliary transport using [<sup>99m</sup>Tc]mebrofenin ([<sup>99m</sup>Tc]MEB), a tracer that is routinely used in the clinic to study function and dysfunction of the liver by planar scintigraphy. Wild type, bile duct ligated (mechanical inhibition), Oatp1a/1b knock-out (KO), Mrp2 KO and rifampicin treated (pharmacological inhibition) mice were evaluated by means of dynamic SPECT imaging after [<sup>99m</sup>Tc]MEB injection. It was demonstrated that the transport activities of Oatp1a/1b (hepatic uptake) and Mrp2 (biliary efflux) could be



quantified simultaneously *in vivo*. Moreover, pharmacological modulation of these activities was demonstrated in a dose-dependent manner using rifampicin as a model drug.

In **Chapter 6**, the quantification of normal and disturbed hepatobiliary transport was further refined by using tracer kinetic modeling of [<sup>99m</sup>Tc]MEB. A two-tissue compartmental model was proposed and the dynamic SPECT data of WT, Mrp2 KO and rifampicin treated mouse was analyzed. Additionally, a non-invasive image-derived method was evaluated to obtain the blood input function and showed similar metrics compared to manual blood sampling, which is the gold standard. The kinetic parameters were also able to quantify altered hepatobiliary transport by Oatp and Mrp2, and to discriminate between altered uptake and efflux.

**Chapter 7** characterized [<sup>99m</sup>Tc]MEB transport in chimeric mice with a humanized liver. These mice were transplanted with human hepatocytes and due to their liver disease and immunodeficiency successful engraftment was possible. SPECT imaging demonstrated that humanized mice showed normal hepatic uptake of [<sup>99m</sup>Tc]MEB. However, efflux to gallbladder and intestines was impaired compared to WT mice. Additionally, when the different groups (based on different human albumin levels and different weights) of humanized mice were compared, differences were also observed. Consequently, [<sup>99m</sup>Tc]MEB SPECT imaging was proposed as non-invasive method to select a homogenous group of humanized mice for metabolism studies.

In **Chapter 8**, two primary bile acid analogues were synthesized and evaluated both *in vitro* and *in vivo* to study the effect of pharmacological inhibition on bile acid transport. Additionally, these compounds were compared to [<sup>99m</sup>Tc]MEB. A technetium labeled chenodeoxycholic and cholic acid analogue were evaluated: technetium labeled diethylene triamine pentaacetic acid chenodeoxycholic acid ([<sup>99m</sup>Tc]DTPA-CDCA) and technetium labeled diethylene triamine pentaacetic acid cholic acid ([<sup>99m</sup>Tc]DTPA-CA). OATP1B1/3 and MRP2 were identified as the involved transporters of both compounds. *In vivo* SPECT evaluation showed uptake in the liver and efflux to gallbladder and intestines. Pharmacological inhibition with rifampicin blocked almost all the transport of the compounds.

A general conclusion and an overview of the broader international context, relevance, and future perspectives were given in **Chapter 9** and **Chapter 10**, respectively.

## Samenvatting

De lever is een belangrijk orgaan voor homeostase. De meest belangrijke functies van de lever zijn glycogeen opslag, productie van plasmaproteïnen en galzuren, eliminatie van endogene stoffen en secretie van toxische stoffen zoals geneesmiddelen, carcinogenen, etc. Geneesmiddelen kunnen interfereren met deze belangrijke functies, en dat kan dan leiden tot geneesmiddel geïnduceerde leverschade. Geneesmiddel geïnduceerde leverschade is één van de voornaamste oorzaken van het uit de handel nemen van geneesmiddelen of van de vroegtijdige stopzetting van de ontwikkeling van nieuwe geneesmiddelkandidaten. Daarenboven is meer dan 15% van de gevallen van acute leverschade in Europa en de Verenigde Staten een gevolg van geneesmiddel geïnduceerde leverschade. Een voorbeeld van interferentie van geneesmiddelen met leverfunctionaliteit is via inhibitie van transporters die aanwezig zijn in de lever. Bijgevolg is er een nood aan nieuwe strategieën om interactie van mogelijk nieuwe geneesmiddelen met deze transporters vroegtijdig te identificeren en te kwantificeren. In deze thesis worden niet-invasieve methodes om normaal en verstoord hepatobiliair transport te onderzoeken voorgesteld, als alternatief voor de bestaande invasieve, tijdrovende en dure preklinische *in vivo* experimenten.

**Hoofdstuk 1** gaf een overzicht van de leverfuncties. De nadruk lag op de enterohepatische cyclus van galzuren en hun biosynthese, de meest voorkomende galzuurtransporters en een introductie in verband met geneesmiddel geïnduceerde leverschade. Daarenboven werden de voornaamste eigenschappen van moleculaire beeldvorming besproken, en meer specifiek, van preklinische functionele SPECT en PET beeldvorming. Dynamische beeldvorming en kinetische modelering aan de hand van tracers werd ook uiteen gezet. In **Hoofdstuk 2** lag de focus op functionele lever beeldvorming en hepatobiliary speurstoffen voor MR, optische beeldvorming (fluorescentie), PET en SPECT beeldvorming. Galzuuranalogen werden in detail besproken. In **Hoofdstuk 3** werden de doelstellingen van deze thesis overlopen.

In **Hoofdstuk 4** werd een overzicht gegeven van de kalibratie curves van de NaI(Tl) scintillatie detector en de SPECT camera. Deze kalibratiecurves werden in de experimentele hoofdstukken gebruikt worden om de output van de meettoestellen om te zetten naar exacte hoeveelheden en concentraties radioactiviteit.

**Hoofdstuk 5** beschreef een niet-invasieve *in vivo* methode om normaal en verstoord hepatobiliair transport te visualiseren en te kwantificeren gebruik makende van [<sup>99m</sup>Tc]mebrofenin ([<sup>99m</sup>Tc]MEB). [<sup>99m</sup>Tc]MEB wordt routinematig gebruikt in de nucleaire

geneeskunde om de functie en disfunctie van de lever te onderzoeken met behulp van planaire scintigrafie. Wild type muizen, muizen met een galwegligatie (mechanische inhibitie), Oatp1a/1b knock-out (KO), Mrp2 KO en rifampicine behandelde (farmacologische inhibitie) muizen werden onderzocht met behulp van dynamische SPECT beeldvorming na [<sup>99m</sup>Tc]MEB injectie. Het werd aangetoond dat het mogelijk is om de transportactiviteiten van Oatp1a/1b (lever opname) en Mrp2 (biliare efflux) simultaan te kwantificeren *in vivo*. Daarenboven kon farmacologische modulatie van deze transporters aangetoond worden op een dosisafhankelijke manier met rifampicine als modelgeneesmiddel.

In **Hoofdstuk 6** werd nagegaan of de kwantificatie van normaal en verstoord hepatobiliair transport kon uitgebreid worden via kinetische modelering van [<sup>99m</sup>Tc]MEB. Een twee compartimenteel model werd voorgesteld en de dynamische SPECT data van WT, Mrp2 KO en rifampicine behandelde dieren werden geëvalueerd met behulp van dit model. Daarenboven werd een niet-invasieve methode geëvalueerd om de bloedcurve te bekomen van [<sup>99m</sup>Tc]MEB. Deze curve werd vergeleken met degene die verkregen werd na manuele bloedname, welke de gouden standaard is, en gelijkaardige curves werden bekomen. De kinetische parameters die berekend werden met behulp van het model konden gebruikt worden om normaal en verstoord hepatobiliair transport te kwantificeren. Daarnaast was deze methode ook in staat verstoorde opname en efflux van elkaar te onderscheiden.

**Hoofdstuk 7** karakteriseerde [<sup>99m</sup>Tc]MEB transport in een chimeer muismodel met een gehumaniseerde lever. Deze muizen werden getransplanteerd met humane levercellen, en door het feit dat ze immunodeficiënt zijn en een leverziekte hebben, was succesvolle transplantatie mogelijk. Na SPECT beeldvorming werd aangetoond dat deze muizen normale opname vertoonden van [<sup>99m</sup>Tc]MEB. Efflux naar galblaas en darmen was echter verstoord in vergelijking met wild type muizen. Daarenboven werd er een verschil in efflux waargenomen tussen de verschillende groepen (indeling gebaseerd op hun verschillend humaan albuminegehalte en gewicht) van gehumaniseerde muizen. Bijgevolg werd SPECT beeldvorming van [<sup>99m</sup>Tc]MEB voorgesteld als niet-invasieve method om een homogene groep van gehumaniseerde muizen te selecteren voor metabolisatie studies.

In **Hoofdstuk 8** werden twee primaire galzoutanalogen gesynthetiseerd en *in vitro* en *in vivo* geëvalueerd. Daarnaast werden beide stoffen vergeleken met [<sup>99m</sup>Tc]MEB. Een technetium gelabeld chenodeoxycholzuur and cholzuur analoog werden geëvalueerd: technetium gelabeld diethylene triamine pentaacetic acid chenodeoxycholic acid ([<sup>99m</sup>Tc]DTPA-CDCA) en

technetium gelabeld diethylene triamine pentaacetic acid cholic acid, ( $^{99m}\text{Tc}$ ]DTPA-CA). OATP1B1/3 en MRP2 werden geïdentificeerd als betrokken transporters van beide stoffen.

SPECT evaluatie toonde opname in de lever en efflux naar galblaas en darmen aan. Farmacologische inhibtie met rifampicine blokkeerde bijna al het levertransport van de stoffen.

Een algemene conclusie en een overzicht van de bredere internationale context, relevantie en toekomstperspectieven zijn beschreven in **Hoofdstuk 9** en **Hoofdstuk 10**, respectievelijk.

# Curriculum Vitae

## PERSONALIA

---

Sara Neyt

Born: January 18th 1987, Gent (Belgium)

## EDUCATION

---

- 1999-2005**            Wetenschappen – modern talen  
                              Sint-Franciscusinstituut Evergem
- 2005-2008**            Bachelor in Sciences: Biomedical Sciences  
                              Ghent University, cum laude
- 2008-2010**            Master in Sciences: Biomedical Sciences  
                              Ghent University, magna cum laude
- 2010-Today**            PhD in Pharmaceutical Sciences  
                              Ghent University

## COURSES/TRAINING

---

- 2015**            Project Management – T.O.M., Tom Jacobs  
                              Translational Biomedical *In vivo* Imaging, Ghent University
- 2013**            Effective Scientific Communication, Principae  
                              Basic Kinetic Modelling in Molecular Imaging, Copenhagen University  
                              Hospital
- 2012**            Statistics, Ghent University
- 2011**            Basic course in laboratory animal sciences, FELASA B+C, Ghent University  
                              Avanced Academic Englisch: Writing Skills, Ghent University  
                              PMOD Small Animal Imaging and Analysis Course, Zürich  
                              Experimental design and practical data analysis in Positron Emission  
                              Tomography, Imperial College London
- 2008**            Business English, Ghent University

### PEER REVIEWED PUBLICATIONS

---

**Neyt S.**, Huisman M., Vanhove C., De Man H., Vliegen M., Moerman L., Dumolyn C., Mannens G., and De Vos F. *In vivo* visualization and quantification of (disturbed) Oatp mediated hepatic uptake and Mrp2 mediated biliary excretion. *Journal of Nuclear Medicine*. 2013; 54 (4): 624-630.

**Neyt S.**, Vliegen M, Verreet B, De Lombaerde S, Braeckman K, Vanhove C, Huisman MT, Dumolyn C, Kersemans K, Hulpia F, Van Calenbergh S, Mannens G, De Vos F. Synthesis, in vitro and *in vivo* evaluation of technetium labeled bile acid analogues to study (altered) hepatic transporter function. *Nucl Med Biol* 2016; 43:642-649.

**Neyt S.**, Vanhove C, De Lombaerde S, Deblaere K, De Vos F. Kinetic modeling of <sup>99m</sup>Tc-Mebrofenin to quantify altered hepatobiliary transport in wild type, Mrp2 knock-out and rifampicin treated mice. Submitted to *Contrast Media & Molecular imaging*.

Van Laeken N, Taylor O, Polis I, **Neyt S.**, Kersemans K, Dobbeleir A, Saunders J, Goethals I, Peremans K, De Vos F. *In vivo* Evaluation of Blood Based and Reference Tissue Based PET Quantifications of [<sup>11</sup>C]DASB in the Canine Brain. *Plos One*. 2016;11(2):eCollection 2016.

Dumolyn C., Schoonooghe S., Moerman, L., **Neyt S.**, Haustraete J. and De Vos F. Generation and *in vivo* characterization of a chimeric alphavbeta5-targeting antibody 14C5 and its derivatives. *European Journal of Nuclear Medicine and Molecular Imaging Research*. 2013; 3 (1): 25.

De Lombaerde S, **Neyt S.**, Kersemans K, Verhoeven J, Devisscher L, Van Vlierberghe H, Vanhove C, De Vos F. Synthesis, in vitro and in vivo evaluation of <sup>3</sup>B-<sup>18</sup>F-fluorocholeic acid to detect drug-induced cholestasis in mice. Submitted to *J Nucl Med* 2016.

Van Welden S, De Vos M, Wielockx B, Tavernier S, Dullaers M, **Neyt S.**, et al. Hematopoietic prolyl hydroxylase-1 deficiency promotes M2 macrophage polarization and is both necessary and sufficient to protect against experimental colitis. Submitted to *J Pathol* 2016.

### ORAL PRESENTATIONS

---

Neyt S, Vliegen M, Verreet B, De Lombaerde S, Braeckman K, Vanhove C, Huisman MT, Dumolyn C, Kersemans K, Mannens G, De Vos F. Technetium labeled bile acid analogues: synthesis, in vitro and *in vivo* evaluation to study (altered) hepatic transporter function. *Knowledge for Growth* 2016, Gent, Belgium.

Neyt S., Vliegen M, Verreet B, Kersemans B, Huisman MT, Mannens G, De Vos F. Synthesis of technetium labeled bile acid analogue to study hepatic transporter function. IIS-CED Meeting, 2013, Heidelberg, Germany.

Neyt S., Huisman M.T., Mannens G., De Man H., Vliegen M., Moerman L., Bruneel S, De Vos F. *In vivo*  $\mu$ SPECT visualisation of transport-mediated hepatic uptake and efflux of a Tc-labeled HIDA analogue, and inhibition thereof. 15th Forum of Pharmaceutical Sciences, 2011, Spa, Belgium.

POSTER PRESENTATIONS

---

**Neyt S.**, Vliegen M, Verreet B, Huisman MT, Braeckman K, Dumolyn C, Vanhove C, Steemans K, Kersemans K, Denecker N, Vandendriessche V, Mannens G, De Vos F. Technetium labeled (deoxy)cholic acid analogues: Synthesis, *in vitro* and *in vivo* evaluation to study (altered) hepatic transporter function. World Molecular Imaging Congress, 2015, Honolulu, USA.

**Neyt S.**, Vanhove C, Huisman MT, Mannens G, De Vos F. *In vivo*  $\mu$ SPECT imaging of  $^{99m}\text{Tc}$ -mebrofenin to assess impaired hepatobiliary transport: a pharmacokinetic modeling study. World Molecular Imaging Congress, 2015, Honolulu, USA.

**Neyt S.**, Vliegen M, Verreet B, Huisman MT, Kersemans K, Dumolyn C, Vanhove, Geert Mannens C, De Vos F. Synthesis of technetium labeled bile acid analogues to study hepatic transporter function in mice. World Molecular Imaging Congress, 2014, Seoul, Korea.

**Neyt S.**, Meuleman P., Verhoye L., Vanhove C., Mannens G., De Vos F. (2013).  $^{99m}\text{Tc}$ -mebrofenin disposition in human liver uPA SCID mice. World Molecular Imaging Congress, 2013, Savannah, USA.

**Neyt S.**, Huisman M.T., Dumolyn C., Vliegen M., Van hove C., Mannens G., De Vos F. Non-invasive method to obtain blood curves of  $^{99m}\text{Tc}$ -mebrofenin (2013). World Molecular Imaging Congress, 2013, Savannah, USA.

**Neyt S.**, Huisman M., Mannens G., De Man H., Vliegen M., Dumolyn C., Vanhove C., De Vos F. (2012). Molecular imaging as a non-invasive tool to visualize impaired hepatobiliary transporter function in *slco1a/1b* and *abcc2* knock-out mice. Society of Nuclear Medicine and Molecular Imaging, 2012, Miami. USA. 3rd place posteraward winner

**Neyt S.**, Huisman M.T., Mannens G., De Man H., Vliegen M., Moerman L., De Vos F. (2011). *In vivo*  $\mu$ SPECT visualisation of transport-mediated hepatic uptake and efflux of  $^{99m}\text{Tc}$ -mebrofenin, and inhibition thereof with rifampicin. World Molecular Imaging Congress, 2011, San Diego, USA.